AQUEOUS SUSPENSION PLASMA SPRAYING OF YTTRIA STABILIZED ZIRCONIA SOLID OXIDE FUEL CELL ELECTROLYTES

by

David Waldbillig

A THESIS SUBMITTED IN PARTIAL FULFILLMENT OF

THE REQUIREMENTS FOR THE DEGREE OF

DOCTOR OF PHILOSOPHY

in

THE FACULTY OF GRADUATE STUDIES

(Materials Engineering)

THE UNIVERSITY OF BRITISH COLUMBIA

(Vancouver)

August 2010

Abstract

In order to meet increasing world energy demand in a sustainable manner, clean and efficient new energy technologies need to be developed. Fuel cells have been proposed as a potential energy conversion technology to help facilitate this transition to cleaner energy. Solid oxide fuel cells (SOFC) in particular are thought to be a practical, near term clean energy technology; however, current state-of-the-art wet ceramic fabrication techniques make SOFC manufacturing labour-intensive, fairly expensive and difficult to automate, and the high firing temperatures required limit the usable materials sets and increase production times.

Plasma spraying (PS) is a potential next generation SOFC fabrication process that can rapidly produce fully sintered ceramic layers without the need for post deposition heat treatments; however, it is difficult to produce the thin, fully dense layers required for SOFC electrolytes using conventional plasma spray techniques, as the carrier gas based feeding configurations typically require large feedstock powders. Suspension plasma spraying (SPS) is a modification of conventional PS processes that uses micron or sub-micron sized feedstock powders suspended in a carrier liquid. SPS has the potential to significantly improve coating quality and microstructural control. Thus plasma spray manufacturing methods may have the ability to both reduce cell fabrication and material costs and improve cell performance, making them an important step toward successful SOFC commercialization.

This project investigated the properties of metal supported aqueous SPS yttria stabilized zirconia (YSZ) layers that could be used as SOFC electrolytes and developed a thorough understanding of the relationships between the base layers (substrate and cathode), suspension and plasma spraying parameters and the resulting coating properties. Using this understanding, plasma sprayed full cells (cathode, electrolyte and anode) with optimized electrolyte microstructures with 96% density were produced and electrochemically tested. The measured open circuit voltage values were approximately 90% of the Nernst voltages, and electrolyte area specific resistances below 0.1 Ω cm^2 were

obtained at 750^{o}C for electrolyte thicknesses below 20 μm. Least-squares fitting was used to estimate the contributions of the YSZ bulk material, its microstructure, and the contact resistance to the measured series resistance values.

Table of Contents

List of Tables

List of Figures

Acknowledgements

I would like to thank the faculty, staff and my fellow graduate students at the University of British Columbia and at the University of Toronto who helped me make this project possible and who inspired me to take this project much farther than I would have been able to alone. I would especially like to acknowledge my supervisor Dr. Olivera Kesler for her support and guidance and for the addition of many commas to this thesis and the help of past and present colleagues within our group especially Brad White, Lars Rose, Craig Metcalfe, Michael Poon, Nir Ben-Oved, Jeff Harris, and Joel Kuhn.

I am deeply grateful for the advice and assistance of the technical staff in Materials Engineering, Mining Engineering, the Materials Engineering machine shop, NRC IFCI and Northwest Mettech especially Mary Fletcher, Gary Lockhart, Rudy Cardeno, Sally Finora, Pius Lo, Ross McLeod, Carl Ng, David Torok, Mark Robertson, Sing Yick and Dave Dolomont.

Thank you to both of my families for their love, encouragement and unwavering support and especially my parents for instilling in me a love of learning.

Dedication

To Beth, for always finding the silver lining. I couldn't have done this without you.

Co-authorship Statement

In the work presented in Chapters 2, 4, 5, and 6 the research programs were designed by me with input from Dr. Olivera Kesler and all experimental work and initial data analysis was done by me. The first drafts of the manuscripts were written by me with subsequent editorial assistance from Dr. Olivera Kesler.

The research performed in Chapter 3 of this thesis was performed in collaboration with Olga Arevalo-Quintero, a MSc. student in the Departments of Mechanical and Industrial Engineering at the University of Toronto supervised by Dr. Olivera Kesler.

The design of the research program for work done in this section was jointly developed by Olga, Dr. Kesler, and me as a natural extension of work done previously in my research project (see Chapter 2 of this thesis).

Experimental data collection was performed separately by Olga and me and the results were combined together. In the work, particle size and native pH measurements for YSZ batch C in Table 3.1 and 3.2 and for YSZ in Table 3.3, and all electroacoustic zeta potential measurements were performed by me as well as the initial analysis of the data arising from these experiments.

The first draft of the manuscript for Chapter 3 was written by Olga, but required extensive modifications which were performed by me. After the initial draft and rewriting, the manuscript was jointly edited by me, Olga, and Dr. Kesler.

1 Introduction

1.1 Overview

The US Energy Information Administration's 2009 International Energy Outlook report predicts that world energy consumption will increase by 44 percent from 2006 to 2030 [1]. To meet this demand in a sustainable manner, clean and efficient new energy technologies need to be developed. Fuel cells have been proposed as a potential energy conversion technology to help facilitate this transition to cleaner energy. Solid oxide fuel cells (SOFCs) in particular are thought to be a practical near term clean energy technology due to their inherently high efficiencies, ability to produce high temperature waste heat suitable for cogeneration of electricity or heating space or water, and fuel flexibility that allows SOFCs to operate on hydrocarbon and other fuels. However, current state-of-the-art wet ceramic fabrication techniques make SOFC manufacturing labour-intensive, fairly expensive, and difficult to automate, and the high firing temperatures required limit the usable materials sets and slow down production rates. Plasma spraying (PS) is a potential next generation SOFC fabrication process that can rapidly produce fully sintered ceramic layers without the need for post deposition heat treatments [2,3]. This process is relatively easy to automate, and thus would allow SOFC manufacturing costs to be reduced significantly. However, it is difficult to produce the thin (<20 μm), fully dense layers required for SOFC electrolytes using conventional plasma spray techniques, as the carrier gas based feeding configurations typically require feedstock powders between ~25 and 150 μm in diameter. Suspension plasma spraying (SPS) is a promising modification to conventional PS processes that enhances control over coating microstructure and porosity and enables thinner layers to be produced by feeding micron or sub-micron sized feedstock powders that are suspended in a carrier liquid such as water or ethanol. Suspension plasma spraying (SPS) has the potential to significantly improve coating quality and microstructural control while maintaining the rapid deposition and lack of post deposition heat treatment requirements of powder based PS processes. However, much work is required in order to understand the relationships

between substrate, feedstock, and plasma spraying parameters and the resulting coating and process characteristics such as thickness, permeability, porosity, and deposition efficiency for suspension plasma sprayed layers.

1.2 Fuel cells

Fuel cells are a clean, efficient energy conversion technology that produces electricity by the direct electrochemical combination of a fuel with an oxidant. This direct production of electricity effectively bypasses the conversion of the fuel's chemical energy into thermal and mechanical energy and thus allows higher efficiencies to be achieved compared to combustion-based processes for electricity production [4]. Solid oxide fuel cells (SOFC) are a type of fuel cell that uses a solid, ionically conducting ceramic oxide as an electrolyte. Due to the inherently low ionic conductivity of the solid electrolytes at lower temperatures, these cells typically operate at temperatures between 600 and 1000°C.

SOFCs have many advantages over other fuel cell types. They have the highest efficiency of all types of fuel cells. This efficiency can be increased further by using the high grade byproduct heat produced by SOFCs in a gas turbine for cogeneration, or to provide heat for endothermic fuel reforming processes [5]. SOFC also have a relatively high power density, which enables compact designs to give excellent power outputs.

Another significant advantage of SOFCs is that they can utilize both hydrocarbon and hydrogen based fuels, because the electrolyte material conducts oxide ions (O^{2-}) rather than hydrogen ions (H^{+}) [6]. As a result, an SOFC can use CO as fuel rather than being poisoned by it, as is the case for low temperature fuel cell types. SOFCs are also more tolerant to fuel contaminants such as sulfur than other types of fuel cells [7].

The elevated operating temperature of an SOFC provides several more competitive advantages over other fuel cell types. The heat allows the internal reformation of hydrocarbon fuels, which removes the requirement for complicated and expensive external fuel reformers. As well, elevated temperatures allow non-noble metal catalysts such as nickel to be used.

The final important advantage SOFCs have over other types of fuel cells is an all solid-state construction. Since the electrolyte is solid, corrosion problems that occur in liquid fuel cell systems are not present. In addition, water management, catalyst layer flooding and slow oxygen reduction kinetics difficulties seen in PEMFCs are not a problem due to the fact that SOFC systems have only gas and solid phases. The all solid-state construction of SOFCs also allows cell components to be fabricated into thin layers to minimize resistive losses and into unique shapes that are unachievable in liquid electrolyte systems.

1.2.1 Fuel cell components

The major components of an SOFC are the same as in all fuel cells and consist of a cathode, an electrolyte, and an anode. Multiple cells are grouped into stacks in order to build up voltage (or current). The cells are electrically connected together by interconnects. Depending on the design of the cell and stack, high temperature seals may also be required. A schematic diagram of an SOFC stack is shown in Figure 1.1.

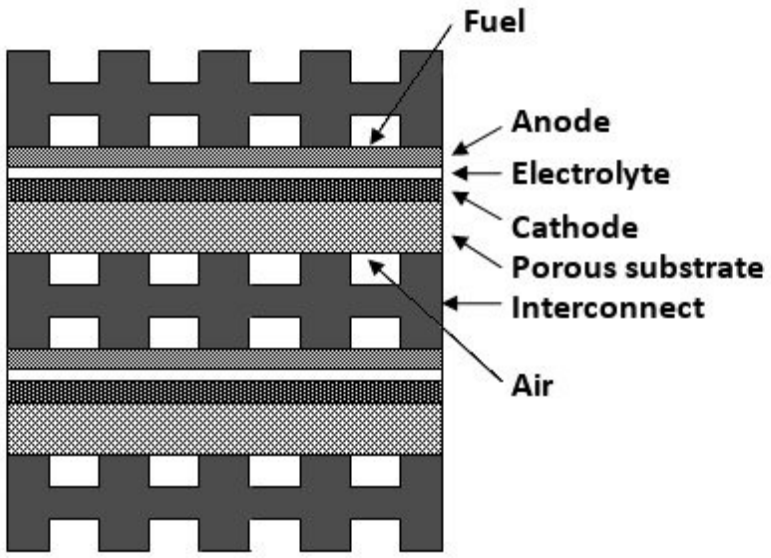

Figure 1.1: Schematic diagram of an SOFC stack.

1.2.2 Fuel cell reactions

All fuel cells produce electricity by the electrochemical oxidation of a fuel. In the simplest case, if H_2 is used as the fuel, the overall reaction can be shown by Equation 1.1.

$$H_2 + \frac{1}{2} O_2 \rightarrow H_2O \qquad (1.1)$$

A schematic diagram showing an operating SOFC is shown in Figure 1.2. A detailed explanation of the functions of and reactions at the cathode, electrolyte, and anode electrochemically active layers is given in the following sections. Fuel cell reactions occur at the triple phase boundary area of the electrodes, the areas where the electronically conductive material, the ionically conductive material, and the pores containing the oxidizing or fuel gas are in contact.

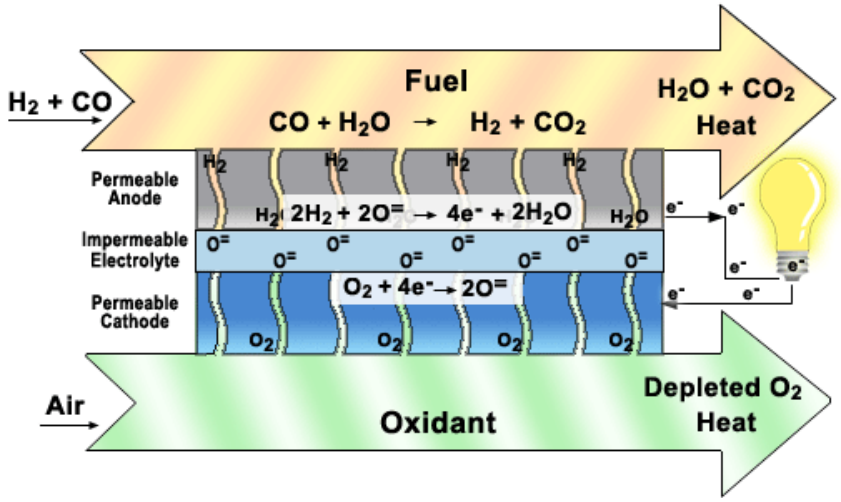

Figure 1.2: Schematic diagram of an operating SOFC [8].

1.2.3 Cathode layers

Fuel cell cathodes provide reaction sites for the electrochemical reduction of the oxidizing gas, which is most commonly oxygen from air. Cell performance may be increased by increasing the partial pressure of oxygen in the oxidizing gas [4].

The overall cathode reaction takes place by the reaction shown in Equation 1.2.

$$\frac{1}{2}O_2 + 2e^- \rightarrow O^{2-} \qquad (1.2)$$

Cathode microstructures need to be fine and porous to maximize the number of reaction sites and to ensure that there is adequate porosity to allow the air to reach the triple phase boundary area.

Cathode materials should be catalytic for oxygen reduction and should have reasonably high electronic or mixed ionic/electronic conductivity (MIEC). They also need to be stable in oxidizing environments and non-reactive with the other cell components under cell fabrication and operating conditions. Finally, cathode materials should have similar thermal expansion coefficients (TEC) to other cell components to limit differential expansion and should be low in cost.

The oxidizing conditions at the cathode and the high operating temperatures of SOFCs narrow the choice of cathode materials to noble metals such as platinum, electronically conductive oxides such as strontium doped lanthanum manganite (LSM), and mixed ionic/electronic conducting (MIEC) oxides such as the perovskite $La_{0.8}Sr_{0.2}Co_{0.8}Fe_{0.2}O_{3-y}$ (LSCF) [9]. However, many of these candidate materials react with typical electrolyte materials at electrolyte firing temperatures (1400°C); therefore, cathode material selection is frequently limited by compatibility issues with other fuel cell components [10]. Most commonly, a porous composite cathode consisting of an electronic or mixed ionic and electronically conductive (MIEC) perovskite oxide combined with YSZ or doped ceria that provides a structure with a large triple phase boundary area is used.

1.2.4 Electrolyte layers

SOFC electrolytes consist of an ionically conductive ceramic oxide which conducts the O^{2-} ions produced at the cathode to the anode. The electrolyte also serves as a barrier to separate the fuel and oxidizing gases.

Electrolyte layers should be as thin and dense as possible in order to minimize resistive losses and prevent the fuel and oxidizing gases from mixing. Potential electrolyte materials need to have high ionic conductivities and minimal electronic conductivities. They also should be stable in both reducing and oxidizing environments and non-reactive with the other cell components at cell fabrication and operating conditions. Finally, electrolyte layers need to have a good thermal expansion coefficient (TEC) match with other cell components and be low in cost.

The most commonly used SOFC electrolyte material is zirconia (ZrO_2), which is usually doped with 8 mol% yttria (Y_2O_3) in order to stabilize the cubic phase and to enhance the ionic conductivity by increasing the number of oxygen ion vacancies [4]. Yttria stabilized zirconia (YSZ) has excellent stability and ionic conductivity at high temperatures (1000^{o}C), but as the temperature decreases, the ionic conductivity decreases, thus increasing the layer resistance. At low electrolyte thickness, YSZ can be used with minimal losses to temperatures close to 650°C; however, at operating temperatures below 650°C, materials with higher ionic conductivities will likely have to be used.

Scandia stabilized zirconia (SSZ), samaria or gadolinia doped ceria (SDC, GDC), and doped perovskites such as strontium and magnesium doped lanthanum gallate (LSGM) all have higher ionic conductivities than YSZ, especially at lower operating temperatures [11]. Unfortunately, all of these materials are less stable than YSZ, especially in reducing atmospheres, and SSZ and LSGM may inter-react with other cell components during the high temperature processing required to fabricate the cells. Therefore, intermediate barrier layers or novel processing techniques are required in order to fabricate SOFCs with these high performing electrolyte materials [10].

A comparison of the ionic conductivity of many commonly studied high temperature oxygen ion conductors is shown in Figure 1.3.

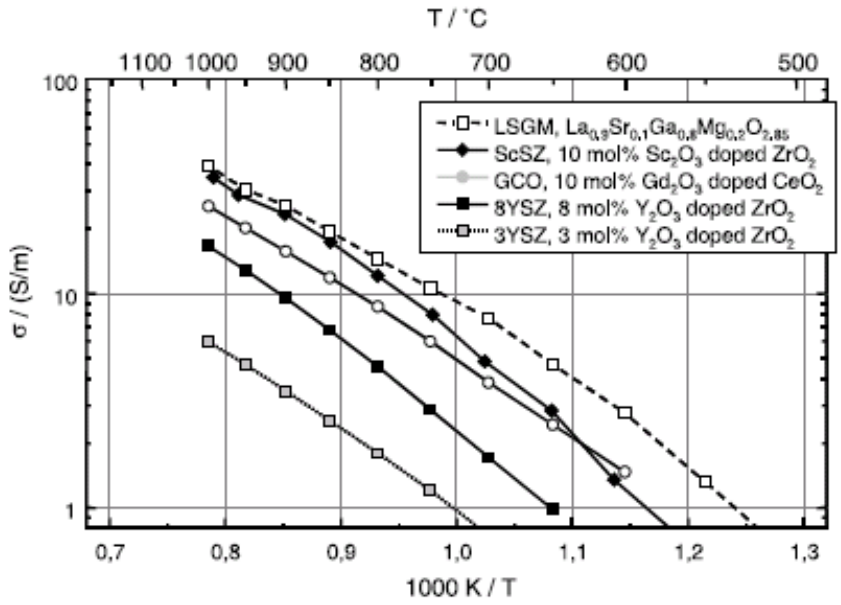

Figure 1.3: Ionic conductivity of various high temperature ionic conductors[1] [12].

1.2.5 Anode layers

In a fuel cell, the anode provides the reaction sites for electrochemical oxidation of the fuel. The overall reaction that takes place depends on the fuel being used, but in an SOFC oxidation typically takes place via the reactions shown in Equations 1.3 and 1.4.

$$H_2 + O^{2-} \rightarrow H_2O + 2e^- \qquad (1.3)$$

or if CO is used as the fuel:

$$CO + O^{2-} \rightarrow CO_2 + 2e^- \qquad (1.4)$$

Other reactions such as the direct oxidation of hydrocarbons may take place if unreformed or partially reformed hydrocarbon fuels are used.

[1] Reprinted from Journal of Power Sources, 127 / 1-2, A. Weber and E. Ivers-Tiffee, Materials and concepts for solid oxide fuel cells (SOFCs) in stationary and mobile applications, 273-283, Copyright (2004), with permission from Elsevier.

Anode materials should be catalytic for fuel oxidation and have reasonably high electronic or MIEC. They need to be stable in reducing atmospheres and non-reactive with the other cell components under cell fabrication and operating conditions. Anode materials should also have similar thermal expansion coefficients (TEC) to other cell components to limit differential expansion and be low in cost. Finally, it would be beneficial for anode materials to be resistant to coking, tolerant to fuel impurities such as sulfur, and able to resist degradation in the presence of slightly oxidizing atmospheres (redox tolerance).

The reducing conditions of the anode chamber narrow the choice of anode materials to metals, electronically conducting oxides, and mixed conducting oxides. Metallic anode materials are limited to copper, nickel, cobalt, and noble metals due to the high operating temperatures and catalytic requirements. Most commonly, SOFC anodes are fabricated from a NiO/yttria-stabilized zirconia (YSZ) ceramic composite and are reduced in-situ, during operation, to form a Ni/YSZ cermet with at least 40 vol% Ni content and greater than 30% porosity. Nickel has excellent catalytic activity for CO and H_2 oxidation, electrical conductivity, and mechanical properties, and is relatively inexpensive; however, Ni anodes often have poor redox and sulfur tolerances and may catalyze carbon deposition if hydrocarbon fuels are used [6].

Copper/ceria anodes are a promising novel materials set in order to address reduction/oxidation (redox), sulfur and carbon deposition issues; however, they are impractical to fabricate using traditional wet ceramic fabrication methods and may not have sufficient long term stability due to the sintering and creep of the copper component [13,14].

All ceramic anodes such as $SrTiO_3$ or $La_{0.8}Sr_{0.2}Cr_{0.97}V_{0.03}O_3$ (LSCV) have significantly improved redox and sulfur tolerance and are often non-coking; however, they are much more expensive, have poor electronic conductivity, and usually inter-react with other fuel cell components [15,16].

1.2.6 Interconnect layers

The interconnect is used to electrically connect the cathode of one cell to the anode of an adjacent cell to allow multiple cells to be connected in series to build up the voltage. Cells can also be connected in parallel in order to build up current to prevent cells from being electrically isolated if one cell fails; in that case, adjacent cathodes would be connected together and adjacent anodes would be connected.

Interconnect layers should be dense to prevent the fuel and oxidizing gases from mixing and have high electronic conductivity and minimal ionic conductivity. The layers must be stable in both reducing and oxidizing environments and non-reactive with the other cell components at cell fabrication and operating conditions. These layers should be low in cost and have thermal expansion coefficients (TEC) similar to those of other cell components.

The choice of interconnect material is often dependent on the desired cell operating temperature. At high operating temperatures (1000^{o}C) electronically conductive oxides such as doped $LaCrO_3$ (LC) are commonly used [17]. At operating temperatures lower than 850^{o}C, it becomes feasible to use high temperature oxidation resistant metal alloys for interconnects. Metallic interconnects have better thermal and electronic conductivity, are easier to fabricate and machine, and are less expensive than ceramic interconnects.

Ferritic stainless steels are the most commonly used metallic interconnect material due to their good oxidation resistance, excellent thermal expansion match with other components, and relatively low cost [18]. Other specialty metal alloys such as Cr-based alloys or Ni-based high temperature superalloys have also been investigated [19].

1.2.7 Mechanical support layers

Planar SOFC designs typically have one thicker layer that provides the mechanical support and provides a base for the other layers to be deposited onto. Cells may be anode, cathode, electrolyte, or interconnect supported. Originally, many cell designs were electrolyte supported in order to ensure that the electrolyte was fully dense; however, many developers have moved to an anode supported design in order to minimize

electrolyte ohmic losses by reducing electrolyte thickness. SEM images of anode supported and electrolyte supported cells are shown in Figures 1.4 and 1.5 respectively.

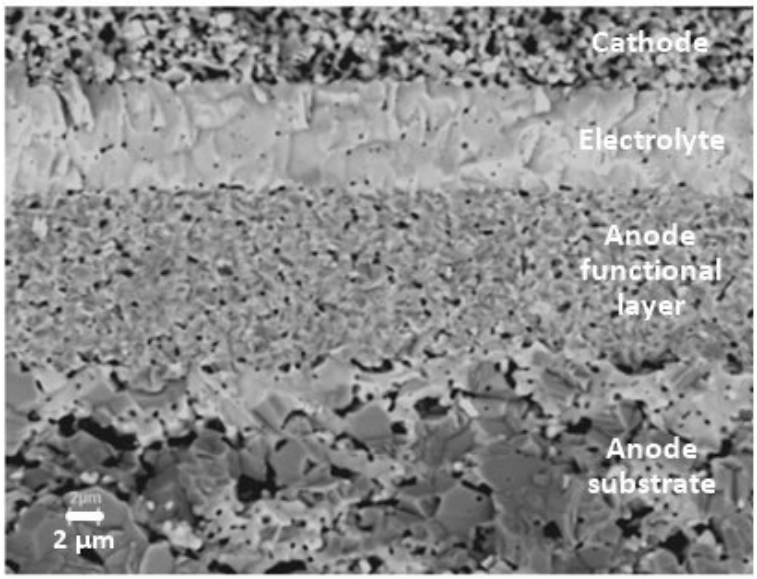

Figure 1.4: Typical microstructure of an anode supported SOFC[2] [20].

[2] Reprinted from Solid State Ionics, 176 / 9-10, D. Waldbillig, A. Wood, and D.G. Ivey, Thermal analysis of the cyclic reduction and oxidation behaviour of SOFC anodes, 847-859, Copyright (2004), with permission from Elsevier.

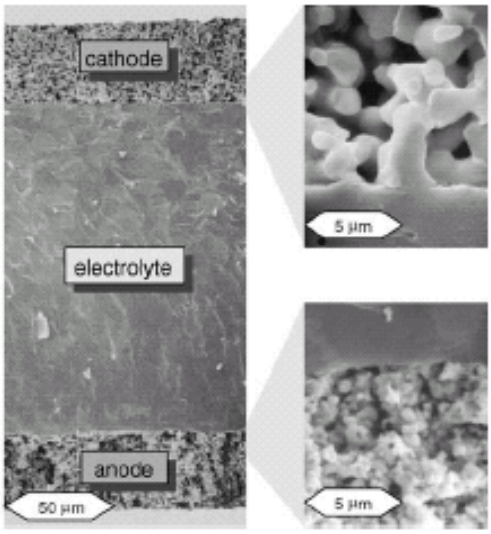

Figure 1.5: Typical microstructure of an electrolyte supported SOFC[3] [12].

A number of groups have begun to work on a cell design that is supported by a metallic layer (usually ferritic stainless steel) [21,22]. Metal supported cells would be significantly cheaper, have better thermal conductivity, and be much tougher than the state-of-the-art cermet or ceramic support layers typically used. Metal supports also allow conventional low cost metal forming and joining techniques such as stamping and welding to be used. However, the metallic substrate ultimately limits the fabrication and maximum operating temperature of the fuel cell system, since most metals are not stable at high temperatures in oxidizing atmospheres. An SEM image of a metal supported SOFC is shown in Figure 1.6.

[3] Reprinted from Journal of Power Sources, 127 / 1-2, A. Weber and E. Ivers-Tiffee, Materials and concepts for solid oxide fuel cells (SOFCs) in stationary and mobile applications, 273-283, Copyright (2004), with permission from Elsevier.

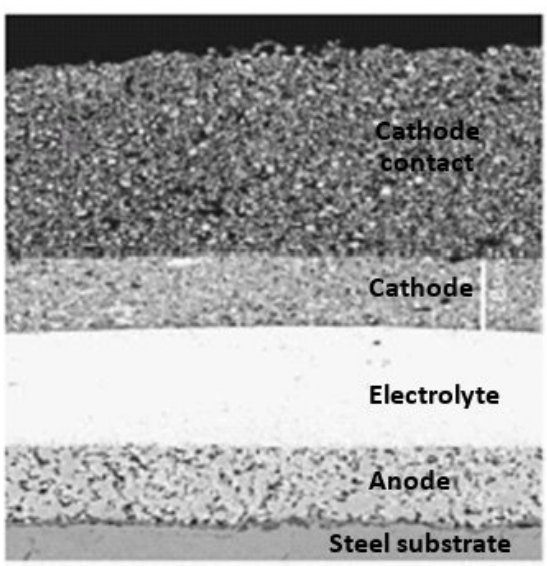

Figure 1.6: Polished cross-section of a metal (interconnect) supported SOFC[4] [22].

1.2.8 Traditional SOFC production methods

The traditional wet ceramic cell fabrication method for planar anode supported SOFCs is often made up of three major unit operations: support fabrication, active layer deposition, and firing [23]. First, a thick anode substrate support layer between 200 μm and several mm thick is produced via a single layer tape cast process or by other thick film deposition processes such as extrusion, pressing, roll compaction, etc. After the support layer is formed, the electrochemically active layers (anode functional layer, electrolyte and cathode) are deposited onto green (unfired) or fired anode substrates using methods such as screen printing, aerosol spraying, spin coating, vacuum slip casting, dip coating, etc. The next processing step is firing, which may combine support and active layer binder burnout, high temperature sintering, and cooling into a single firing step, but more commonly consists of a number of discrete firings. Images of the process equipment and cells

[4] Reprinted from Journal of Power Sources, 131 / 1-2, P. Bance, N.P. Brandon, B. Girvan, P. Holbeche, S. O'Dea, B.C.H. Steele, Spinning-out a fuel cell company from a UK University - 2 years of progress at Ceres Power, 86-90, Copyright (2004), with permission from Elsevier.

produced using Versa Power System's (VPS) TSC-2 wet ceramic SOFC production processes are shown in Figure 1.7.

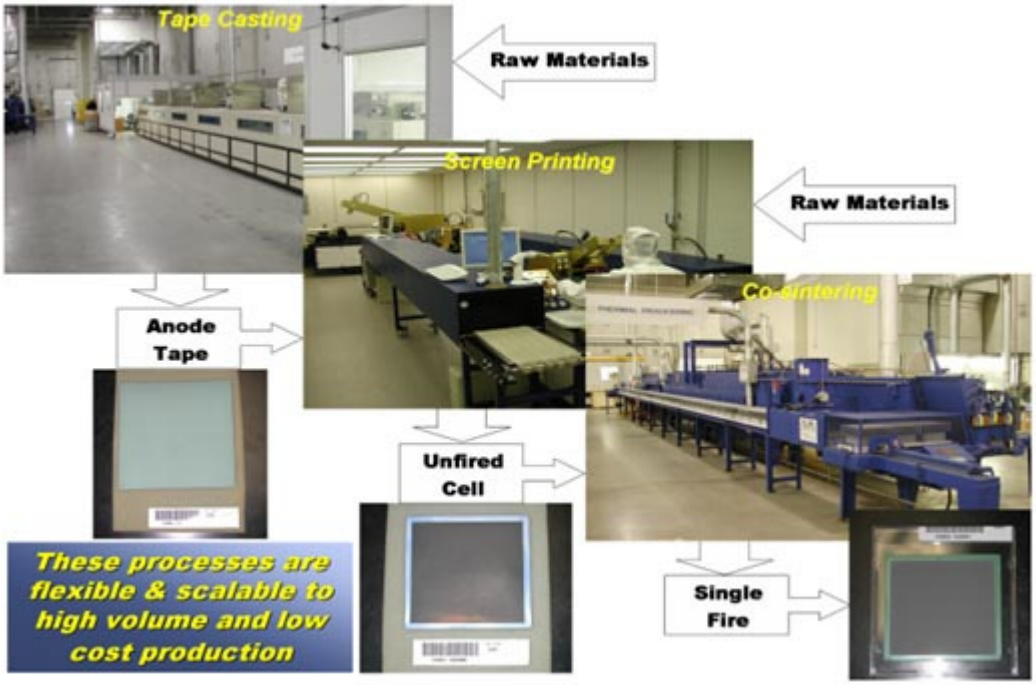

Figure 1.7: Major unit operations for SOFC production at VPS[5] [23].

The traditional wet ceramic method of SOFC production uses well established manufacturing processes that are moderately capital intensive, uses relatively cheap feedstock materials, has reasonably high yields, and produces cells with good microstructures. However, this method may have lower cell production rates than other fabrication routes due to the larger number of unique unit operations and the duration of the high temperature firing steps.

Possibly the most limiting unit operations in the wet ceramic fabrication method are the high temperature firing steps. Usually there are between two and four firing steps, each taking approximately 24 hours to complete. Firing temperatures of up to 1400°C are

[5] Reproduced by permission of the Electrochemical Society.

required in order to fully densify the electrolyte. Frequently, the cathode is applied after the electrolyte firing step and the cell is fired again to somewhat lower temperatures in order to sinter the cathode, but minimize inter-reactions between the electrolyte material and the cathode.

High temperature firings put two major constraints on SOFC production: lower cell production rates due to the number and length of firings, and inability to utilize higher performing or more cost effective materials due to incompatibilities with either the maximum sintering temperature (e.g. CuO melts at temperatures less than 1400°C) or with other cell components (e.g. many perovskite materials react with YSZ at temperatures above 1000 to 1200°C). Eliminating the requirement for a high temperature firing step by developing a new cell fabrication method would remove these limitations and thus significantly improve both cell production rates and performance.

1.3 Plasma spraying

Plasma spraying is a thermal spraying technique in which finely divided materials are deposited in a molten or semi-molten state. The thermal source used is a plasma, which may reach temperatures above 10000 K. The high plasma temperatures mean that in theory this technique may process any material; however, in practice it is difficult to achieve satisfactory deposition efficiencies for materials with vapourization or decomposition temperatures less than 300 K higher than their melting temperatures [24]. Combinations of Ar, N_2, H_2, or He are often used as the plasma forming gases. In typical plasma spraying configurations, powdered materials are injected radially (perpendicular to the plasma gas flow direction) or axially (parallel to the plasma flow) using a carrier gas into the plasma, which accelerates and melts the particles. The melted particle droplets impact onto a substrate, where they flatten and rapidly cool to form solid "splats". A coating is built up by the layering of subsequent splats. A schematic of a plasma spray process using radial injection is shown in Figure 1.8.

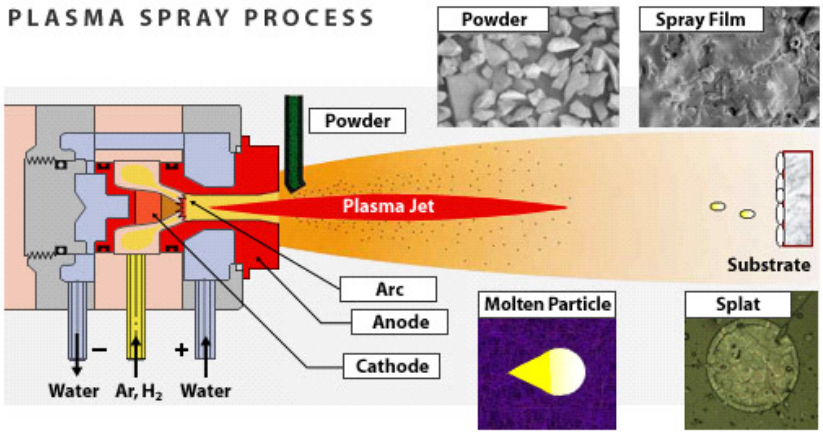

Figure 1.8: Schematic diagram of a plasma spray process [25].

1.3.1 Background of PS applications

Since the development of plasma spraying in the 1960's, many industries have adopted PS as a method to produce value added coatings to enhance wear resistance, temperature resistance, and to repair parts [24]. Currently, plasma sprayed coatings are commonly used as thermal barrier coatings in gas turbines and diesel engines and as wear resistant coatings on print rolls.

1.3.2 Plasma gases

Argon, nitrogen, hydrogen and helium are the most commonly used plasma gases [2]. Argon is frequently the gas of choice during start up as it easily forms a plasma and less aggressively wears away at the nozzle and electrodes of the torch. Argon produces a relatively cool plasma and thus is commonly used with a secondary gas to increase the plasma energy. Nitrogen may be used either as a primary gas for high energy plasmas or as a secondary gas to increase the energy of argon based plasmas. Nitrogen plasmas are able to supply large amounts of energy due to the reversible dissociation of the molecular gas to an atomic gas [2,26]. This effect allows energy to be transferred to the sprayed material efficiently without a large drop in plasma temperature. Hydrogen and helium are commonly used as secondary gases to increase plasma thermal conductivity. Due to its

high cost, helium is typically used only if hydrogen additions have a deleterious effect on the materials being sprayed.

1.3.3 Spraying atmosphere

In order to reduce system costs and facilitate high production volumes, the spraying atmosphere is often not controlled (atmospheric plasma spraying, APS). However, interactions between the cold atmospheric gases and the plasma increase plasma turbulence and make it more difficult to deposit high density coatings.

Plasma spraying in a soft vacuum was developed in the 1970's in order to improve coating quality [24]. The reduced chamber pressure enables a long, laminar, high velocity plasma plume to be formed and reduces interactions with cold surrounding gases. These improved spray conditions make it easier to form high density coatings; however, controlling the spray atmosphere may increase spraying costs by up to one order of magnitude [24], and makes it difficult to achieve continuous production.

1.3.4 Feedstock materials

Traditional PS configurations use powder feedstock typically between 25 and 150 μm in diameter that are delivered by a carrier gas. This results in a somewhat coarse microstructure of laminae of flattened splats and interlaminar pores with poor control over microstructures and porosity. The use of finer feedstock materials would improve the ability to control the microstructure and porosity of PS coatings; however, this is a non-trivial challenge, as particles smaller than approximately 10 – 25 μm require carrier gas flow rates so large that they may significantly perturb the plasma jet [24]. In order to address these issues, three alternative feedstock technologies have been developed to plasma spray finer structured layers: agglomerated powders, powder suspensions, and liquid precursors that react in the plasma to form small particles of the desired materials.

Small particles can be agglomerated using techniques such as spray drying and loosely sintered together to produce agglomerates that are large enough to be delivered by carrier gases [27]. The agglomerates can then be sprayed at conditions that partially melt the

particles, thus causing many small splats upon impact, or alternatively, the agglomerates can be loosely sintered so that they remain together during particle delivery but are fragmented into the component powders upon entering the plasma. The agglomeration technique allows finer microstructures to be formed; however, the agglomeration step increases feedstock powder cost.

Another option is to modify the feedstock supply system to allow liquid delivery. This allows micron to sub-micron sized particles to be suspended in a carrier liquid such as water or ethanol and sprayed directly. However, significant modifications to the plasma spray system are required, and much work is involved to optimize the suspension by choosing the best suspending liquid, solid concentration, and dispersant. The choice of suspending liquid must take into account factors such as cost and availability, as well as the ability of the liquid to form good droplets i.e. liquid viscosity, surface tension, etc, and the liquid's effect on the plasma. Suspension spraying has been used successfully to produce finer microstructured layers for SOFCs [28,29], nanostructured TiO_2 coatings [30], and ultrafine hydroxyapatite powders [31].

Liquid spraying systems can also be used to spray liquid precursor solutions such as nitrates, acetates, or hydroxides. These precursors react in the plasma to form solid nano-particles of the desired material, which then deposit on the substrate. However, precursor solutions may be significantly more expensive than powders and may severely corrode the torch and liquid delivery system. Liquid precursor spraying has been used previously to form alumina and zirconia coatings [32].

1.3.5 Feeding geometries

There are two main feed geometries that have been developed for plasma spray systems: radial and axial. Radial geometries feed the spray material from the outside of the torch into the plasma jet at an angle close to perpendicular to the plasma gas flow direction [33]. This geometry relaxes dimensional constraints on the feed lines, but may result in lower deposition efficiencies and requires feedstock powders with a narrow particle size distribution, since small particles may not have sufficient momentum to penetrate into the

plasma jet, while large particles may pass directly through the plasma jet. Axial configurations inject the powder through the torch, directly into the centre of the plasma and parallel to the plasma gas flow direction [34]. This improves deposition efficiencies by ensuring that virtually all the injected particles pass through the hottest part of the plasma jet; however, this configuration imposes significant restrictions on the torch and feed design, as the feed tube must pass through the centre of the torch.

1.4 Plasma sprayed SOFCs

Interest has been building in PS as a next generation SOFC manufacturing process [2]. PS SOFCs have a number of potential cost and performance advantages compared to wet-ceramic SOFC manufacturing processes. The rapid deposition rate and elimination of high temperature firing operations allow for high throughputs, simple process flow, and easy automation, which lowers process, equipment, and labour costs. In addition, PS SOFC manufacturing may be able to improve SOFC performance and reduce material costs by allowing higher performing or more inexpensive material sets to be used for electrochemically active layers, since the extremely rapid cooling of PS layers gives the layers little time for the normally diffusion based inter-reactions to occur. PS fabrication also allows stainless steel mechanical supports to be used without any additional cost or performance trade-offs. Finally, PS processes may allow finer control over the composition, size or nature of functional layers, allowing these layers to be functionally graded in order to reduce thermal stresses, improve electrochemical properties, or enhance functional features such as internal reforming. However, there are still a number of technical challenges to be overcome before plasma spraying can be adopted as a commercially viable option for SOFC fabrication.

1.4.1 Drivers for PS SOFCs

1.4.1.1 Increased cell production rates

One of the most important drivers to develop PS SOFCs is to increase cell production rates and manufacturability. The current state-of-the-art wet ceramic processing method may

have up to 10 separate unit operations involving a number of different pieces of equipment, which will likely prove difficult and costly to fully automate. SOFCs can be fabricated by plasma spraying in one deposition step by changing the feedstock materials, or in three steps in which the anode, electrolyte, and cathode are deposited by dedicated plasma spray torches. Either of these processes would be extremely easy to automate and very fast due to the inherently fast deposition rates for PS.

The other processing advantage of plasma spray fabrication routes is the elimination of the costly and time consuming high temperature firing steps. With wet ceramic processes, cells are fired multiple times at temperatures between 1200 and 1400°C to sinter the deposited layers, and may require up to 24 hours for each firing due to organic burnout steps and to minimize thermal shock. This firing step is frequently the bottleneck in the entire process.

1.4.1.2 Expanded materials set

The elimination of the high temperature firing step also reduces the maximum temperature experienced by the cell from 1400°C to the cell operating conditions, which are usually between 600 and 850°C. This change significantly expands the materials that can be used for SOFCs, enabling more cost effective and higher performing materials to be chosen.

Most high performance perovskite cathode materials such as doped $LaCoO_3$ or $LaFeO_3$ react strongly with YSZ at temperatures above 1000 to 1200°C to form insulating zirconate phases [35]. Typically this inter-reaction is suppressed by depositing the cathode material after the initial high temperature firing step that sinters the electrolyte and adding an additional firing step at temperatures between 1000 and 1250°C to sinter the cathode; however, the addition of another high temperature firing step increases cell cost and increases cell production times. Alternatively, a thin layer of a material such as ceria that doesn't react with the cathode material can be added between the electrolyte and cathode to act as a barrier layer [36]. However, ceria and zirconia also inter-react at sintering temperatures above approximately 1000^oC, making this approach most useful only when the cathode and ceria interlayer can both be fired at temperatures below 1000^oC, thus compromising mechanical bonding of the cathode to the electrolyte. PS deposition of

cathode materials reduces the amount of time that the cathode material is at elevated temperatures from hours to seconds or less, which acts to suppress the formation of the diffusion limited inter-reaction phases. Relaxing inter-reaction limitations for SOFC cathodes may make new classes of higher performing cathode materials feasible for use.

New highly ionically conductive electrolyte materials such as strontium and magnesium doped lanthanum gallates (LSGM) often react severely with other cell components at sintering temperatures, but are sufficiently stable at operating temperatures. Plasma spray deposition of these materials will suppress these inter-reactions and make these high performing electrolyte materials feasible for use [37].

All ceramic anodes such as yttrium doped $SrTiO_3$ [15] and $La_{0.75}Sr_{0.25}Cr_{0.5}Mn_{0.5}O_3$ [16] have been developed in order in enhance redox and sulfur tolerance and reduce carbon deposition. Plasma spray deposition of these materials would limit any inter-reactions between cell components that may occur and thus would make these materials more feasible for use.

Copper-ceria based anodes that facilitate direct oxidation of hydrocarbons and have enhanced sulfur tolerance have been proposed as alternative anode materials. However, the low melting temperature of CuO means that these anodes are not able to be produced using traditional wet ceramic processing techniques. A novel nitrate infiltration process has been developed to process these materials [13]; however, this process is slow, time-consuming, and difficult to scale up. Plasma spray deposition of Cu/ceria anodes would allow these materials to be fabricated in a more cost effective, higher throughput process that would make these anodes much more feasible for widespread use [14].

Typical SOFCs are mechanically supported on a tape cast Ni/YSZ layer which is between ~200 μm and several mm thick. This cermet appears to provide a good combination of mechanical properties, cost, stability, conductivity, and ability to withstand firing temperatures; however, it is not very strong and is relatively brittle.

Metal supports have been put forward as a potential alternative to the traditional anode supported design. These supports have much better strength and toughness, allowing

thinner supports to be used, which could significantly improve stack volumetric power densities. Metals have superior thermal conductivity to cermet or ceramic supports, which simplifies thermal management by better removing the excess heat generated by fuel cell reactions and enables faster heat up times and improved thermal cycling behaviour. Material costs will also be reduced by replacing the expensive materials used in the thick anode support by a thinner layer composed of a cheaper material – steel. Anode sealing may also be simplified for metal supported cells as welded seals can be used, which are cheaper and more gas tight. There are a few groups that are developing metal supported cells (typically ferritic stainless steels) using wet ceramic processing methods in order to enhance support properties [38,39]. However, in order to enable these supports to survive cell processing, firing temperatures are typically lowered and firings are often performed in an inert atmosphere. Inert atmosphere firings significantly increase fabrication costs, and low temperature firings result in less dense electrolytes and force the use of sinter aids, which often increase the amount of electronic conductivity within the electrolyte, thus decreasing cell performance. Plasma spraying would allow SOFC layers to be applied directly to metallic mechanical supports without high temperature firing steps, which would enable metal supported cells to be fabricated without making the traditional performance trade-offs.

1.4.1.3 Functionally graded microstructures

Another driver towards plasma sprayed SOFCs is the ability to produce functionally graded layers by changing the feedstock materials or spraying conditions during deposition. For example, the anode porosity could be increased near the interconnect to enhance gas diffusion and decreased closer to the electrolyte in order to maximize triple phase boundary sites, or the nickel content could be increased near the anode substrate in order to better match the thermal expansion coefficient of the anode substrate and increase the electronic conductivity, and lowered near the electrolyte to better match the thermal expansion coefficient of the electrolyte and increase the redox tolerance [40]. Functional grading of SOFC layers could result in optimized microstructures with enhanced layer

adhesion, decreased electrical resistance between layers, improved delamination resistance, and enhanced redox, thermal cycling, and sulfur tolerance. These optimized microstructures are difficult to achieve using the discrete layer deposition methods such as screen printing used in the traditional wet ceramic method.

1.4.1.4 Deposition on complex geometries

One final advantage of plasma spray deposition is the ability to deposit layers on non-flat or complex geometries. Tubular or other complex SOFC geometries can have significant advantages such as ease of sealing and better thermal shock resistance and can be easily processed using plasma spraying.

1.4.2 Challenges

There are still a number of technical challenges to be overcome before plasma spraying can be adopted as a commercially viable option for SOFC fabrication.

1.4.2.1 Coarse microstructures

Conventional PS setups typically use powder feedstock that has particle sizes between 25 and 150 μm. These feedstock powders allow very high deposition rates, but produce relatively coarse microstructures. Since fuel cell layers are typically between 10 and 25 μm thick and have very fine microstructures to maximize the amount of reactive area, small feedstock particles will have to be used. In order to produce finer microstructures, agglomerated nanoparticles that break apart upon impact or in the plasma are an option, but these feedstock powders are more expensive. Nanopowders suspended in liquids or liquid precursor spraying can also be used in order to deposit layers with finer microstructures, but significant modifications need to be made to the spray configuration in order to spray liquids, and there may be a significant penalty to deposition rates.

1.4.2.2 Suboptimal porosity

Plasma sprayed coatings typically have microstructures composed of in-plane splats with porosity between 5 and 15% [41]. This is too porous for dense SOFC electrolytes and not

porous enough for the electrode layers. This means that significant modifications to plasma spray conditions already developed for other applications must be made in order to deposit SOFC layers with sufficient porosity/lack of porosity. A number of groups have been looking at depositing dense or very porous layers by plasma spraying, but there is still a lot of work to be done to optimize the microstructures produced in order to give good fuel cell performance.

Another area of research seeks to densify plasma sprayed layers by post-spraying treatments. Impregnation of zirconium and yttrium nitrate solutions into APS YSZ layers followed by a heat treatment to 400^{o}C to decompose the nitrates has been shown to improve layer density and gives cells with an open circuit voltage of up to 1.07 V at 850^{o}C [42]. However, more than ten impregnation steps were required in order to sufficiently densify the sprayed YSZ layer, which makes this method impractical. Khor et al. have densified deposited YSZ layers using spark plasma sintering. This technique combines pressure and a pulsed direct current to rapidly densify materials [43]. They claim that the density of plasma spray deposited electrolytes can be increased to close to the theoretical density by several 3 minute spark plasma sintering sessions at elevated temperatures.

1.4.2.3 Poor microstructures for composite electrodes

Depositing the composite structures required for high performing SOFC electrodes is also very challenging using PS. Optimal spray conditions must be developed for components that may have more than a 1000°C difference in melting temperatures or that may be unstable in some spraying conditions. For example, plasma gases containing H_2 tend to decompose LSM during deposition [44]. It may be quite a challenge to find compromise spray conditions that sufficiently melt stable ceramics such as YSZ, but do not vapourize or decompose less stable materials such as LSM or CuO.

1.4.2.4 Low deposition efficiencies

Traditional plasma spraying methods using radial injection also have significantly higher amounts of wasted material compared to wet ceramic methods. Since SOFC materials are

typically quite expensive, deposition efficiency must be maximized and overspray minimized in order to minimize the amount of wasted material.

1.5 Suspension plasma sprayed SOFCs

One method to overcome many of the microstructural control limitations of PS is to use suspension plasma spraying (SPS). SPS techniques use particles with diameters between 100 nm and several μm that have been suspended in a carrier liquid, often water or alcohol, as feedstock. These smaller particles produce smaller splats, which may allow finer microstructural control and may produce a more gas-tight coating for a given thickness. The smaller feedstock powders also make it easier to spray thinner coatings. This combination of microstructural control and rapid deposition may make SPS a high throughput, automatable, and cost-effective manufacturing method to produce high-performing SOFCs.

However, there are many challenges that need to be addressed in order to produce good quality SPS coatings. The first and most important issue is to develop feedstock suspensions that have well dispersed particles. This means that a comprehensive study of the pH, viscosity and zeta potential of suspensions in order to characterize particle dispersion at native pH and the effect of controlling suspension pH, solid content, and dispersant additions on particle dispersion is very important. In addition, developing methods to effectively deliver and atomize the suspensions are non-trivial challenges.

1.5.1 The behaviour of particles in suspensions

A suspension usually consists of many small particles dispersed in a suspending medium, which is often a liquid. Since the contact area between the dispersed particles and the solvent is high, surface and interparticle forces strongly influence the suspension stability, i.e., the ability of the particles to remain in suspension. The suspension stability may be determined by the total interparticle potential energy, which is given in Equation 1.5 [45].

$$V_{total} = V_{vdW} + V_{electrostatic} + V_{steric} + V_{structural} \quad (1.5)$$

where: V_{vdW} is the attractive potential energy due to long-range van der Waals interactions

$V_{electrostatic}$ is the repulsive potential energy due to interactions between similarly charged particle surfaces

V_{steric} is the repulsive potential energy due to steric interactions between the particle surfaces coated with polymeric species

$V_{structural}$ is the potential energy due to the presence of nonadsorbed species in the solution

Long range van der Waal forces between like particles are ever-present and always attractive in nature. In order to prepare stable, well-dispersed suspensions, these forces need to be countered by repulsive electrostatic or steric forces.

Electrostatic forces can be created by generating strong like-charges on the surface of the suspended particles. These like surface charges repulse adjacent particles, thus keeping them suspended in the solution. The surface charge of the particle will be positive or negative depending on the suspension pH and isoelectric point. Although the surface charge of the particles themselves is difficult to measure directly, the electrical potential at the slip boundary between ions adsorbed on the particle surface and the surrounding fluid that moves freely can be readily measured, and is called the zeta potential (ZP). A schematic diagram showing the distribution of positive and negative ions present in a colloid system is shown in Figure 1.9. The ions that are adsorbed directly on the particle surface and additional ions farther from the surface generally move with the particle if an electric field is applied, with the boundary of ions that move with the particle forming the plane at which the zeta potential is defined. The isoelectric point is the value of pH at which the particles have a zeta potential equal to zero. If the suspension pH is higher (more basic) than the isoelectric point, the particles will have a net negative charge, while in more acidic conditions the particles will have a net positive charge. Electrostatic forces are large enough to stabilize most suspensions when the absolute value of the zeta potential is greater than ~30mV [46].

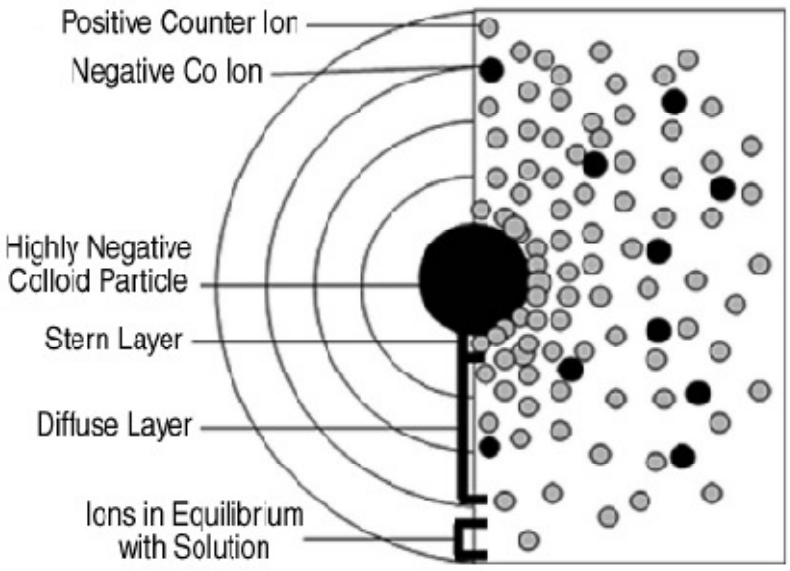

Figure 1.9: Schematic diagram showing the distribution of positive and negative ions in a colloid system[6] [47].

Steric stabilization uses a layer of adsorbed organic molecules to induce steric repulsions. The adsorbed layer must be strongly anchored to the particle surface and be sufficiently thick and dense to overcome the van der Waal attractive forces.

There are a number of polyelectrolyte dispersants that can provide both electrostatic and steric stabilization. These polyelectrolytes typically consist of an ionizable group such as carboxylic acid and a polymeric, chain-like structure. The adsorption properties of these polyelectrolytes are very dependent on the chemical and physical properties of the particle surfaces and solvent medium [45].

Structural forces can occur between large suspended particles and non-adsorbed smaller species such as fine colloidal particles, non-adsorbed polyelectrolytes, etc. These species may promote stabilization or flocculation of the primary suspended particles.

---

[6] With kind permission from Springer Science+Business Media: JOM, Colloidal stability by surface modification, 57, 2005, 52-56, S. Kuchibhatla, A.S. Karakoti, and S. Seal, Figure 2.

A schematic diagram summarizing differences between electrostatic, steric and structural interactions is shown in Figure 1.10.

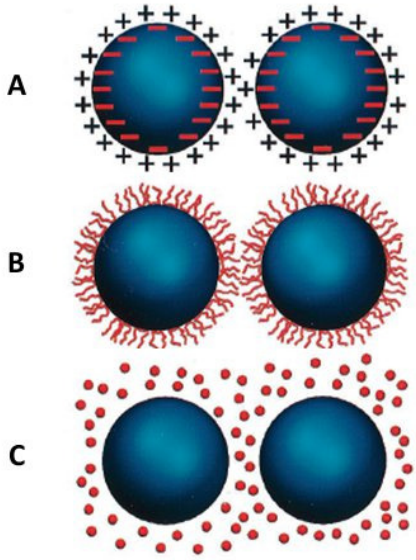

Figure 1.10: Schematic diagram showing the mechanisms of stabilization for A – electrostatic, B – steric, and C – structural forces, modified from[7] [45].

1.5.2 Effect of pH

The pH of a suspension has a significant effect on both the surface charge of the solid particles and the charge and conformation of the polyelectrolyte dispersant [48]. As mentioned in the previous section, at pH values below the isoelectric point, solid particles are positively charged, whereas at pH values above the isoelectric point, solid particles are negatively charged.

[7] Reprinted from Journal of the American Ceramic Society, 83 / 10 , J.A. Lewis, Colloidal Processing of Ceramics, 1106-1113, Copyright (2000), with permission from John Wiley and Sons.

Anionic dispersants such as polyacrylic acid (PAA) contain carboxyl groups that can dissociate to become negatively charged. At pH values below the pK_a value (pH ~ 4.5 for PAA), the PAA molecules have more undissociated groups (-COOH) compared to the dissociated $-COO^-$ groups and the solid particles interact with the polymer mostly by hydrogen bonding [49,50]. As the pH increases to a value above the pK_a but below the isoelectric point, more dissociated $-COO^-$ groups form and electrostatic interactions between the positively charged particle surfaces and the negatively charged dissociated groups will be favoured. Above the isoelectric point, particle surfaces are negatively charged and the polymer will be almost completely dissociated. Under these conditions, the similar charge provides a barrier that limits the amount of adsorption that occurs. However, in practice some limited adsorption does occur, which indicates that chemical interactions occur at high pH values that can overcome the repulsive electrostatic forces [51].

The thickness of adsorbed polymer layer and the conformation of the polymer chains are also dependent on pH values. At low pH values, the more undissociated nature of the polymer molecules and attractive nature of the opposing particle surface charge and dispersant charge cause the polymer chains to strongly bond to the particle surfaces in a thin, flattened conformation that results in mostly electrostatic stabilization [52]. As pH values increase and especially at values greater than the isoelectric point, the increasingly negative surface charge and larger number of dissociated $-COO^-$ groups within the polymer chains cause repulsive interactions to occur. These interactions produce vertical chain orientations that impart significant steric effects of the polymer on the particles [51,53].

Cationic dispersants such as polyethyleneimine contain $-NH_2$ and =NH groups that dissociate to become positively charged at pH values below the pK_a value (pH ~ 8.4 for PEI) [54]. At pH values below the isoelectric point, the positive particle surface charge and positively charged dissociated groups on the polymer chain will repel each other, lowering the amount of polymer that adsorbs on the particle surface. Any adsorption that does occur under these conditions is likely due to hydrogen bond interactions. Above the isoelectric

point, the opposing values of the negative particle surface charge and positive polymer charge facilitate electrostatic type adsorption.

For cationic polymers, the adsorbed polymer layer thickness and conformation are also affected by the pH value [54]. As the suspension pH decreases, the adsorbed layer thickness increases. The effect is caused by the increasingly positive charges on the particle surface and the polymer that occur as the pH decreases. In addition, as the pH decreases, the number of dissociated functional groups within the polymer increases, and these groups also tend to repel each other. Thus the polymer will exhibit vertical conformations that promote steric stabilization. At pH values above the isoelectric point, but below the polymer pK_a value, the increasingly negative particle surface charge causes the positively charged polymer to strongly bond to the particle surface, resulting in thin flattened conformations. As the pH increases further, above the pK_a value of the polymer, fewer dissociated groups form, which reduces the magnitude of the positive charge within the polymer. This decrease in polymer charge lowers the strength of the particle surface - polymer bonds and results in less flattened conformations.

1.5.3 Aqueous YSZ suspensions

Aqueous YSZ suspensions have been characterized in a number of studies; however, the majority of studies have focused on tetragonal zirconia partially stabilized with 3 to 4 mol% yttria. There is significant variation in published isoelectric points for YSZ depending on the phase, yttria content, and preparation and testing methods. In most studies, isoelectric point values typically fall in the range of 6 to 8 [55-66]. Most studies agree that as the amount of yttria is increased in YSZ, the isoelectric point increases closer to a pH value of 8.

The most commonly used dispersants for aqueous zirconia slurries are polyelectrolytes, typically an ammonium stabilized polyacrylic acid. These dispersants typically provide both electrostatic and steric stabilization. Table 1.1 lists a number of recent studies of aqueous YSZ suspensions with various dispersant types.

Table 1.1: Commonly used dispersants for aqueous zirconia suspensions.

Group	Powder	Dispersant	Reference
Sun, et al.	T-3YSZ	Ammonium polyacrylic acid (PAA)	55
Bergstrom, et al.	T-3YSZ	PAA	56
Liu, et al.	T-3YSZ	PAA, acrylic acid/arcylate ester copolymer, PBCTA	46, 57 ,58
Biggs, et al.	M-ZrO_2	Citric acid	59
Zhang, et al.	T-3YSZ	Triton X-114	60
Ewais, et al.	T-3YSZ	Tri-ammonium citrate	61
Briscoe, et al.	C-8YSZ	Aluminon, Tiron	62
Shojai, et al.	T-3YSZ	Ammonium polymethacrylic acid	63
Tan, et al.	T-3YSZ	Ammonium PAA	64
Tang, et al.	T-3YSZ	Darvan C (Ammonium polymethacrylic acid), Polyethylene imine (PEI), Diammonium citrate (DAC)	65
Zhang, et al.	C-8YSZ	PAA	66

M-ZrO_2 = Monoclinic ZrO_2

T-3YSZ = Tetragonal - 3 mol% Y_2O_3 partially stabilized ZrO_2

C-8YSZ = Cubic – 8 mol% Y_2O_3 stabilized ZrO_2

PAA = Polyacrylic acid

1.5.4 Suspension feeding and atomization

Methods of feeding suspensions for SPS systems is a non-trivial problem due to the abrasive nature of the suspended ceramic particles and the need for even flow rates in order to

maintain consistent coating properties. To date most SPS systems have used either peristaltic pumps or pressurized canisters for suspension delivery [67,68,69] and two-fluid atomizing nozzles [70,71]. Atomization is extremely important for radially injected suspensions in order to allow droplets to enter and become well-entrained in the plasma plume rather than passing through or bouncing off the plasma. Atomization may be less critical for axial injection systems, as the suspension is injected directly into the center of the plasma plume, so a pencil stream of suspension can be injected and the plasma itself can be used to atomize the suspension stream.

1.6 Thesis objectives

The primary objective of this thesis work was to improve the understanding of the relationships between substrate, feedstock, and plasma spraying parameters and the resulting coating and process characteristics such as thickness, permeability, porosity, and deposition efficiency for aqueous axial injection suspension plasma sprayed YSZ layers. This goal was achieved using a series of systematic experimental investigations. After a general understanding of the relationship between spraying parameters and coating microstructural and physical properties was achieved, PS SOFCs were produced and electrochemically characterized to develop an understanding of the effect of the unique microstructures produced by PS processes on the electrochemical behaviour of the SOFC electrolyte layer.

1.7 Experimental methodology

1.7.1 Input materials characterization

The first task of this project was to gain a thorough knowledge of the input material properties using a variety of characterization techniques. For the purpose of this study, input materials consist of: ferritic stainless steel substrates, cathode layers, and feedstock powders.

2.54 cm diameter porous 430 ferritic stainless steel substrates (Mott Corporation, Farmington, CT, USA) were used for all tests. These substrates come in a variety of media grade sizes (MG) and one of the first characterization studies involved determining the effect of MG on the amount and size of pores, permeability, and surface roughness of the substrate and the subsequent effect of these parameters on deposited coatings. This substrate material is most commonly used as a filter medium, and the media grade designation refers to the smallest diameter of particles in micrometers that can be captured in the filter. These materials were characterized by SEM, image analysis, surface profilometry, and He permeation testing.

A mixture of spray dried 48.2 wt% lanthanum strontium manganite ($La_{0.8}Sr_{0.2}MnO_{3-\delta}$, LSM) and 51.8 wt% 8 mol% yttria-stabilized zirconia (YSZ) powders (Inframat Advanced Materials, Farmington, CT, USA) was used for the fabrication of the cathode layers. Cathode powder preparation and layer deposition parameters were developed by a previous student and for the intent of this thesis the deposited cathode layers were treated as input materials with no further process development other than a brief investigation of the effect of cathode thickness on surface roughness and permeability. These layers were characterized by SEM, surface profilometry, and He permeation testing.

Non-spray dried 8 mol% YSZ powder (Inframat Advanced Materials, Farmington, CT, USA) was used as the electrolyte feedstock. These powders were characterized by SEM and PSA.

1.7.2 Suspension development

After the input materials were characterized, the properties of the feedstock aqueous YSZ suspensions were examined by measuring the native pH, viscosity, and zeta potential of the suspensions. The dispersion of particles in the suspension is very important to produce high quality coatings and to enable easy feeding of the feedstock suspensions. After an initial characterization study of the effect of solid loading on suspension viscosity, three dispersants were chosen based on a literature study, and the effect of dispersant type and loading on the suspension properties was examined.

1.7.3 Suspension feeding equipment development

In order to feed and atomize the feedstock suspensions, significant modifications to the PS delivery system are required. A first generation suspension delivery system was designed and built by a previous MEng student using a progressive cavity pump to deliver the suspensions and a two fluid atomizing nozzle to atomize the injected suspension [72]; however, this design was not effective, as the pump seals were rapidly degraded by the abrasive suspension. The suspension delivery system was redesigned to use a pressurized canister to deliver the suspension in order to provide reproducible suspension delivery without seal wear due to the lack of moving parts. The pressure vessels were produced in house by the Materials Engineering machine shop. The nozzle design was adapted to use a pencil stream of liquid, as it was determined that sufficient atomization of the suspension was produced by the plasma itself and that the two-fluid atomizing nozzle decreased the deposition efficiency of the process, as the wide spray diameter caused significant deposition on the torch nozzle and widened the injection angle of the particles so that a greater percentage of the particles escaped the plasma edges. A third generation pressurized canister system was designed in order to improve the ease of use and sealing of the pressure vessels, and this design was also fabricated by the Materials Engineering machine shop.

1.7.4 Coating development and characterization[8]

After the input materials and suspensions were characterized and the suspension delivery system was built, a number of systematic parameter studies were made. These studies were the primary focus of the thesis work and aimed to improve the understanding of the relationships between substrate, feedstock, and plasma spraying parameters and the resulting coating and process characteristics such as thickness, permeability, porosity, and deposition efficiency[9]. Single variable parameter studies were used to investigate the effect

[8] A list of the plasma parameter studies performed can be found in Appendix J.
[9] A description of the sources of error in these measurements can be found in Appendix M.

of substrate parameters such as substrate type and cathode thickness, of suspension parameters such as solid content, dispersant nature and concentration, and suspension flow rate, and of plasma spray parameters such as pre-heat temperature, stand-off distance, nozzle size, plasma gas flow rate, and plasma gas composition on the resulting coating permeability, density, microstructure, and deposition efficiency.

1.7.5 Electrochemical characterization

Using the understanding of the processing – property relationships developed in the coating development studies, plasma sprayed full cells (cathode, electrolyte and anode) were produced for electrochemical testing. During the electrochemical testing, the effect of electrolyte microstructure and thickness on the open circuit voltage (OCV) and series resistance (R_s) was determined for three distinct electrolyte microstructures that were produced at different spraying conditions and for three electrolyte thicknesses (15 µm, 30 µm and 45 µm). In order to better understand the root causes of the various electrolyte losses, the measured series resistance (R_s) was separated into three parts: R_{YSZ}, R_μ, and R_C. R_{YSZ} corresponds to the area specific resistance caused by the limited ionic conductivity of YSZ, R_μ is the resistance due to the microstructural features within the electrolyte layer, such as porosity or splat boundaries, and R_C is the resistance due to the contact interfaces present between the cell and test station. Characterizing the microstructural resistance of the electrolyte layer is of great interest for plasma spray produced electrolytes in order to determine the effect of the microstructural features such as porosity and splat boundaries present due to plasma spray processing on the electrolyte performance.

1.8 Description of thesis chapters

The work completed in this project has been divided into 7 chapters. Chapter 1 consists of an introduction to the thesis aims and background information on the areas of fuel cells, plasma spraying and some of the benefits and challenges of plasma sprayed SOFCs. Chapter 2 details some of the suspension characterization work and investigates the effect of dispersants on the suspension viscosity and coating properties. Chapter 3 finalizes the

suspension development and characterization research and reports the detailed PSA, pH studies, rheological studies, zeta potential measurements, and the effect of dispersants for aqueous YSZ suspensions. Chapter 4 gives a general overview of the properties of SPS SOFC electrolyte layers and characterizes the effect of electrolyte thickness, pre-heat temperature, and stand-off distance on coating properties. The chapter also presents the first electrochemical results for SOFCs produced entirely using PS methods in this study. Chapter 5 is a detailed study of the energy requirements of SPS, and the effect of plasma gas flow rate and composition and nozzle size on the coating density, deposition efficiency, permeation rate, and microstructure. Chapter 6 examines three electrolyte microstructures produced from different SPS conditions and at three electrolyte thicknesses in order to determine the effect of electrolyte microstructure and thickness on the cell open circuit voltage (OCV) and series resistance (R_s). In order to better understand the root causes of the various electrolyte losses, the measured series resistance (R_s) is separated into three parts and the resistance due to the unique microstructural features within the electrolyte layer such as porosity or splat boundaries is determined. Chapter 7 summarizes the work and places the results in a broader context. Thirteen appendices have been added to the thesis to present some of the early thesis experiments that were presented as conference papers, to give further details of the experimental equipment and procedures, and to provide additional background information.

1.9 References

1. Energy Information Administration, US Department of Energy, International Energy Outlook 2009, Retrieved April 30, 2010 from http://www.eia.doe.gov/oiaf/ieo/pdf/0484(2009).pdf.
2. R. Hui, Z.W. Wang, O. Kesler, L. Rose, J. Jankovic, S. Yick, R. Maric, D. Ghosh, J Power Sources, 170(2) (2007) 308-323.
3. R. Henne, Journal of Thermal Spray Technology, 16(3) (2007), 381-403.
4. J. Larminie and A. Dicks, Fuel Cell Systems Explained, John Wiley & Sons Ltd., West Sussex, England, 2000.
5. X. Zhang, S.H. Chan, G. Li, H.K. Ho, J. Li, Z. Feng, Journal of Power Sources, 195(3) (2010) 685–702.
6. C. Sun, U. Stimming, Journal of Power Sources, 171(2) (2007), 247–260.
7. M. Gong, X. Liu, J. Trembly, C. Johnson, Journal of Power Sources, 168(2) (2007), 289–298.
8. NETL: Solid State Energy Conversion Alliance. Retrieved June 14, 2004 from http://www.seca.doe.gov.
9. C. Sun, R. Hui, J. Roller, Journal of Solid State Electrochemistry, 14(7) (2010), 1125–1144.
10. A. Mai, V.A.C. Haanappel, S. Uhlenbruck, F. Tietz, D. Stover, Solid State Ionics, 176(15-16) (2005), 1341 – 1350.
11. J.W. Fergus, Journal of Power Sources, 162(1) (2006), 30–40.
12. A. Weber and E. Ivers-Tiffee, Journal of Power Sources, 127(1-2) (2004), 273-283.
13. R.J. Gorte, S. Park, J.M. Vohs, C.H. Wang, Advanced Materials 12(19) (2000), 1465-1469.
14. N. Ben-Oved, O. Kesler, Advanced Materials Research 15-17 (2006), 287-292.
15. S.Q. Hui, A. Petric, Journal of the European Ceramic Society, 22(9-10) (2002), 1673-1681.
16. S.W. Tao, J.T.S. Irvine, Nature Materials, 2(5) (2003), 320-323.
17. J.W. Fergus, Solid State Ionics, 171(1-2) (2004), 1 –15.
18. J.W. Fergus, Materials Science and Engineering A 397(1-2) (2005) 271–283.
19. W.J. Quadakkers, J. Piron-Abellan, V. Shemet, L. Singheiser, Materials at High Temperatures, 20(2) (2003), 115-127.

20. D. Waldbillig, A. Wood, D.G. Ivey, Solid State Ionics, 176(9-10) (2004), 847-859.
21. I. Villarreal, C. Jacobson, A. Lemming, Y. Matus, S. Visco, L. De Jonghe, Electrochemical and Solid-State Letters, 6(9) (2003), A178-A179.
22. P. Bance, N.P. Brandon, B. Girvan, P. Holbeche, S. O'Dea, B.C.H. Steele, Journal of Power Sources, 131(1-2) (2004), 86-90.
23. E. Tang , F. Martell, R. Brulé, K. Marcotte, B. Borglum, pp. 935-943 in proceedings of SOFC VIII, Edited by S.C. Singhal and M. Dokiya, The Electrochemical Society Proceedings Series. Paris, France, 2003.
24. P. Fauchais, Journal of Physics D: Applied Science, 37(9) (2004), R86-R108.
25. TSET. Retrieved August 14, 2006 from www.tosohset.com/images/plasma_spray_process.jpg.
26. G . England, Plasma Flame Theory. Thermal Spray Coatings. Retrieved November 20, 2006, from http://www.gordonengland.co.uk/pft.htm.
27. B.D. White, O. Kesler, N. Ben-Oved, A. Burgess, in Proceedings of the International Thermal Spray Conference (ITSC). ASM International. Seattle, USA, 2006, e-proceedings.
28. V. Rat, C. Delbos, C. Bonhomme, J. Fazilleau, J.F. Coudert, P. Fauchais, High Temperature Material Processes, 8(1) (2004), 95-117.
29. S. Bouaricha, J. Oberste-Berghaus, J.G. Legoux, D. Ghosh, C. Moreau in Proceedings of the International Thermal Spray Conference (ITSC). German Welding Society. Basel Switzerland, 2005.
30. F. L. Toma, G. Bertrand, S. O. Chwa, C. Meunier, D. Klein, C. Coddet, Surface & Coatings Technology, 200(20-21) (2006), 5855-5862.
31. R. Kumar, P. Cheang, K.A. Khor, Biomaterials 24(15) (2003), 2611.-2621.
32. J. Karthikeyan, C. C. Berndt, S. Reddy, J. Wang, A. H. King, H. Herman, Journal of the American Ceramic Society, 81(1) (1998), 121.-128.
33. P. Fauchais, A. Vardelle, B. Dussoubs, Journal of Thermal Spray Technology 10(1) (2001), 44-66.
34. F. Tarasi, M. Medraj, A. Dolatabadi, J. Oberste-Berghaus, and C. Moreau, Journal of Thermal Spray Technology, 17(5-6) (2008), 685-691.

35. S. Skinner, International Journal of Inorganic Materials, 3(2) (2001), 113-121.
36. T.L. Nguyen, K. Kobayashi, T. Honda , Y. Iimura, K. Kato, A. Neghisi, K. Nozaki, F. Tappero, K. Sasaki, H. Shirahama, K. Ota, M. Dokiya, T. Kato, Solid State Ionics, 174(1-4) (2004), 163-174.
37. X.Q. Ma, H. Zhang, J. Dai, J. Roth, R. Hui, T.D. Xiao, D.E. Reisner, Journal of Thermal Spray Technology, 14(1) (2005), 61-66.
38. N.P. Brandon, D. Corcoran, D. Cummins, A. Duckett, K. El-Khoury, D. Haigh, R. Leah, G. Lewis, N. Maynard, T. McColm, R. Trezona, A. Selcuk, M. Schmidt, Journal of Materials Engineering and Performance, 13(3) (2004), 253-256.
39. Y.B. Matus, L.C. De Jonghe, C.P. Jacobson, S.J. Visco, Solid State Ionics, 176(5-6) (2005), 443-449.
40. D. Waldbillig, A. Wood, D.G. Ivey, Journal of the Electrochemical Society, 154(2) (2007), B133-B138.
41. O. Kesler, Materials Science Forum, 539-543 (2007), 1385-1390.
42. C.J. Li, C.X. Li, X.J. Ning, Vacuum, 73(3-4) (2004), 699-703.
43. K.A. Khor, L.G. Yu, S.H. Chan, X.J. Chen, Journal of the European Ceramic Society, 23(11) (2003), 1855-1863.
44. B.D. White, O. Kesler, Advanced Materials Research 15-17 (2006), 299-304.
45. J. A. Lewis, Journal of the American Ceramic Society, 83(10) (2000), 2341-2359.
46. Y.Q. Liu, and L. Gao, Journal of the American Ceramic Society 86(7) (2003), 1106-1113.
47. S. Kuchibhatla, A. S. Karakoti, and S. Seal, JOM, 57(12) (2005), JOM, 52-56.
48. S. Chibowski, M. Knipa, Journal of Dispersion Science and Technology, 21(6) (2000), 761-783.
49. S. Liufu, J. Xiao, Y. Li, Journal of Colloid and Interface Science, 281 (2005), 155-163.
50. S. Chibowski, E. Opala Mazur, J. Patkowski, Materials Chemistry and Physics, 93 (2005), 262-271.
51. H. Guldberg-Pedersen, L. Bergstrom, Acta mater. 48 (2000), 4563-4570.
52. A. Vaccaro, J. Hierrezuelo, M. Skarba, P. Galletto, J. Kleimann, M. Borkovec, Langmuir, 25(9) (2009), 4864-4867.

53. S. Chibowski, M. Wisniewska, A.W. Marczewski, S. Pikus, Journal of Colloid and Interface Science, 267 (2003), 1-8.
54. S. Chibowski, J. Patkowski, E. Grzadka, Journal of Colloid and Interface Science, 329 (2009), 1-10.
55. J. Sun and L. Gao, in the Proceedings of High-Performance Ceramics 2001, Key Engineering Materials, 224-2 (2002), 663-666.
56. L. Bergstrom, E. Blomberg, and H. Guldberg-Pedersen, Novel Synthesis and Processing of Ceramics: Key Engineering Materials, 159-1 (1999), 119-126.
57. Y.Q. Liu, and L. Gao, Materials Chemistry and Physics, 78(2) (2002), 480.
58. Y.Q. Liu, L. Gao, and J. Sun, Journal of the European Ceramic Society, 22(6) (2002), 863-871.
59. S. Biggs, P. J. Scales, Y. K. Leong, and T. W. Healy, Journal of the Chemical Society-Faraday Transactions, 91(17) (1995), 2921-2928.
60. J. X. Zhang, F. Ye, J. Sun, D. L. Jiang, and M. Iwasa, Colloids and Surfaces a-Physicochemical and Engineering Aspects, 254(1-3) (2005), 199-205.
61. E. Ewais, A. A. Zaman, and W. Sigmund, Journal of the European Ceramic Society, 22(16) (2002), 2805-2812.
62. B.J. Briscoe, A. U. Khan, and P. F. Luckham, Journal of the European Ceramic Society, 18(14) (1998), 2169.
63. F. Shojai, A. B. A. Pettersson, T. Mantyla, and J. B. Rosenholm, Journal of the European Ceramic Society, 20(3) (2000), 277-283.
64. Q.Q. Tan, Z. L. Tang, Z. T. Zhang, W. H. Yao, and K. M. Fang, Materials Science and Engineering B-Solid State Materials for Advanced Technology, 99(1-3) (2003), 374-377.
65. F.Q. Tang, X. X. Huang, Y. F. Zhang, and J. K. Guo, Ceramics International, 26(1) (2000), 93-97.
66. Y.L. Zhang, H. F. Gao, D. K. Peng, M. Y. Meng, and X. Q. Liu, Ceramics International, 30(6) (2004), 1049.
67. P. Fauchais, V. Rat, J.F. Coudert, R. Etchart-Salas, G. Montavon, Surface & Coatings Technology, 202 (18) (2008), 4309-4317.

68. F.L. Toma, G. Bertrand, S. Begin, C. Meunier, O. Barres, D. Klein, C. Coddet, Applied Catalysis B: Environmental 68 (1-2) (2006), 74-84.
69. L. Pawlowski, Surface & Coatings Technology, 203 (2009), 2807-2829.
70. R. Rampon, C. Filiatre, G. Bertrand, Journal of Thermal Spray Technology, 17 (1) (2008), 105-114.
71. P. Fauchais and G. Montavon, Journal of Thermal Spray Technology, 19(1-2) (2010), 226-239.
72. P. Daniel, M.Eng. Project Report, University of British Columbia, Vancouver, BC, 2006.

2 The effect of solids and dispersant loadings on the suspension viscosities and deposition rates of suspension plasma sprayed YSZ coatings[10,11]

2.1 Introduction

Fuel cells are energy conversion devices that electrochemically oxidize a fuel to produce an electric current with higher efficiencies than combustion engines. Solid oxide fuel cells (SOFCs) use an ionically conductive ceramic, typically yttria-stabilized zirconia (YSZ), as an electrolyte material. SOFCs are usually produced using wet ceramic processing techniques such as tape casting or screen printing and are fired multiple times to temperatures up to 1400^{o}C. This requirement for multiple unit operations and high temperature firings makes SOFCs labour-intensive and somewhat expensive to manufacture and leads to material incompatibility issues.

Plasma spraying is a well established technique that allows ceramic coatings to be produced rapidly without the need for post deposition heat treatments, resulting in much recent interest in fabricating SOFCs using this technique [1,2,3]. Plasma spraying also facilitates use of ferritic stainless steel supports for SOFCs, which are inexpensive and have better mechanical, thermal and electrical properties than the cermet substrates currently used in state-of-the-art SOFCs. Plasma spraying also has the ability to produce functionally graded layers which could result in higher performing microstructures. However, it is difficult to produce the thin (< 20 μm), fully dense layers required for SOFC electrolytes by powder plasma spraying, as plasma spray feedstock powders are typically between approximately 10 and 100 μm in diameter.

---

[10] A version of this chapter has been published. D. Waldbillig, O. Kesler, The effect of solids and dispersant loadings on the suspension viscosities and deposition rates of suspension plasma sprayed YSZ coatings, Surface & Coatings Technology, 203(15) (2009), 2098-2101.

[11] Reprinted from Surface & Coatings Technology, 203 / 15, D. Waldbillig, O. Kesler, The effect of solids and dispersant loadings on the suspension viscosities and deposition rates of suspension plasma sprayed YSZ coatings, 2098-2101, Copyright (2009), with permission from Elsevier.

In order to spray coatings with finer microstructures and lower porosities, suspension plasma spraying (SPS) techniques are being developed [4,5,6]. In SPS, the feedstock consists of particles typically between 100 nm and several μm in diameter suspended in a carrier liquid such as water or ethanol. These smaller particles produce smaller splats, which should produce more gas-tight coatings for a given thickness and finer microstructures. The properties of the resulting coatings are very dependent on the feedstock suspension properties. Therefore, to produce optimized coatings, both the suspension properties and spray conditions must be optimized.

Surface and interparticle forces strongly influence the suspension stability, i.e., the ability of the particles to remain in suspension. Dispersants are added to suspensions in order to modify the electrostatic or steric properties of the suspended particle surfaces to enhance their dispersion. Electrostatic forces can be created by generating strong like-charges on the surface of the suspended particles. These like surface charges repulse adjacent particles, thus keeping them suspended in the solution. Steric stabilization uses a layer of adsorbed organic molecules to induce steric repulsions. There are a number of polyelectrolyte dispersants that can provide both electrostatic and steric stabilization. These polyelectrolytes typically consist of an ionizable group such as carboxylic acid and a polymeric, chain-like structure. The adsorption properties of these polyelectrolytes are very dependent on the chemical and physical properties of the particle surfaces and solvent medium. These dispersants may be anionic (negatively charged) or cationic (positively charged).

This study examines the effect of dispersant type and concentration on the spraying behaviour of an aqueous YSZ suspension. SPS electrolyte layers were deposited on plasma sprayed composite lanthanum strontium manganite (LSM)/YSZ cathode layers that were first deposited on porous stainless steel substrates, to simulate the substrate that would be present in fuel cell electrolyte manufacturing. High solid loading suspensions were used in order to increase YSZ deposition rates and thereby decrease manufacturing times.

2.2 Experimental procedure

2.2.1 Suspension preparation

Aqueous YSZ suspensions with solid loadings between 1 and 20 vol% relative to the overall suspension volume (5.6 to 59.6 wt%) were prepared using deionized water as the solvent. 8 mol% YSZ powder (Inframat Advanced Materials, Farmington, CT, USA) was used as the feedstock powder for this study. The powder had a d_{50} agglomerate size of approximately 1.5 µm, with sizes ranging from 0.5 µm to 15 µm, as determined by laser light scattering (Mastersizer 2000, Malvern Instruments, Worcestershire, UK) [7].

Three different dispersant types: ammonium polyacrylic acid (PAA) (Ciba Specialty Chemicals, Basel, Switzerland), polyethylene imine (PEI) (Sigma Aldrich, St. Louis, MO, USA), and 2-phosphonobutane-1,2,4-tricarboxylic acid (PBTCA) (Solutia, St. Louis, MO, USA) at various concentrations were evaluated and their ability to enhance solid particle dispersion in the suspensions was measured. PAA and PBTCA are anionic dispersants, while PEI is a cationic dispersant [8,9,10]. During suspension preparation, the dispersant was first dissolved in deionized water and then solid powders were added. The weight percent of dispersant added corresponds to the weight of dispersant added compared to the total weight of solids in the suspension.[12]

2.2.2 Plasma spray processing

An Axial III Series 600 (Northwest Mettech Corp., North Vancouver, BC, Canada) atmospheric plasma spray system was modified with a pressurized delivery system to deliver the suspension axially to the feed tube of the plasma torch. The suspensions were stirred with a magnetic stirrer during spraying to prevent solids from settling. The suspension was injected through a needle type nozzle (ID = 0.84 mm) positioned directly behind the torch convergence into the centre of the plasma jet, where it was atomized. The

[12] Additional background information on the dispersants investigated can be found in Appendix I.

pressure in the pressurized vessel was fixed at 40 psi (275.8 kPa), which results in a suspension flow rate of 129.2 mL/min or a solid flow rate of 38.1 g/min (with a 5 vol% YSZ suspension)[13]. LSM/YSZ cathode deposition was carried out onto 2.54 cm diameter porous ferritic stainless steel 430 substrates (Mott Corporation, Farmington, CT, USA) mounted on a rotating turntable, using spraying conditions developed previously [11]. The torch gun moves vertically at a rate of 3.7 cm/s, while the substrate turns at 400 rpm at a radial position of 13.9 cm from the rotation axis. Electrolytes were suspension sprayed on the previously-deposited cathode layers using the conditions in Table 2.1.

Table 2.1: Plasma spraying parameter values.

Parameter	Value
Plasma gas flow rate (slpm)	220
Plasma gas composition	80% N_2 / 20% H_2
Torch current (A per electrode)	250
Nozzle size (mm)	12.7
Standoff distance (mm)	80

2.2.3 Suspension characterization

The YSZ suspension viscosities were measured using a Thermo Haake VT550 viscometer (Thermo Electron Corporation, Karlsruhe, Germany) in the coaxial cylinder configuration. Viscosity measurements were taken as the shear rate was increased to a maximum value of 400 s^{-1} and then decreased to 0. Average viscosity values were taken at a shear rate of 200 s^{-1}, at which the viscosity was no longer dependent on shear rate.

[13] A more detailed description of the suspension delivery and injection equipment can be found in Appendix D.

2.2.4 Coating characterization

Polished cross sections of the deposited layers were examined in a Hitachi S-3000N scanning electron microscope (SEM) (Hitachi High Technologies America, Pleasanton, CA, USA). Samples were cut using a low speed diamond saw, mounted in epoxy, polished using diamond polishing suspensions, and gold coated to ensure conductivity.

2.3 Results and discussion

2.3.1 Effect of solid content on suspension viscosity

Viscosity values were constant at shear rates higher than 100 s^{-1}, as shown in Figure 2.1. Figure 2.2 illustrates the effect of solid loading on the suspension viscosity. As expected, the viscosity increased as the solid loadings increased. For solid loadings higher than 15 vol% the viscosity increased rapidly.

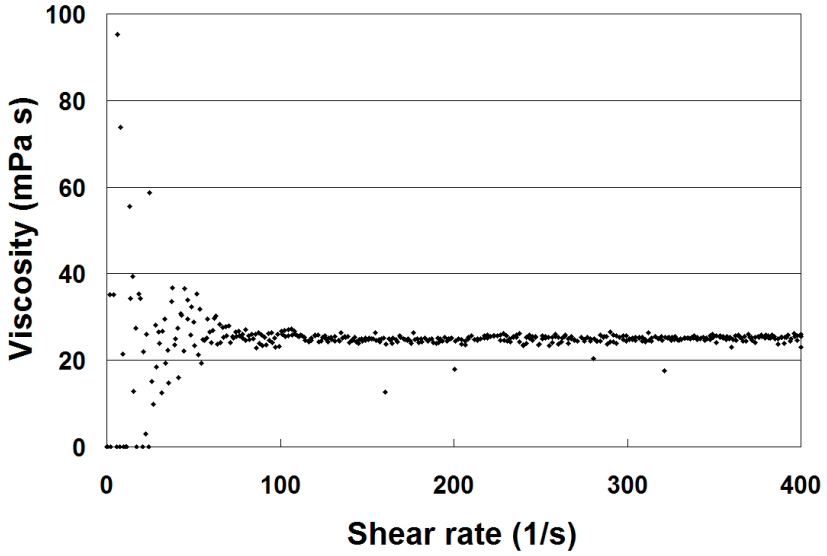

Figure 2.1: Viscosity vs. shear rate for an aqueous suspension with 20 vol% YSZ[14].

[14] See Appendix I for a more detailed explanation of the suspension viscosity behaviour at various shear rates.

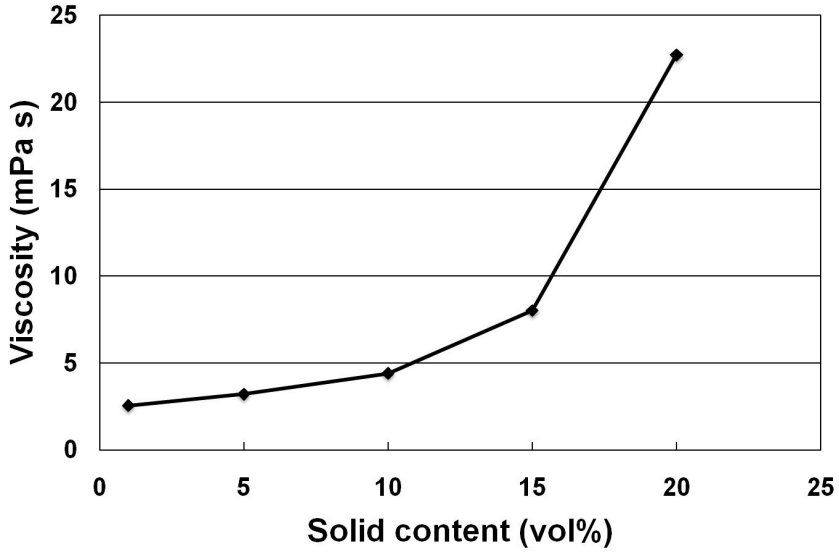

Figure 2.2: Viscosity vs. solid loading for an aqueous suspension with no dispersant.

2.3.2 Effect of dispersants on suspension viscosity

Three different dispersants were evaluated in order to stabilize the dispersion of the suspension. Suspensions were produced at a variety of dispersant concentrations and the viscosity was measured (Figure 2.3). The dispersions were considered optimized for the dispersant loading range that produced a minimum viscosity. At the optimal dispersant content, 0.005 wt% for PAA, 0.05 wt% for PEI, and 0.05 wt% for PBTCA, all three dispersants reduced the viscosity for a 20 vol% solid suspension from 23 mPa s to a value of approximately 8 mPa s. However, suspensions with PEI and PBTCA dispersants exhibited this minimum viscosity for a greater range of dispersant concentrations (0.001 to 0.05 wt% for PEI and PBTCA dispersant compared to 0.001 to 0.005 wt% for PAA dispersants). At dispersant concentrations out of this optimal range, the viscosity increased significantly, and suspensions with high dispersant content (≥ 0.1 wt% for PAA, ≥ 0.5 wt% for PEI, and ≥ 0.1 wt% for PBTCA) exhibited shear thinning behaviour. All measurements were taken at the native pH of the suspension, which was 5.5 for the concentrations studied.

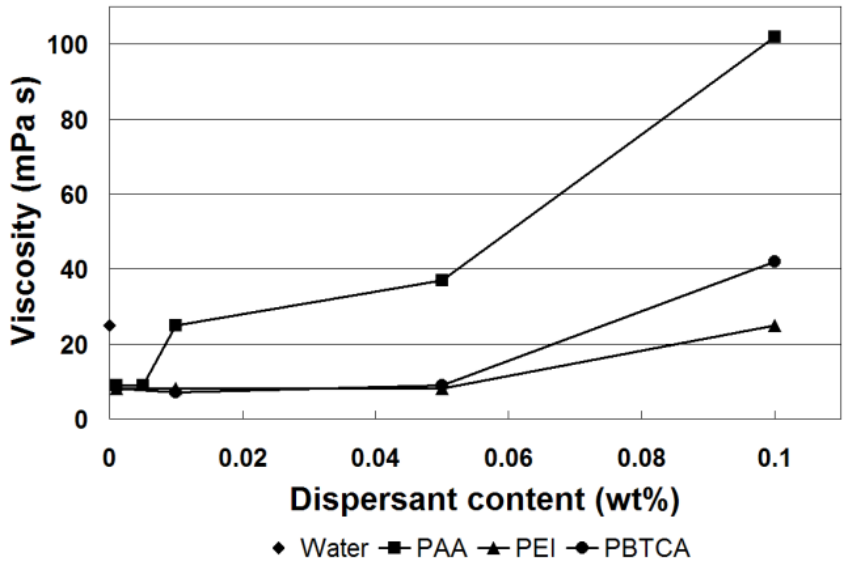

Figure 2.3: Viscosity vs. dispersant loading at 20 vol% solid content.

Figure 2.4 compares the viscosity of a YSZ suspension with and without PEI dispersant for different solid contents. At high solid loadings, dispersant decreases the suspension viscosity significantly. However, at lower solid contents, the viscosity values are similar regardless of whether or not a dispersant is added. This behaviour likely occurs because at higher solid loadings, particle-particle interactions are much more important, so the dispersant, added to optimize the particle-particle repulsive surface charges, has a larger effect. However, dispersant additions were also important for suspensions with lower solid contents, as suspensions without dispersants settled rapidly and formed a layer of settled particles that was difficult to redisperse. Suspensions containing dispersants settled at a slower rate, and it was easier to redisperse the particles if they settled out.

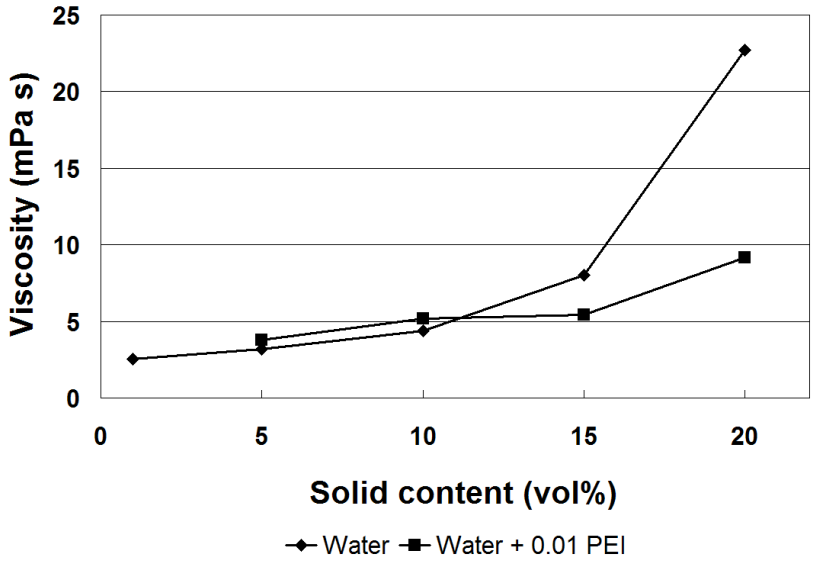

Figure 2.4: Viscosity vs. solid content at the optimum PEI dispersant loading.

2.3.3 Suspension feedability

During spraying, some solid deposition on the torch nozzle leading to clogging of the torch convergence was observed for all suspensions, especially for long spray runs (~5 min) or for high solid content suspensions. Less solid deposition was observed for suspensions with PBTCA additions and for low solid content suspensions (1 vol%). No decrease in suspension flow rates due to clogging was measured during the duration of each typical spray run (approximately 90 seconds), but for longer spray runs, the clogging issue needs to be addressed before the suspension spraying technique can be adopted more widely.

2.3.4 Coating characterization

Sprayed coatings were sectioned and polished and the cross sections were examined in the SEM (Figure 2.5). All of the layers were continuous and fully covered the cathode. Layer thicknesses were measured from the SEM micrographs and are summarized in Figure 2.6. Layers produced from suspensions with PAA dispersants were significantly thinner than the other coatings, while layers produced from suspensions with PBTCA dispersants were thicker than the other layers. PEI dispersed suspensions led to coatings with approximately

the same thickness as the layers produced from the control suspensions that contained no dispersants. Since all of these coatings were deposited under the same spraying conditions and for the same spray run duration, the additional thickness of the PBTCA suspension layers may indicate that the addition of PBTCA to suspensions as a dispersant increases layer deposition efficiency for the spraying conditions examined. Coatings were produced at a rate of approximately 1 μm/pass; however, it is worth noting that the laboratory-scale rotating turntable available for mounting the substrates resulted in the samples spending only 3% of the total deposition time in front of the plasma torch.

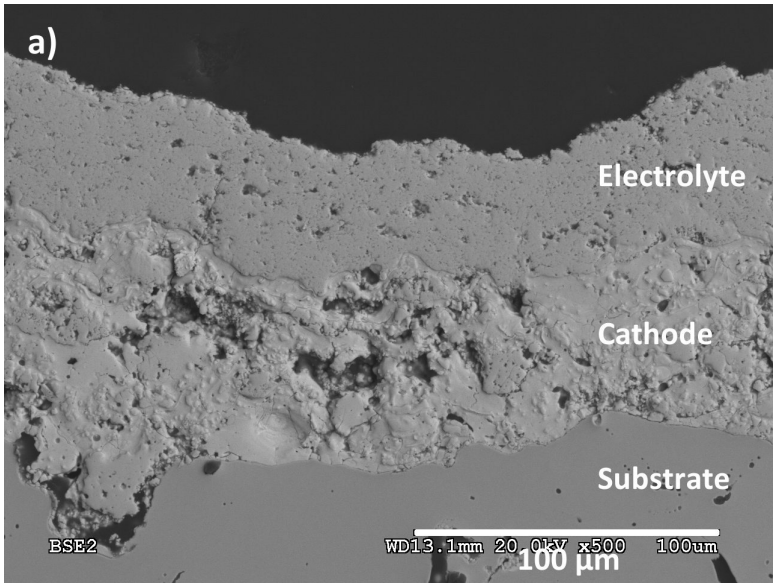
a)
Electrolyte
Cathode
Substrate
BSE2
WD13.1mm 20.0kV x500 100um
100 µm

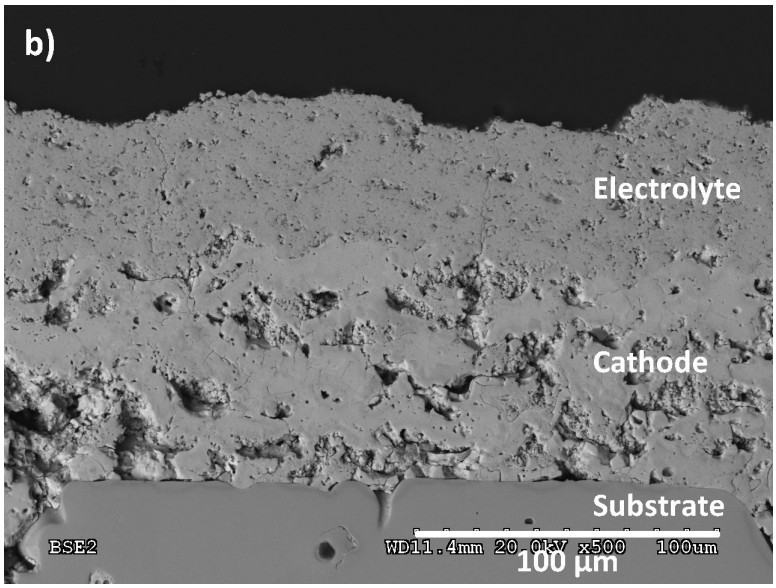
b)
Electrolyte
Cathode
Substrate
BSE2
WD11.4mm 20.0kV x500 100um
100 µm

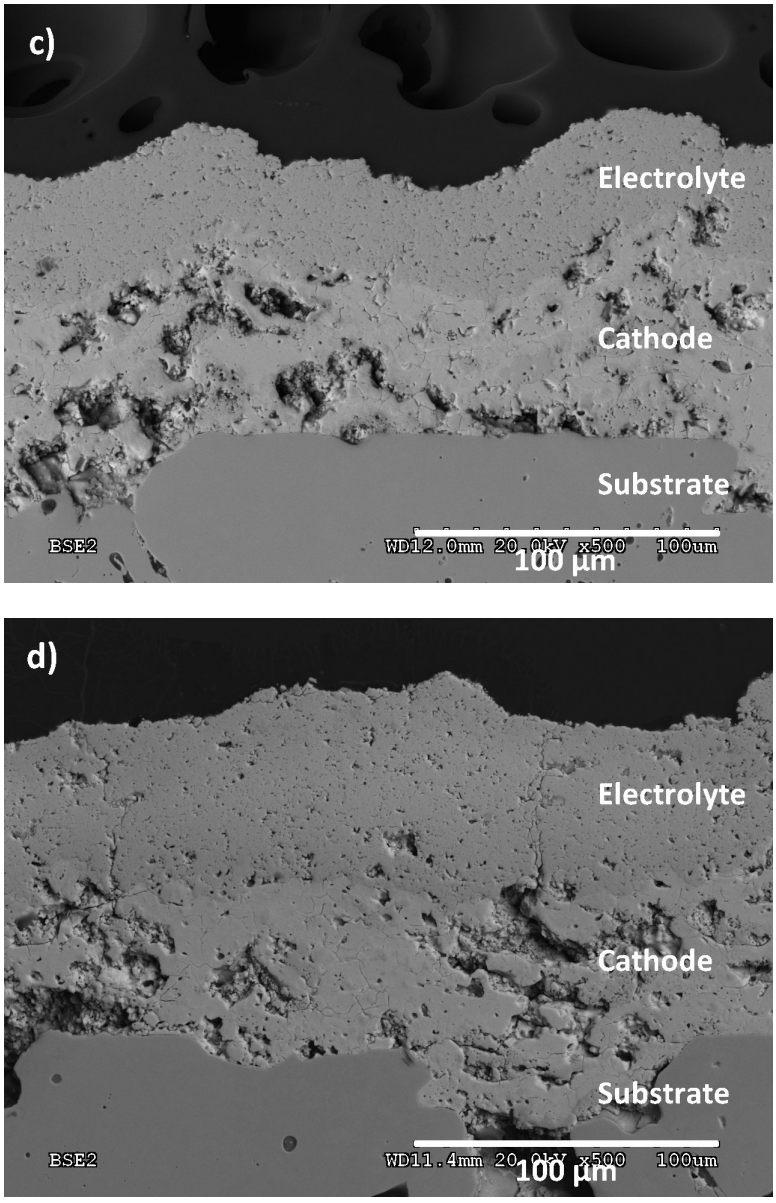

Figure 2.5: SEM image of a YSZ layer sprayed from an aqueous 5 vol% YSZ suspension with (a) no dispersant, (b) 0.01 wt% PEI, (c) 0.005 wt% PAA, and (d) 0.01 wt% PBTCA.

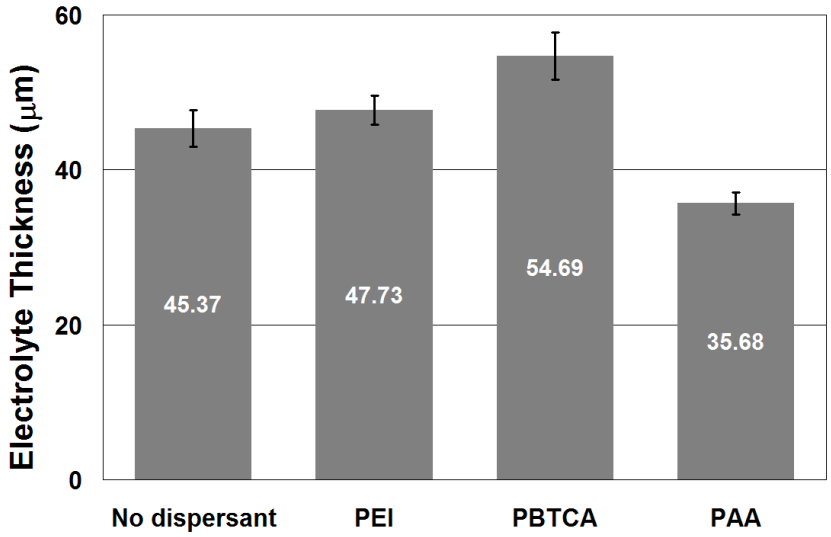

Figure 2.6: Summary of electrolyte thickness measurements.

2.3.5 Spraying higher solid loading suspensions

Electrolyte layers have also been sprayed from suspensions with solid loadings of up to 20 vol% (~60 wt%). Continuous layers were produced at deposition rates (µm/pass) 50% higher than those with lower solid content feedstock suspensions (Figure 2.7). However, it is difficult to spray these high solid content suspensions without clogging the torch convergence during spraying, and such high solid content suspensions may result in an excess of thermal mass being introduced into the torch, potentially resulting in incomplete particle melting.

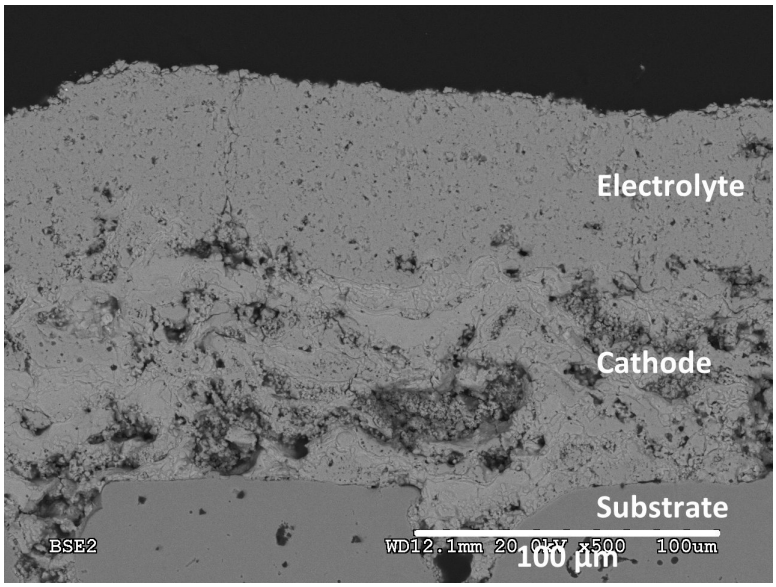

Figure 2.7: SEM image of a YSZ layer sprayed from an aqueous 20 vol% YSZ suspension with 0.01 wt% PEI.

2.4 Conclusions

Suspension plasma spraying was successfully used to spray continuous, fully stabilized YSZ SOFC electrolyte layers on LSM/YSZ cathode layers previously deposited on porous stainless steel substrates. The viscosity of the feedstock suspensions was measured to investigate the effect of solid loadings and dispersant content on the particle dispersion in the suspension. The suspension viscosity increased as the solid loadings increased, especially for solid loadings >15vol% (51wt%), but this viscosity increase could be counteracted by dispersant additions. All three dispersant types (PAA, PEI and PBTCA) decreased suspension viscosities, and an optimum dispersant concentration range where the viscosity was minimized was determined for each dispersant type. At dispersant concentrations out of this range, the suspension viscosity increased sharply. During spraying, some solid deposition on the torch nozzle leading to clogging of the torch convergence was observed for all suspensions; however, less deposition was seen for suspensions with PBTCA additions. Layers sprayed from suspensions containing PBTCA dispersants were thicker than coatings sprayed from other feedstocks after the same number of coating passes,

indicating that the addition of PBTCA dispersant to suspensions may increase the deposition efficiency for the spraying conditions examined.

2.5 Acknowledgements

The authors gratefully acknowledge financial support from the Natural Sciences and Engineering Research Council of Canada, Northwest Mettech Corporation, and the BC Innovation Council, as well as the assistance of Bradley White with plasma spraying and Pius Lo and Marjorie Colebrook with viscosity measurements.

2.6 References

1. R. Hui, Z. Wang, O. Kesler, L. Rose, J. Jankovic, S. Yick, R. Maric, D. Ghosh, Journal of Power Sources, 170(2) (2007), 308-323.
2. R. Henne, Journal of Thermal Spray Technology, 16(3) (2007), 381-403.
3. C. Zhang, H.L. Liano, W.Y. Li, G. Zhang, C. Coddet, C.J. Li, C.X. Li, X.J. Ning, Journal of Thermal Spray Technology 15(4) (2006), 598-803.
4. P. Fauchais, R. Etchart-Salas, V. Rat, J.F. Coudert, N. Caron, K. Wittmann-Teneze, Journal of Thermal Spray Technology 17(1) (2008), 31-59.
5. H. Kassner, R. Siegert, D. Hathiramani, R. Vassen, D. Stoever, Journal of Thermal Spray Technology 17(1) (2008), 115-123.
6. R. Rampon, F.L. Toma, G. Bertrand, C. Coddet, Journal of Thermal Spray Technology, 15(4) (2006), 682-688.
7. D. Waldbillig, O. Kesler, Z. Tang, A. Burgess, pp. 677-682 in Proceedings of the 2007 International Thermal Spray Conference (ITSC), Edited by B. Marple, M. Hyland , Y.C. Lau, C. J. Li, R. Lima, and G. Montavon. ASM International. Beijing, China, 2007.
8. Y. Zhang, J. Gao, D. Peng, M. Guangyao, X. Liu, Ceramics International, 30 (2004), 1049–1053.
9. F. Tang, X. Huang, Y. Zhang, J. Guo, Ceramics International, 26 (2000), 93-97.
10. Y. Liu, L. Gao, Journal of the American Ceramic Society, 86(7) (2003), 1106–1113.
11. B.D. White, O. Kesler, L. Rose, Journal of Power Sources, 178(1) (2008), 334-343.

3 An investigation of the dispersion of YSZ, SDC, and mixtures of YSZ/SDC powders in aqueous suspensions for application in suspension plasma spraying of SOFC electrolytes[15]

3.1 Introduction

Fuel cells are energy conversion devices that electrochemically convert the chemical energy of a fuel into electrical energy. Solid oxide fuel cells (SOFCs) use a ceramic electrolyte that conducts oxide ions. Due to the low ionic conductivity of the ceramic electrolytes at low temperatures, SOFC typically operate at temperatures between 600 and 1000^{o}C. Decreasing the operating temperature of SOFCs to the low end of range can enhance the lifetime of the cells and reduce the cost of the balance of plant materials. Yttria-stabilized zirconia (YSZ) is the mostly commonly used SOFC electrolyte material. YSZ has adequate and purely ionic conductivity at temperatures greater than 700^{o}C, good chemical stability in both reducing and oxidizing atmospheres, and good mechanical properties. However, YSZ may react with cathode materials during fabrication or operation and has low conductivity at temperatures below 700^{o}C. Samaria doped ceria (SDC) is an alternative electrolyte material with better low temperature conductivity than YSZ and less tendency to inter-react with cathode materials; however, SDC has very poor mechanical properties and the Ce^{4+} cation is easily reduced to Ce^{3+} in the reducing atmosphere of the anode, which causes significant electronic conductivity within the electrolyte layer, leading to decreased fuel efficiency.

In order to combine the superior properties of these two electrolyte materials and overcome their limitations, a bi-layer structure may be fabricated [1, 2]. In this configuration, a very thin and low porosity YSZ layer is deposited next to the anode to

[15] A version of this chapter will be submitted for publication. O. Arevalo-Quintero, D. Waldbillig, O. Kesler (2010) An investigation of the dispersion of YSZ, SDC, and mixtures of YSZ/SDC powders in aqueous suspensions for application in suspension plasma spraying of SOFC electrolytes.

minimize the SDC layer's exposure to a reducing atmosphere, and a thicker SDC layer is deposited between the YSZ layer and the cathode to act as a barrier to minimize cathode-YSZ inter-reactions. These bi-layers may improve cell performance, but add an additional processing step, and may introduce higher stresses within the cell due to the thermal expansion mismatch of the layers. These higher stresses can lead to delamination between the electrolyte layers [3]. The layers can also inter-react with each other to form a less-conductive solid solution inter-layer [4].

An alternative method to improve electrolyte performance may be to produce a compositionally graded electrolyte layer. This layer would vary continuously over the electrolyte layer thickness from 100% YSZ at the anode-electrolyte interface to 100% SDC at the cathode-electrolyte interface. This compositional grading will reduce the thermal expansion mismatch stresses in the layers, while still providing the enhanced stability and performance of the two material systems. However, if conventional wet ceramic and co-sintering manufacturing processes are used to fabricate the graded layer, undesirable inter-reactions that form new phases and decrease the electrolyte performance may occur between the YSZ and SDC components during sintering, as with the bi-layered electrolytes.

Plasma spraying (PS) has been proposed as a potential manufacturing technique to overcome the limitations introduced by the traditional wet ceramic and sintering SOFC manufacturing processes. PS is a well established industrial technique that rapidly produces fully sintered ceramic layers without the need for post deposition heat treatments, and has been used successfully in the past to produce both anode and cathode layers [5-8] and to produce graded coatings [9-10]. However, it is difficult to manufacture thin, dense SOFC electrolytes with conventional PS techniques, as the minimum feedstock particle size is typically on the order of 10 μm. In order to enhance control over PS coating microstructures, the PS system can be modified to feed particles of 100 nm to several microns in diameter that are suspended in a liquid carrier such as water or alcohol. A number of groups have used suspension plasma spraying (SPS) to produce coatings that could serve as SOFC electrolytes [11-14] and extensive research on the SPS process has been carried out to gain a better understanding of the process [15-19].

The first step to produce good quality SPS coatings is to study the stability and particle distribution of the feedstock suspensions to improve feedability and to optimize the dispersion of suspended particles in order to obtain more uniform coatings [20]. In general, colloidal stability depends on the distribution of particle surface charges and the total potential energy of the particle, which is the summation of different forces acting on the particles in the liquid medium [21-23]. Ceramic powders tend to aggregate in liquid media due to van der Waals attractive forces, and thus dispersability is achieved by introducing repulsive forces on the surface of the particles. The simplest technique to adjust the particle surface charge is to change the pH of the suspension to a very high or low value, but if this is not feasible, a dispersant may be added to modify the particle surface without large pH changes. A dispersant may be a large molecule polymer that adsorbs onto the particle surface and introduces steric repulsive forces, or it may modify the surface charge of the particle (anionically or cationically) to electrostatically stabilize the particle dispersion [24].

Previous studies of the dispersability of aqueous YSZ and SDC ceramic powder suspensions are mainly based on rheology tests and zeta potential (ZP) measurements. Rheology studies typically measure the viscosity of various suspensions with different dispersant loadings. If the dispersant enhances the particle dispersion, the suspension viscosity will decrease as the dispersant loading increases. Beyond the optimum amount of dispersant addition, the viscosity will increase. The dispersant loading corresponding to the minimum viscosity achieved is the optimum dispersant loading [25]. ZP measurements give an indication of the overall surface charge of a solid material in a liquid medium. Therefore, the ZP value is an indicator of how well particles are dispersed in a suspension. When the ZP absolute value is greater than approximately 30 mV the particle surface charge is generally thought be high enough to produce a well dispersed suspension [26]. When the ZP value is equal to zero, the isoelectric point (IEP), suspended particles agglomerate very quickly. A study of suspension stability (ZP and IEP) over a wide pH range is often done by combining ZP analysis with pH titration. When examining the ZP and IEP of a ceramic powder, surface chemistry and impurities, bulk chemistry, and powder processing routes may play an

important role in the measured values, thus leading to a broad range of IEPs reported in the literature for nominally the same ceramic powders [26-27].

This study investigates the dispersion of YSZ, SDC, and mixtures of YSZ and SDC powders in aqueous suspensions in order to evaluate these materials as potential feedstock suspensions for SPS SOFC electrolyte layers. Three batches of YSZ powder from the same vendor were analyzed and the powder particle size distribution and native pH were measured in order to determine batch-to-batch property variation. Ion dissolution within the suspension was examined by inductively coupled plasma atomic emission spectrometry (ICP-AES) measurements. After the initial powder characterization was complete, the effect of three electrosteric dispersants (ammonium polyacrylic acid (PAA), polyethyleneimine (PEI), and 2-phosphonobutane-1, 2, 4-tricarboxylic acid (PBTCA)) on the suspension dispersion was examined by particle size analysis (PSA), rheometry, and zeta potential measurements. Two methods of ZP measurement were employed: electrophoresis for dilute suspensions and electroacoustic techniques for concentrated suspensions, and these results were compared. Optimum suspension formulations and dispersant concentrations for the YSZ, SDC, and YSZ/SDC mixtures were determined.

3.2 Experimental procedure

3.2.1 Materials

Three batches of $(ZrO_2)_{0.92}(Y_2O_3)_{0.08}$ (YSZ) and one batch of $Ce_{0.85}Sm_{0.15}O_{1.925}$ (SDC) ceramic powders (Inframat Advanced Materials, Farmington, CT, USA), denoted A, B, C, and D, respectively, were used in this study. An initial characterization of the powders was performed in order to determine whether the three YSZ batches had similar properties. Deionized water with a resistivity of 18.2 MΩ·cm at 25°C (Millipore Corporation, Billerica, MA, U.S.A) or distilled water was used to prepare all suspensions. Three dispersants, ammonium polyacrylic acid (PAA) (Ciba Specialty Chemicals, Basel, Switzerland), polyethyleneimine (PEI) (Sigma Aldrich, St. Louis, MO, USA), and 2-phosphonobutane-1, 2, 4-tricarboxylic acid (PBTCA) (Thermphos Trading GMBH, Switzerland) were used to enhance

particle dispersion in the suspensions. PAA and PBTCA are anionic dispersants, while PEI is a cationic dispersant[16].

3.2.2 Particle size measurements

Particle size measurements of suspensions were made by laser light scattering (Mastersizer 2000, Malvern Instruments, Worcestershire, UK). Samples were tested in water using a Hydro 2000 S sample dispersion unit.

3.2.3 Rheological characteristics of suspensions

Suspension viscosity was measured using a sine-wave vibro viscometer (Model SV-10, A&D Instruments Limited, Oxfordshire, UK). Powders were dried at 110°C for 24 hours prior to mixing. Suspensions were prepared in deionized or distilled water at solid loadings ranging from 5 to 60 wt% using one of three dispersants, PAA, PEI or PBTCA. Dispersant concentrations ranging from 0.01 to 5 wt% relative to the solid mass in the suspension were used to determine the optimum amount of dispersant to obtain a minimum viscosity. During suspension preparation, the dispersant was first fully dissolved in deionized or distilled water and then the solid powders were added.

3.2.4 Zeta potential measurements

3.2.4.1 Zeta potential measurements by electrophoresis

Electrophoretic zeta potential measurements used a Zetasizer Nano-series zeta potential analyzer (ZEN 3600 -Malvern Instruments, Worcestershire, UK). The suspensions were prepared by mixing YSZ or SDC powders (0.01 vol%) that had been dried for 24 hours at 110 °C in deionized water. Titrations were performed from a pH of 2.5 to 10.5 using nitric acid for acidic adjustments and ammonium hydroxide for basic adjustments. PEI or PBTCA

[16] Additional background information on the dispersants investigated can be found in Appendix I.

dispersants at concentrations between 0.01 and 3 wt% were added to evaluate their effectiveness in maintaining the powder dispersion in the suspensions.

3.2.4.2 Zeta potential measurements by electroacoustic method

Electroacoustic zeta potential measurements were performed using a ZetaProbe zeta potential analyzer (Colloidal Dynamics LLC, North Attleboro, MA, USA). The ZetaProbe instrument measures zeta potential using a multi-frequency electroacoustic method that allows concentrated suspensions to be analyzed. Titrations were performed from a pH of 2.5 to 12.0 using HCl for acidic adjustment and NaOH for basic adjustment. A constant background concentration of 0.01 mol% KCl was used for the zeta potential measurements. Aqueous YSZ suspensions with solid loadings between 0.5 and 3 vol% relative to the overall suspension volume (2.9 to 15.4 wt%) were prepared using distilled water as the solvent. Two dispersants, PEI (Sigma Aldrich) and PBTCA (Thermphos Trading GMBH), at concentrations between 0.01 and 3 wt%, were evaluated for their ability to enhance solid particle dispersion in the suspensions. Dispersant types were chosen based on viscosity measurements from a previous study [25]. During suspension preparation, the dispersant was first fully dissolved in distilled water and then the solid powders were added. The weight percent of dispersant added corresponds to the weight of dispersant added compared to the total weight of solids in the suspension. After suspension preparation, the suspension was mixed for a minimum of 12 hours on a horizontal rolling mill.

3.2.5 pH measurements

The pH of the YSZ and SDC suspensions was measured using a pH benchtop digital meter (ORION 3-Start plus, Environmental Instruments, Beverly, U.S.A.). Three calibration points were taken with buffers of pH 4, 7, and 10. The pH of the suspensions was measured every hour for the first 8 hours and for up to a maximum of 21 hours to determine the change in pH with time. The pH at different solid loadings was measured after 18 to 21 hours of stirring.

3.2.6 Inductively coupled plasma atomic emission spectrometry (ICP-AES) measurements

ICP testing was performed by the Analytical Laboratory for Environmental Science Research and Training (ANALEST) (Department of Chemistry, University of Toronto). Suspensions of 1 wt% YSZ and 1 wt% SDC powders in deionized water were prepared with 0.75% or 2.25 wt% PEI, respectively, or without dispersant, and passed through a 0.22 µm filter after 1, 2, 4, or 6 hours of mixing. An Optima 7300 ICP AES analyzer was then used to determine the elemental composition of yttrium (Y), zirconium (Zr), samarium (Sm), and cerium (Ce) in the filtrates.

3.3 Results and discussion

3.3.1 Powder characterization

Three batches of YSZ powder (A, B, C) and one batch of SDC (D) from the same supplier were characterized in order to determine whether there was any significant batch to batch variability that would affect the results of this study.

3.3.1.1 Particle size analysis (PSA)

PSA measurements were performed on the four powder batches; the results are summarized in Table 3.1. In order to investigate the effect of particle agglomeration within the suspension, PSA measurements were taken at one of three conditions during testing. Suspensions were measured after no agglomeration breakup method was used prior to measurement (none), after agitation by the PSA instrument impellor set to 3500 rpm (stirring), or after five minutes of ultrasonication (ultrasound). During the actual PSA measurements, all suspension types were stirred at either 2000 or 1500 rpm.

Table 3.1: Particle size distribution of YSZ and SDC suspensions with various agglomeration breakup methods utilized.

Material	Batch	Mechanical agitation method	D10 (μm)	D50 (μm)	D90 (μm)
YSZ	C	None	1.71	7.41	32.11
YSZ	A	Stirring	0.91	2.97	6.33
YSZ	B	Stirring	0.81	2.64	6.38
YSZ	A	Ultrasound	0.94	2.81	6.37
YSZ	B	Ultrasound	0.79	2.58	6.32
YSZ	C	Ultrasound	1.51	3.24	6.97
SDC	D	Stirring	0.13	2.08	81.33
SDC	D	Ultrasound	0.11	1.35	3.58

As can be seen in Table 3.1, when no agglomeration breakup method is employed, the D50 and D90 of the YSZ powder are 2 and 4 times greater, respectively, than the values obtained when powder agglomerates are exposed to either ultrasound or stirring, indicating that significant particle agglomeration occurs within the suspensions. It appears that both stirring and ultrasonication are able to break up the loosely bonded agglomerates present in the YSZ suspensions, and that the three YSZ powder batches investigated in this study had very similar particle size distributions when the agglomerates were broken up by either method. For SDC suspensions, it appears that stirring is unable to fully break up agglomerates, as shown by the large D90 value in Table 3.1; however, the ultrasonic treatment is able to produce less agglomerated suspensions.

3.3.1.2 Native pH

The native pH of the three batches of YSZ powders and of the single batch of SDC powder was measured for aqueous suspensions with solid loadings ranging from 5 to 60 wt% for

YSZ and from 5 to 30 wt% for SDC after 18 to 21 hours of mixing. Table 3.2 shows the interpolated values at a concentration of 15 wt%. It was found that the three YSZ powder batches from the same vendor and with the same nominal composition had native pH values that varied from 5.4 to 5.9. This difference may be attributable to variations in particle surface chemistry caused by batch-to-batch processing differences.

Table 3.2: Native pH of YSZ and SDC 15 wt% aqueous suspensions.

Material	Batch	Native pH
YSZ	A	5.8
YSZ	B	5.4
YSZ	C	5.9
SDC	D	6.5

The three YSZ powder batches were found to have similar particle size distributions and native pH values that varied only by approximately 10% from the lowest native pH value to the highest one; thus, the three powders were used interchangeably.

3.3.2 Characterization of YSZ and SDC ceramic suspensions

After the powder characterization was complete, the properties of YSZ and SDC aqueous suspensions were measured using rheometry, pH, PSA and zeta potential techniques. The ability of three different dispersants to enhance suspension stability was also investigated.

3.3.2.1 Rheological studies

The viscosities of aqueous YSZ and SDC suspensions were measured at various solid loadings (Figure 3.1). As expected, the measured viscosity increased as the solid content increased. Above solid contents of 50 wt% YSZ and 20 wt% SDC, the suspension viscosity rapidly increased. YSZ suspensions with 60 wt% solid content reached a viscosity of 17.3

mPa s, beyond which the suspension had a paste-like viscosity. SDC suspensions with a solid content of 30 wt% exhibited a viscosity of 28.2 mPa s. At this high viscosity, the mixture was densely packed, and uniform stirring was hard to achieve. As a result, the maximum solid contents for the rheological studies were set to 60 wt% YSZ and 30 wt% SDC.

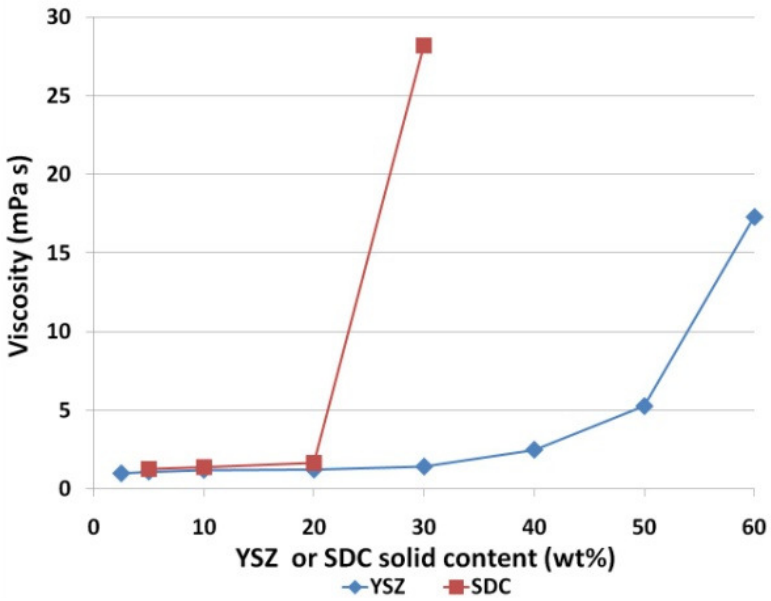

Figure 3.1: Viscosity vs. solid content of YSZ and SDC suspensions.

In order to enhance particle dispersion at high solid contents, three different dispersants (PBTCA, PAA, and PEI) were evaluated. These dispersants were selected based on viscosity measurements performed in a previous study [25]. Dispersant concentrations from 0.01 to 1 wt% relative to solid mass in the suspension were evaluated for YSZ suspensions, while PEI concentrations from 0.01 to 5 wt% were tested for SDC suspensions. The viscosity measurements for YSZ and SDC suspensions with the three dispersants are shown in Figures 3.2a and 3.2b, respectively. Figures 3.2c and 3.2d show expanded views of the 0 to 0.1 wt% dispersant range corresponding to YSZ and SDC suspensions, respectively. For YSZ suspensions, it was found that all three dispersants reduced the viscosity; however, PAA and PBTCA dispersants were only effective at very low concentrations (0.01 and 0.005 wt%, respectively). The PEI dispersant reduced the YSZ suspension viscosity at higher dispersant

contents (0.75 wt %) and over a very broad range of dispersant concentrations. For SDC suspensions, PBTCA and PAA did not enhance the electrostatic stability for the range of compositions tested, i.e., no minimum viscosity was reached. On the other hand, PEI dispersant was very effective in reducing SDC suspension viscosities for dispersant contents greater than 2.0 wt%, with a broad minimum in viscosity achieved at 2.25 wt%.

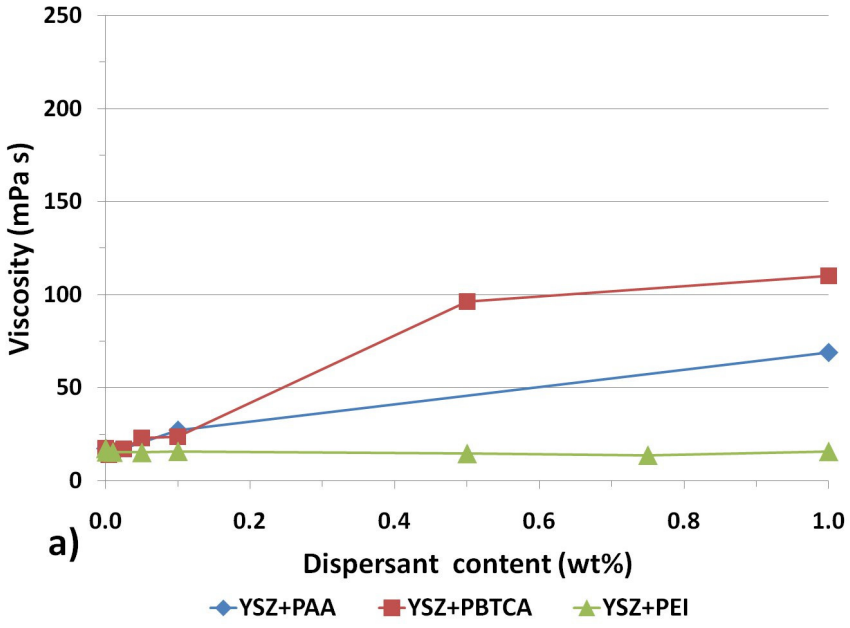

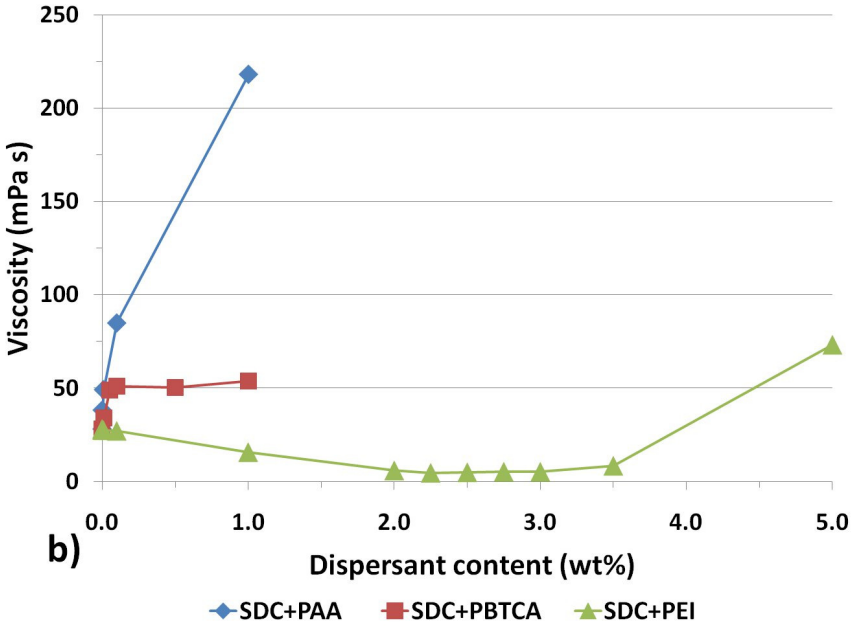

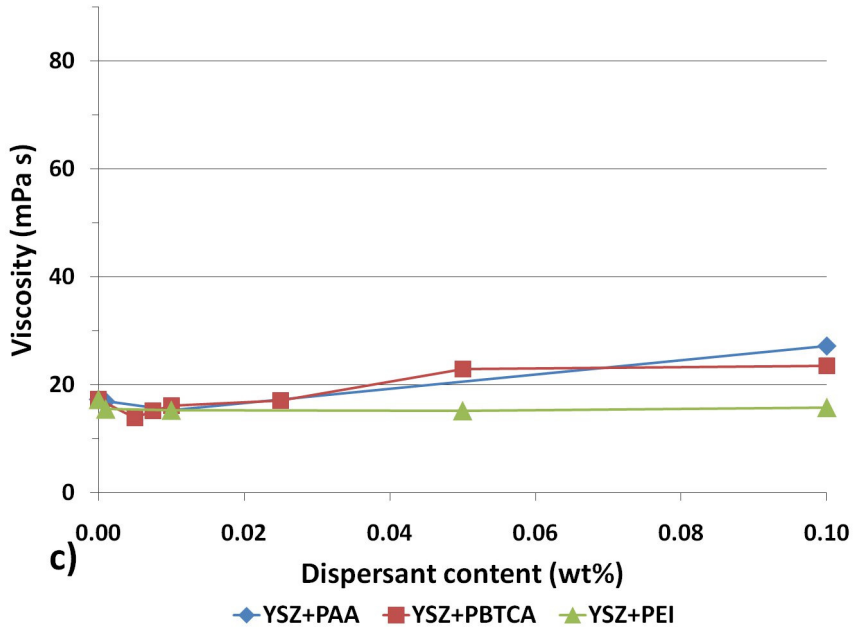

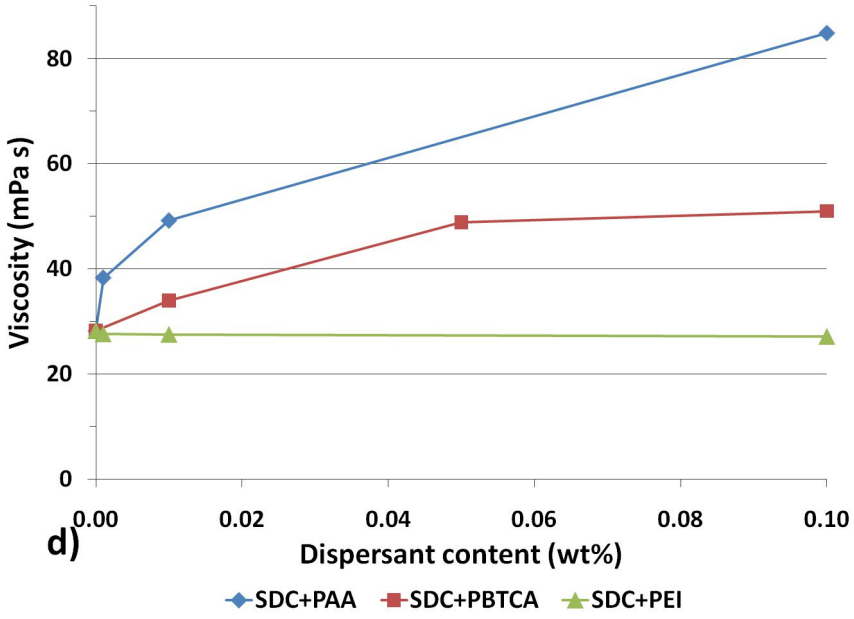

Figure 3.2: Viscosity vs. dispersant content for (a) YSZ and (b) SDC suspensions, with PAA, PEI, or PBTCA additions, and expanded views of the 0 to 0.1 wt% dispersant range for (c) YSZ and (d) SDC suspensions.

3.3.2.2 Effect of solid content, dispersant addition, and mixing time on pH

The effects of solid content and dispersant additions on the pH of YSZ and SDC suspensions are shown in Figure 3.3. YSZ suspensions with 5 wt% solids had a native pH of 5.53, while SDC suspensions with 5 wt% solids had a native pH of 6.68. As the solid content increased, the suspension native pH decreased slightly, with the largest decreases happening at concentrations lower than 10 wt% solids. For YSZ suspensions, 0.01 wt% PBTCA additions did not affect the suspension pH, likely due to the very low dispersant concentration. When 0.75 and 2.25 wt% PEI was added to the YSZ and SDC suspensions, respectively, the pH increased by approximately 5% and 10%, respectively. For the SDC suspensions, increases or decreases in the PEI concentration modified the suspension native pH linearly.

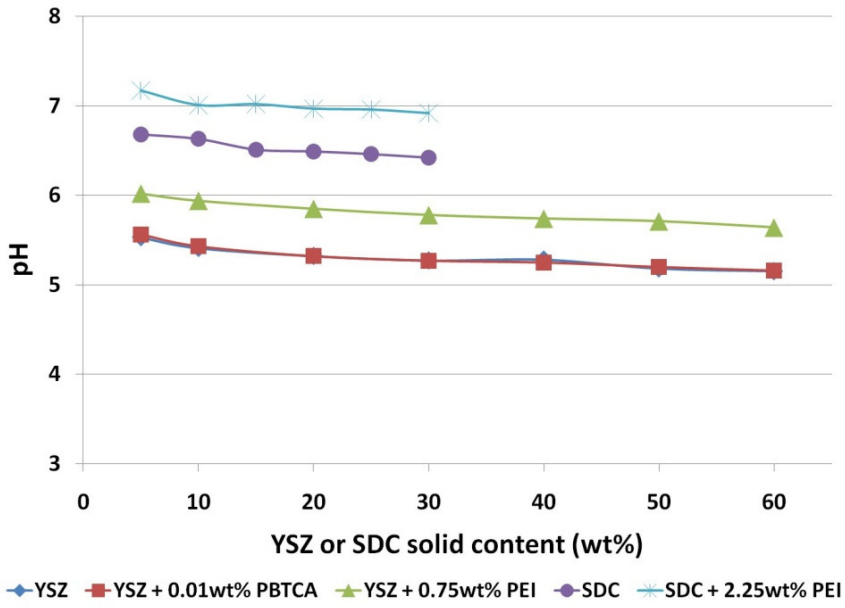

Figure 3.3: pH vs. solid content of YSZ and SDC suspensions with and without dispersant additions.

It was observed that suspension pH values changed slightly after long mixing times; therefore, the effect of mixing time on pH was measured by monitoring the suspension pH over a 24 hour period for 60 wt% YSZ or 30 wt% SDC suspensions with and without PEI dispersants (Figure 3.4). During the first hour of mixing, the pH of YSZ and SDC suspensions

rapidly increased. After 6 hours of mixing, pH values stabilized, with less than 2% change in values between measurements taken after 6 hours of mixing and those taken after 21 hours of mixing.

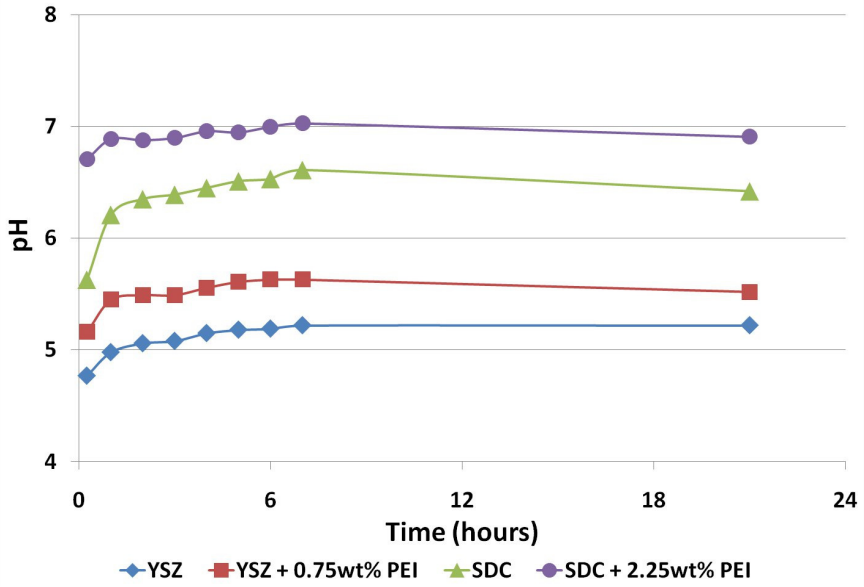

Figure 3.4: Variation of 60 wt% YSZ or SDC suspension pH with time.

Changes in suspension pH over time may be caused by cation dissolution [26]. In order to measure this effect, ICP-AES was performed after various mixing durations for 1 wt% YSZ and SDC suspensions with and without PEI dispersant additions (Figure 3.5). After 1 hour of mixing, a concentration of 28.65 mg/L of yttrium was observed for YSZ suspensions, while 106.86 mg/L of dissolved Sm was observed in SDC suspensions. These values correspond to 2.65% of the total Y content and 8.20% of the total Sm content. Dissolved Zr or Ce was not observed during these measurements, since their concentration was below the detection limit. When PEI dispersants (0.75 wt% for YSZ suspensions, or 2.25 wt% for SDC suspensions) were added to the suspensions, the amounts of dissolved Y and Sm were decreased by 35% and 51%, respectively; however, some dissolved Zr or Ce was observed within the suspension. The ICP results for the suspensions with PEI dispersants show that the highest dissolution of ions occurred within the first hour of mixing, and that the

concentration of ions changed less rapidly after 6 hours of mixing. This result was in agreement with the trend seen in the pH analysis, that changes in the pH value were negligible after 6 hours of mixing. After 6 hours of mixing, the Zr ion concentration decreased to a value close to zero, which may indicate that the dissolved Zr can adsorb or precipitate onto the powder surface.

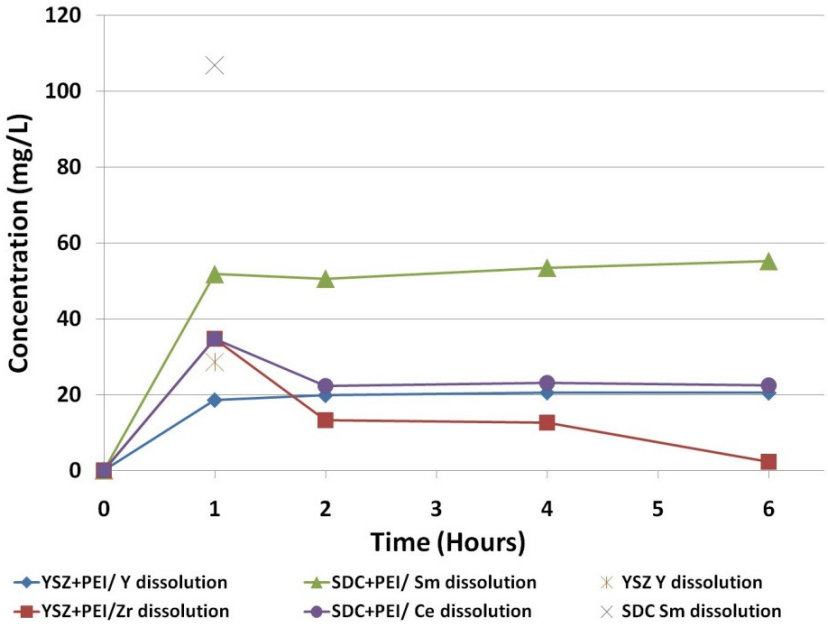

Figure 3.5: ICP elemental analyses for YSZ and SDC suspensions.

3.3.2.3 Effect of dispersants on particle size distribution

The ability of dispersants to suppress the formation of agglomerates in the suspension was verified by measuring the particle size distribution of YSZ and SDC suspensions with PBTCA or PEI dispersant additions (Table 3.3). For YSZ suspensions, samples either contained no dispersant (none), 0.01 wt% PBTCA, or 0.75 wt% PEI. SDC suspensions either contained no dispersant or 2.25 wt% PEI.

For YSZ suspensions, D50 and D90 values were lower for suspensions containing dispersants, which indicates that both PBTCA and PEI reduced the tendency of YSZ particles to form large agglomerates when in suspension. The PEI dispersant worked especially well

and produced suspensions with a particle size distribution similar to that of YSZ suspensions that had been ultrasonicated. SDC suspensions with PEI dispersants formed fewer large agglomerates in stirred suspensions, as shown by the lower D90 value, although large agglomerates were still present, as evidenced by the D90 value. The agglomerates in the ultrasonically treated SDC suspensions were already completely broken up, so no difference in particle size distribution was seen when PEI was added. These beneficial dispersant effects confirm the trends seen previously in the rheometry studies.

Table 3.3: Particle size distribution of YSZ and SDC suspensions with and without dispersants.

Material	Mechanical agitation method	Dispersant	D10 (μm)	D50 (μm)	D90 (μm)
YSZ	None	None	1.71	7.41	32.11
YSZ	None	0.01 PBTCA	2.84	5.46	10.49
YSZ	None	0.75 PEI	0.68	2.54	6.84
YSZ	Ultrasound	None	1.51	3.24	6.97
SDC	Stirring	None	0.13	2.08	81.33
SDC	Stirring	2.25 PEI	1.03	2.47	34.77
SDC	Ultrasound	None	0.11	1.35	3.58
SDC	Ultrasound	2.25 PEI	0.11	1.55	4.38

3.3.3 Suspension electrostatic stability determined by zeta potential measurements

Zeta potential measurements were used to identify the pH ranges in which suspensions are stable and to verify the effectiveness of the optimum concentrations of PEI and PBTCA tested. Two zeta potential measurement methods were used: electrophoresis on very dilute suspensions in order to investigate the fundamental behaviour of the particles in

suspension, and an electroacoustic method, which allows the zeta potential of concentrated suspensions to be measured.

3.3.3.1 Electrophoretic and electroacoustic methods

Figure 3.6 presents ZP results of YSZ suspensions tested by electrophoretic and electroacoustic methods. In the electrophoretic measurements, dilute YSZ suspensions with no dispersant had a native pH of 5.7 and exhibited a ZP value of approximately 31 mV. The IEP of YSZ as measured by electrophoresis was approximately 8.9. This value was close to those found by Jin et al. [28], who reported an IEP of 8.7, and Greenwood and Kendall [26], who reported a value of 9.3. However, acidic YSZ IEPs have also been reported, at pH values of 4.5 [29], 6.82 [30], and 6.5 [31-32]. Suspensions measured by the electroacoustic method had a native pH of 6.0 and exhibited a ZP value of approximately 31 mV. An IEP of 11.8 was measured, which is significantly higher than the value measured using the electrophoretic method.

Greenwood and Kendall [26] reported pure zirconia IEP values obtained by Bernston that varied from pH values of 5 to 8 and IEPs of pure yttria that varied from pH values of 9 to 10.6. The IEP found in the present study was closer to those reported of yttria, which could indicate that more yttrium ions were present on the particle surface [26]. Yttrium dissolution from YSZ has been reported by a number of authors [26-30] and was observed by ICP elemental analysis in the present study. Yttrium ions might leach out from the YSZ particles at the suspension native pH and precipitate or adsorb onto the particle surface, thus modifying the YSZ surface charge and shifting the IEP to a more positive pH value [26]. However, the ICP-AES results obtained in the present study suggest that yttrium ions do not readsorb or precipitate on the particle surface over a period of 6 hours of testing. The IEP may also be shifted for powders prepared by different routes or at different temperatures [33]. In addition, the level of hydration of powders and any impurities on the particle surface will modify the particle surface charge [27].

A constant background electrolyte concentration of 0.01 mol% KCl was used for the electroacoustic zeta potential measurements, while the electrophoretic measurements

were performed with no KCl additions. Zeta potential measurements for the two methods with and without a KCl background electrolyte were therefore done to determine the effect of the KCl buffer on the values obtained. These results are also shown in Figure 3.6. It was found that for dilute measurements, the presence of KCl shifted the IEP of YSZ from 8.9 to 10; however, no effect was found on the concentrated electroacoustic measurements. Due to the effect of KCl, all further electrophoretic testing was done with no KCl additions in order to minimize any other interactions that could affect the ZP readings.

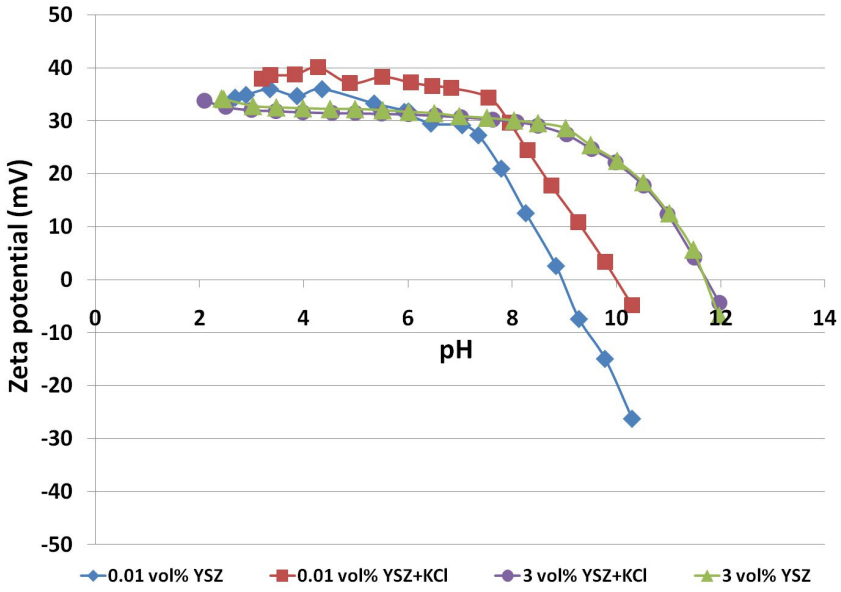

Figure 3.6: Electrophoretic and electroacoustic zeta potential measurements of diluted and concentrated YSZ suspensions with and without KCl.

3.3.3.2 Effect of dispersant additions on electrostatic properties of YSZ

In order to verify viscosity measurements previously presented in this work, the electrostatic behaviour of YSZ suspensions with PBTCA or PEI dispersant additions was examined. The viscosity measurements indicated that PBTCA was an effective dispersant only at very low concentrations (<0.01 wt%) in YSZ suspensions. The effect of anionic dispersant (PBTCA) on YSZ zeta potential was measured at concentrations from 0.005 wt%

to 1.5 wt% using both electrophoresis and electroacoustic methods (Figures 3.7a and 3.7b). When no dispersant was added, a stable plateau with values above 30 mV was reached for a range of pH values between 3 and 7 in the electrophoretic measurements, and the suspension had an IEP of 8.9. For suspensions containing a low amount of PBTCA dispersant (<0.01 wt%), the zeta potential value increased to approximately 40 mV for pH values between 3 and 7, with an IEP of approximately 9.8. At PBTCA concentrations of 0.5 wt% and higher, the suspension IEP shifted to more acidic values, and a broad range of suspension instability at pH values ranging from approximately 3 to 8.5 was observed, which agreed with the viscosity behaviour of the YSZ suspensions tested at the same dispersant concentrations. Electroacoustic zeta potential measurements followed the same general trend as electrophoretic measurements. At low PBTCA concentrations, a broad stable region was seen for pH values between 2.5 and 8.5, while at PBTCA concentrations of 0.5 wt% and higher, zeta potential values decreased. Measured IEPs were higher than those measured using electrophoresis, and the IEP decreased as the PBTCA content increased beyond 0.01 wt%.

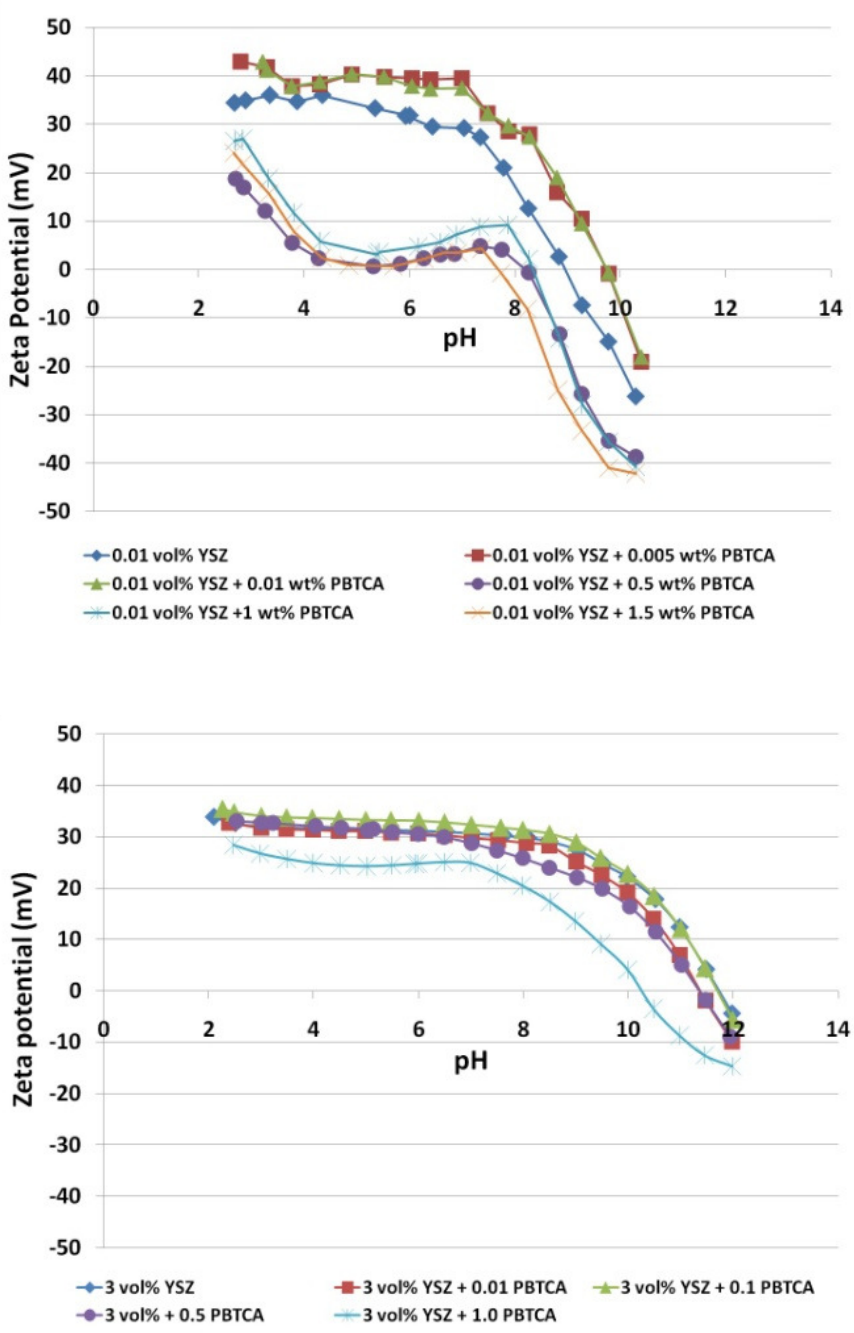

Figure 3.7: Zeta potential measurements of YSZ suspensions at various PBTCA concentrations performed by (a) electrophoretic method and (b) electroacoustic method.

Viscosity measurements had indicated that PEI was an effective dispersant for YSZ suspensions over a broad range of concentrations, with an optimal concentration of 0.75

wt%. Thus, the effect of cationic dispersant (PEI) on YSZ zeta potential was measured at concentrations from 0.1% to 1.0 wt% using both electrophoresis and electroacoustic methods (Figures 3.8a and 3.8b). Electrophoretic measurements of suspensions containing small amounts of PEI dispersant (0.5 wt %) had higher zeta potential values compared to the suspensions with no dispersant. These suspensions were stable between pH values of 3 and 8, and the IEP was shifted to more basic pH values. At the optimal dispersant concentration determined by viscosity measurements (0.75 wt%), the zeta potential at the stable plateau was greater than 40 mV and the suspension IEP value was beyond the maximum basic pH value tested. At a PEI concentration of 1.0 wt%, the zeta potential value and IEP values were lower than at the optimal PEI concentration of 0.75 wt%, as expected from the trends seen during the rheometry studies. Electroacoustic zeta potential measurements exhibited similar trends for PEI concentrations from 0% to 0.75%, with a stable zeta potential of 30 mV for pH ranges of 3 to 8 and an IEP of 11.8.

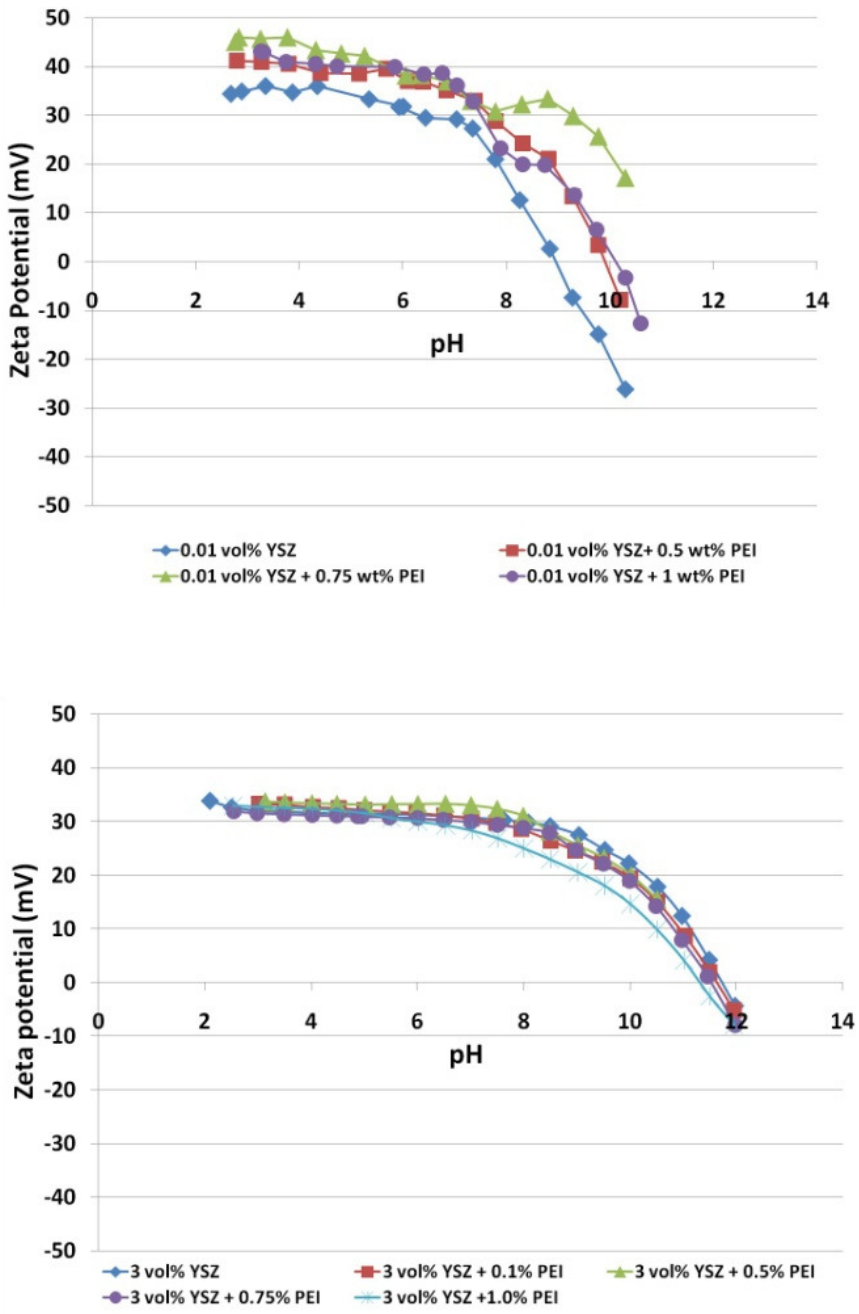

Figure 3.8: Zeta potential measurements of YSZ suspensions at various PEI concentrations performed by (a) electrophoretic method and (b) electroacoustic method.

3.3.3.3 Effect of dispersant additions on electrostatic properties of SDC

The zeta potential of SDC suspensions with and without dispersant was also examined using both electrophoretic and electroacoustic techniques (Figure 3.9). During electrophoretic measurements, an SDC suspension with no dispersant exhibited a ZP value close to 24 mV at its native pH of 7.4, which is likely too low to prevent flocculation. The non-monotonic trend in the electrophoretic data was due to the automatic titration process. During the titration of SDC from low to high pH without dispersant, the pH decreased near a pH of 5 and then increased again during each experiment in a repeatable manner. The IEP of SDC as determined by electrophoretic measurements was approximately 9.3 in the absence of dispersant, which is very different from the value of 3.66 reported by Fu and Chen [34]. As in the case of YSZ, the presence of samarium ions in the SDC suspensions was confirmed by elemental analysis. The changes in surface chemistry due to samarium dissolution might explain the differences between the results obtained in this study and those in the literature. Suspensions measured by the electroacoustic method exhibited a ZP value of approximately 40 mV at a native pH of 6.9. No IEP point was measured for SDC suspensions over the range of pH values tested using the electroacoustic method.

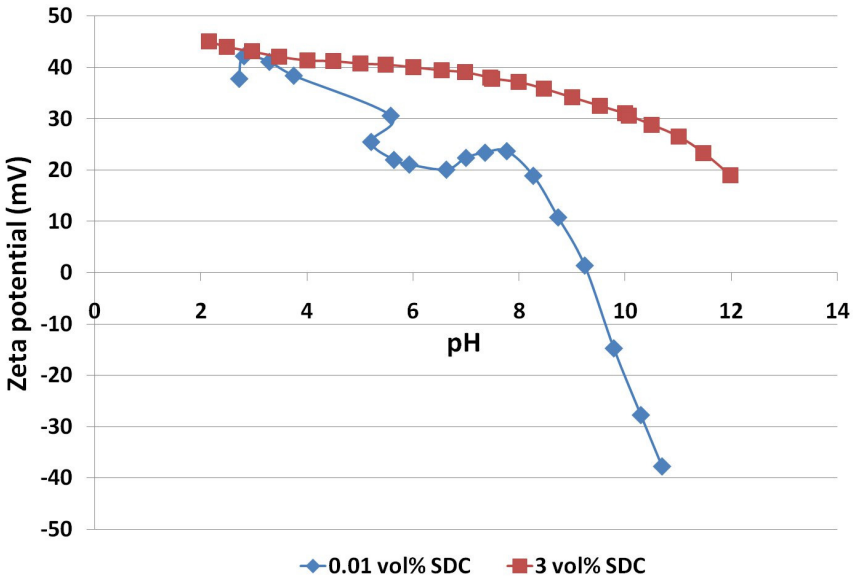

Figure 3.9: Zeta potential measurements of SDC suspensions performed by electrophoretic and electroacoustic methods at concentrations of 0.01 and 3 vol%, respectively.

The effect of anionic dispersant (PBTCA) on SDC zeta potential was measured using the electrophoretic method at concentrations of 0.5, 1, and 1.5 wt% dispersant, and the results are shown in Figure 3.10. Viscosity measurements presented previously in this work had indicated that no amount of PBTCA reduced suspension viscosity, i.e., PBTCA is not an effective dispersant for SDC. The zeta potential measurements agreed with these results, as all PBTCA concentrations examined in this study resulted in zeta potential values near zero and multiple IEPs that were shifted to a more acidic range.

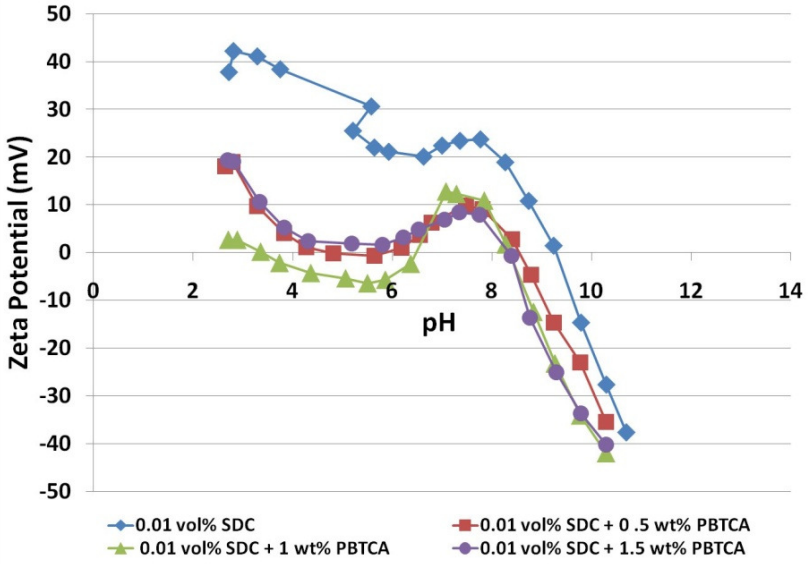

Figure 3.10: Zeta potential measurements of SDC suspensions at various PBTCA concentrations performed by electrophoretic method.

The effect of PEI dispersant additions on SDC suspensions was examined for PEI concentrations between 1 and 3 wt%. In electrophoretic tests, PEI additions increased the zeta potential and the range of stable pH values and shifted the IEP to more basic values, as can be seen in Figure 3.11a. Electrophoretic measurements showed that 2.25 wt% PEI suspensions had the highest zeta potential value and did not reach an IEP in the pH range examined, in agreement with the rheological measurements. Electroacoustic measurements (Figure 3.11b) followed similar trends for all PEI contents, but no IEP was observed for the pH range tested.

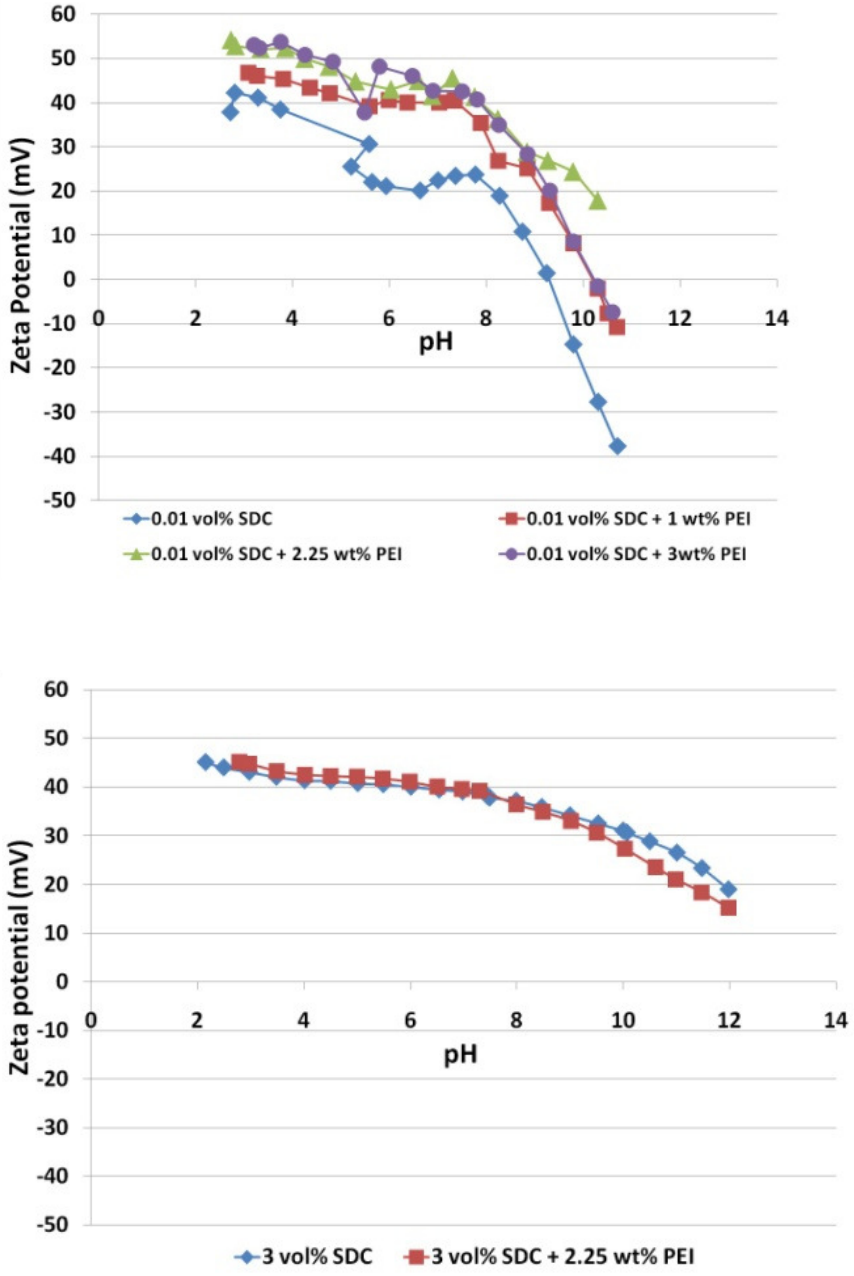

Figure 3.11: Zeta potential measurements of SDC suspensions at various PEI concentrations performed by (a) electrophoretic method and (b) electroacoustic method.

Differences between electrophoretic and electroacoustic methods could be partially explained by the difference in measurement techniques and concentrations used in each

technique. In the electrophoresis technique, due to the instrument design (in which scattered light is detected at a forward angle), samples have to be optically clear to allow the beam to pass through the sample and be detected. The dilute regime used in the electrophoresis method is more sensitive to small changes in charges due to the low solid concentration of samples. In the electroacoustic method, more concentrated suspensions are used and as a result, interaction between particles plays a major role in electrostatic measurements. Data obtained from the electrophoretic measurements in the dilute regime confirmed the optimum dispersant values as determined by the rheology measurements of more concentrated suspensions. Therefore, the zeta potential data obtained at low concentration were found to be able to identify optimum dispersant loadings that could be applied when processing suspensions with higher concentrations.

3.3.4 Characterization of YSZ and SDC mixed suspensions

The stability of YSZ/SDC mixed suspensions was examined by measuring the viscosity and zeta potential of mixtures of 5 wt% YSZ suspensions and 5 wt% SDC suspensions with or without PEI dispersants. PEI was chosen as the dispersant for the mixtures due to its effectiveness in dispersing both YSZ and SDC suspensions. Anionic dispersants reduced the stability of SDC suspensions; therefore, PEI was used in the study of mixed SDC/YSZ suspension dispersion stability to avoid de-stabilizing SDC suspensions by mixing them with YSZ suspensions having PBTCA as a dispersant. When preparing the suspensions, the desired amount of dispersant (0.75 wt% for YSZ suspensions or 2.25 wt% for SDC suspensions) was first dissolved in deionized water, the appropriate amount of YSZ or SDC was then added, and the individual suspensions were stirred. After stirring, the individual suspensions were combined in the desired proportions to form YSZ/SDC mixtures with compositions varying from 0% YSZ (100% SDC) to 100% YSZ. Figure 3.12 shows viscosity and zeta potential values measured by electrophoresis for different YSZ/SDC mixtures. Due to the low solid loadings, viscosities were low even for suspensions with no dispersants; however, the viscosity readings were lower for suspensions with PEI additions compared to those with no dispersants. As the amount of the more acidic YSZ suspension increased, the

native pH of the mixture decreased linearly from a value of approximately 6.7 for 100% SDC suspension to approximately 5.5 for 100% YSZ suspension without dispersant added. When PEI was added, the pH decreased linearly from a value of approximately 7.2 for 100% SDC suspension to approximately 5.6 for 100% YSZ suspension. Suspensions with PEI dispersant showed ZP values greater than 43 mV at all YSZ/SDC compositions, approximately 10% higher than those of SDC/YSZ mixed suspensions with no dispersant. These results indicate that all proportions of SDC/YSZ mixed suspensions are stable at their native pH, and are even more stable when PEI dispersants are added. In addition to the electrostatic improvements that slow the initial settling rate of the suspensions and the rheological improvements that facilitate the feeding of suspensions, it was found that the addition of PEI as a dispersant made it easier to re-disperse suspensions that had already settled with simple mechanical agitation, even more than 6 months after suspension preparation.

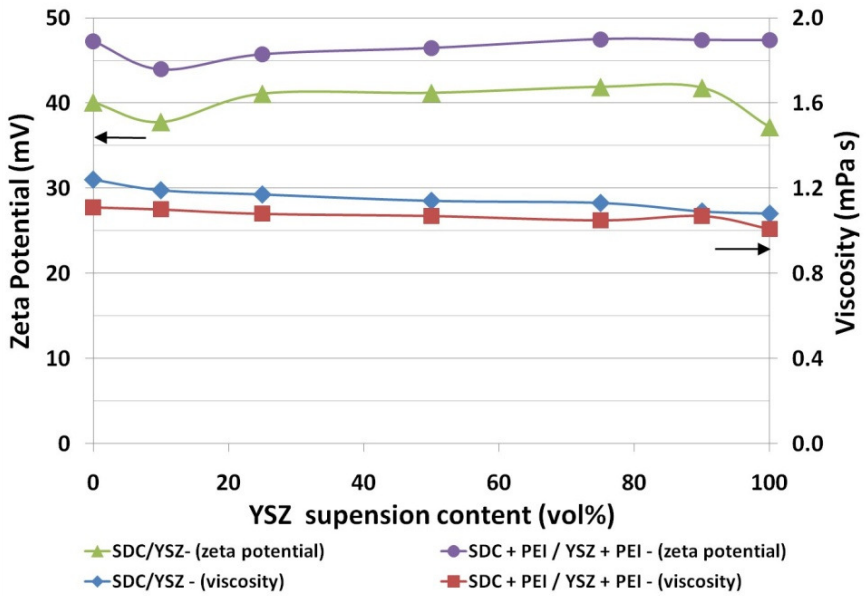

Figure 3.12: Viscosity and electrophoretic zeta potential measurements of YSZ/SDC mixtures as a function of YSZ suspension content.

3.4 Conclusions

In order to produce good quality SPS coatings, feedstock suspensions should be stable and the suspended particles within the suspensions should be well dispersed. This study investigated the dispersion behaviour of YSZ, SDC, and mixtures of YSZ and SDC powders in aqueous suspensions in order to evaluate these materials as potential feedstock suspensions for SPS SOFC electrolyte layers. Initially, the particle size distribution and native pH for three batches of YSZ from the same supplier and one batch of SDC were measured. It was found that batch-to-batch variation in particle size distribution was not significant and that the native pH varied by approximately 10% between the batches of YSZ powders. For YSZ powders, the native pH was measured to be approximately 5.7, while SDC native pH values were approximately 6.5. ICP-AES of the YSZ and SDC suspensions determined that there was some dissolution of Y and Sm from the powders during mixing; however, for mixing times between one to six hours, the ion concentration within the suspensions was essentially constant except for the Zr ion concentration in suspensions containing PEI. After the initial powder characterization, the effect of three potential dispersant materials (PAA, PBTCA, and PEI) on the dispersion of YSZ and SDC particles in suspension was examined. The ability of these dispersants to enhance particle dispersion was characterized by rheometry and confirmed by PSA electrophoretic and electroacoustic zeta potential measurement techniques, and optimum dispersant concentrations were determined. For YSZ suspensions, the anionic dispersants (PAA and PBTCA) were found to be effective at very low concentrations (0.01 wt% and 0.005 wt%, respectively); however, these dispersants were not effective for SDC at any dispersant concentration examined in this study. The cationic PEI dispersant effectively enhanced the dispersion of both YSZ and SDC suspensions, with optimum PEI concentrations found to be 0.75 wt% for YSZ suspensions and 2.25 wt% for SDC suspensions. Since PEI was effective at stabilizing both YSZ and SDC suspensions, it was chosen as the dispersant material for mixtures of YSZ and SDC suspensions. 5 wt% YSZ and SDC mixed suspensions with PEI dispersants at the optimized levels showed a great level of electrostatic stability, with a ZP above 43 mV and a high degree of flowability, as confirmed by viscosity measurements. The enhanced flowability

and high stability of the optimized suspensions found in this study would make them excellent candidates for use as feedstock suspensions for SPS YSZ or SDC SOFC electrolyte layers or for compositionally graded YSZ/SDC layers.

3.5 Acknowledgements

The authors gratefully acknowledge financial support from the Natural Sciences and Engineering Research Council of Canada, Northwest Mettech Corporation, and the BC Innovation Council, as well as the assistance of Dan Mathers from the ANALEST laboratory at university of Toronto with the ICP-AES testing, Sally Finora with zeta potential measurements at the University of British Columbia, Professor Heiko Heerklotz for providing the zeta potential analyzer and viscometer at the University of Toronto, and Ken Kletsky of Thermphos Trading Gmbh for the provision of dispersant samples.

3.6 References

1. X. Zhang, M. Robertson, C. Decès-Petit, Y. Xie, R. Hui, W. Qu, O. Kesler, R. Maric, D. Ghosh, Journal of Power Sources, 175 (2008), 800-805.
2. D. Yang, X. Zhang, S. Nikumb, C. Decès-Petit, R. Hui, R. Maric, D. Ghosh, Journal of Power Sources, 164 (2007), 182-188.
3. M. Matsuda, T. Hosomi, K. Murata, T. Fukui, M. Miyake, Journal of Power Sources, 165 (2007), 102-107.
4. A. Tsoga, A. Gupta, A. Naoumidis, D. Skarmoutsos, P. Nikolopoulos, International Journal of Ionics, 4 (1998), 234-240.
5. N. Ben-Oved, O. Kesler, Advanced Materials Research, 15-17 (2007), 287-292.
6. B.D. White, O. Kesler, L. Rose, Journal of Power Sources, 178 (2008), 334-343.
7. N. Ben-Oved, O. Kesler, Journal of Power Sources, 193 (2009), 454-461.
8. J. Oberste Berghaus, J.G. Legoux, C. Moreau, R. Hui, D. Ghosh, Materials Science Forum, 539-543 (2007), 1332-1337.
9. O. Kesler, J. Matejicek, S. Sampath, S. Suresh, T. Gnaeupel-herold, P. Brand, J. Prask, Material Science and Engineering A, 257 (1998), 215-224.
10. H. Kassner, R. Siegert, D. Hathiramani, R. Vassen, D. Stoever, Journal of Thermal Spray Technology, 17 (2008), 115-123.
11. D. Waldbillig, O. Kesler, Journal of Power Sources, 191 (2009), 320-329.
12. D. Waldbillig, O. Kesler, Z. Tang, A. Burgess, pp. 677-682 in Proceedings of the 2007 International Thermal Spray Conference (ITSC), Edited by B. Marple, M. Hyland , Y.C. Lau, C. J. Li, R. Lima, and G. Montavon. ASM International. Beijing, China, 2007.
13. C. Delbos, J. Fazilleau, J.F. Coudert, P. Fauchais, L. Bianchi, K. Wittmann-Teneze, pp. 661-669 in Proceedings of Thermal Spray 2003: Advancing the Science and Applying the Technology, Edited by B.R. Marple and C. Moreau, ASM International. Orlando, FL, USA, 2003.
14. V. Rat, C. Delbos, C. Bonhomme, J. Fazilleau, J.F. Coudert, P. Fauchais, High Temperature Material Processes, 8 (2004), 95-117.

15. J. Oberste Berghaus, S. Bouaricha, J.G. Legoux, C. Moreau, pp. 1434-1440 in Proceedings of International Thermal Spray Conference (ITSC), Edited by E. F. Lugscheider, German Welding Society. Basel, Switzerland, 2005.
16. P. Fauchais, Journal of Physics D: Applied Physics, 37 (2004), 86-108.
17. P. Fauchais, R. Etchart-Salas, C. Delbos, M. Tognionvi, V. Rat, J.F. Coudert, T. Chartier, Journal of Physics D: Applied Physics, 40 (2007), 2394-2406.
18. C. Delbos, V. Rat, C. Bonhomme, J. Fazilleau, J.F. Coudert, P. Fauchais, High Temperature Material Processes, 8 (2004), 397-406.
19. P. Fauchais, V. Rat, C. Delbos, J.F. Coudert, T. Chartier, L. Bianchi, IEEE Transactions on Plasma Science, 33 (2005), 2.
20. P. Fauchais, V. Rat, C. Delbos, J.F. Coudert, T. Chartier, L. Bianchi, IEEE Transactions on Plasma Science, 33 (2005), 920-930.
21. M. W. Sigmund, N. Bell, L. Bergstrom, Journal of the American Ceramic Society, 83 (2000), 1557-1574.
22. J. Lewis, Journal of the American Ceramic Society, 83 (2000), 2341-2359.
23. S. Tripathy, A. Raichur, Journal of Dispersion Science and Technology, 29 (2008), 230-239.
24. R. Zhang, P. Somasundaran, Advances in Colloid and Interface Science, 123 (2006), 213-229.
25. D. Waldbillig, O. Kesler, Surface & Coatings Technology, 203 (2009), 2098-2101.
26. R. Greenwood, K. Kendall, Journal of the European Ceramic Society, 20 (2000), 77-84.
27. G. Parks, Chemical Reviews, 65 (1965), 177-198.
28. L. Jin, X. Mao, S. Wang, M. Dong, Ceramics International, 35 (2009), 925-927.
29. S. Ramanathan, K. Krishnakumar, P. De, S. Banerjee, Journal of Materials Science, 39 (2004), 3339-3344.
30. Y. Zhang, J. Gao, D. Peng, M. Guangyao, X. Liu, Ceramics International, 30 (2004), 1049-1053.
31. Y. Wang, X. Liu, G. Meng, Ceramics International, 33 (2007), 1025-1031.

32. B.J. Briscoe, A.U. Khan, P.F. Luckmam, Journal of the European Ceramic Society, 18 (1998), 2169-2173.
33. M. Schultz, S. Grimm, W. Burckhardt, Solid State Ionics, 63-65 (1993), 18-24.
34. Y. Fu, S. Chen, Ceramics International, 35 (2009), 821-825.

4 Characterization of metal-supported axial injection plasma sprayed solid oxide fuel cells with aqueous suspension plasma sprayed electrolyte layers[17,18]

4.1 Introduction

The demand for energy continues to increase and with it, interest has grown in alternatives to hydrocarbon fuels and increased energy efficiency. Fuel cells have been proposed as energy conversion devices that have the potential to address both of these issues [1].

Fuel cells electrochemically oxidize fuel to directly produce electricity and heat. There are a number of different types of fuel cells currently being developed, but one of the most promising is the solid oxide fuel cell (SOFC). This fuel cell type uses an ionically conductive ceramic material (often yttria stabilized zirconia – YSZ) as the electrolyte. Because ceramic materials typically have low and thermally activated electrical conductivities and high stability at elevated temperatures, SOFCs typically operate at temperatures between 600 and 1000°C. Elevated temperature operation helps to reduce electrochemical losses and facilitates the use of high quality waste heat in cogeneration applications. The high operating temperature and oxide ion conducting nature of SOFCs also gives them the ability to use a wide variety of fuels such as hydrogen, natural gas, alcohols, and liquid hydrocarbons.

SOFCs are typically manufactured using wet ceramic techniques such as tape casting and screen printing or aerosol spraying combined with multiple high temperature (up to

---

[17] A version of this chapter has been published as D. Waldbillig, O. Kesler, Characterization of metal-supported axial injection plasma sprayed solid oxide fuel cells with aqueous suspension plasma sprayed electrolyte layers, Journal of Power Sources, 191(2) (2009), 320-329.

[18] Reprinted from Journal of Power Sources, 191 / 2, D. Waldbillig, O. Kesler, Characterization of metal-supported axial injection plasma sprayed solid oxide fuel cells with aqueous suspension plasma sprayed electrolyte layers, 320-329, Copyright (2009), with permission from Elsevier.

1400°C) sintering steps [2]. This makes large scale manufacturing based on these processes capital-intensive and time-consuming for mass production, and makes the use of low-cost metallic supports challenging.

Recently, it has been proposed to replace the current state-of-the-art Ni-YSZ cermet substrates with porous stainless steel substrates [3]. These metallic substrates have superior thermal, mechanical, and electrical properties to the cermet ones and are less expensive. However, it is difficult to incorporate metallic substrates into current manufacturing processes due to the high sintering temperature required to fully densify electrolyte layers. Inert atmosphere sintering with electrolyte sintering aids has been used to address these issues; however, inert atmospheres increase process costs and sintering aids usually introduce some level of electronic conductivity into the electrolyte, which decreases cell performance [4]. Plasma spraying (PS) has been proposed as a novel manufacturing method for SOFCs to address these issues with conventional manufacturing methods [1,5,6].

Plasma spraying is a well-established manufacturing technique first developed in the 1960's to produce value added coatings to enhance wear resistance, temperature resistance, and to repair parts [7]. Plasma sprayed coatings are most commonly used as thermal barrier coatings in gas turbines and diesel engines. Plasma spraying uses a hot, energetic plasma to melt feedstock powders, which impact with a substrate and rapidly solidify, forming solid splats. Subsequent splats form on previously deposited ones to produce coatings. Plasma temperatures may be up to 10000 K, so in theory any material may be deposited. Fully sintered coatings may be produced rapidly without the need for post deposition heat treatments. This ability to rapidly produce ceramic layers without post deposition sintering processes can allow metal supported SOFCs to be manufactured rapidly and relatively inexpensively.

Most of the original plasma sprayed SOFC work used vacuum plasma spraying (VPS) techniques. The German aerospace center (DLR) has produced VPS SOFCs for many years [8,9,10]. VPS operates in low pressure atmospheres, which enable a longer and less

turbulent plasma flame to be formed. Unfortunately, VPS systems require more equipment and are more expensive to operate [7] and thus much recent interest has arisen in developing methods to produce plasma sprayed SOFCs using atmospheric plasma spray (APS) systems that operate at atmospheric pressure [5].

Plasma spray systems usually use feedstock powders that are typically 10 – 100 µm in diameter. The powders are typically delivered by suspending them in a flowing gas, and most plasma spray SOFC research has focused on using these conventional powder spraying routes to produce fuel cell layers (e.g. [11,12]). However, it is challenging to produce fuel cell microstructures with the required properties, since it is difficult to feed powders < 5 µm in diameter [1] and due to the horizontal splat orientation of the microstructure. It is also quite challenging to find spraying conditions to produce the porous, high surface area microstructures required for high performing SOFC composite electrodes or thin (<10 µm), fully dense microstructures required for electrolytes.

Recently, plasma spray systems have been modified in order to use nano- to micro-sized powders suspended in a liquid as feedstocks [13-18]. These smaller powders improve the ability of plasma spraying to produce finer microstructures and controlled porosity. However, much work remains to be done to develop methods to deliver and atomize the suspension, to deal with the liquid effects on the plasma, and to find optimal spraying conditions to produce layers with the desired microstructures.

Many suspension plasma spraying (SPS) SOFC studies have used relatively low powered plasma torches and have injected the feedstock suspensions radially. Low torch power limits the ability to use high solid content suspensions and often requires suspensions to be alcohol based [19] to lower the energy required to vapourize the suspending liquid. The low solid content limitations reduce coating deposition rates, and non-aqueous suspensions are typically more expensive and less environmentally friendly than water based ones. Radial injection of feedstock suspensions makes suspension atomization, droplet size, and velocity extremely important parameters, because it is very difficult to achieve good penetration of nano- to micro-sized suspended powders from the periphery to the center of

the plasma plume. Axial injection of feedstock suspensions simplifies a number of injection issues, as the suspension is fed directly into the center of the plasma plume and thus does not have to pass through the more turbulent outer fringes of the plasma. However, axial feedstock injection increases the complexity of the plasma torch and limits the size of suspension feeding lines, since the lines have to pass between the torch electrodes.

Many previous studies have focused on spraying individual SOFC layers or on depositing layers on standard plasma spray substrates (sand blasted glass or steel plate). However, the substrate parameters can have a large effect on coating properties, and thus coatings sprayed on sand blasted flat sheet substrates may have very different properties to those of coatings sprayed on porous SOFC substrates. In addition, due to the multi-layer nature of SOFCs, it is very important to deposit each subsequent layer on top of a previously deposited fuel cell layer in order to better duplicate the substrate heat transfer conditions that would be observed during fuel cell manufacturing. Thus the deposition of anodes or cathodes directly onto porous metal substrates and of electrolyte layers onto previously sprayed anode or cathode layers allows the effect of surface morphology of substrates and initial coating on subsequent coatings to be determined.

This work reports initial results in the development of a fully plasma sprayed SOFC deposited on a porous stainless steel support. A high powered axial injection plasma spray torch was used to deposit cathode, electrolyte, and anode layers. Composite LSM/YSZ cathodes and NiO/YSZ anodes were deposited from conventional powder feedstocks. High solid content (23.7 wt%) aqueous YSZ suspensions were used as feedstocks for electrolyte layers. Full cells were built up by the sequential deposition of cathode, electrolyte and anode layers on the porous metallic substrate. This study focuses mainly on SPS electrolyte development and substrate selection, and selected electrolyte suspension plasma spray parameter optimization studies are reported. Cathode and anode spray parameters are being optimized in parallel studies and are reported elsewhere (e.g. [20]).

The cathode-first deposition configuration was selected due to the potential to obtain several benefits compared to the more traditional anode-first deposition configuration

commonly used in the manufacture of planar cells. First, because the cathode is typically entirely made of hard ceramic, while the anode is traditionally a cermet composite with more compliant metal present, the anode can more readily establish a good electrical contact with the interconnect through mild deformation when loaded in a stack, so by spraying the cathode directly onto the metallic support, the melting of the cathode material and its solidification directly onto the metal, following the substrate contours, has the potential to establish a good electrical contact without the use of wet contact pastes. In addition, since metal has a higher thermal conductivity than the zirconia used in the electrolyte, the deposition of the cathode directly onto the metal has the potential to remove heat more rapidly than if the cathode were deposited onto a ceramic layer. This rapid heat removal provides a mechanism for the introduction of additional porosity into the cathode by allowing the more rapid freezing of partially melted structures to create porosity through partial melting, which is more critical for the cathode than for the anode, since the latter can obtain additional porosity through the reduction of NiO to Ni prior to operation of the cell.

Furthermore, the formation of a direct contact between the cathode and interconnect can reduce the extent of oxidation at the porous metal support-cathode interface, thus decreasing the extent of series resistance increase with time. Finally, the establishment of a pre-formed contact between cathode and metal support allows coatings for the minimization of oxidation and chromium evaporation to be placed on the metal after the electrical contact between the cathode and porous metal has been established. As a result, the protective coatings do not have to be electrically conductive, and so they can be designed to obtain the closest match in thermal expansion with the porous metal, or for ease of processing, without the additional requirement of electrical conductivity limiting the choice of materials.

Initially very energetic plasma spraying conditions were chosen in order to ensure full evaporation of the water and melting of the YSZ. After the initial spray runs, preheat temperature, standoff distance, and number of deposition passes were varied to determine

the effect on electrolyte permeability and deposition efficiency to develop a more optimized process window.

The effect of two different porous stainless steel substrate types, denoted as media grades (MG) 2 and 5, were examined during this study. Both substrate types have comparable total porosity levels, but MG 5 has larger surface pores. These pores can enhance layer adhesion by facilitating the mechanical interlocking of the sprayed cathode with the rough substrate; however, some of the pores are too large for the splats to bridge over, which can result in discontinuous layers. The effect of substrate media grade on the surface roughness, permeability, and microstructure of deposited fuel cell layers is examined.

Finally, full cells consisting of an APS cathode and anode and an SPS electrolyte on a porous metal support were fabricated and electrochemically tested.

4.2 Experimental procedure

4.2.1 Material preparation

A mixture of 48.2 wt% lanthanum strontium manganite (LSM) and 51.8 wt% 8 mol% yttria-stabilized zirconia (YSZ) powders were used for the cathode layers. Spray dried cathode powders were sieved and mechanically mixed before plasma spraying. The detailed powder preparation procedure has been reported previously [20].

8 mol% YSZ powder (Inframat Advanced Materials, Farmington, CT, USA) was used as the electrolyte feedstock for this study. The as-received powder had a d_{50} agglomerate size of approximately 1.5 μm, with sizes ranging from 0.5 μm to 15 μm, as determined by laser light scattering (Mastersizer 2000, Malvern Instruments, Worcestershire, UK) (Figure 4.1). Aqueous YSZ suspensions with a solid loading of 5 vol% (23.7 wt%) were prepared using deionized water. PBTCA (2-Phosphonobutane-1,2,4-Tricarboxylic acid) was used to enhance the particle dispersion in the suspensions. An optimized dispersant concentration was determined in a previous study [21].

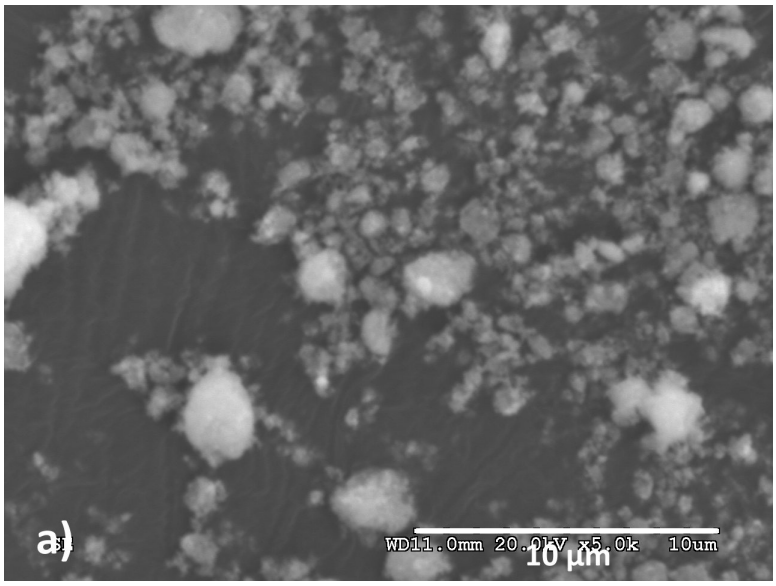

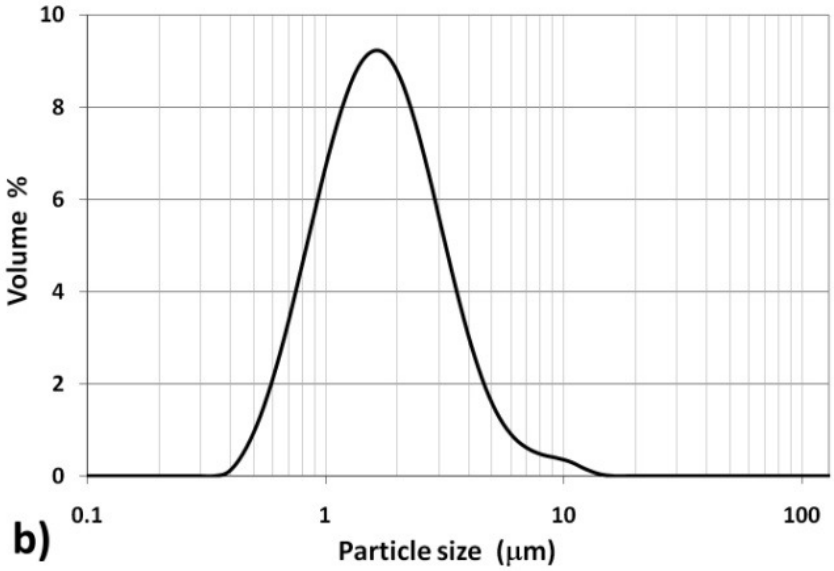

Figure 4.1: (a) SEM image and (b) histogram showing the particle size distribution, for the YSZ powder used for SPS of the electrolyte.

Anode powders were sieved and then mechanically mixed. The powder consisted of a mixture of 46 wt% NiO, 38wt% YSZ, and 16 wt% carbon black pore former.

4.2.2 Plasma spray processing

An Axial III Series 600 (Northwest Mettech Corp., North Vancouver, BC, Canada) atmospheric plasma spray system was used for all layer depositions (Figure 4.2a). This torch injects the feedstock axially between 3 electrodes, which ensures that virtually all of the powder injected passes through the hottest part of the plasma jet. For cathode and anode layers a Thermico (model CPF-2HP, Germany) powder feeding system was used. For the electrolyte layer, the plasma spraying system was modified to add a pressure vessel in order to deliver the suspension to the feed tube of the plasma torch (Figure 4.2b). The suspension was injected through a needle type nozzle (ID = 0.84 mm) positioned directly behind the torch convergence into the centre of the plasma jet, where it was atomized[19].

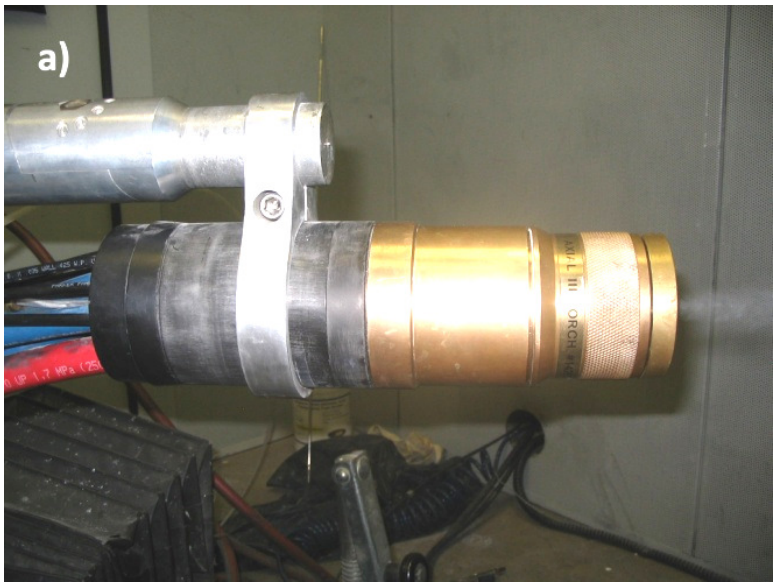

[19] A more detailed description of the suspension delivery and injection equipment can be found in Appendix D.

Figure 4.2: a) Mettech Axial III plasma spray torch. b) Pressure vessel based suspension delivery system.

The substrates were preheated directly by the plasma torch, before the powder or suspension feeding systems were turned on, to a temperature above the desired preheat temperature, and then were allowed to cool to the desired preheat temperature while the powder / suspension flow stabilized. Substrate temperatures during spraying were measured directly by positioning a Type K thermocouple in contact with the back of the metal substrate, and were monitored during spraying. Figure 4.3 shows the temperature profile measured during a typical spraying run.

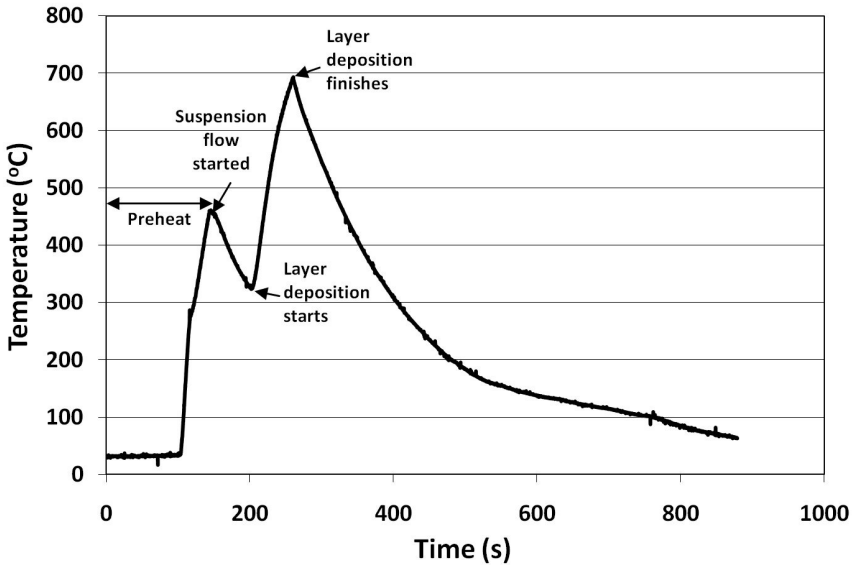

Figure 4.3: Temperature measurements during spraying

Deposition was carried out onto 2.54 cm diameter porous 430 ferritic stainless steel substrates (Mott Corporation, Farmington, CT, USA) mounted on a rotating turntable. Two different media grades (MG) of stainless steel substrates were examined, MG 2 and MG 5. These substrates are most commonly used as filter media, and the media grade designation refers to the smallest diameter particle in microns that can be captured by the filter material.

Plasma sprayed composite LSM / YSZ cathode layers were first deposited on the steel substrates, followed by the suspension sprayed electrolyte layer. Finally, for the cells that were electrochemically tested, a 1 cm diameter NiO / YSZ anode layer was deposited through a mask in the centre of the electrolyte layer.

The initial electrolyte spraying runs varied one parameter (either preheat temperature, number of passes, or standoff distance) to systematically study the effect of each parameter on the electrolyte permeability, deposition efficiency (thickness), and microstructures.

The plasma spraying parameters used for deposition of each layer are shown in Table 4.1. Each layer was deposited during a separate spray run of approximately 1 to 4 minutes in duration, with no post-deposition heat treatments.

Table 4.1: Plasma spraying parameter values.

Parameter	Cathode	Electrolyte	Anode
Feedstock	48.2 wt% LSM / 51.8 wt% YSZ powder	23.7 wt% YSZ aqueous suspension	46 wt% NiO / 38 wt% YSZ / 16 wt% carbon black powder
Particle size	−45+32 µm / −32+25 µm	D_{50} = 1.5 µm	−45+32 µm / 5 µm / 20-30 µm
Plasma gas flow rate (slpm)	250	220	250
Plasma gas composition	23.3% N_2, 76.7% Ar	80% N_2, 20% H_2	23.3% N_2, 76.7% Ar
Torch current (A per cathode)	183	250	183
Nozzle size (mm)	9.5	12.7	12.7
Number of passes	60	25, **50**, 100[a]	80
Preheat temperature (°C)	300	20, **325**, 450[a]	300
Standoff distance (mm)	100	70, **80**, 90[a]	100

[a]Values in bold were held fixed during variation of other parameters.

4.2.3 Characterization of plasma sprayed fuel cell layers

The surface roughness of the uncoated and coated samples was measured using surface profilometry (Form Talysurf Series 2, Taylor Hobson Ltd., Leicester, UK). The form analysis software was used to correct for any deviation from horizontal in the substrate-coating pair

by using a least squares arc geometric reference. Average roughness values were then calculated.

Helium permeation measurements were performed using an in-house designed fixture in order to measure the gas permeability of the substrates and each deposited layer. The supply of helium gas was regulated at a pressure of 3.5 kPa by a pressure controller (Alicat Scientific, model PCD-5PSIG-D, Tucson, AZ, USA). The flow through the sample was then measured at the outlet of the fixture by a mass flow meter (Alicat Scientific, model M-0.5SCCM-D_H2, Tucson, AZ, USA)[20].

The flow rate through the sample can be related to the layer permeability using Darcy's law (Equation 4.1).

$$Q = \frac{-\kappa A}{\mu}\frac{(P_b - P_a)}{L} \qquad (4.1)$$

where: Q is the flow rate (m^3/s)
κ is the permeability (m^2)
A is the cross-sectional area to flow (m^2)
($P_b - P_a$) is the pressure drop (Pa)
μ is the dynamic viscosity (Pa s)
L is the length over which the pressure drop takes place

For our testing setup, a relative permeability can be calculated by assuming that the cross-sectional area, pressure drop, and dynamic viscosity are constant for each coating tested. Thus a relative permeability (κ) can be calculated by multiplying the measured flow rate (Q) and the electrolyte layer thickness (L). The absolute coating permeability was not directly determined because the substrates were also porous, but since the substrate and cathode

[20] A detailed explanation of the permeation measurements can be found in Appendix C.

thicknesses were the same for different electrolytes tested, a qualitative comparison between conditions was possible.

Polished cross sections of the deposited layers were examined in a Hitachi S-3000N scanning electron microscope (SEM) (Hitachi High Technologies America, Pleasanton, CA, USA). Samples were cut using a low speed diamond saw, mounted in epoxy, and then polished using diamond polishing suspensions. The polished samples were gold coated to provide sufficient sample conductivity for SEM imaging. The electrolyte layer thickness was measured directly from SEM images.

Electrochemical testing was performed using a custom electrochemical test stand and a Solartron 1480 Multistat (Solartron Analytical, Farnborough, U.K.). Testing was performed at 650, 700, and 750°C, and used a humidified (3% H_2O), 20%/80% H_2/N_2 mixture as the fuel and air as the oxidant. Fuel and air flow rates were set at 200 sccm[21].

4.3 Results and discussion

4.3.1 Initial electrolyte spraying studies

Figure 4.4a shows the microstructure of the control sample, which was sprayed at the conditions designated as "standard" – 50 deposition passes, 325ºC preheat temperature, 80 mm standoff distance. Electrolyte layers sprayed at these conditions were continuous and mostly dense. Three main defect types were seen in the electrolyte layers: vertical cracking, medium sized defects, and small pores (Figure 4.4b). The vertical cracking was likely caused by thermally induced residual stresses produced during spraying. The medium sized defects could be caused by unmelted particles present within the deposited layer, leading to the introduction of porosity around the unmelted particle. Finally, small pores present are likely intersplat porosity.

[21] A more detailed description of the electrochemical testing equipment and test procedures can be found in Appendix E.

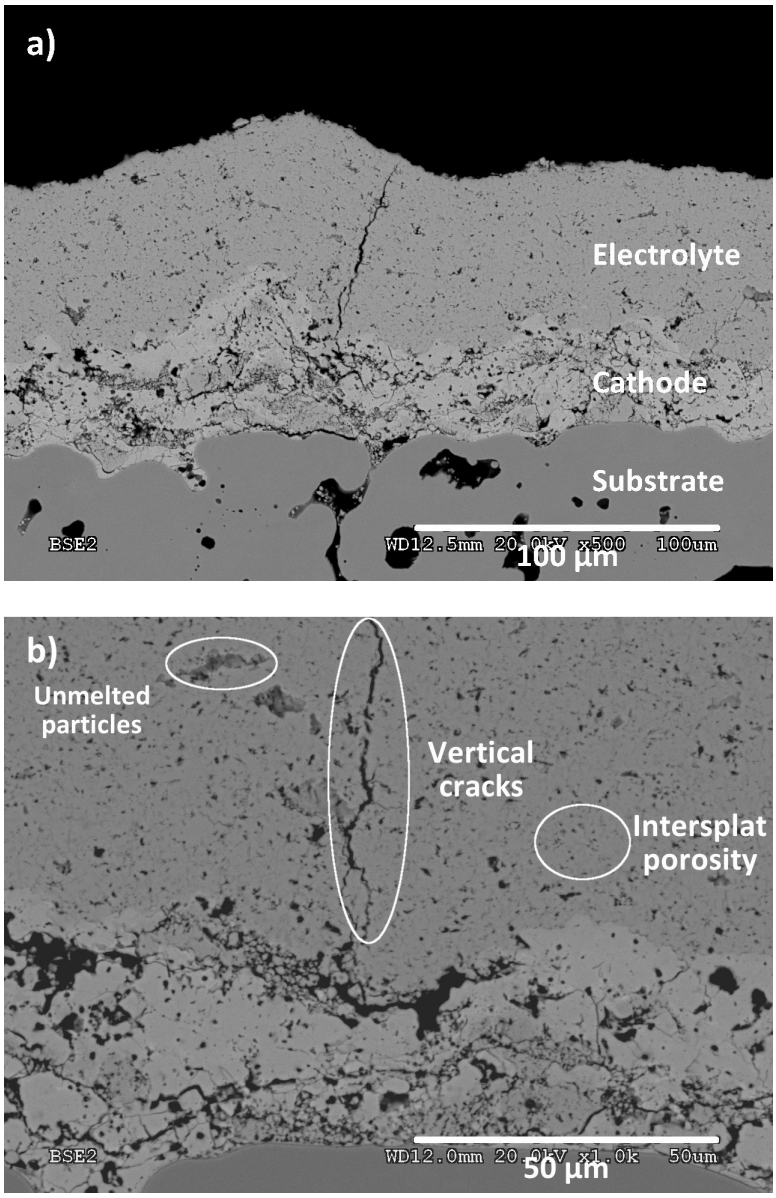

Figure 4.4: (a) SEM image of the polished cross section of the half cell after spraying at the standard conditions (50 deposition passes, 325^{o}C preheat temperature, 80 mm standoff distance). (b) Defect types seen in suspension plasma sprayed electrolyte layers.

The effect of number of deposition passes, preheat temperature, and standoff distance on the electrolyte permeation rate and thickness values as well as the cell microstructures are shown in Figures 4.5 to 4.11. As the number of deposition passes increases, the electrolyte thickness increases and permeation decreases (Figure 4.5). However, the permeability of the coatings increases with increasing coating thickness (Figure 4.6), suggesting that the

porosity of subsequently-deposited coating layers may be higher than the porosity of the initial layers in the coatings, possibly due to different rates of solidification. Although the permeability calculated and shown in Figure 4.6 corresponds to a combined value for the substrate-cathode-electrolyte system, the permeation through the substrate and cathode have been previously found to be substantially higher than that of the substrate-cathode-electrolyte combination [21], so the total permeability is likely dominated by the properties of the electrolyte.

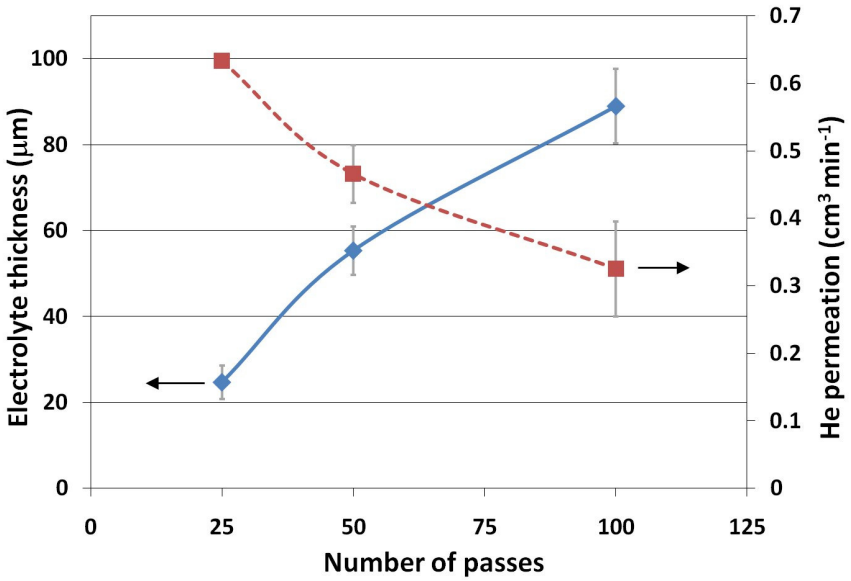

Figure 4.5: Effect of number of deposition passes on electrolyte thickness and permeation at 3.5 kPa.

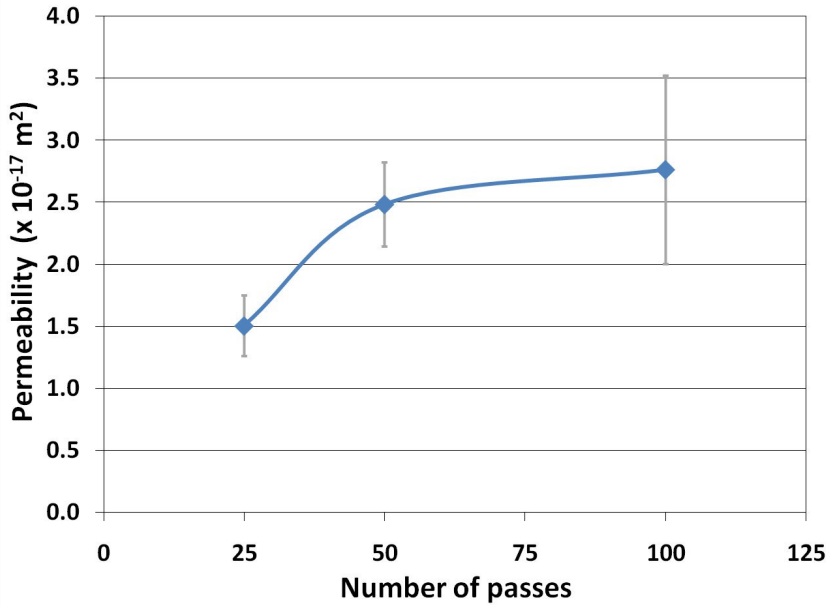

Figure 4.6: Effect of number of deposition passes on the permeability of electrolyte coatings on porous metal + cathode substrates.

Figures 4.7a and 4.7b show the microstructure of the 25 pass and 100 pass electrolyte layer, respectively. Compared to the standard microstructure (Figure 4.4a), the 25 pass electrolyte looks more porous, and it appears that the thinner layer had difficultly bridging over the topography of the cathode surface in places. The thicker electrolyte looks reasonably dense and well adhered to the cathode, but such a thick electrolyte will lead to very high resistive losses during fuel cell operation.

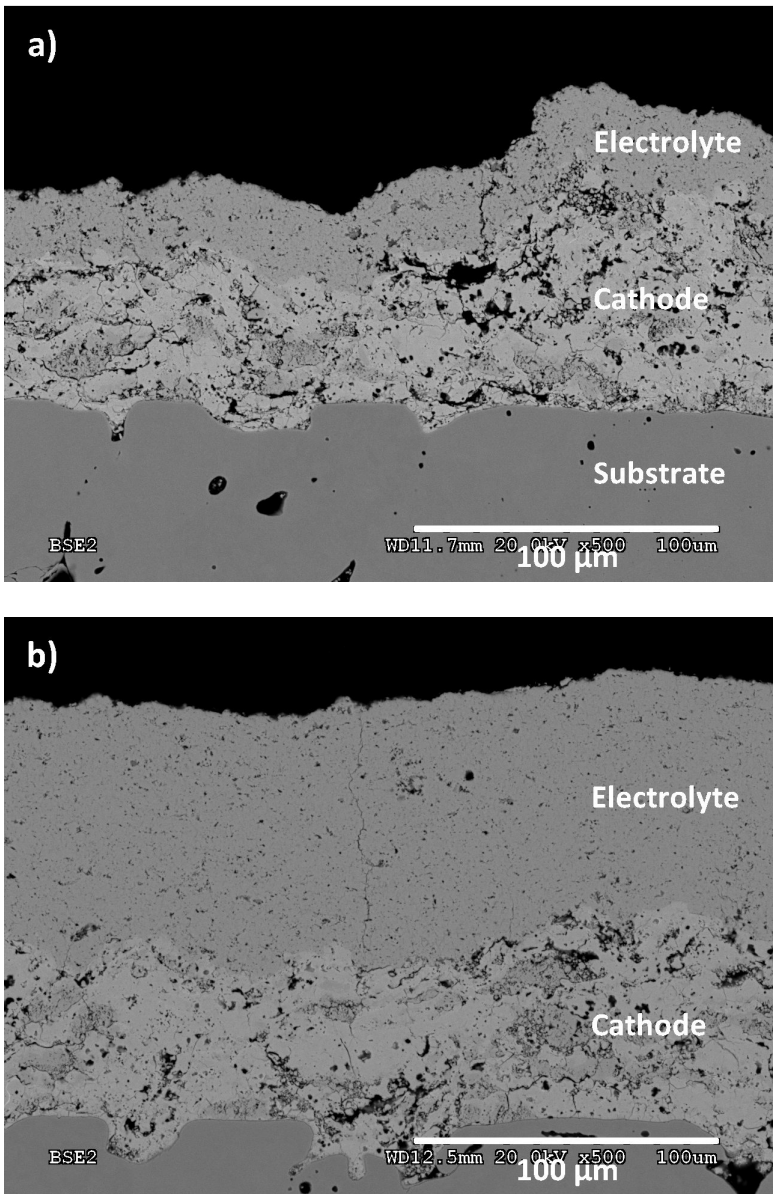

Figure 4.7: SEM image of the polished cross section of the cathode-electrolyte half cell after (a) 25 and (b) 100 electrolyte deposition passes.

Substrate preheat temperature seemed to have little effect on deposition efficiency, but it appeared that too low of a preheat temperature (20°C) significantly increased the electrolyte permeation, as seen in both permeation measurements (Figure 4.8) and in microstructural examination (Figure 4.9), where the unpreheated electrolyte layer (Figure

4.9a) looks significantly more porous than the standard microstructure (Figure 4.4a). Samples with higher preheat temperatures (325 or 450°C) had very similar layer thicknesses, permeations, and microstructures.

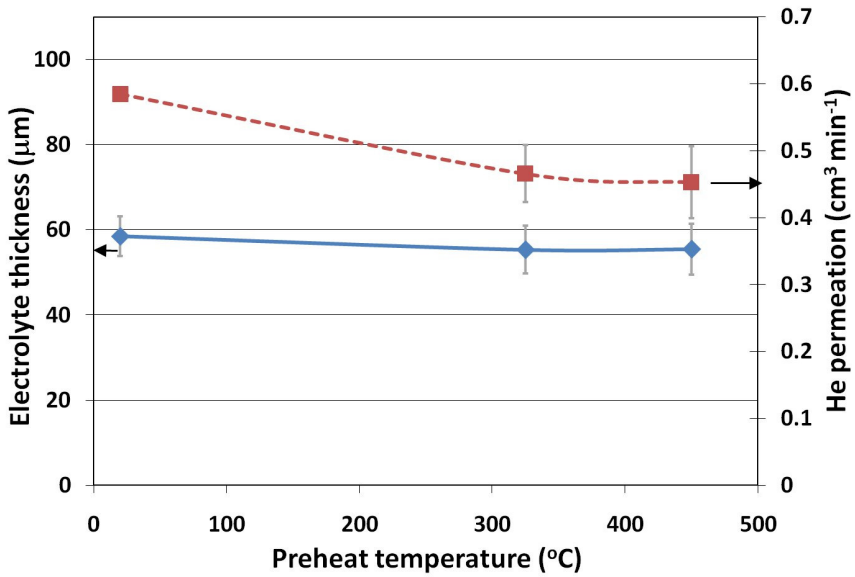

Figure 4.8: Effect of preheat temperature on electrolyte thickness and permeation at 3.5 kPa.

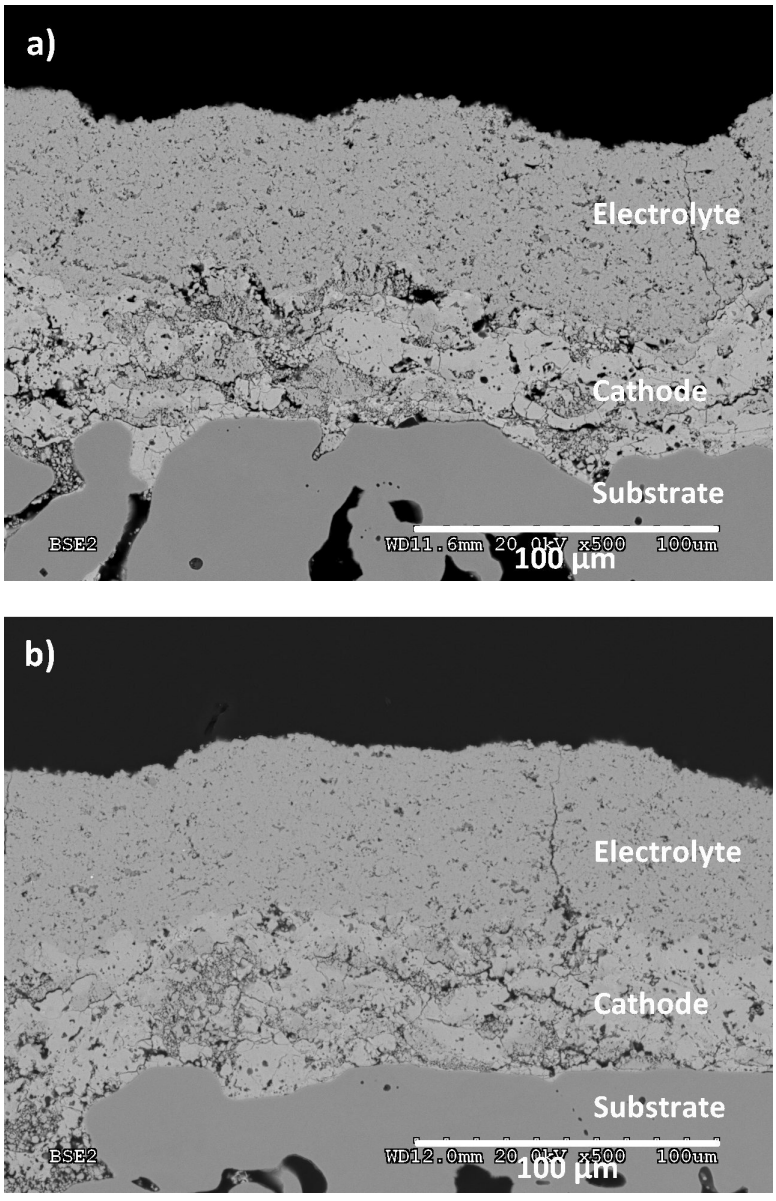

Figure 4.9: SEM image of the polished cross section of half cells with (a) no preheat, and (b) 450^{o}C preheat.

Standoff distance seemed to have no effect on the deposition efficiency for the conditions examined in this study as seen in Figure 4.10, and the layer microstructures looked fairly similar as well (Figure 4.11). The permeation rate of the samples at a standoff distance of 90 mm was significantly higher than those at lower standoff distance, and it appeared that an 80 mm standoff produced coatings with the lowest permeation rate among the standoff distances studied here. The permeabilities of the electrolyte coatings on the substrates as a

function of preheat temperature and of stand-off distance were also found to follow the same trends as the permeations.

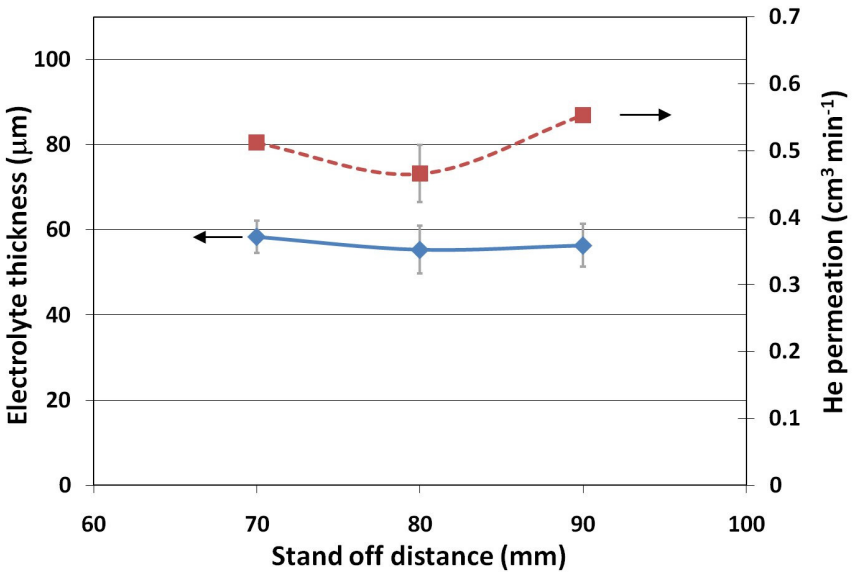

Figure 4.10: Effect of standoff distance on electrolyte thickness and permeation at 3.5 kPa.

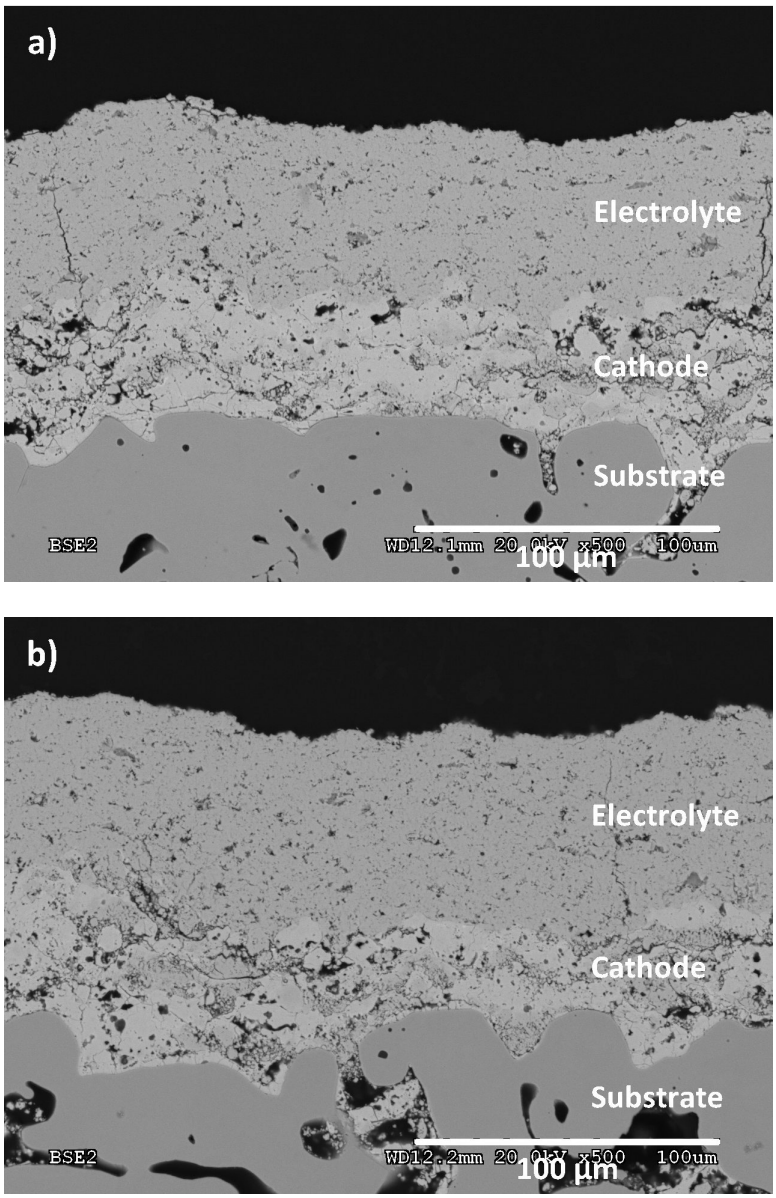

Figure 4.11: SEM image of the polished cross sections of half cells produced at a standoff distance of (a) 70 mm, and (b) 90 mm.

4.3.2 Substrate characterization

The porosities of both substrate types were calculated from measurements of the weight and dimensions of each substrate. The ratio of this calculated value and the density of a fully dense sample of 430 stainless steel [22] gives the porosity values shown in Table 4.2.

Table 4.2: Substrate porosity values.

Substrate	% Porosity
Media grade 2	25.4
Media grade 5	28.1

SEM images of the polished cross sections of the two substrate types are shown in Figures 4.12a and 4.12b. Both the amount of porosity and the average pore size increase as the substrate media grade increases.

In order for these porous media to perform as SOFC mechanical supports, a balance must be struck between high porosity and large pores that enhance gas diffusion across the support and low porosity and small pores that allow splats to more effectively "bridge" over surface pores to produce continuous coatings. The two media grades 2 and 5 were chosen as they appear to have a good compromise of porosity (25 to 30%) and pore size (1 to 50 μm). Figures 4.12c and 4.12d show the microstructures of a substrate with too-small pores (MG 0.5) and with too-large pores (MG 40) for comparison purposes.

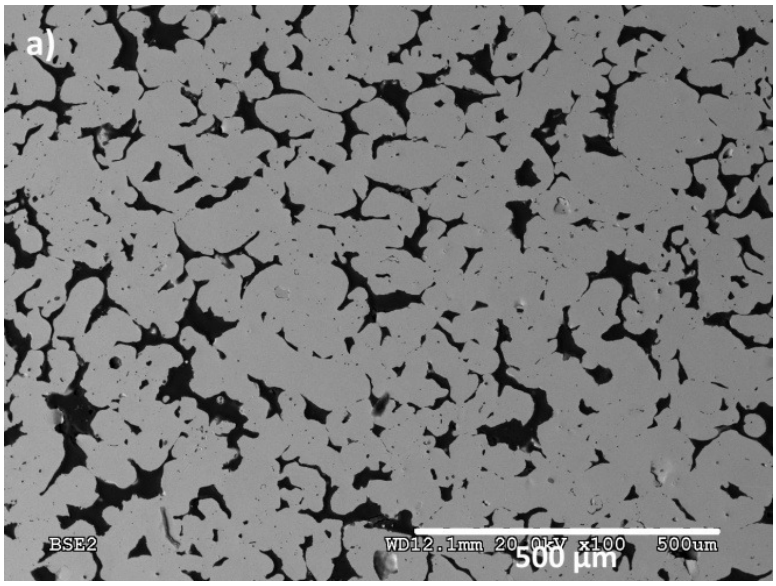
a)
BSE2
WD12.1mm 20.0kV x100 500um
500 µm

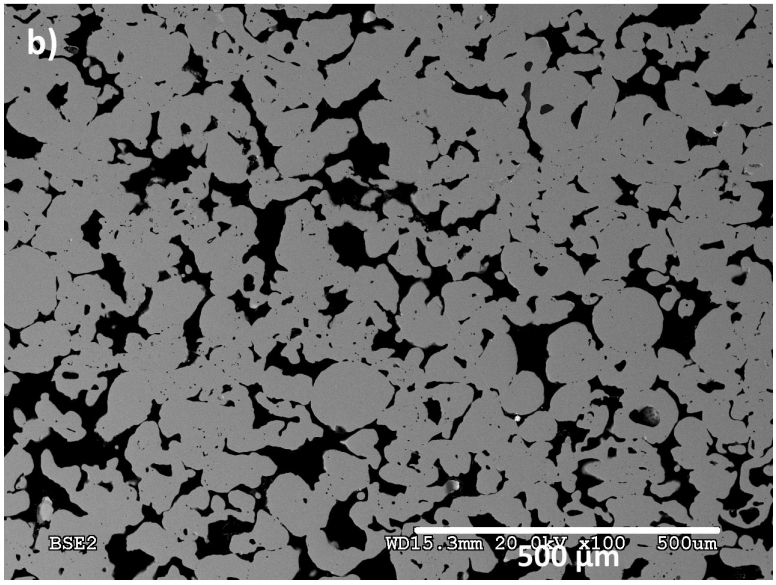
b)
BSE2
WD15.3mm 20.0kV x100 500um
500 µm

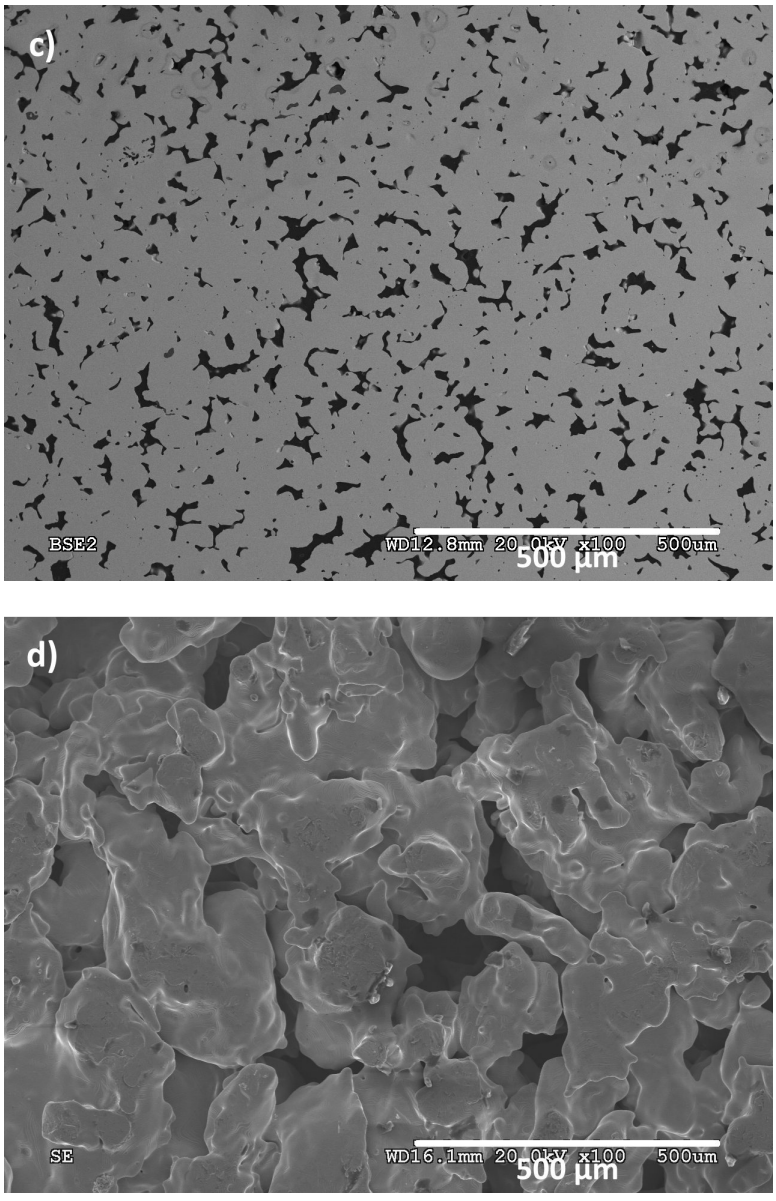

Figure 4.12: SEM image of the polished cross section of (a) the MG 2 substrate, (b) the MG 5 substrate, and (c) the MG 0.5 substrate, and (d) SEM image of the surface of the MG 40 substrate.

4.3.3 Surface profilometry

Surface roughness measurements for the MG 2 and 5 substrates are summarized in Figure 4.13. Additional measurements for samples with smaller pores (MG 0.5) and larger pores (MG 40) are also shown for comparison purposes. For uncoated substrates, the surface

roughness increases with the media grade; however, once a cathode coating is deposited on the porous metal substrates, there is no measurable difference in average cathode surface roughness regardless of which substrate is used for the three lowest media grades studied. Electrolyte surface roughness was also very similar regardless of which substrate was used. Continuous coatings were unable to be deposited on MG 40 substrates due to the large surface pores present.

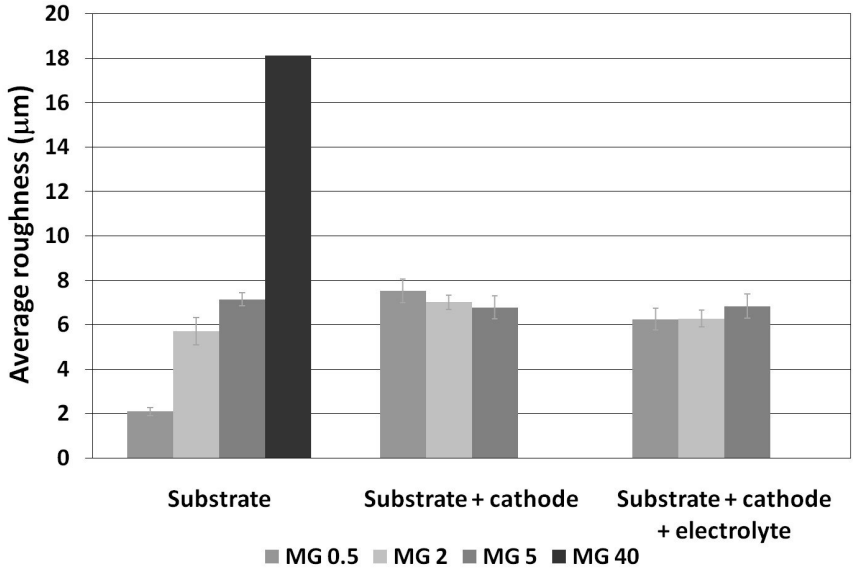

Figure 4.13: Summary of surface profilometry results.

4.3.4 Helium permeation testing

Helium permeation tests compared the permeation rate of cathode-electrolyte half cells sprayed on MG 5 substrates compared to those sprayed on MG 2 substrates. As can be seen in Figure 4.14, coatings on MG 5 substrates had slightly higher permeation rates than those sprayed on MG 2 substrates. This is likely due to the larger surface pores present in the MG 5 substrates. These large pores are difficult for the cathode layer to bridge, resulting in a higher probability of discontinuities within the layers and thus higher permeation rates.

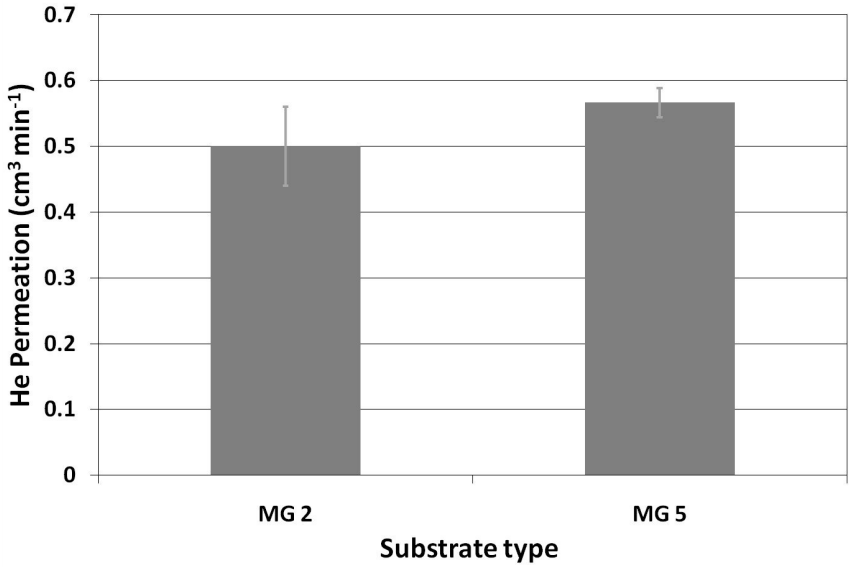

Figure 4.14: Summary of permeation testing results at 3.5 kPa of cathode-electrolyte half cells on metal supports.

4.3.5 Fuel cell microstructure

The overall microstructures of the full cells on the MG 2 and 5 stainless steel substrates are shown in Figure 4.15. The cathode appeared to be well adhered to the porous substrate and was for the most part able to bridge over substrate surface pores. However, there were a few areas where the substrate surface pores were very large, making it difficult for the cathode layer to bridge over the pores (Figure 4.16a). This phenomenon produced areas of localized electrolyte thinning, and may indicate that the use of a substrate with smaller surface pores may improve layer continuity. Figure 4.16b shows an SEM image of a coating on a MG 2 substrate, showing a region of connected porosity within the electrolyte caused by a cathode irregularity. These cathode irregularities are likely caused by clumping within the feedstock cathode powders.

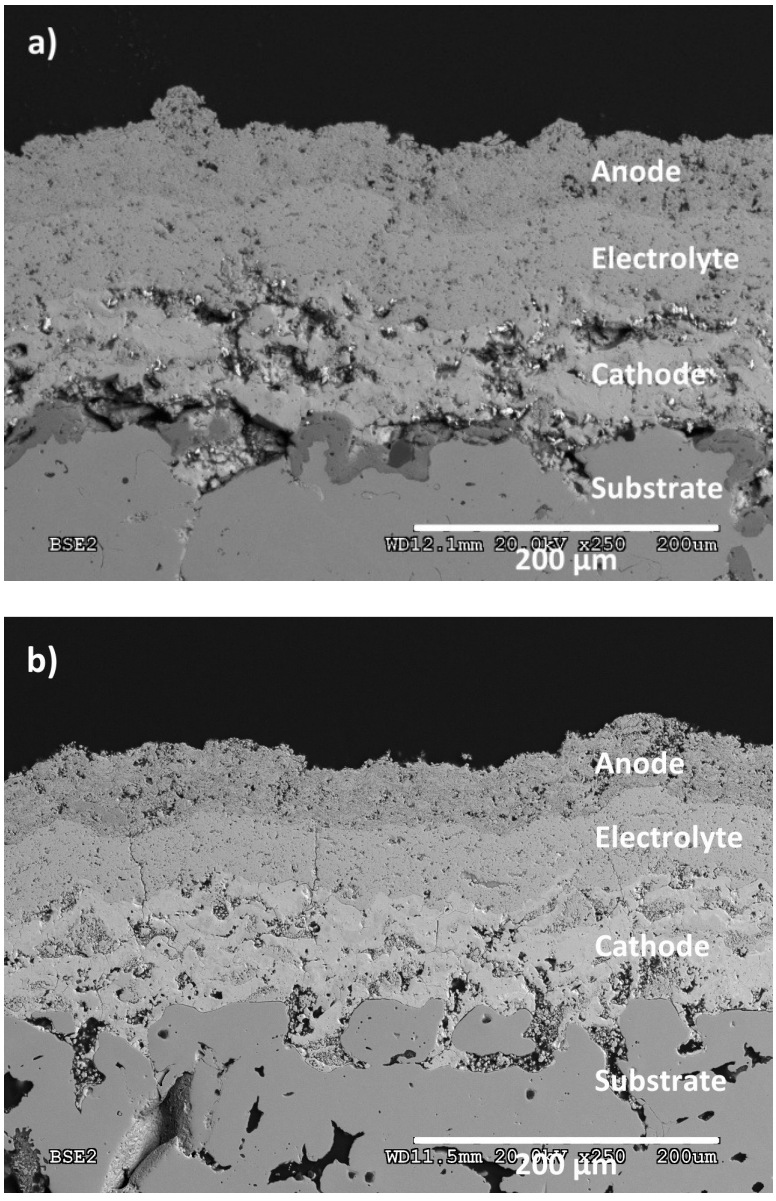

Figure 4.15: SEM image of a tested full cell on (a) a MG 2 substrate, and (b) a MG 5 substrate.

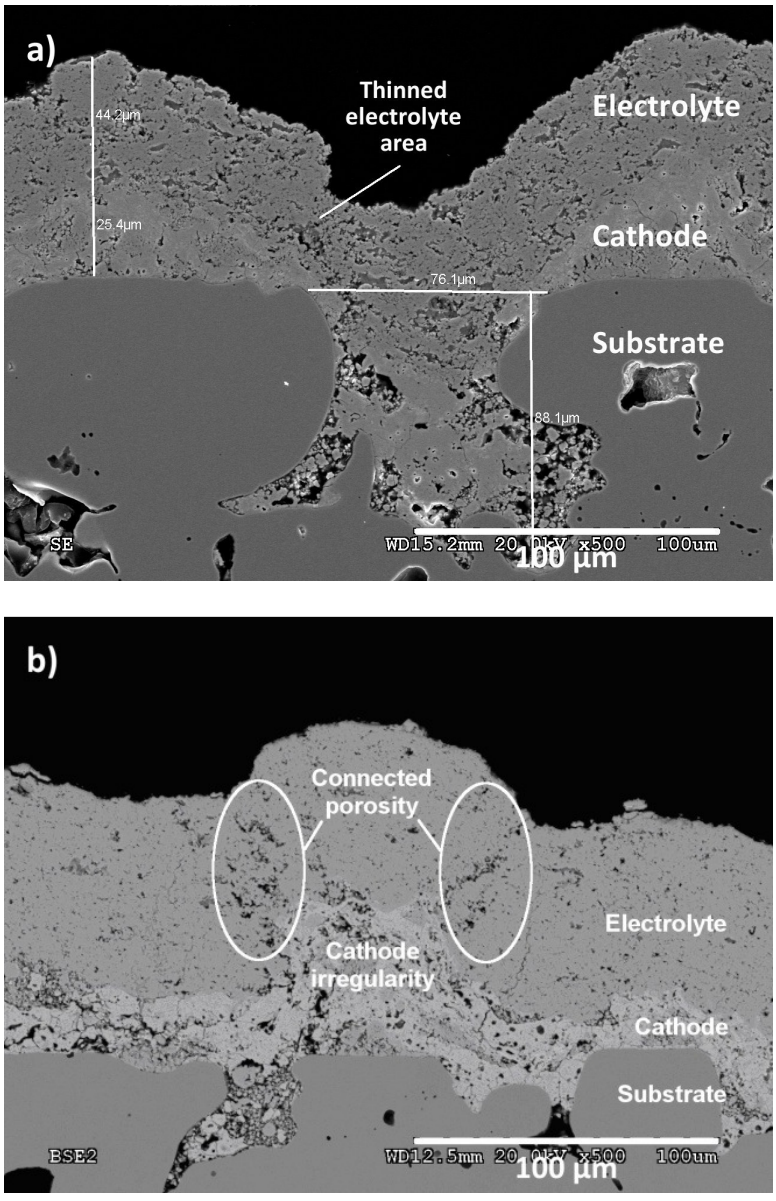

Figure 4.16: SEM image of a cathode-electrolyte half cell (a) on a MG 5 substrate, showing large surface pore and the resulting discontinuity in the cathode and electrolyte layers, and (b) on a MG 2 substrate, showing connected porosity within the electrolyte caused by cathode irregularity.

4.3.6 Deposition rates

Coating thicknesses were measured from the cross-sectional SEM images. From the thicknesses, deposition rates for each layer were calculated. These results are summarized in Table 4.3. Layer deposition rates are very fast compared to vapour phase deposition

techniques such as PVD or CVD. It is also worth noting that the laboratory-scale rotating turntable available for mounting the substrates resulted in the samples spending only 3% of the total deposition time in front of the plasma torch. However, the plasma spray process can be readily scaled up to large two-dimensional flat surfaces. In those circumstances, the coating rate and deposition efficiency would be further improved by a factor of ~34.

Table 4.3: Summary of layer deposition rates.

Substrate	Layer	Thickness of deposited layer (μm)	Number of spraying passes	Duration of spray run (min)	Deposition rate (μm/min)
MG 5	Cathode	57.80	40	1.84	31.4
	Electrolyte	46.79	50	2.30	20.3
	Anode	42.98	80	3.69	11.6
MG 2	Cathode	63.09	40	1.84	34.3
	Electrolyte	59.85	50	2.30	26.0
	Anode	41.00	80	3.69	11.1

4.3.7 Electrochemical testing

Fuel cells on MG 2 and 5 stainless steel substrates were electrochemically tested to determine the gas tightness and electrolyte resistance and the electrode activity. Polarization curves for the electrochemical tests are shown in Figure 4.17. Tests were performed at 650, 700, and 750^{o}C in a 3% humidified 20%/80% H_2/N_2 mixture at the anode with air at the cathode. Open circuit voltage and peak power density values are summarized in Table 4.4. Cells on MG 2 substrates had similar open circuit voltages to MG 5 supported cells, but had much higher power density values, with larger kinetic losses appearing to account for much of the difference in power density, as seen from the

polarization curves at low current densities in Figure 4.17. However, although operating plasma sprayed metal supported fuel cells have been produced, significant optimization work is required to increase both the open circuit voltage and the power density. The elimination of large cathode agglomerate particles from the coatings and use of substrates with fine surface porosities can both contribute towards the elimination of connected electrolyte porosity.

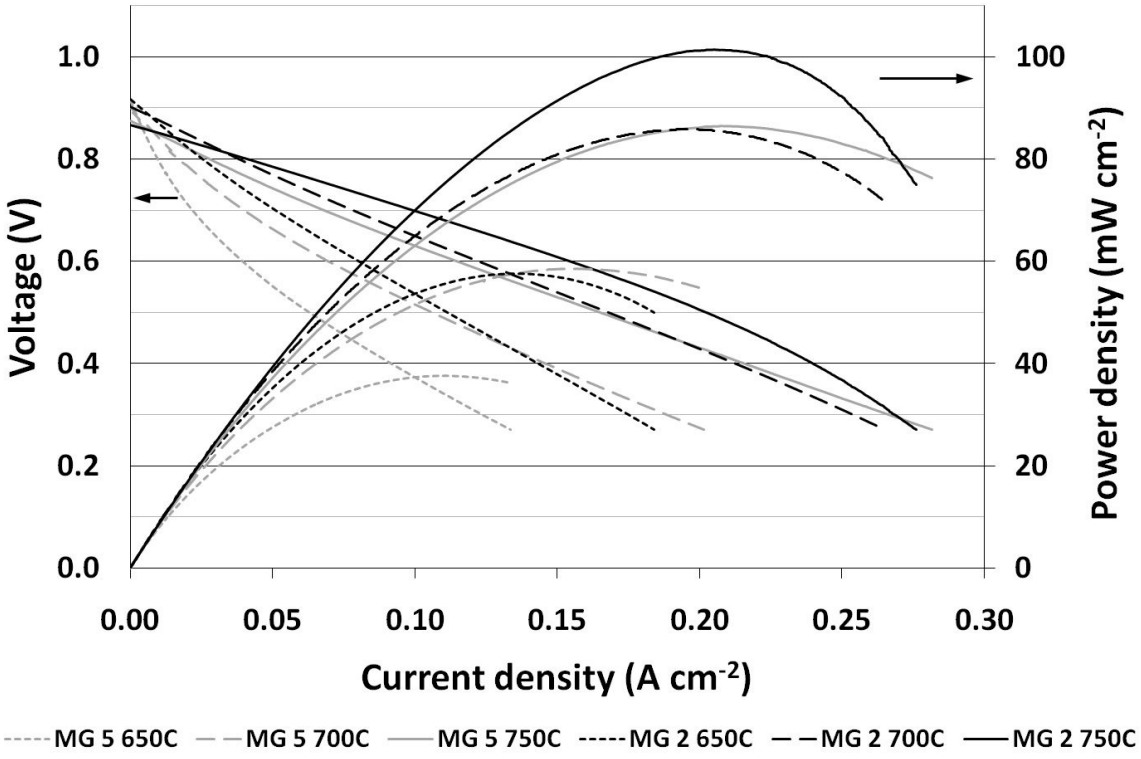

Figure 4.17: Polarization and power density curves of a metal supported plasma sprayed SOFC.

Table 4.4: Summary of polarization testing results.

Substrate type	Temperature (°C)	Open circuit voltage (V)	Peak power density (W/cm^2)
MG 5	650	0.913	0.038
	700	0.901	0.059
	750	0.874	0.086
MG 2	650	0.916	0.058
	700	0.902	0.086
	750	0.866	0.101

4.4 Conclusions

A metal supported SOFC was successfully fabricated using atmospheric plasma spray manufacturing methods. Plasma sprayed composite cathodes, aqueous suspension plasma sprayed electrolytes, and plasma sprayed composite anodes were deposited in succession on a porous steel substrate. Highly energetic suspension spraying conditions were chosen to ensure that electrolyte materials were fully melted (or nearly fully melted). A selected parameter study of electrolyte spraying conditions found more optimized values for the number of deposition passes, preheat temperature, and standoff distance in order to obtain a good trade-off between electrolyte permeability, deposition efficiency, and performance. Three main defect types were seen in suspension plasma sprayed electrolyte layers: vertical cracking caused by thermal stresses built up during coating deposition, pores or defects caused by unmelted particles within the coating, and small intersplat pores.

Two types of stainless steel substrates with different levels of porosity and pore size were also examined and the surface roughness, permeation rate, layer microstructure, and electrochemical performance of fuel cells deposited on each substrate type were

characterized. Surface roughness values were higher for uncoated substrates with larger MG numbers, but once a cathode layer was deposited, there was no significant difference in roughness values. Samples on MG 5 substrates had larger permeation rates than samples on MG 2 substrates, possibly due to the inability of splats to bridge over the large surface pores present in the MG 5 substrates. Cross sectional SEM showed that for the most part, layers appear to be well adhered and continuous. On MG 5 samples, there were a few areas where large substrate surface pores resulted in localized thinning of electrolyte layers, and on both substrate types, occasional cathode irregularities occurred that caused connected porosity within the electrolyte layers. Composite cathode and anode layers appeared to be well mixed and to contain some porosity. Electrolyte layers contained a few small, mostly unconnected pores. Polarization testing showed that cells produced on stainless steel MG 2 and 5 substrates had similar open circuit voltage values, but the fuel cells deposited on MG 2 substrates had a significantly higher power density.

Future work on this project will involve optimization of spraying parameters in order to obtain higher surface area and porosity in electrode layer microstructures and to further increase electrolyte gas tightness. The properties of electrolyte feedstock suspensions will also be characterized in order to improve the suspension feedability and dispersion and the resulting electrolyte layer microstructures.

4.5 Acknowledgements

The authors gratefully acknowledge financial support from the Natural Sciences and Engineering Research Council of Canada, Northwest Mettech Corporation, and the BC Innovation Council, as well as the assistance of Bradley White and Dr. Michael Poon with plasma spraying.

4.6 References

1. R. Henne, Journal of Thermal Spray Technology, 16(3) (2007), 381-403.
2. E. Tang , F. Martell, R. Brulé, K. Marcotte, B. Borglum, pp. 935-943 in proceedings of SOFC VIII, Edited by S.C. Singhal and M. Dokiya, The Electrochemical Society Proceedings Series. Paris, France, 2003..
3. Z.G. Yang, International Materials Reviews, 53(1) (2008), 39-54.
4. X. Zhang, C. Deces-Petit, S. Yick, M. Robertson, O. Kesler, R. Maric, D. Ghosh, Journal of Power Sources, 162(1) (2006), 480-485.
5. R. Hui, Z. Wang, O. Kesler, L. Rose, J. Jankovic, S. Yick, R. Maric, D. Ghosh, Journal of Power Sources, 170(2) (2007), 308-323.
6. C. Zhang, H.L. Liano, W.Y. Li, G. Zhang, C. Coddet, C.J. Li, C.X. Li, X.J. Ning, Journal of Thermal Spray Technology, 15(4) (2006), 598-803.
7. P. Fauchais, Journal of Physics D: Applied Science, 37 (2004), R86-R108.
8. T. Franco, Z. HoshiarDin, P. Szabo, M. Lang, G. Schiller, Journal of Fuel Cell Science and Technology, 4(4) (2007), 406-412.
9. M. Lang, R. Henne, S. Schaper, G. Schiller, Journal of Thermal Spray Technology, 10(4) (2001), 618-625.
10. M. Lang, T. Franco, R. Henne, P. Metzger, G. Schiller, S. Ziehm, in proceedings of SOFC VIII, Edited by S.C. Singhal and M. Dokiya, The Electrochemical Society Proceedings Series. Paris, France, 2003.
11. R. Zheng, X.M. Zhou, S.R. Wang, T.L. Wen, C.X. Ding, Journal of Power Sources, 140 (2005), 217.
12. X.Q. Ma, H. Zhang, J. Dai, J. Roth, R. Hui, T.D. Xiao, D.E. Reisner, Journal of Thermal Spray Technology, 14(1) (2005), 61.
13. J. Oberste Berghaus, S. Bouaricha, J.G. Legoux, C. Moreau, pp. 1434-1440 in Proceedings of International Thermal Spray Conference (ITSC), Edited by E. F. Lugscheider, German Welding Society. Basel, Switzerland, 2005.

14. J. Oberste Berghaus, S. Bouaricha, J.G. Legoux, C. Moreau, T. Chráska, pp. 512-518 in Proceedings of International Thermal Spray Conference (ITSC), Edited by E. F. Lugscheider, German Welding Society. Basel, Switzerland, 2005.
15. C. Delbos, J. Fazilleau, J.F. Coudert, P. Fauchais, L. Bianchi, K. Wittmann-Teneze, pp. 661-669 in Proceedings of Thermal Spray 2003: Advancing the Science and Applying the Technology, Edited by B.R. Marple and C. Moreau, ASM International. Orlando, FL, USA, 2003.
16. V. Rat, C. Delbos, C. Bonhomme, J. Fazilleau, J.F. Coudert, P. Fauchais, High Temperature Material Processes, 8(1) (2004), 95-117.
17. M. Bonneau, F. Gitzhofer, M. Boulos, pp. 929-934 in Proceedings of the International Thermal Spray Conference (ITSC). Montreal, Canada, 2000.
18. J. Oberste Berghaus, J.G. Legoux, C. Moreau, R. Hui, C. Decès-Petit, W. Qu, S. Yick, Z. Wang, R. Maric and D. Ghosh, pp. 183-189 in Proceeding of the 2008 International Thermal Spray Conference (ITSC), Edited by E. Lugscheider. German Welding Society. Maastricht, the Netherlands, 2008.
19. R. Rampon, O. Marchand, C. Filiatre, G. Bertrand, Surface & Coatings Technology 202(18) (2008), 4337-4342.
20. B.D. White, O. Kesler, L. Rose, Journal of Power Sources, 178(1) (2008), 334-343.
21. D. Waldbillig, O. Kesler, Surface & Coatings Technology, 203(15) (2009), 2098-2101.
22. H. E. Boyer, T. L. Gall (Eds.), Metals Handbook Desk Edition, American Society of Metals, Metals Park, Ohio, 1985, pp. 1.49.

5 Suspension plasma spraying of solid oxide fuel cell electrolytes[22]

5.1 Introduction

A fuel cell is an electrochemical device that converts the chemical energy stored in a fuel directly to electrical energy. There are several fuel cell types, which are usually differentiated by the electrolyte material or type of fuel used. Solid oxide fuel cells (SOFCs) are a high temperature, solid-state fuel cell type that most commonly uses oxide-ion conducting ceramics such as yttria-stabilized zirconia (YSZ) as the electrolyte material. SOFCs have high efficiencies, produce high temperature waste heat suitable for cogeneration of electricity or heating space or water, and have the ability to directly and efficiently use hydrocarbon fuels, which may make this fuel cell type a practical near term power solution.

SOFCs are most commonly manufactured by wet ceramic processing techniques such as tape casting and screen printing, and the layer deposition processes are often followed by one or more sintering steps at temperatures up to 1400^{o}C. These multiple unit fabrication operations make SOFC manufacturing labour-intensive, fairly expensive and difficult to automate, and the high firing temperatures may limit the usable materials set in order to limit material inter-reactions. In particular, high electrolyte sintering temperatures make the use of robust, low cost metallic structural supports challenging.

Plasma spraying (PS) has been proposed as a potential next generation SOFC fabrication process [1]. PS of ceramic coatings has a greater than 50 year history and allows coatings to be produced rapidly without the need for post deposition heat treatments. Plasma spray processing of SOFCs would also facilitate the use of metallic mechanical supports, which are lower in cost and have superior mechanical properties compared to cermet supports. PS processing would also allow higher performing functionally graded microstructures to be produced in a continuous deposition process. However, it is difficult to produce the thin (<

[22] A version of this chapter will be submitted for publication. D. Waldbillig, O. Kesler, (2010) Suspension plasma spraying of solid oxide fuel cell electrolytes.

20 µm), fully dense layers required for SOFC electrolytes using conventional powder plasma spray techniques, as plasma spray feedstock powders are typically between 10 and 100 µm in diameter due to the requirement of flowing the powders in a carrier gas.

Suspension plasma spraying (SPS) is a modification of traditional PS techniques that is being developed to enhance control over plasma sprayed microstructures, especially for thin, low porosity coatings. This technique uses particles with diameters between 100 nm and several µm that have been suspended in a carrier liquid, typically water or alcohol, as feedstock. These smaller particles produce smaller splats, which may allow finer microstructural control and may produce a more gas-tight coating for a given thickness.

The present study builds on previous work that characterized and optimized the dispersion of particles in a suspension [2,3] and that investigated the effect of substrate and plasma sprayed cathode layer properties on the resulting SPS electrolyte layer properties [4,5,6]. This work begins by examining the energetic effects of feeding aqueous suspensions to a plasma spray torch and then maps the effect of various spray parameters on the torch power in order to aid in the selection of spraying parameter ranges to evaporate the water, melt the YSZ, and impart enough momentum to the small particles to produce low porosity coatings. A number of spraying runs were performed that varied parameters such as plasma gas flow rate and composition and nozzle size and the resulting coating density, deposition efficiency, and permeation rate were characterized. Finally, five conditions from the initial spraying runs were chosen to study in greater depth to determine which conditions were most likely to produce the highest performing electrolyte layers.

5.2 Experimental procedure

5.2.1 Substrate and feedstock material

Coating were deposited onto 2.54 cm diameter porous 430 ferritic stainless steel substrates with a media grade (MG) of 2 (Mott Corporation, Farmington, CT, USA). This substrate material is most commonly used as a filter medium, and the media grade designation refers to the smallest diameter of particles in micrometers that can be captured in the filter.

A mixture of spray dried 48.2 wt% lanthanum strontium manganite ($La_{0.8}Sr_{0.2}MnO_{3-\delta}$, LSM) and 51.8 wt% 8 mol% yttria-stabilized zirconia (YSZ) powders (Inframat Advanced Materials, Farmington, CT, USA) was used for the fabrication of the cathode layers. Spray dried cathode powders were sieved and mechanically mixed before plasma spraying. The detailed cathode powder preparation procedure has been reported previously [4,6].

Non-spray dried 8 mol% YSZ powder (Inframat Advanced Materials, Farmington, CT, USA) was used as the electrolyte feedstock for this study. The as-received powder had a d_{50} agglomerate size of approximately 1.6 µm, with sizes ranging from 0.5 µm to 15 µm, as determined previously by laser light scattering (Mastersizer 2000, Malvern Instruments, Worcestershire, UK) [6]. Aqueous YSZ suspensions with a solid loading of 3 vol% (15.4 wt%) were prepared using deionized water and 0.01 wt% PBTCA (2-Phosphonobutane-1,2,4-Tricarboxylic acid) dispersant referenced to the ceramic solid weight.

5.2.2 Plasma spray processing

An Axial III Series 600 atmospheric plasma spray system (Northwest Mettech Corp., North Vancouver, BC, Canada) was used to deposit all SOFC layers. This system injects the feedstock axially between three electrode pairs, which ensures that virtually all of the powder injected passes through the hottest part of the plasma jet. A powder feeding system (Thermico model CPF-2HP, Germany) was used to fabricate the cathode layers. For electrolyte layer deposition, the plasma spraying system was modified to add a pressure vessel to deliver the suspension to the feed tube of the plasma torch as described previously [6]. The suspension was injected through a needle type nozzle (ID = 0.84 mm) positioned directly behind the torch convergence into the centre of the plasma jet, where it was atomized by the plasma plume. During SPS, the 3 vol% YSZ suspension was fed to the torch at a rate of 104 mL/min, resulting in a total solid flow rate of 18.5 g/min[23].

[23] A more detailed description of the suspension delivery and injection equipment can be found in Appendix D.

The substrates were mounted on a rotating turntable and preheated directly by the plasma torch to a temperature between 300 and 350^{o}C before the powder or suspension feeding systems were activated. Substrate temperatures during spraying were measured directly by a Type K thermocouple in contact with the back of the metal substrate.

A plasma sprayed composite LSM / YSZ cathode layer was first deposited on the steel substrates at conditions described previously [4,6] and an SPS YSZ electrolyte layer was then deposited on top of the cathode layer. This procedure provides substrate conditions that are similar to those in actual fuel cells during electrolyte deposition.

5.2.3 Characterization of plasma sprayed layers

After YSZ layers were deposited, the coating density, deposition efficiency, permeation rate and microstructure were characterized.

Layer density was calculated by dividing the weight gained by the substrate during electrolyte spraying runs by the spraying area and the coating thickness as measured by scanning electron microscopy (SEM). Between 15 and 40 electrolyte thickness measurements evenly spaced over three to five regions of the sample cross sectional length (25.4 mm) were averaged in order to calculate the coating thickness.

Deposition efficiency was calculated as the ratio of the weight gained by the substrate during the electrolyte spraying run per unit area multiplied by the full spray area to the weight of YSZ delivered during the spraying run, as determined from suspension flow rate measurements performed during initial calibration tests without plasma gas flow. It should be noted that all such calculations underestimate the deposition efficiency of powder reaching the substrate area, because acceleration and deceleration times of the torch robot are not taken into account when using the full spray area to calculate the process deposition efficiency. On the other hand, overspray (spraying of powders outside of the substrate area) is also not accounted for in the deposition efficiency calculations. Scaling up to larger substrates and using robots with higher acceleration rates both reduce the extent of overspray, and powder not delivered to the substrates could also potentially be recycled

in a scaled-up manufacturing process, whereas the deposition efficiency of powder reaching the substrate is a function of the spray conditions and substrate properties, and would likely remain more constant with process scale-up. Therefore, deposition efficiency rather than overspray was emphasized in this study as being the process efficiency parameter most relevant to a scaled-up manufacturing process and the one that is most dependent on the spray conditions used in the process. The underestimation of deposition efficiency values, while not quantified in this study, is assumed to be constant for all of the spraying conditions examined, since it is caused by the acceleration and deceleration times of the torch robot, which was the same for all coatings studied. Therefore, comparisons of the deposition efficiencies from one spray condition to another could still be made even without the values being known with full accuracy, since the primary source of inaccuracy was the same for each coating studied.

Helium permeation measurements were performed using an in-house designed fixture in order to measure the gas permeability of the deposited layers. The supply of helium gas was regulated at a pressure of 3.5 kPa gage by a pressure controller (Alicat Scientific, model PCD-5PSIG-D, Tucson, AZ, USA). The flow through the sample was then measured at the outlet of the fixture by a mass flow meter (Alicat Scientific, model M-0.5SCCM-D_H2, Tucson, AZ, USA)[24]. The outlet was open to atmosphere. The flow rate through the sample was then used to calculate the layer permeability using Darcy's law [6,7].

Polished cross sections of the deposited layers were examined in a Hitachi S-3000N SEM (Hitachi High Technologies America, Pleasanton, CA, USA). Samples were mounted in epoxy, cut using a low speed diamond saw, and then polished using diamond polishing suspensions. The polished samples were gold coated to provide sufficient sample conductivity for SEM imaging. The back-scattered electron (BSE) imaging mode was used for all SEM images in order to enhance the contrast between the individual SOFC component materials.

---

[24] A detailed explanation of the permeation measurements can be found in Appendix C.

5.3 Results and discussion

5.3.1 Energy requirements of SPS compared to dry powder APS

A simple comparison of the power required for aqueous suspension plasma spraying (SPS) and plasma spraying with dry powder feedstock (PPS) is shown in Figure 5.1. The power ratio (P_R) in Figure 5.1c is the ratio of the power required to heat and evaporate the water, heat the steam, and melt the YSZ powder in the suspension (P_{SPS}) to the power required to heat the argon carrier gas and heat and melt the YSZ powder in a powder plasma spray process (P_{PPS}) at the same total solid flow rate, as shown in Equation 5.1. Argon atomization gas is not required in the SPS configuration considered here, due to the axial injection of feedstock suspensions. Equations 5.2 to 5.7 show the calculations used to determine each of the quantities in Equation 5.1. Although this calculation is very simplified, it allows a comparison to be made of the power requirement trends in this system for different feedstock properties.

These calculations do not account for the dissocation of the water present in the suspension, which may become significant at temperatures greater than 1200 K [8]. Bucker et al. have developed a model to calculate the contributions of dissociation to the overall enthalpy during combustion; however, this model is only valid to a maximum temperature of 2000 K, and it assumes complete combustion conditions and air-to-fuel ratios greater than 1.05, which means that this model cannot by applied for the plasma spray conditions used in this study [8]. Very little has been reported in the plasma spray literature on the thermodynamic or kinetic effects of water dissociation within plasmas; for example, see Bruggeman [9].

$$P_R = \frac{P_{SPS}}{P_{PPS}} \tag{5.1}$$

$$P_{PPS} = P_{Ar} + 0.92\, P_{ZrO_2} + 0.08\, P_{Y_2O_3} \tag{5.2}$$

$$P_{Ar} = \dot{n}_{Ar} C_{p\,(\,Ar_{(g)}\,)}\,(2983 - 298) \tag{5.3}$$

$$P_{ZrO_2} = \dot{n}_{ZrO_2}\left[\int_{298}^{1500} C_{p\,(ZrO_{2(s)})}\,dT + C_{p\,(ZrO_{2(s)},1500K)}\,(2983-1500) + \Delta H_{m\,(ZrO_2)}\right] \quad (5.4)$$

$$P_{Y_2O_3} = \dot{n}_{Y_2O_3}\left[C_{p\,(Y_2O_{3(s)})}\,(2983-298) + \Delta H_{m\,(Y_2O_3)}\right] \quad (5.5)$$

$$P_{SPS} = P_{H_2O} + 0.92\,P_{ZrO_2} + 0.08\,P_{Y_2O_3} \quad (5.6)$$

$$P_{H_2O} = \dot{n}_{H_2O}\left[\int_{298}^{373} C_{p\,(H_2O_{(l)})}\,dT + \Delta H_{v\,(H_2O)} + \int_{373}^{1500} C_{p\,(H_2O_{(g)})}\,dT + C_{p\,(H_2O_{(g)},1500K)}\,(2983-1500)\right] \quad (5.7)$$

Where: P_{Ar} = the total power required to heat Ar from 298 K to the YSZ melting point (2983 K) (kW)

P_{ZrO2} = the total power required to heat ZrO_2 from 298 K to 2983 K and melt the ZrO_2 (kW)

P_{Y2O3} = the total power required to heat Y_2O_3 from 298 K to 2983 K and melt the Y_2O_3 (kW)

P_{H2O} = the total power required to heat H_2O liquid from 298 K to 373 K, vaporize the water, and heat the H_2O vapour from 373 K to 2983 K (kW)

$\dot{n}_x$ = the molar flow rate of species x, with x representing Ar, ZrO_2, Y_2O_3 and H_2O (mol/s)

$C_{p\,(x)}$ = the heat capacity at constant pressure of species x, with x representing Ar, ZrO_2, Y_2O_3, and H_2O (kJ/ (mol K))* [10]

$\Delta H_{v\,(H2O)}$ = the enthalpy of vaporization of H_2O (kJ/mol) [10]

$\Delta H_{m\,(y)}$ = the enthalpy of melting of species y, with y representing ZrO_2 and Y_2O_3 (kJ/mol) [10]

* Note: C_p values that incorporated the effect of temperature were used for the $H_2O_{(l)}$, $H_2O_{(g)}$ and $ZrO_{2(s)}$ components for the relevant ranges specified in the literature (usually 298 K to 1500 K). At temperatures greater than the maximum temperature recommended for the C_p equation, a constant C_p value at the maximum temperature (1500 K) was used. Ar C_p values are constant at all temperatures of interest to this study. No C_p equations that incorporated temperature were found in the literature for Y_2O_3 so a constant C_p value was used.

In Figure 5.1a, the effect of argon carrier gas flow rate on the power requirement for PPS is illustrated. As can be seen in the figure, the power required for PPS increases linearly with

argon flow rate and the percent of the total power requirement solely needed to heat the argon carrier (right axis) can vary from 20 to 67% over the range of argon flow rates available. Figure 5.1b shows the effect of solid flow rate on the power requirement for PPS and for SPS with various suspension solid contents. The Ar flow rate for PPS was held constant at 15 slpm for the calculation. At solid contents of 20 vol% or higher, power requirements are similar for PPS and SPS, but as the solid content in suspension decreases, the power required for SPS increases significantly for a given solid feed rate, due to the increased amount of water present. As the solid flow rate increases, the power required increases linearly, but the rate at which this power increase occurs is much higher for low solid content suspensions compared to high solid content suspensions or PPS. Figure 5.1c shows P_R as a function of Ar carrier gas flow rate during PPS. As seen in Figure 5.1a, increases in the Ar carrier gas flow rate can significantly increase the power required for PPS, thus decreasing P_R. This effect is especially significant when low solid content suspensions are used. The effect of solid flow rate on P_R for SPS processes with 1, 3, 5 or 20 vol% solid content feedstock suspensions is shown in Figure 5.1d. In the figure, it can be seen that P_R increases as the solid flow rate increases and as suspension solid content decreases. P_R is extremely high for dilute suspensions, and decreases with increasing suspension solid contents, approaching 1 at high solid contents. Coatings have been produced at solid contents as high as 20 vol%, but it is likely that in order to produce low porosity coatings, solid contents between 1 and 5 vol% should be used [2]. These calculations indicate that suspension plasma sprayed coatings would require between approximately 5 to 50 times more power to fabricate compared to dry powder feedstock coatings if similar solid flow rates to PPS were maintained. However, the flow rate of Ar required to carry the YSZ powder for PPS can have a very large effect on P_R, especially at low suspension solid contents. For example, at a solid content of 1 vol%, P_R can vary between ~20 and 50 depending on the Ar flow rate.

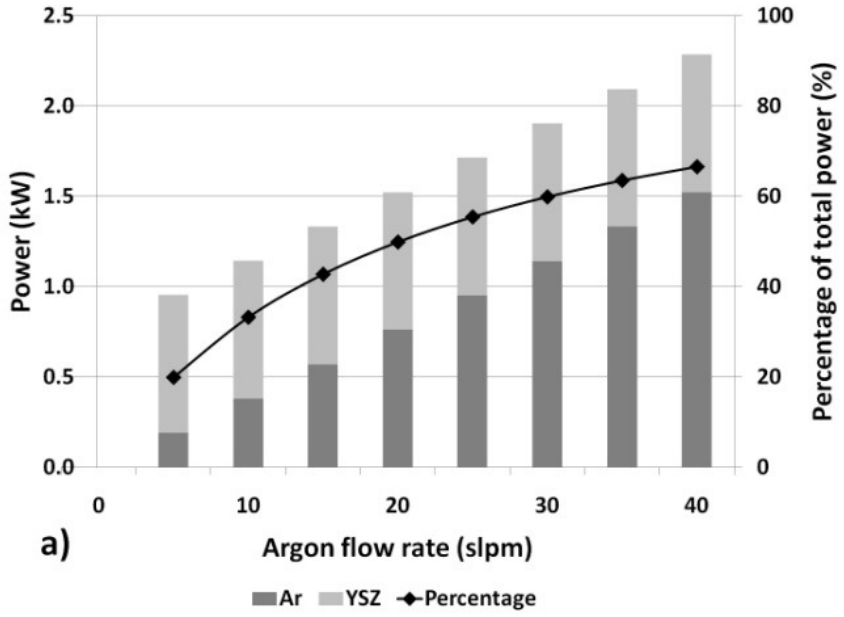
2.5
2.0
1.5
1.0
0.5
0.0
Power (kW)
100
80
60
40
20
0
Percentage of total power (%)
0
10
20
30
40
a)
Argon flow rate (slpm)
Ar
YSZ
Percentage

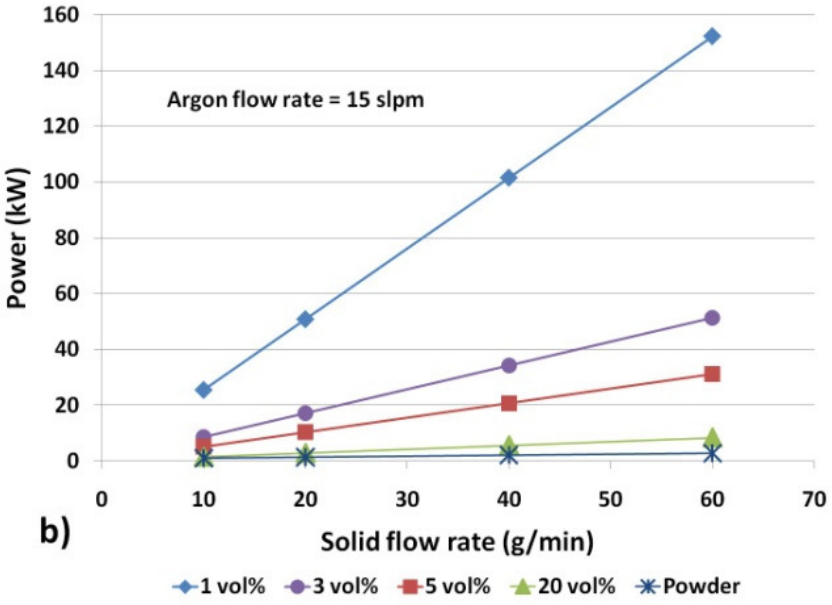
160
140
120
100
80
60
40
20
0
Power (kW)
Argon flow rate = 15 slpm
0
10
20
30
40
50
60
70
b)
Solid flow rate (g/min)
1 vol%
3 vol%
5 vol%
20 vol%
Powder

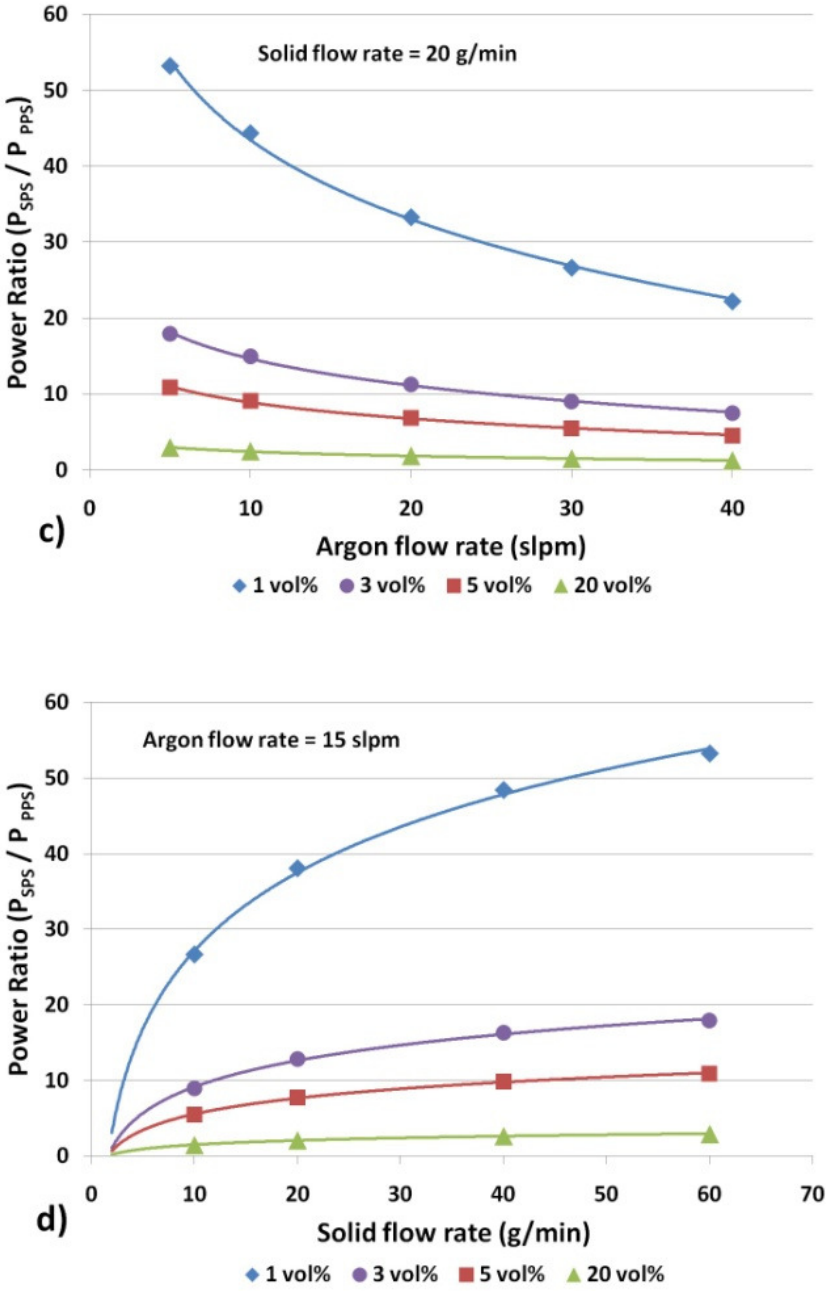

Figure 5.1: Effect of a) argon carrier gas flow rate on the power requirement for PPS and b) solid flow rate on the power requirements for SPS and PPS. Power ratio for aqueous YSZ suspensions at 1, 3, 5 and 20 volume % solid content as a function of c) argon carrier gas flow rate and d) solid flow rate.

It should be noted that the energy required to heat and evaporate the water, heat the steam, and heat and melt the solid powder must be transferred from the plasma to the

water droplets and solid particles. Therefore, the retained power within the plasma must be significantly higher than the power required to treat the feedstock (Figure 5.1), due to the inefficient nature of heat transfer from the plasma gases to the feedstock. Thus, the torch power required to produce fully melted particles and dense coatings will, in general, be significantly higher than the minimum power level required to fully treat the feedstock. The efficiency of heat transfer from the plasma to the feedstock may be influenced by factors that affect residence time, such as plasma gas flow rate or nozzle size, or by the plasma gas composition. The presence of hydrogen in the plasma can significantly increase plasma enthalpy and thermal conductivity, as reported by Zhang et al., who observed a linear increase in particle temperature as the H_2 flow rate increased [11]. In addition, the droplet and particle sizes may play a significant role in the rate of heat transfer to the feedstock during the limited residence time of the feedstock in the plasma, even when the retained plasma power is nominally sufficient to fully melt the powder and evaporate the liquid, based on feed rate alone. Therefore, atomization effects such as droplet size may ultimately play a significant role in the manufacturing of fully dense coatings.

In order to reduce the power requirements, the feed rate for SPS processes may be reduced compared to PPS processes, with a corresponding increase in the spraying time. The power requirements for SPS could also be reduced by replacing some of the water with a combustible liquid that might add energy to the system, but this approach may result in additional engineering challenges, such as clogging of the feed tube [12] and lower particle in-flight velocities [13]. From a manufacturing cost perspective, it is worth noting that the increased power consumption required to spray coatings from a suspension compared to coatings fabricated from dry powder is very small compared to the overall manufacturing cost, which is much more strongly influenced by material, equipment, and labour costs [14]. From an environmental perspective, the energy used to manufacture SOFCs has also been found to be very small compared to the energy saved during the operating lifetime of the devices, due to their high operating efficiency [15]. Therefore, the primary goal of determining power requirements for the production of coatings is to ensure that the energy

transferred to the feedstock is sufficient to fully melt the particles during their residence time in the plasma.

5.3.2 Torch power parameter study

In order to determine the effect of torch parameters on the torch power, spraying runs were performed with plasma gas flow rates varying from 200 slpm to 300 slpm with various N_2, Ar, and H_2 concentrations. During these tests, the current was set at the maximum value of 250 A per electrode pair. Due to equipment limitations, the total N_2 flow rate was limited to 200 slpm. A summary of these spraying parameters showing the effect of plasma gas flow rate and composition on the torch power is shown in Figure 5.2a. It can be seen that high plasma gas flow rates (>250 slpm), high N_2 contents (>70%) and moderate H_2 contents (5 -10%) produced the highest power conditions.

Not all of the power produced by the torch is retained in the plasma due to the flow of cooling water that prevents the torch from overheating. The difference between the torch power and the enthalpy removed from the torch in the cooling water stream is the retained plasma power. As the torch power increases, the retained power in the plasma also increases, but at a slower rate (Figure 5.2b). Therefore, increasing the torch power alone may not be sufficient to achieve a fully dense coating if the retained plasma power is insufficient to fully process the feedstock. Other factors, such as particle size, droplet size, residence time, and heat transfer efficiency from the plasma to the feedstock will all influence the kinetics of water evaporation and solid particle melting, beyond the effect of the retained plasma power.

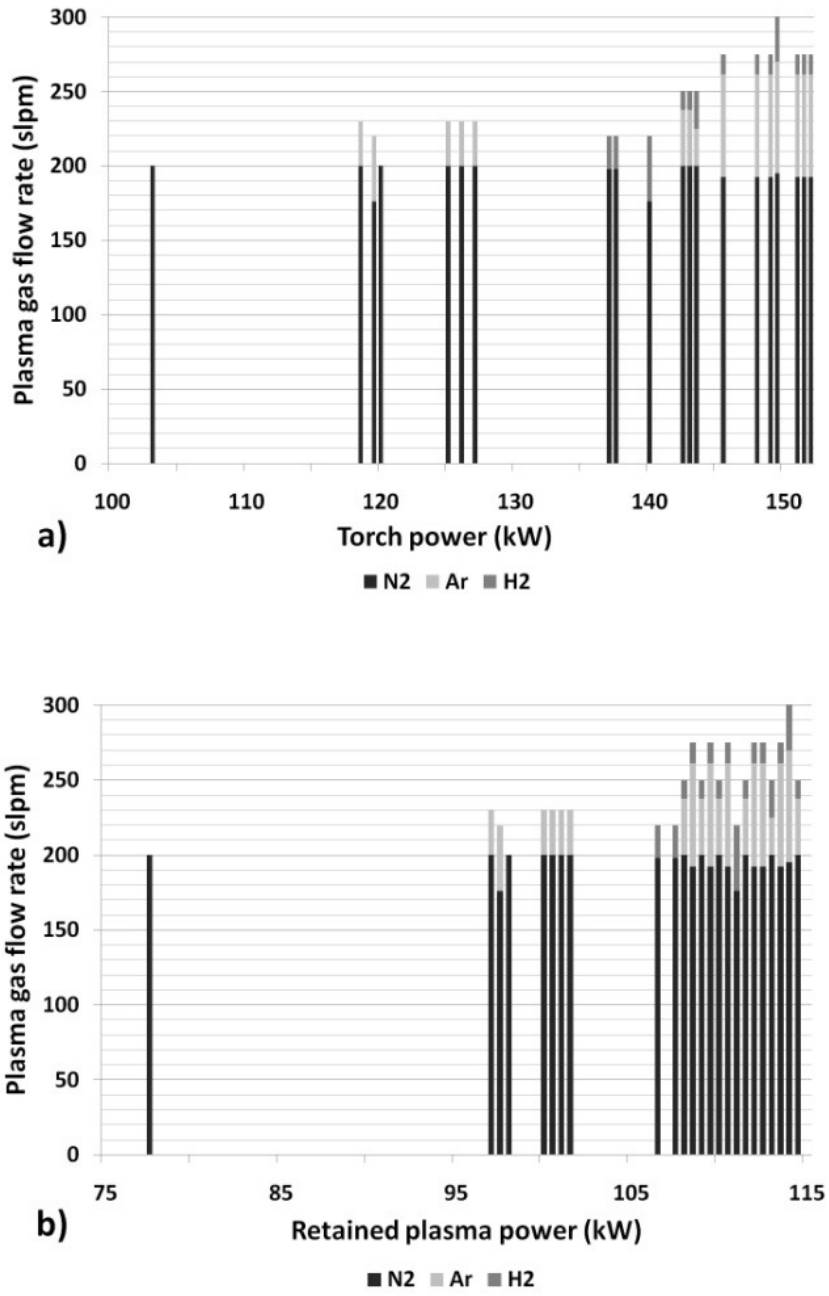

Figure 5.2: Effect of plasma gas flow rate and composition on a) the torch power and b) the retained plasma power.

5.3.3 SPS parameter study

After determining the relationship between plasma spray parameters for SPS and the resulting torch power and retained plasma power, a number of spraying runs that varied

torch power or particle velocity were performed. Over the course of these studies, the effect of plasma gas flow rate and composition and nozzle size on the coating density, deposition efficiency, permeation rate and microstructure was investigated. A summary of the conditions studied is shown in Table 5.1. In total, 20 spraying runs were performed and 85 individual fuel cell specimens were analyzed.

Table 5.1: Plasma spray parameter ranges.

Parameter	Value
Plasma gas flow rate (slpm)	200 – 300
Plasma gas composition (%)	65 – 100 N_2, 0 – 25 Ar, 0 – 20 H_2
Current (A per cathode)	250
Nozzle size (mm)	9.53, 11.11, 12.70, 14.30
Substrate preheat temperature (°C)	300 - 350
Standoff distance (mm)	80 - 90

The effects of plasma gas flow rate and torch power on coating density and deposition efficiency are shown in Figures 5.3 and 5.4, respectively, for the different nozzles utilized. Each point on the graph corresponds to one spraying run and consists of an averaged value of at least three individual coatings. Increasing the plasma gas flow rate should increase both the torch power, as shown in Figure 5.2, and the plasma velocity.

Figure 5.3a shows the effect of plasma gas flow rate on the resulting coating density, while Figure 5.3b illustrates the effect of torch power on the resulting coating density for the four nozzles investigated. Coating density generally increased as the plasma gas flow rate increased. However, at high flow rates, density values appeared to level off, likely due to

the decrease in the particle residence time. At all plasma gas flow rates examined, smaller nozzles produced higher density coatings compared to those produced from larger nozzles at the same plasma gas flow rate. As the torch power increased, coating density increased, and coatings produced from smaller nozzles were generally more dense than those produced from larger nozzles at similar power values. Small additions of H_2 to the plasma significantly increased the torch power (see Figure 5.2) and have been shown to improve plasma thermal conductivity [11], which resulted in higher coating densities.

For all of the density measurements, the average density value never exceeded the YSZ theoretical density value of 5.96; however, in some cases, the upper error bar range did include values that were greater than the maximum theoretical density. The large scatter in density values is due to variations in electrolyte coating thickness measurements, which typically had standard deviation values between 5 and 11% of the average value. These variations were likely caused in part by the rough LSM/YSZ composite cathode layers on which the electrolyte was deposited. Electrolyte layers deposited on previously-polished cathodes, in contrast, resulted in 40-55% lower thickness variability, with 3-6% standard deviations from the average thickness values observed. However, these coatings were not further characterized, as the more complex manufacturing process would make such coatings impractical for mass production.

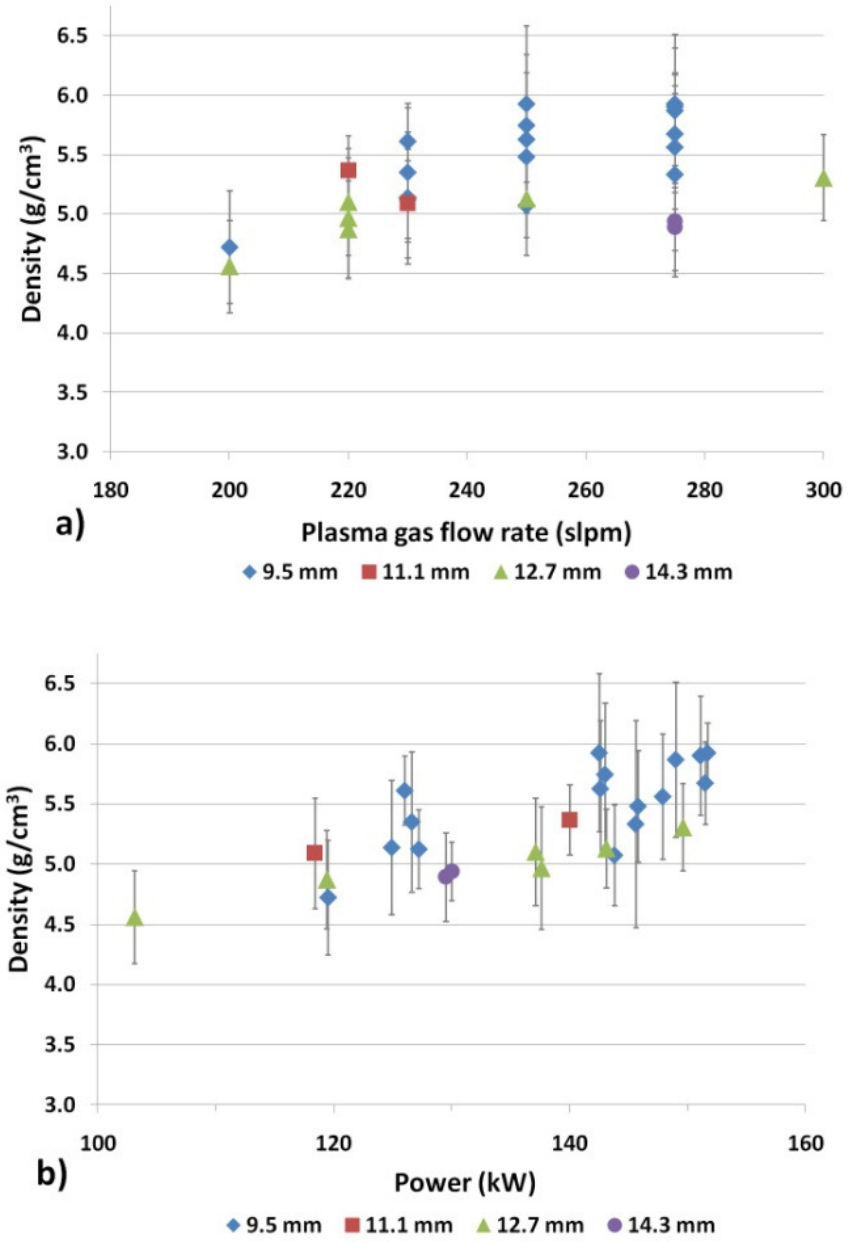

Figure 5.3: Effect of a) plasma gas flow rate and b) torch power on coating density for various nozzle sizes.

Figure 5.4a shows the effect of plasma gas flow rate on the resulting coating deposition efficiency, while Figure 5.4b illustrates the effect of torch power on the resulting coating deposition efficiency for the four nozzles examined. As the plasma gas flow rate increased from 200 slpm to 250 slpm, the deposition efficiency for the 12.7 mm nozzle increased

rapidly. At plasma gas flow rates greater than 250 slpm, deposition efficiency values levelled off at a value of 60%. The smaller 9.5 mm nozzle had its highest deposition efficiency (38%) at flow rates between 200 and 230 slpm, and its deposition efficiency decreased at higher plasma gas flows. This decrease likely indicates that use of the small nozzle results in insufficient residence time with the high plasma gas flow rates to fully melt all the YSZ powder for the solid feed rate used in these studies. At the lowest plasma gas flow rate investigated (200 slpm), the 9.5 mm nozzle had a higher deposition efficiency than the 12.7 mm nozzle. This result may have been caused by re-solidification of the particles during flight for the low velocity spraying condition with a large nozzle and a low plasma gas flow rate. Because the calibration of suspension flow rates had to be performed in the absence of plasma gases, it is possible that the true suspension feed rate in the presence of plasma may have been different from the calibrated values, which would result in true deposition efficiency values that are different from those calculated using the calibrated flow rates. Similarly, neglecting the torch acceleration and deceleration times results in an under-estimation of the deposition efficiency, as discussed in Section 3.3. However, comparisons between the deposition efficiencies obtained with different spray conditions can still provide insight into the effects of different nozzle sizes and plasma gas flow rates on the resulting relative process efficiencies.

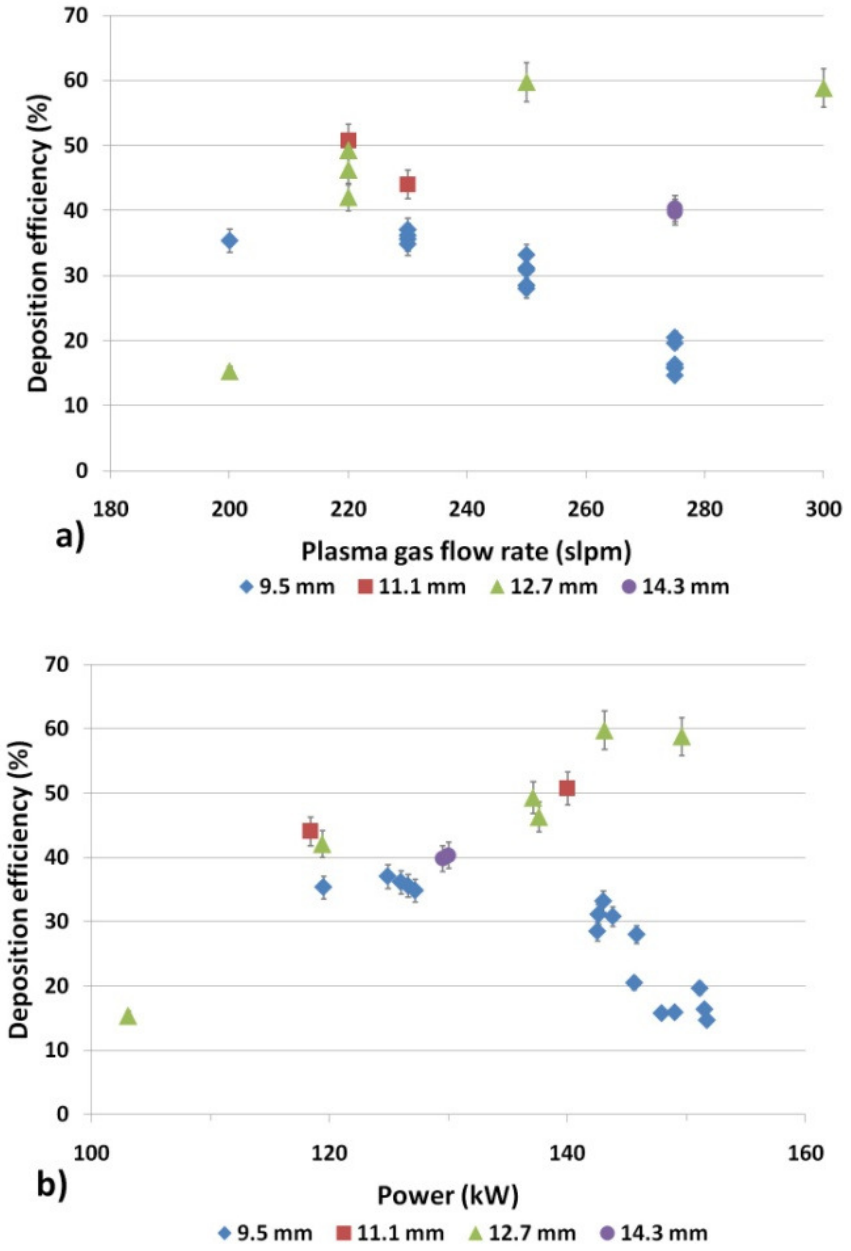

Figure 5.4: Effect of a) plasma gas flow rate and b) torch power on deposition efficiency for various nozzle sizes.

A plot of the density versus deposition efficiency (Figure 5.5) confirms that smaller nozzles produce higher density coatings but generally result in lower deposition efficiencies. This may indicate that a compromise between the small nozzle with high plasma gas flow conditions that produce the densest coatings and the large nozzles that produce the highest

deposition efficiencies may have to be found. A few coatings were produced using the medium-sized 11.1 mm nozzle. These coatings generally exhibited higher densities than the coatings produced with the 12.7 mm nozzle and improved deposition efficiencies compared to the coatings produced with the 9.5 mm nozzle. Therefore, additional studies using that nozzle size may be helpful in order to further investigate the density – deposition efficiency trade-offs.

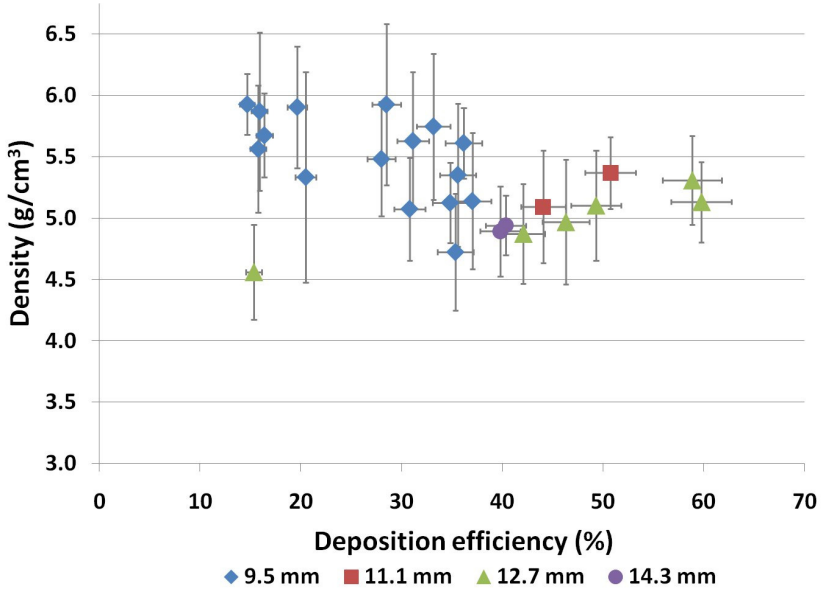

Figure 5.5: Density vs. deposition efficiency for SPS YSZ coatings.

In order to investigate the ability of the YSZ layers to serve as dense electrolytes, the rate at which helium permeates through the layers was measured (Figure 5.6) and this value was used together with the thickness to calculate the layer permeability. The permeation rate and permeability values varied significantly over the spraying conditions measured, but generally the permeation rate values decrease as the coating thickness increases and the permeability rates increase as the coating thickness increases. The decrease in permeation rate with thickness is expected, but the increase in permeability with thickness is unexpected and might be attributed to an increase in the total elastic strain energy present in the coating as the coating thickness increases. Increases in the coating strain energy may

lead to more vertical cracking to relieve the strain energy and thus result in higher permeabilities for thicker coatings. In Figure 5.6b, it can be seen that the permeability values varied between ~5.5 x 10^{-18} and 1.8 x 10^{-17} for the conditions studied. These values are slightly lower than the range of permeability values measured by Zhang et al. for APS SOFC YSZ electrolyte coatings [11] (4.80 x 10^{-17} to 1.28 x 10^{-16} m^2) or by He et al. for electron beam physical vapour deposited SOFC YSZ electrolyte coatings (1.95 x 10^{-17} m^2) [16].

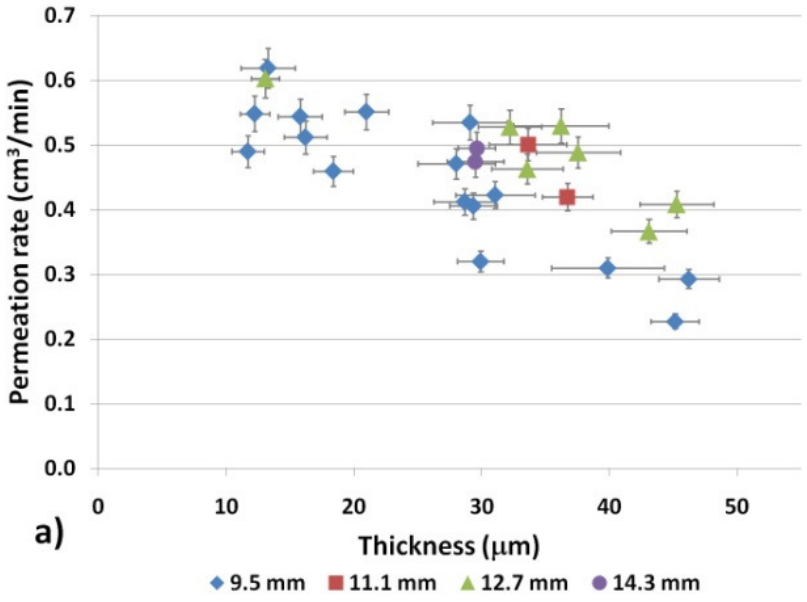

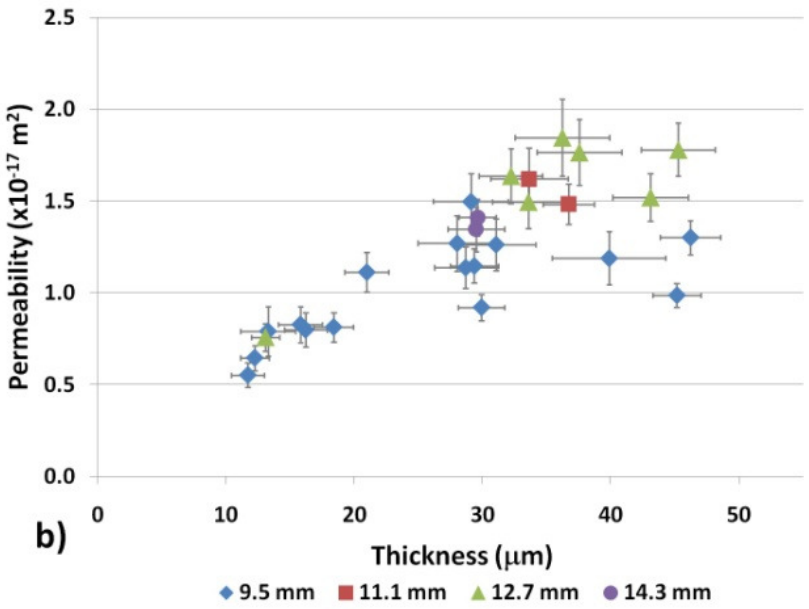

Figure 5.6: a) Permeation rate for a 3.5 kPa pressure drop and b) permeability variation with coating thickness.

In order to minimize the effect of thickness on permeation measurements, only coatings with thicknesses of 32 μm ± 5 μm were included in the subsequent permeation study. The effects of two factors that influence velocity, nozzle size and plasma gas flow rate, on the permeation rate are shown in Figures 5.7a and 5.7b, respectively. As expected, permeation rates decreased as the coating density increased. Thus, coatings produced with high velocity conditions such as small nozzles or high plasma gas flow rates tended to have higher densities and lower permeation rates compared to coatings produced from low velocity conditions.

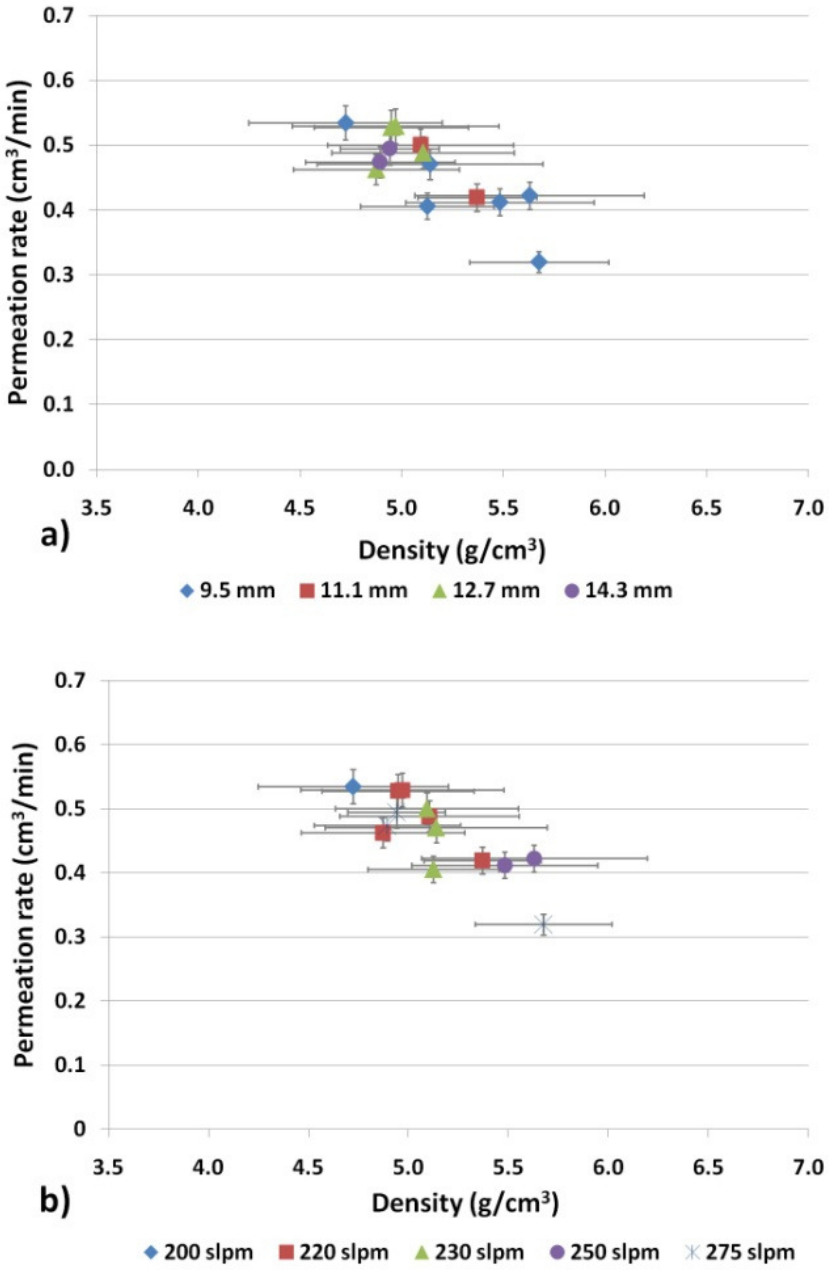

Figure 5.7: Effect of a) nozzle size and b) plasma gas flow rate on the density and permeation rate of SPS YSZ coatings.

5.3.4 Evaluation of SPS YSZ coatings as potential SOFC electrolytes

In order to compare the effects of specific combinations of nozzle size and plasma gas flow rate on coating properties, five spray conditions (Table 5.2) were chosen for more detailed

studies, and an evaluation of the feasibility of using these coatings as SOFC electrolyte layers was made. For all spraying conditions, the current was held at a fixed value of 250 A per electrode pair and the preheat temperature varied between 300 and 350^{o}C. The study examined one condition with a small nozzle and high plasma gas flow rate, one with a large nozzle and a high plasma gas flow rate, one with a small nozzle and low plasma gas flow rate, and one with a large nozzle and low plasma gas flow rate. In addition, one intermediate condition with a small nozzle and intermediate plasma gas flow rate was also examined. The density and deposition efficiency of the sprayed coatings are summarized in Figure 5.8. Each value in the figure corresponds to one spraying run and consists of an averaged value of at least three individual coatings.

Table 5.2: Summary of spraying conditions.

Spraying condition	Plasma gas flow rate (slpm)	Plasma gas composition (%)	Nozzle size (mm)	Standoff distance (mm)	Torch Power (kW)	Retained Plasma Power (kW)
1	275	70 N_2, 25 Ar, 5 H_2	9.53	90	149.8	112.0
2	300	65 N_2, 25 Ar, 10 H_2	12.70	80	149.6	114.3
3	230	87 N_2, 13 Ar	9.53	80	126.4	101.1
4	220	80 N_2, 20 Ar	12.70	80	119.4	97.2
5	250	80 N_2, 15 Ar, 5 H_2	9.53	80	143.6	111.7

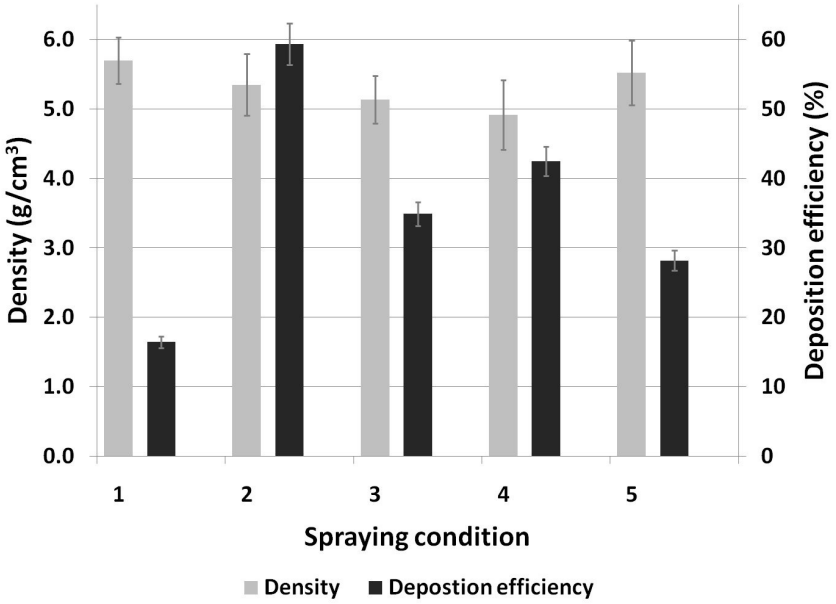

Figure 5.8: Summary of density and deposition values for the five SPS conditions investigated.

The highest density coatings were produced from condition 1; however, this condition also had very low deposition efficiency, possibly due to the high particle velocity caused by the small nozzle and high plasma gas flow rate of this condition and the correspondingly short residence time available for melting of the particles. Condition 2 had a high plasma gas flow rate with a large nozzle and produced coatings with intermediate densities and the highest deposition efficiencies.

All of the electrolyte layers produced from the five spraying conditions exhibited the same three main defect types: vertical cracking, medium sized defects, and small pores, as seen previously [6]. Vertical cracking was likely caused by thermally induced residual stresses produced during spraying, the medium sized defects may be caused by unmelted particles present within the deposited layer or by cathode layer surface topography (for example, see Figure 5.11b), and the small pores present are likely intersplat porosity visible in all coatings.

SEM images of typical cross-sectional microstructures for the two high plasma gas flow conditions are shown in Figure 5.9. Qualitatively, condition 1 microstructures appear to

have low porosities, which agrees with the calculated densities. Condition 2 microstructures appear to have slightly higher vertical crack densities than the other coatings, likely caused by residual stresses induced by the high velocity and high deposition rate, but it is difficult to quantify this factor solely by cross-sectional SEM.

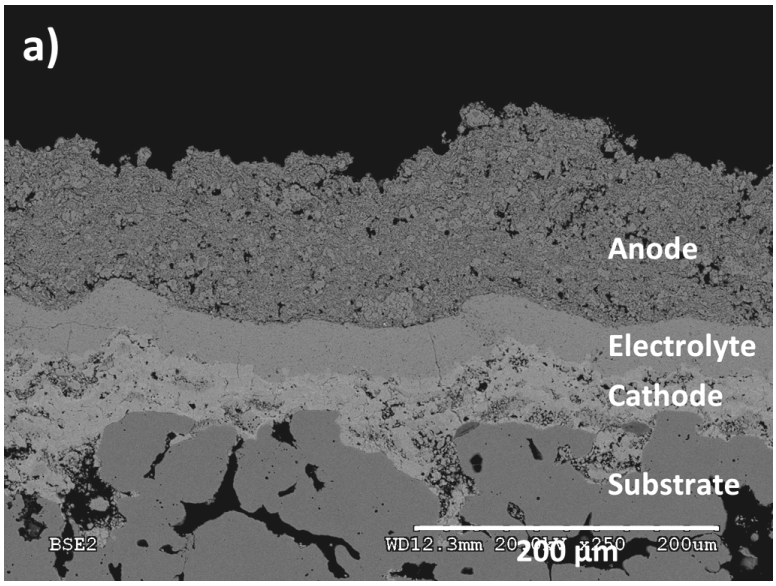
a)
Anode
Electrolyte
Cathode
Substrate
BSE2
200 µm

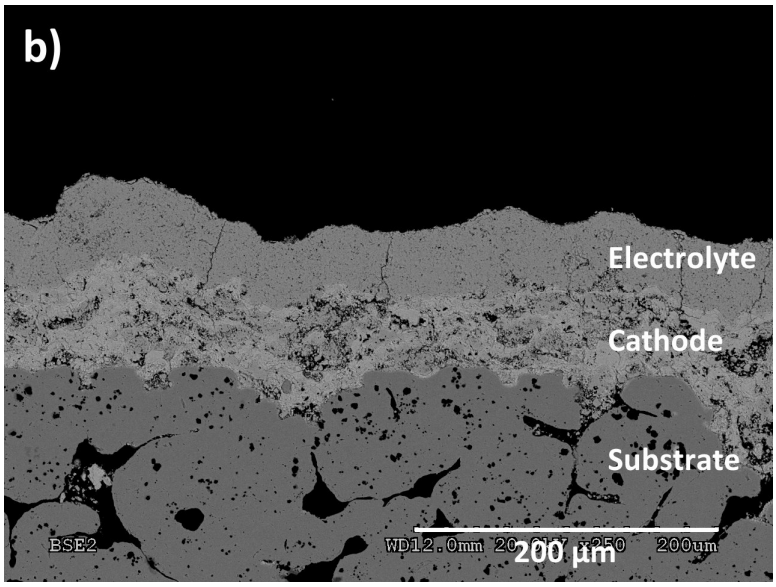
b)
Electrolyte
Cathode
Substrate
BSE2
200 µm

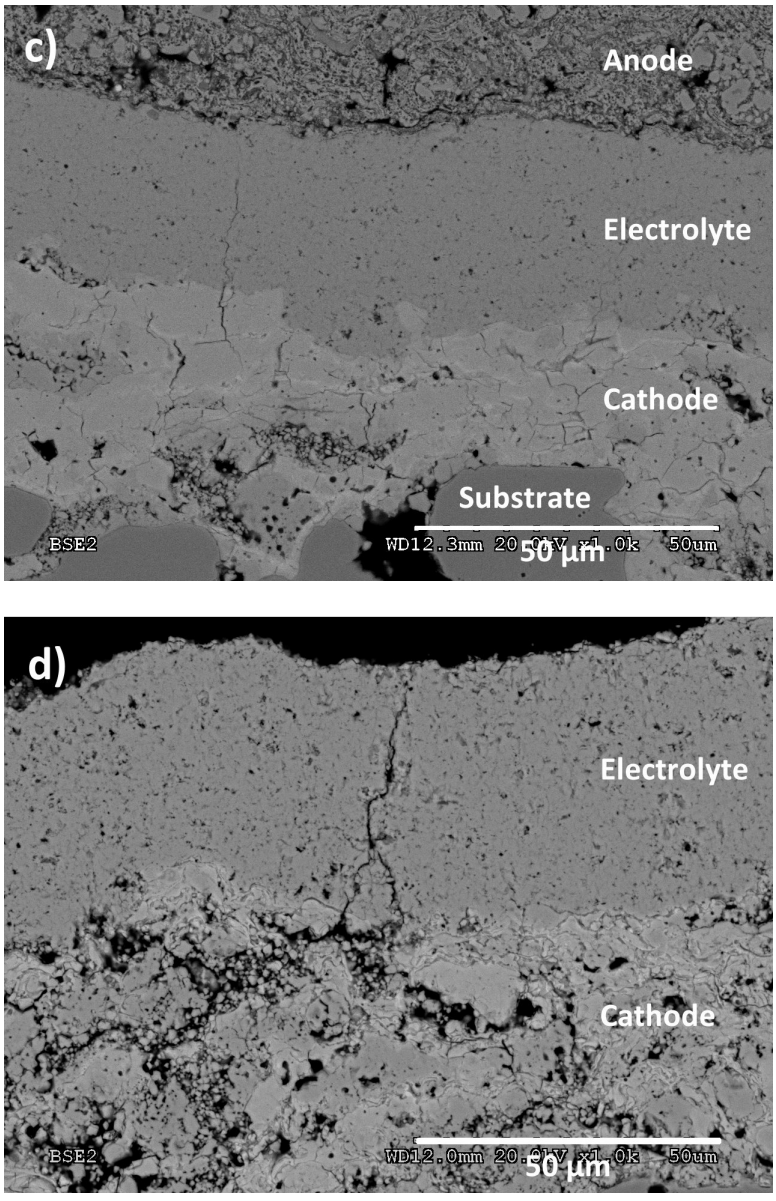

Figure 5.9: Low magnification BSE SEM images of typical microstructures sprayed at: a) Condition 1, b) Condition 2. Higher magnification BSE SEM images of typical microstructures sprayed at: c) Condition 1, d) Condition 2.

Coatings with intermediate densities and deposition efficiencies were produced from the low plasma gas flow rate and small nozzle of condition 3, which may indicate that the residence time was sufficient to allow a greater percentage of the YSZ to melt compared to the coatings produced using condition 1. Condition 4 had a low plasma gas flow rate and a

large nozzle. This low velocity condition produced coatings with low densities and intermediate deposition efficiencies.

Typical cross-sectional microstructures for the low plasma gas flow rate conditions are shown in Figure 5.10. Qualitatively, both microstructures look more porous than the microstructures produced with high plasma gas flow conditions shown in Figure 5.9, but both conditions appear to have lower vertical crack densities compared to the coatings produced by condition 2.

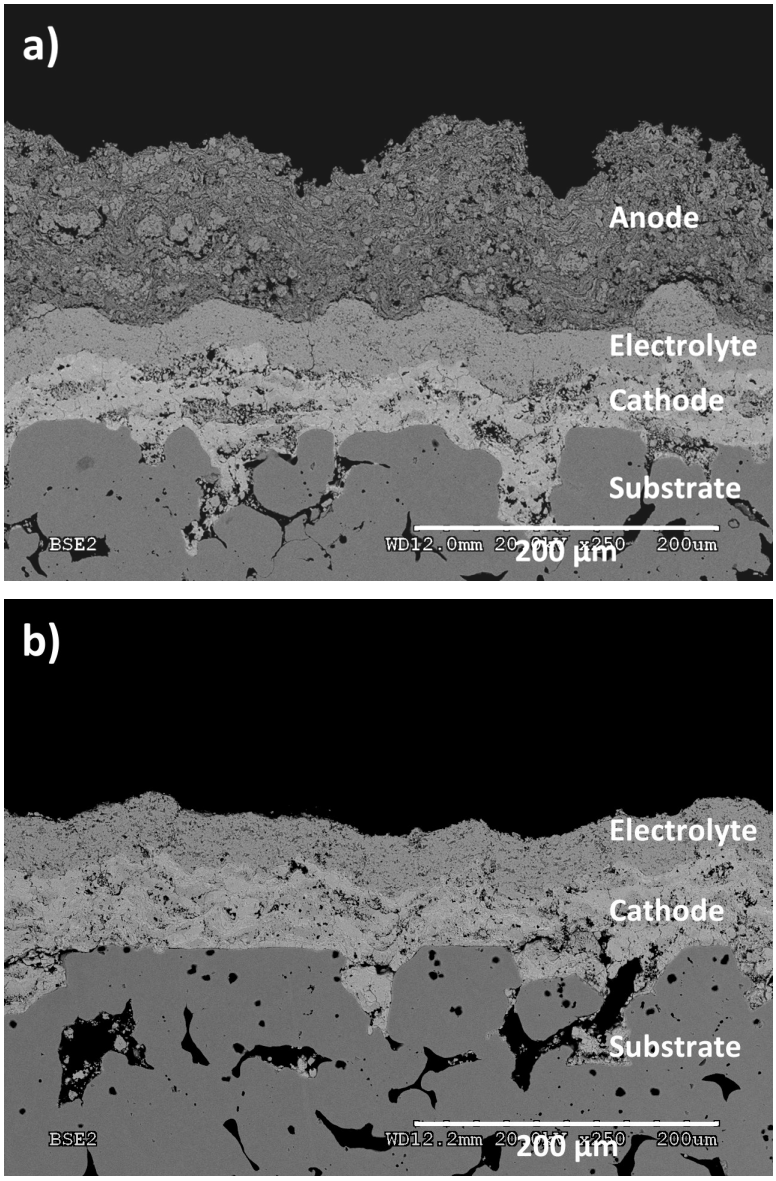

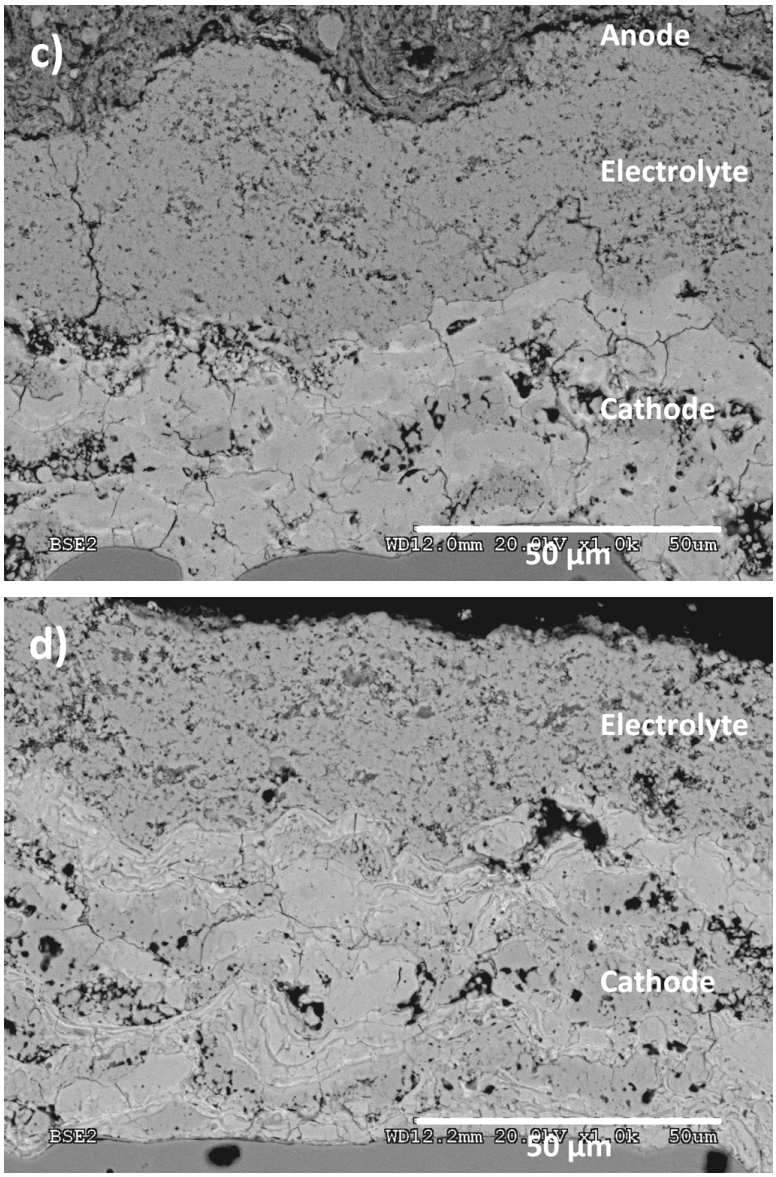

Figure 5.10: Low magnification BSE SEM images of typical microstructures sprayed at: a) Condition 3, b) Condition 4. Higher magnification BSE SEM images of typical microstructures sprayed at: c) Condition 3, d) Condition 4.

In order to increase the deposition efficiency while maintaining high coating density, a fifth condition with a small nozzle and intermediate plasma gas flow rate was tested. Coatings produced with this condition had higher densities than all coatings except those produced with condition 1, with deposition efficiency values over 70% higher than those of the first

condition. SEM images (Figure 5.11) of this compromise condition coating show that the microstructure has low porosity with few vertical cracks.

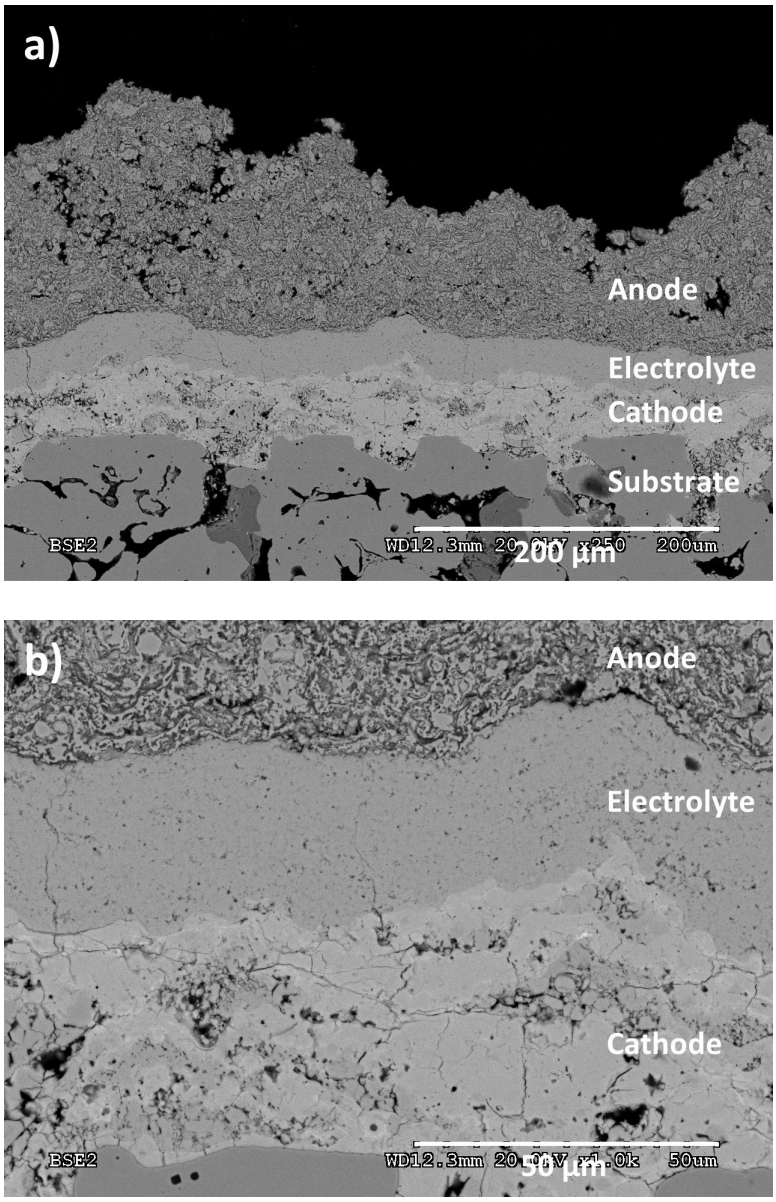

Figure 5.11: a) Low magnification and b) higher magnification BSE SEM images of typical microstructures sprayed at Condition 5.

In order to determine whether the porosity present in the samples is inter-connected, the rate at which helium permeates through the coatings was measured. Low permeation rate

values are essential for SOFC electrolyte layers in order to isolate the fuel and air streams within the cell. Permeation rate results are shown as a function of the coating thickness in Figure 5.12. As was seen previously, the permeation value decreased as thickness increased; thus, it is best to compare the permeation rates of coatings with similar thicknesses.

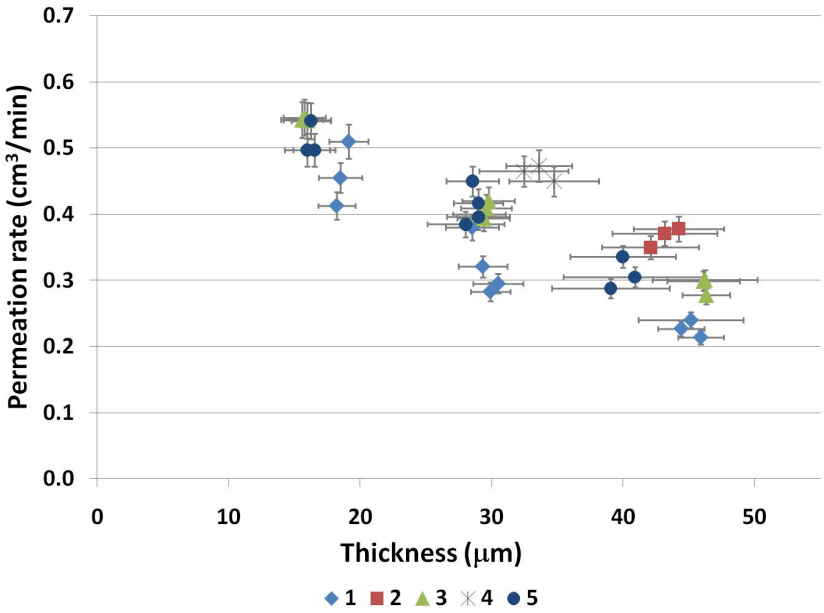

Figure 5.12: Summary of permeation rates for the five SPS conditions investigated.

The high density condition 1 coatings also exhibited the lowest permeation rates at all thicknesses investigated. The high plasma gas flow rate large nozzle condition 2 coatings had intermediate densities, but had the highest permeation rates. These high permeation rates are likely due to the extensive vertical cracking seen in these coatings. The condition 3 coatings had lower densities than those produced at condition 2, but had the second or third lowest permeation rates of all the coatings produced. This result indicates that condition 3 coatings may be better SOFC electrolytes than condition 2 coatings even though condition 2 coatings are denser, since the condition 3 coatings have fewer vertical cracks. Condition 4 produced low density, high permeation rate coatings. The compromise

condition 5 coatings had the second highest density, low permeation rates, and had deposition efficiency values 70% greater than the highest density condition 1 coatings, and thus might be the most promising combination of density, permeability, and deposition efficiency of the five coating types evaluated.

A summary of the characterization results of the five conditions sprayed is shown in Table 5.3, with the density column presenting both the value of density and the percentage of theoretical density. The theoretical density of 8 mol% YSZ is 5.96 g/cm^3 [17]. The data in the table illustrate that large plasma gas flow rates are beneficial and small nozzles are essential for high density, low permeation coatings, but that very high plasma gas flow rates combined with small nozzles may severely restrict deposition efficiencies. The fairly low permeation rates seen for coatings produced at conditions 1, 3 and 5 may make them good candidates for SPS SOFC electrolytes.

Table 5.3: Summary of SPS coating properties.

Spraying condition	Plasma gas flow rate (slpm)	Nozzle size (mm)	Density (g/cm^3 / %)	Deposition efficiency (%)	Permeation rate 30 ± 2 μm coating (cm^3/min)	Permeation rate 44 ± 3 μm coating (cm^3/min)
1	275	9.5	5.7 / 96	16.4	0.30	0.22
2	300	12.7	5.3 / 90	59.3	-	0.36
3	230	9.5	5.1 / 86	34.9	0.40	0.29
4	220	12.7	4.9 / 82	42.5	0.46	-
5	250	9.5	5.5 / 93	28.2	0.40	0.30

5.4 Conclusions

This study built on previous suspension characterization and preliminary PS studies to characterize the effect of torch power and velocity on the density, deposition efficiency,

permeation rate, and microstructure of aqueous SPS YSZ coatings. A simplified thermodynamic analysis of the power requirements of SPS compared to conventional atmospheric plasma spraying with dry powder feedstock showed that SPS coatings require significantly greater amounts of plasma energy to fully treat the feedstock suspensions. Thus, lower solid flow rates compared to PS with dry powder feedstock may be required for SPS processes.

After an initial mapping of the effect of torch parameters on torch power was completed, a study of the effect of torch power and nozzle diameter on coating density, deposition efficiency, and permeation rate was made. It was found that high density, low permeation coatings could be produced from high velocity conditions created by small nozzles or high plasma gas flow rates; however, these conditions may result in lower deposition efficiencies.

Finally, five conditions from the initial spraying runs were chosen to study in greater depth to determine which conditions were most likely to produce the highest performing electrolyte layers. The study confirmed the general trends seen previously that large plasma gas flow rates are beneficial and small nozzles are essential for high density, low permeation coatings, but that very high plasma gas flow rates combined with small nozzles may severely restrict deposition efficiencies. In addition, it was observed that even though some conditions may produce coatings with high densities, these coatings may have high permeation rates due to the presence of vertical cracking. The low permeation rates seen for coatings produced at conditions 1, 3 and 5 may make them good candidates for SPS SOFC electrolytes, thus meriting further electrochemical study of these coatings.

5.5 Acknowledgements

The authors gratefully acknowledge financial support from the Natural Sciences and Engineering Research Council of Canada, Northwest Mettech Corporation, and the BC Innovation Council.

5.6 References

1. R. Hui, Z. Wang, O. Kesler, L. Rose, J. Jankovic, S. Yick, R. Maric, D. Ghosh, Journal of Power Sources, 170(2) (2007), 308-323.
2. D. Waldbillig, O. Kesler, Surface & Coatings Technology, 203(15) (2009), 2098-2101.
3. O. Arevalo-Quintero, D. Waldbillig, O. Kesler, Journal of Colloids and Interface Science (2010), submitted.
4. B.D. White, O. Kesler, L. Rose, Journal of Power Sources, 178(1) (2008), 334-343.
5. D. Waldbillig, O. Kesler, Z. Tang, A. Burgess, pp. 201-206 in Proceeding of the International Thermal Spray Conference (ITSC), Edited by E. Lugscheider. German Welding Society. Maastricht, the Netherlands, 2008.
6. D. Waldbillig, O. Kesler, Journal of Power Sources, 191(2) (2009), 320-329.
7. A.C. Fox, T.W. Clyne, Surface & Coatings Technology, 184(2-3) (2004), 311-321.
8. D. Bucker, R. Span, W. Wagner, Journal of Engineering for Gas Turbines and Power, 125 (2003), 374-384.
9. P. Bruggeman, D.C. Schram, Plasma Sources Sciences and Technology, 19 (2010), 1-10.
10. C.L. Yaws, Yaws' Handbook of Thermodynamic Properties for Hydrocarbons and Chemicals. Knovel - Technical Engineering Reference Information. Retrieved May 1, 2010, from http://knovel.com/web/portal/browse/display?_EXT_KNOVEL_DISPLAY_bookid=2380&VerticalID=0.
11. C. Zhang, A.F. Kanta, C.X. Li, C.J. Li, M.P. Planche, H. Liao, C. Coddet, Surface & Coatings Technology, 204(4) (2009), 463-469.
12. D. Waldbillig, O. Kesler, Z. Tang, A. Burgess, pp. 677-682 in Proceedings of the International Thermal Spray Conference (ITSC), Edited by B. Marple, M. Hyland , Y.C. Lau, C. J. Li, R. Lima, and G. Montavon. ASM International. Beijing, China, 2007.
13. R. Rampon, O. Marchand, C. Filiatre, G. Bertrand, Surface & Coatings Technology, 202(18) (2008), 4337-4342.
14. D. Gallagher, Master of Engineering Project Report, University of Toronto, Toronto, ON, Canada, 2009.

15. V. Karakoussis, N.P. Brandon, M. Leach, R. van der Vorst, Journal of Power Sources, 101(1) (2001) 10-26.
16. X. He, B. Meng, Y. Sun, B. Liu, M. Li, Applied Surface Science, 254(22) (2008), 7159-7164.
17. I.R. Gibson, G.P. Dransfield, J.T.S. Irvine, Journal of Materials Science 33(17) (1998), 4297-4305.

6 Electrochemical testing of suspension plasma sprayed solid oxide fuel cell electrolytes[25]

6.1 Introduction

Solid oxide fuel cells are a highly efficient technology that produces electricity and high temperature byproduct heat from a fuel source. SOFCs are able to use a wide variety of fuels and are inherently more tolerant to species such as carbon monoxide that poison other types of fuel cells due to the oxide ion conducting nature of the SOFC electrolyte, the high operating temperature, and the lack of a requirement for noble metal electrode catalysts. These qualities make SOFCs a promising near term energy production device.

Widespread adoption of SOFCs is mostly limited by durability and cost issues. One of the main sources of SOFC durability limitations is the inherent brittleness of the commonly used ceramic or cermet mechanical support layers. Stainless steel has been proposed as a potentially more robust support material [1]; however, it is difficult to fabricate metal supported SOFCs using the wet ceramic SOFC manufacturing processes, as the high temperature firing operations required to sinter and densify SOFC layers severely degrade the metal support. Sinter aids or inert atmosphere firing have been proposed as potential methods to reduce the support degradation during processing, but these methods may be detrimental to the electrolyte conductivity or expensive [2,3]. Infiltration methods have also been proposed as an alternative method to fabricate metal supported SOFCs [4]; however, these techniques are slow and may be quite difficult to scale up to the large manufacturing volumes required to bring down SOFC costs. At low production volumes, SOFC systems cost on the order of $10,000/kW [5], and while system costs are expected to decrease significantly as more efficient manufacturing processes are developed and scaled up, it will still be challenging to achieve the US Department of Energy's cost target of $400 per kilowatt [6] with wet ceramic cell fabrication processes.

---

[25] A version of this chapter will be submitted for publication. D. Waldbillig, O. Kesler, (2010) Electrochemical testing of suspension plasma sprayed solid oxide fuel cell electrolytes.

Materials, equipment, and labour costs make up the majority of SOFC manufacturing costs. Materials costs consist of the cost of the raw materials required to produce the SOFC support and electrochemically active layers. A recent economic study determined that materials costs represent more than 50% of the total cell cost at sufficiently large production volumes for which the cost/kW converges to a stable value and that the cermet support layer for wet ceramic produced cells represents ~75 % of the total material cost [5]. If metal supports are used, support layer costs can be decreased to ~12% of the total cost, which decreases the total cell cost by approximately 40%. In addition to being less expensive, metal supports also have superior mechanical, thermal and electrical properties compared to Ni/YSZ cermet supports. SOFC equipment costs at the low production volumes needed for early market entry may also be reduced by lowering the number and complexity of unit operations, and labour costs can be decreased by increasing the amount of automation in the manufacturing process.

Plasma spraying is a well-established manufacturing technique that can produce fully sintered ceramic coatings rapidly and without the need for post deposition heat treatments. This technique has been used for over 50 years to produce many different types of coatings such as the thermal barrier coatings in gas turbines. Plasma spraying can produce coatings extremely rapidly and is relatively easy to automate; however, this technique has difficulty producing coatings with high porosity (>25%) or low porosity (<10%) and in producing uniform coatings of less than 50 μm in thickness due to the large size of the feedstock particles (10 to several 100 μm). In order to enhance the ability of PS processes to control the microstructure and porosity and to enable thinner layers to be produced, a micron or sub-micron sized feedstock powder suspended in a carrier liquid can be used. This technique is called suspension plasma spraying (SPS) and has the potential to significantly improve coating quality and control while keeping the rapid deposition and lack of post deposition heat treatment requirement of conventional powder based PS processes.

PS SOFCs have a number of potential cost and performance advantages compared to wet-ceramic SOFC manufacturing processes. PS processes allow stainless steel mechanical supports to be used without any additional cost or performance trade-offs specific to the

use of the metallic supports. The rapid deposition rate and elimination of high temperature firing operations allow for high throughputs, simple process flow, and easy automation, which lowers process, equipment, and labour costs. PS processing can also realize significant cost savings even at fairly low production volumes due to the use of metal supports and to the scalability of the equipment requirements for different production levels [5]. In addition, the rapid nature of PS SOFC manufacturing may have the potential to improve SOFC performance by allowing higher performing or less expensive material sets that may inter-react or decompose at the high temperatures required to sinter electrolyte layers to be used for electrochemically active layers, since the extremely rapid cooling of PS layers gives the layers little time for the normally diffusion-based inter-reactions to occur. Finally, PS processes may allow finer control over the composition, size or nature of functional layers, allowing these layers to be functionally graded in order to reduce thermal stresses, improve electrochemical properties, or enhance functional features such as internal reforming.

However, much work is still required in order to determine the effects of PS parameters on SOFC layer microstructures and to characterize the effect of PS layer features such as splat boundaries on the electrochemical activity of PS SOFCs. This study investigates the electrochemical properties of SOFCs fabricated from three promising SPS conditions identified in a previous study [7] on porous ferritic stainless steel mechanical supports and examines the effect of electrolyte thickness and microstructure on the open circuit voltage (OCV) and series resistance (R_s) values. Three different nominal electrolyte thicknesses were tested (15 μm, 30 μm and 45 μm).

Cathode and anode layers were produced by conventional PS processes and are being optimized in parallel studies [8,9,10] and thus will only be briefly discussed in this work.

6.2 Experimental procedure

6.2.1 Substrate and feedstock material

SOFCs were deposited onto 2.54 cm diameter porous ferritic stainless steel 430 substrates with a media grade (MG) of 2 (Mott Corporation, Farmington, CT, USA). This substrate type is most commonly used as a filter medium, and the media grade designation refers to the smallest diameter particle in micrometers that can be captured in the filter.

A 48.2 – 51.8 wt% mixture of individually spray dried lanthanum strontium manganite ($La_{0.8}Sr_{0.2}MnO_{3-\delta}$, LSM) and 8 mol% yttria-stabilized zirconia (YSZ) powders (Inframat Advanced Materials, Farmington, CT, USA) was used for the cathode layers. Spray dried cathode powders were sieved and mechanically mixed before plasma spraying. The detailed cathode powder preparation procedure has been reported previously [8].

Non-spray dried 8 mol% YSZ powder (Inframat Advanced Materials, Farmington, CT, USA) was used as the electrolyte feedstock for this study. The as-received powder had a d_{50} agglomerate size of approximately 1.6 μm, with sizes ranging from 0.5 μm to 15 μm, as determined previously by laser light scattering (Mastersizer 2000, Malvern Instruments, Worcestershire, UK) [11]. Aqueous YSZ suspensions with a solid loading of 3 vol% (15.4 wt%) were prepared using deionized water and 0.01 wt% PBTCA (2-Phosphonobutane-1,2,4-Tricarboxylic acid) dispersant referenced to the ceramic solid weight.

A sprayed dried, preagglomerated mixture of 70 wt% NiO and 30 wt% YSZ powder (Inframat Advanced Materials, Farmington, CT, USA) was used for the anode layer feedstock. The anode powders were calcined at 1200^{o}C for 2 hours to prevent agglomerate break up during feeding and then sieved. 9.3 wt% of a commercially available flour (Robin Hood All-purpose Flour, Smuckers Foods of Canada, Markham, ON, Canada) was added to the anode powder before plasma spraying to serve as a pore former.

6.2.2 Plasma spray processing

All SOFC layers were deposited using an axial injection APS system (Axial III Series 600, Northwest Mettech Corp., North Vancouver, BC, Canada) that was modified to deliver liquid

suspensions using a pressured canister as described previously [11]. A needle type nozzle with an inner diameter of 0.84 mm that was positioned directly behind the torch convergence injected the suspension directly into the centre of the plasma jet, where it was atomized by the plasma plume. During SPS, the feedstock suspension was fed to the torch at a rate of 104 mL/min, which resulted in a total solid flow rate of 18.5 g/min[26].

During spraying runs, the substrates were mounted on a rotating turntable and the torch was moved vertically. Before the powder or suspension feeding systems were started, the substrates were preheated directly by the plasma torch to a temperature between 300 and 350^{o}C, as measured directly by a Type K thermocouple in contact with the back surface of the metal substrate.

A plasma sprayed composite LSM / YSZ cathode layer was first deposited on the steel substrates at conditions described previously [8,11] and an SPS YSZ electrolyte layer was then deposited on top of the cathode layer. Suspension plasma sprayed electrolyte layers were produced from one of the three conditions listed in Table 6.1. The spraying conditions were labelled as having high, medium, or low flow rates, which indicates the relative plasma gas flow rates used. A previous study had determined that these conditions produced layers with promising electrolyte microstructures and properties [7]. Electrolytes having three nominal thicknesses of 15, 30, and 45 μm were produced, in order to examine the effect of electrolyte thickness on the physical and electrochemical properties of the cell. Finally, a 1.1 cm in diameter plasma sprayed NiO / YSZ anode layer was deposited on top of the electrolyte layer at conditions described previously [11].

[26] A more detailed description of the suspension delivery and injection equipment can be found in Appendix D.

Table 6.1: Electrolyte suspension plasma processing parameters.

Parameter	High flow rate	Medium flow rate	Low flow rate
Plasma gas flow rate (slpm)	275	250	230
Plasma gas composition (%)	70% N_2, 25% Ar, 5% H_2	80% N_2, 15% Ar 5% H_2	87% N_2, 13% Ar
Current (A per cathode)	250	250	250
Nozzle size (mm)	9.5	9.5	9.5
Preheat temperature (°C)	300 - 350	300 - 350	300 - 350
Standoff distance (mm)	90	80	80

6.2.3 Characterization of plasma sprayed layers

After YSZ layers were deposited, the coating density, deposition efficiency, permeation rate and microstructure were characterized. These results have been described in detail in a previous study [7] and are summarized in Table 6.2, with the density column presenting both the value of density and the percentage of theoretical density. The theoretical density of 8 mol% YSZ is 5.96 g/cm^3 [12]. Layer density was calculated by dividing the weight gain after electrolyte spraying runs by the coating area and the coating thickness as measured by scanning electron microscopy (SEM). Deposition efficiency was calculated as the ratio of the weight gained during the spraying run to the amount of YSZ delivered during the spraying run, as determined from suspension flow rate measurements performed during initial calibration tests without plasma gas flow. Helium permeation measurements were performed using an in-house designed fixture. The supply of helium gas was regulated at a gauge pressure of 3.5 kPa and the flow through the sample was measured by a mass flow

meter[27]. This flow rate was then used to calculate the layer permeability using Darcy's law [11,13].

Table 6.2: Summary of sprayed electrolyte characteristics.

Spraying condition	Density (g/cm^3 / %)	Deposition efficiency (%)	Permeation rate 30 ± 2 μm coating (cm^3/min)	Permeability (m^2)
High flow	5.7 / 96	16.4	0.30	9.21E-18
Medium flow	5.5 / 93	34.9	0.40	1.14E-17
Low flow	5.1 / 86	28.2	0.40	1.15E-17

Polished cross sections of the deposited layers were examined in a Hitachi S-3000N SEM (Hitachi High Technologies America, Pleasanton, CA, USA). Samples were mounted in epoxy, cut using a low speed diamond saw, and then polished using diamond polishing suspensions. The polished samples were gold coated to provide sufficient conductivity for SEM imaging. The back-scattered electron (BSE) imaging mode was used for all SEM images in order to enhance the contrast between the individual SOFC component materials.

6.2.4 Electrochemical testing[28]

6.2.4.1 Test equipment and contact

Single cell test stations (model FCSH-1000, Materials Mates Italia, Milan, Italy) with additional gas flow control hardware and software (Arbin Instruments, College Station, TX, USA) were used for electrochemical testing. Platinum mesh was used for both the anode and cathode side contacts.

---

[27] A detailed explanation of the permeation measurements can be found in Appendix C.

[28] A more detailed description of the electrochemical testing equipment and test procedures can be found in Appendix E.

6.2.4.2 Sealing

A two part sealing system was utilized for the electrochemical tests. First, a wet ceramic seal (Ceramabond 552-VFG, Aremco Products, Inc., Valley Cottage, NY) was painted on the outside edge of the cells in order to limit any leakage from the cell edges. The ceramabond seal was then cured as per the included instructions [14]. A commercially available sealing product (Thermiculite 866, The Flexitallic Group, Houston, USA) was used to seal the face of the cell to the test station tube. An anode supported cell with a screen printed and fired electrolyte achieved an open circuit voltage of 1.02 at 750^{o}C with a hydrogen concentration of 20% while using this sealing system.

6.2.4.3 Cell testing

Electrochemical tests were performed using a Solartron 1470E multi-channel potentiostat and 1260 frequency response analyzer (London Scientific, London, ON, Canada). Cells were first heated to 750^{o}C in a 4% H_2 atmosphere on the anode side and still air on the cathode side. Once the cell reached temperature, the H_2 concentration was slowly increased to 20% and flowing air was introduced on the cathode side. The reduction process continued until the cell open circuit voltage stopped rising, usually after approximately one hour of reduction. The conditions used during cell testing are summarized in Table 6.3. Electrochemical tests were performed with high flow rates in order to overcome diffusion limitations caused by the design of the test station and by the lower than optimal electrode layer porosities. Anode gases were humidified to 3% by passing the gasses through a humidifier containing deionized water at room temperature.

Table 6.3: Electrochemical testing parameters.

Parameter	Value
Anode gas composition (vol%)	20% H_2, 80% N_2
Anode gas flow (sccm)	950
Cathode gas composition (vol%)	Air (79% N_2, 21% O_2)
Cathode gas flow (sccm)	950
Testing temperature (^oC)	600, 650, 700, 750

During electrochemical testing, polarization curves and impedance measurements were made at each testing temperature. Since this study is primarily interested in characterizing the electrochemical performance of the electrolyte layers, the focus of the electrochemical testing was to determine open circuit voltage (OCV) and series resistance values of the cells with different electrolytes. The open circuit voltage (OCV) determined from polarization curves provides information about electrolyte and seal permeability. Series resistance values obtained from the high frequency intercept of the Nyquist impedance plots provide information about the cell losses due to the electrolyte material and microstructural resistivity and any contact resistance present.

6.3 Results

6.3.1 Electrochemical testing

6.3.1.1 Polarization curves[29]

Polarization curves were obtained from open circuit voltage to a voltage of 0.27 V at temperatures of 750, 700, 650 and 600^{o}C. Typical polarization curves of a cell sprayed at

[29] Additional background information on the significance of open circuit voltage values can be found in Appendix K.

the high flow condition showing the voltage – current behaviour (solid lines, left axis) and power density (dashed lines, right axis) are shown in Figure 6.1. The measured open circuit voltage is approximately 10% lower than the Nernst value predicted by thermodynamics. As expected, the cell open circuit voltage values increased as the temperature decreased and the slopes of the curves increased as the temperature decreased, indicating that the electrolyte and polarization resistances were increasing. The concave down nature of the polarization curves at higher current densities and temperatures suggested that there were significant mass transport losses present, which are likely attributable to a combination of low electrode porosity and poor test station gas feed design. A maximum power density of 0.14 W/cm^2 at 750^{o}C was observed for the cells with SPS electrolytes produced with the high flow rate conditions. Maximum power density values found in the SOFC literature vary by more than 3 orders of magnitude from values of ~0.01 to >1 W/cm^2 depending on the materials sets used, microstructures and testing conditions. The highest power density reported to date for an entirely thermally sprayed SOFC is ~0.4 mW/cm^2 at 750^{o}C [15], although power densities of up to ~0.9 W/cm^2 at 700^{o}C have been achieved for cells with plasma sprayed anode and electrolyte layers and screen printed cathode layers [16].

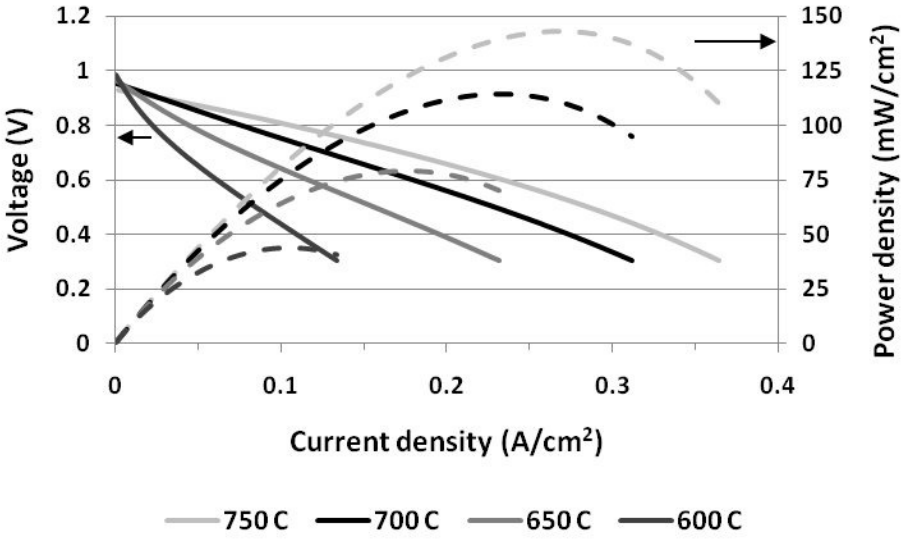

Figure 6.1: Polarization curves for a typical tested cell fabricated at high gas flow conditions.

The effect of temperature on the cell open circuit voltage as a function of electrolyte permeation rates is shown in Figure 6.2a for coatings produced from the high flow spraying condition. As expected, the cell open circuit voltage increases as the testing temperature decreases and as the electrolyte permeation rate decreases. Figure 6.2b shows the effect of electrolyte permeation rate on the open circuit voltage at 750^{o}C for the three electrolyte microstructures examined. It can be seen in the figure that for equivalent permeation rates, the open circuit voltage values for the three microstructures were very similar, as expected. Microstructures produced in high flow rate plasma processing conditions were able to achieve lower permeation rates at equivalent thicknesses compared to the other two conditions at all thicknesses studied.

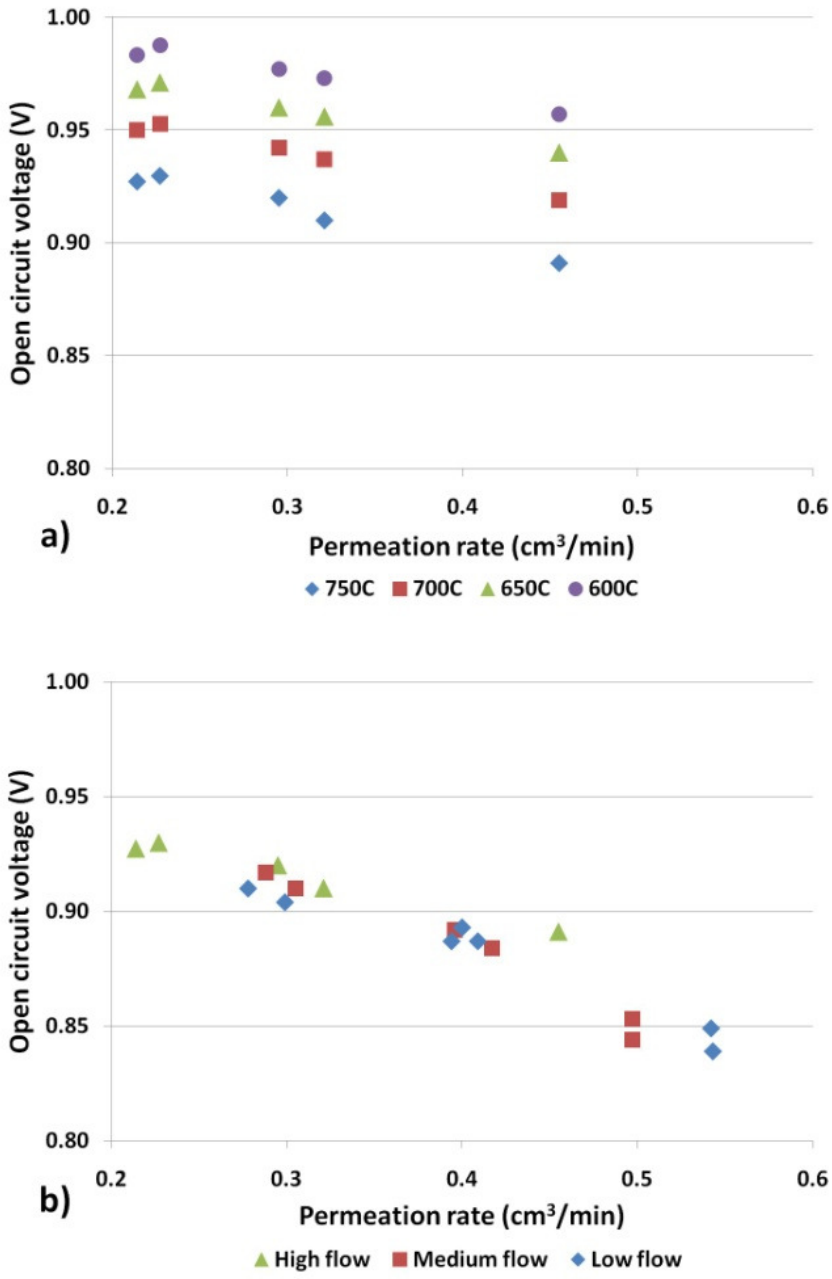

Figure 6.2: Effect of permeation rate on the measured open circuit voltage of electrolyte layers with a) high processing gas flow rate microstructures at temperatures of 600, 650, 700, and 750°C with 20% H_2 and b) low, medium and high processing gas flow rate microstructures at 750°C with 20% H_2.

6.3.1.2 Impedance measurements[30]

Impedance tests were performed at open circuit voltage for the four test temperatures. A blank impedance measurement with no cell loaded was performed for each test station in order to determine the amount of inductance present in the system due to the wires and test station in order to subtract this value from the measured impedance to isolate the cell impedance. Typical Nyquist impedance plots for a cell sprayed at the high flow condition are shown in Figure 6.3. Figure 6.3a shows the measurements before inductance correction, while Figure 6.3b shows the same measurements after the inductance has been subtracted. Series resistance (R_s) values were determined from the high frequency intercepts of the inductance corrected Nyquist plots. These values were separated into three main loss types: YSZ resistivity losses, microstructure based losses, and contact losses.

[30] Additional background information on the ionic conductivity of yttria stabilized zirconia can be found in Appendix K.

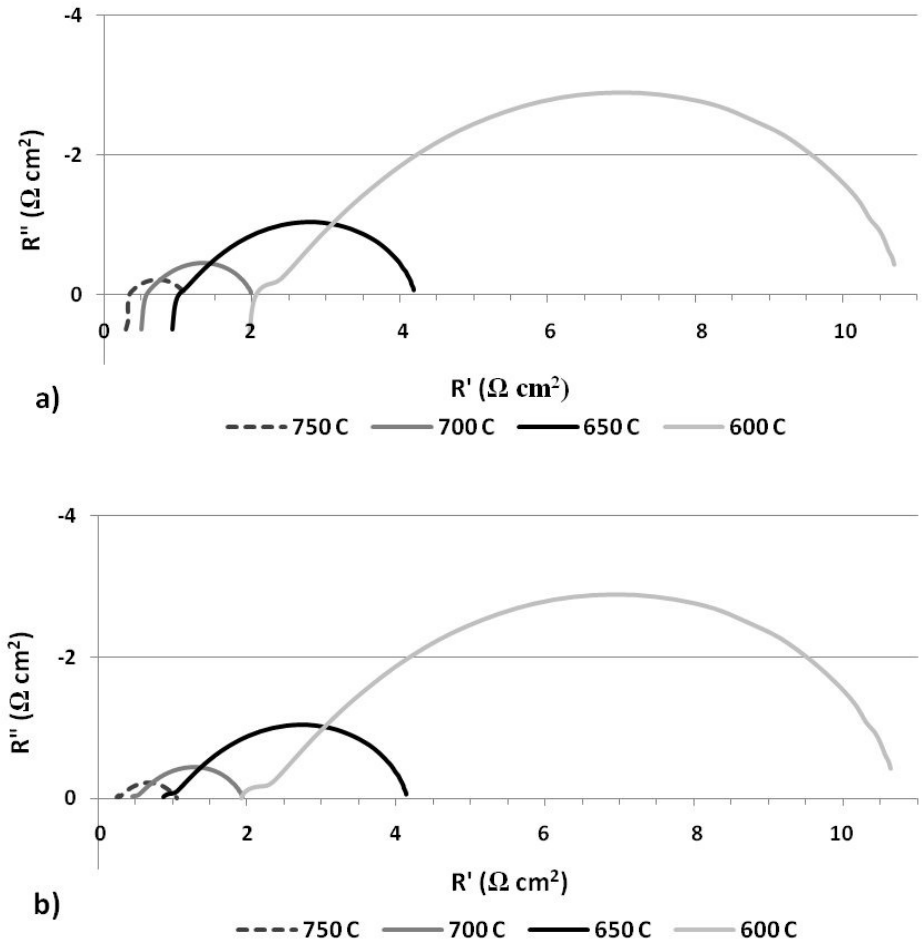

Figure 6.3: Impedance curves a) before and b) after inductance subtraction for a cell produced from high flow rate spraying conditions.

The effect of electrolyte thickness on the measured R_s values for cells produced at the high flow rate spraying condition is shown in Figure 6.4 for the four test temperatures investigated. As expected, the R_s values increase as the thickness increases and as the temperatures decreases.

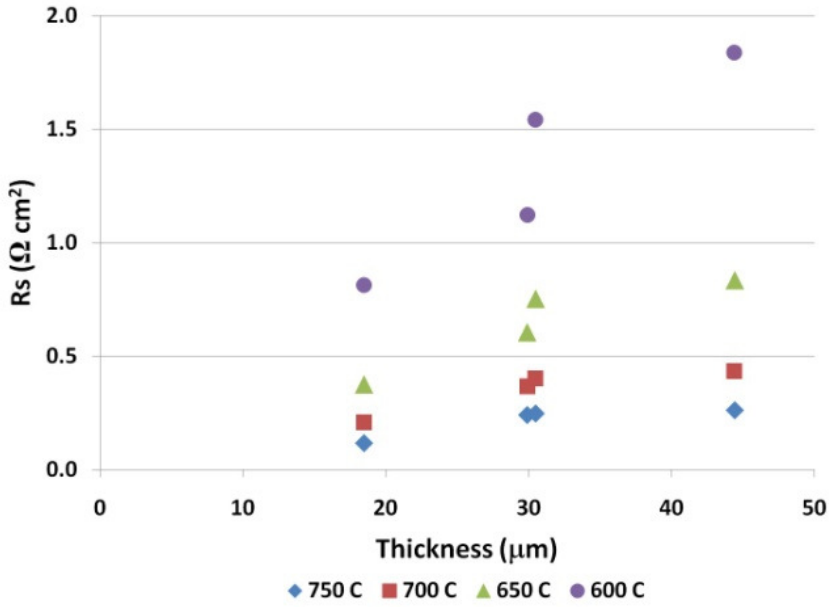

Figure 6.4: Effect of thickness on the measured Rs value for high flow rate microstructures at temperatures of 600, 650, 700, and 750°C with 20% H_2.

6.3.1.3 Series resistance separation[31]

In order to better understand the root causes of the various electrolyte losses, the measured series resistance (R_s) was separated into three parts, as shown in Equation 6.1.

$$R_s = R_{YSZ} + R_\mu + R_C \qquad (6.1)$$

R_{YSZ} corresponds to the area specific resistance caused by the limited ionic conductivity of YSZ and was calculated directly by dividing the electrolyte layer thickness by the conductivity of YSZ [17]. R_μ is the resistance due to the microstructural features within the electrolyte layer such as porosity or splat boundaries, while R_C is the resistance due to the contact interfaces present between the cell and test station. In order to enable R_μ and R_C values to be estimated, a microstructural resistivity (ρ_μ) was calculated by dividing R_μ by the

[31] A more detailed description of the series resistance separation procedure and sample calculations can be found in Appendix F.

electrolyte thickness and a least-squares fitting was used to determine the relative contributions of R_μ and R_C for each cell test. The ρ_μ value was assumed to be constant for a given test temperature and spraying condition, thus allowing the sum of the squared residuals to be minimized to determine the most likely R_C values for each tested cell.

A summary of the results of resistance separation calculations for cells sprayed at the high flow rate condition is shown in Figure 6.5. As expected, R_{YSZ} and R_μ increase as the temperature decreases or as the electrolyte thickness increases, while the R_C generally increases as the temperature decreases during each individual cell test. It is difficult to compare the contact resistance of different cell tests, as this resistance may be significantly affected by inherent test station differences, by variations in cell loading, and by cell-to-cell variations in parameters such as flatness or substrate oxide growth.

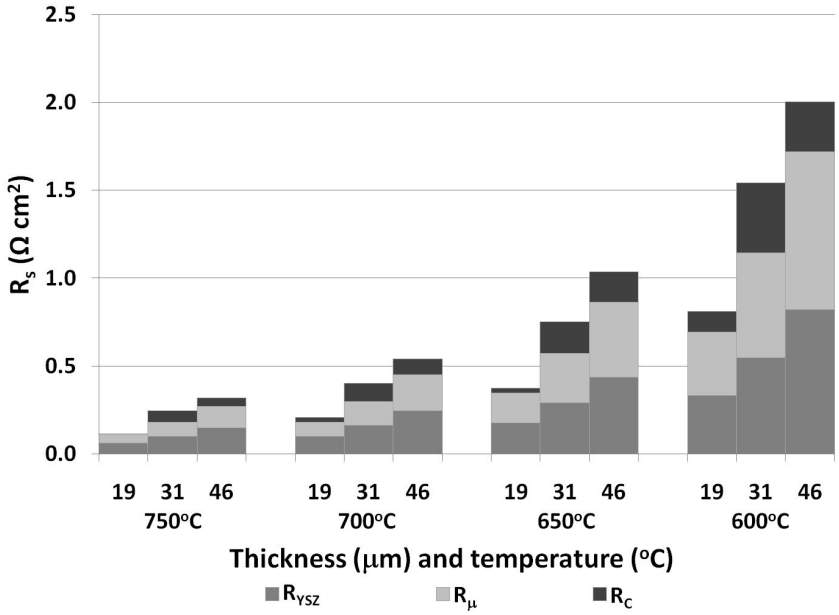

Figure 6.5: Effect of thickness and temperature on the ASRs breakdown for a cell sprayed at the high flow rate condition.

Characterizing the microstructural resistance of the electrolyte layer is of great interest for plasma spray produced electrolytes in order to determine the effect of the microstructural

features such as porosity and splat boundaries present due to plasma spray processing on the electrolyte performance. When the calculated microstructural resistance is divided by the electrolyte layer thickness, the contribution to the overall resistivity resulting from the material microstructure can be determined. A comparison of the resistivity of the three types of electrolyte layers at temperatures between 600 and 750^{o}C is shown in Figure 6.6a. Electrolyte resistivity was strongly dependent on temperature and decreased by approximately an order of magnitude as the temperature was increased from 600 to 750^{o}C. Electrolyte layers produced at the low flow rate condition had significantly higher resistivity than the other electrolyte types. Electrolytes sprayed at the medium flow condition had the lowest calculated microstructural resistivity, with values of less than 10 Ω cm at a temperature of 750^{o}C. A summary of the calculated total electrolyte area specific resistance ($R_{YSZ} + R_{\mu}$) for electrolyte thicknesses below 50 μm is shown in Figure 6.6b. It can be seen in the figure that YSZ electrolytes produced from high or medium flow conditions have electrolyte layer area specific resistances of less than 0.1 Ω cm^2 at 750^{o}C for electrolyte thicknesses less than 20 μm.

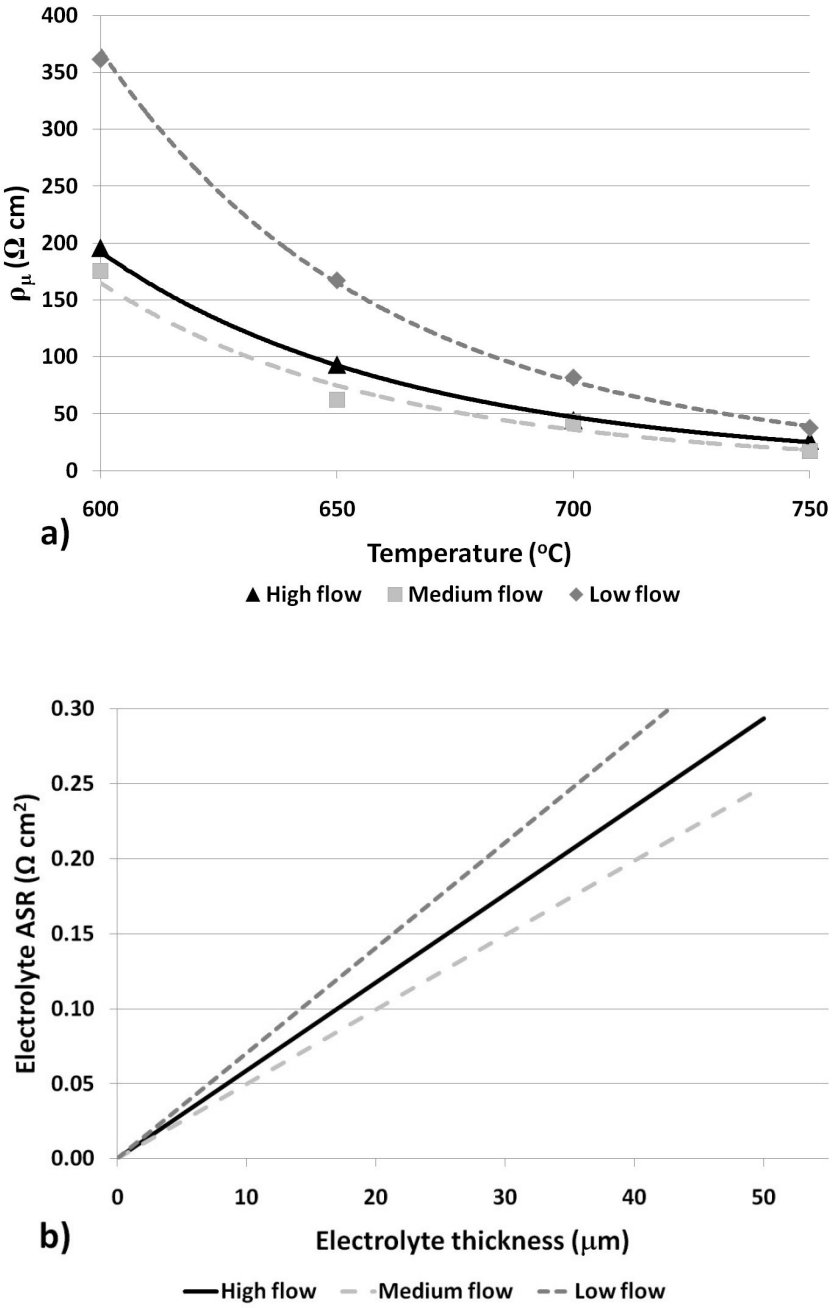

Figure 6.6: Comparison of a) the resistivity of electrolyte layers sprayed at three conditions for temperatures between 600 and 750°C and b) the total area specific resistance of electrolyte layers sprayed at three conditions for various thicknesses at 750°C.

6.3.1.4 Operating point calculations

In order to maximize cell performance, the electrolyte thickness resulting in the lowest voltage losses should be chosen for a given electrolyte microstructure and its corresponding permeability. Therefore, in order to better understand the effect of gas leakage and electrolyte resistance losses on the cell voltage, the open circuit voltage losses and voltage losses resulting from the series resistance contributions of both the bulk electrolyte material and electrolyte microstructure were calculated for operating points of 0.8 V and 0.7 V using Equations 6.2 to 6.6. These voltages represent the endpoints of the most commonly reported operating condition range for SOFCs.

$$\Delta V_x = V_{Leak} + V_{YSZ,x} + V_{\mu,x} + V_{C,x} \quad (6.2)$$

$$V_{Leak} = E_{Ideal} - V_{OCV} \quad (6.3)$$

$$V_{YSZ,x} = R_{YSZ}\, i_x \quad (6.4)$$

$$V_{\mu,x} = R_{\mu} i_x \quad (6.5)$$

$$V_{C,x} = R_C i_x \quad (6.6)$$

In the equations, x is the operating voltage, which is either 0.8 V or 0.7 V. V_{Leak} is the difference between the calculated Nernst voltage (E_{Ideal}) at the test temperature and hydrogen concentration of interest and the measured open circuit voltage (V_{OCV}). This voltage loss is caused by leakages within the cell, seals, and test equipment. V_{YSZ} is the bulk YSZ material resistance (R_{YSZ}) multiplied by the current density measured from a polarization curve at the operating point of interest ($i_{0.8\,V}$ or $i_{0.7\,V}$). This voltage loss decreases as the electrolyte thickness is decreased. V_{μ} is the electrolyte resistance due to the microstructural features within the electrolyte layer such as porosity or splat boundaries (R_{μ}) multiplied by the current density measured from a polarization curve at the operating point of interest ($i_{0.8\,V}$ or $i_{0.7\,V}$). This voltage loss decreases as the electrolyte

thickness is decreased and varies for electrolytes sprayed at different conditions, which will have different microstructures. V_C is the resistance due to the cell and test station contact interfacial resistance (R_C) multiplied by the current density measured from a polarization curve at the operating point of interest ($i_{0.8\ V}$ or $i_{0.7\ V}$). This voltage loss is very dependent on the testing setup and thus varies significantly for different electrochemical testing situations.

The calculated ΔV values for cells sprayed at the high, medium, and low flow rate conditions are shown in Figures 6.7, 6.8, and 6.9, respectively as a function of cell thickness and temperature. In Figures 6.7a, 6.8a, and 6.9a an operating point of 0.8 V is shown and in Figures 6.7b, 6.8b, and 6.9b an operating point of 0.7 V is shown. As the operating point changed from 0.8 V to 0.7 V, the total cell resistance increased. Generally it can be observed that when contact losses are not considered, the V_{Leak} term contributes between 61 and 99% of the electrolyte-related voltage losses in the test, depending on the electrolyte microstructure and thickness and the operating point. This result indicates that electrolyte, seal, and test station leakage result in a larger performance drop than ohmic losses due to the electrolyte resistance, for the electrolyte microstructures studied here.

As the electrolyte thickness and testing temperature vary, V_{Leak}, V_{YSZ}, V_μ and V_C vary. This may allow an optimum electrolyte thickness for which ΔV is minimized to be selected for a given proposed operating temperature and voltage based on ex-situ measurements of electrolyte permeability, and for known electrode R_p's, thus maximizing cell performance. V_{Leak} decreased as the thickness increased (i.e. OCV increased) for all cells, due to the lower permeation rates seen for thicker cells. As the testing temperature decreased, V_{Leak} decreased slightly. This effect may be caused by a reduction in the amount of combustion as the temperature decreases or due to slower mass transport at lower temperatures. V_{YSZ} and V_μ increase as thickness increases or as temperature decreases. V_C generally increases as the temperature decreases and can be improved by the use of contact paste or by interconnect design optimization.

For the highly dense microstructures produced from the high flow conditions, intermediate thicknesses (~30 μm) produced the lowest ΔV for both operating voltages and all temperatures investigated. For coatings produced from the medium flow rate spraying conditions, the thickest electrolyte layers had the lowest ΔV for both operating voltages and at all temperatures investigated. Thicker electrolyte layers may be favoured for these microstructures due to the low microstructural resistivity and higher permeabilities of these electrolyte microstructures. The ΔV trends seen for the low flow rate microstructures illustrate the competing loss mechanisms of leakage and microstructural resistivity. At an operating voltage of 0.8 V and temperatures of 700 or 750^{o}C, the effect of leakage is more significant than the microstructural resistivity. Therefore, the thickest electrolyte layers produce the lowest ΔV values at 0.8 V. However, at an operating point of 0.8 V and lower temperatures (650 and 600^{o}C) at which electrolyte conductivity is lower, the effect of microstructural resistance became more significant, and the lowest ΔV values were observed at the intermediate electrolyte thicknesses. At an operating voltage of 0.7 V, the voltage drop due to the increase in the microstructural resistivity was more significant than that due to gas leakage across the electrolyte, seals, and test station, and thus the lowest ΔV values were observed at the intermediate electrolyte thicknesses.

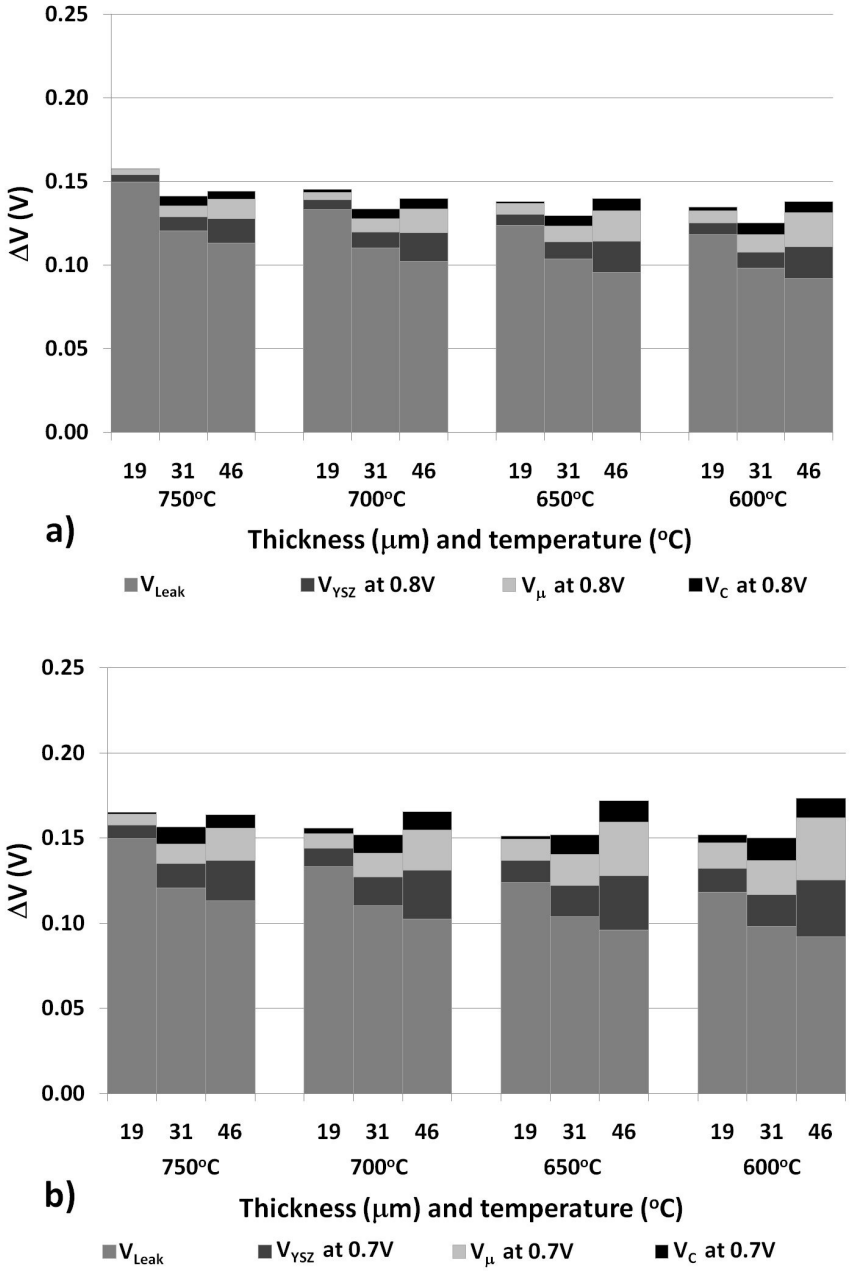

Figure 6.7: Voltage losses for cells sprayed at the high flow condition at various electrolyte thicknesses and testing temperatures at an operating point of a) 0.8 V and b) 0.7 V.

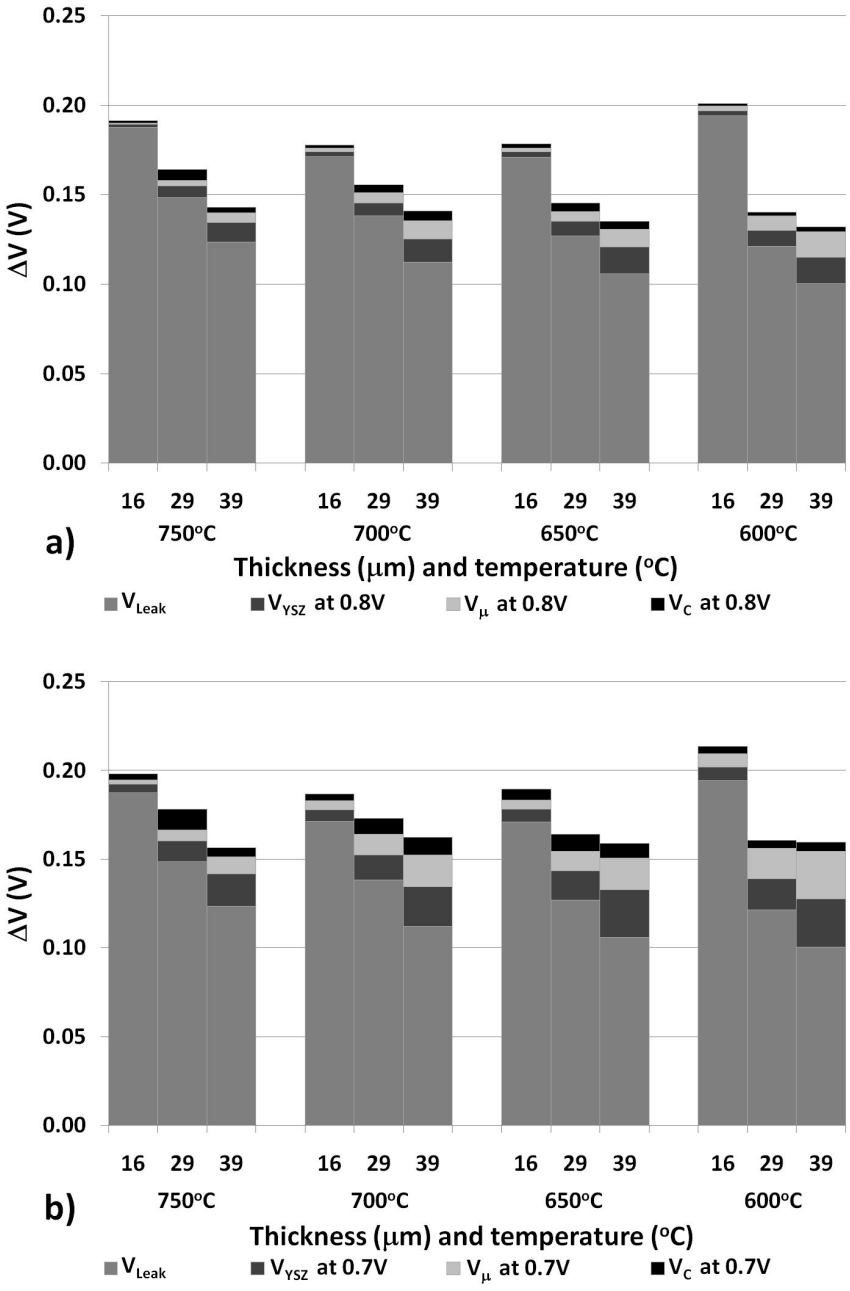

Figure 6.8: Voltage losses for cells sprayed at the medium flow rate condition at various electrolyte thicknesses and testing temperatures at an operating point of a) 0.8V and b) 0.7V.

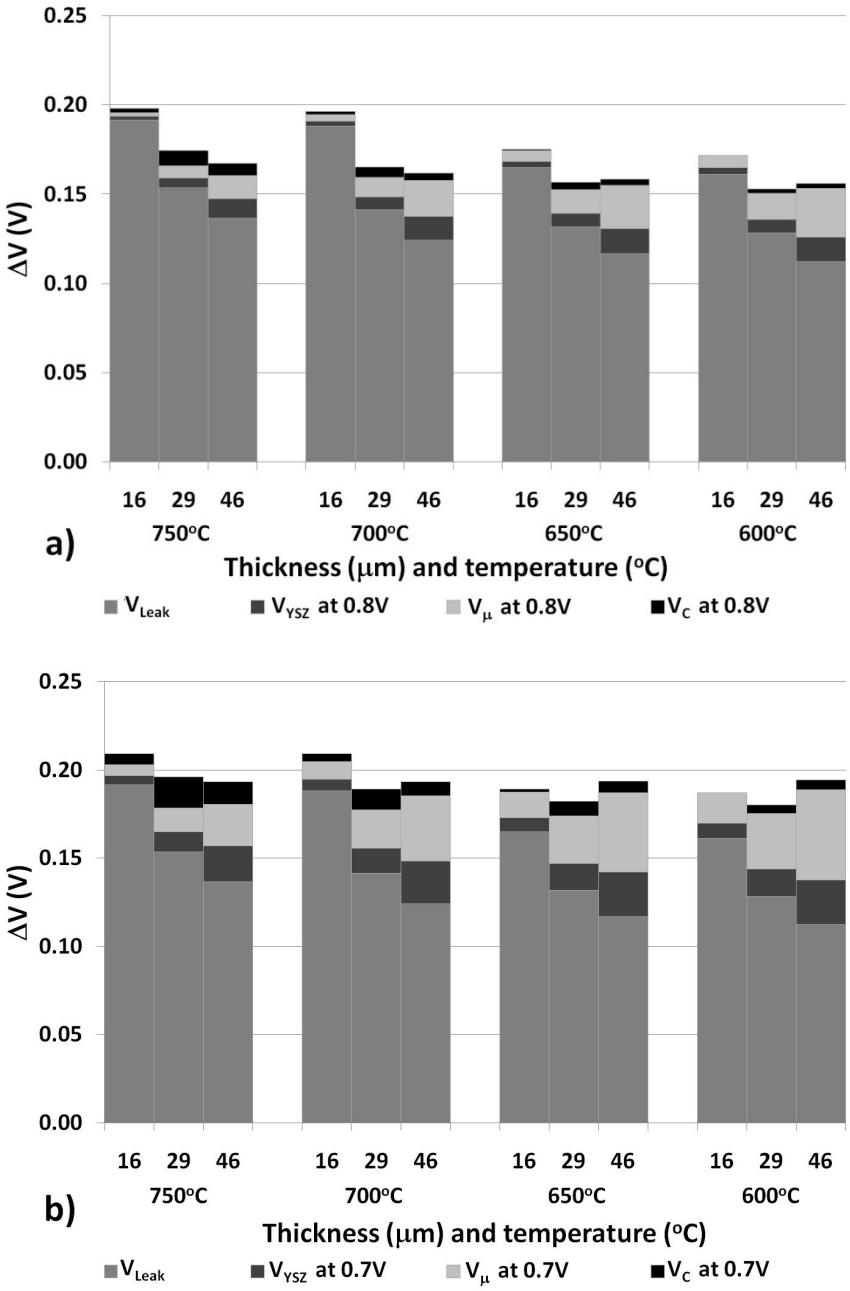

Figure 6.9: Voltage losses for cells sprayed at the low flow rate condition at various electrolyte thicknesses and testing temperatures at an operating point of a) 0.8V and b) 0.7V.

Comparisons of the ΔV results for the three spraying conditions investigated as a function of electrolyte thickness and of testing temperature are shown in Figures 6.10a and 6.10b respectively. The high flow rate condition layers had the lowest V_{Leak} value for all

thicknesses and temperatures, which indicates that these layers were the least permeable. Since V_{Leak} comprises the majority of voltage losses affected by the electrolyte, high flow condition cells also had the lowest total ΔV values attributable to the electrolyte. Medium flow rate condition coatings had the lowest V_{μ}, which indicates that these cells had the lowest electrolyte microstructural resistance of the cell types tested. Low flow rate condition coatings had both the highest V_{Leak} and the highest V_{μ}, indicating that these layers were both the most permeable and had the highest microstructural resistance. The desired operating voltage and temperature influence which electrolyte microstructure and thickness produce the lowest total ΔV values. High operating temperatures favour thicker electrolytes to minimize electrolyte permeability losses, while lower operating temperatures favour thinner electrolytes to minimize electrolyte resistive losses. At higher operating voltages, leakage losses contribute a greater proportion of the total losses, while at operating voltages of 0.7 V, electrolyte resistances become more significant.

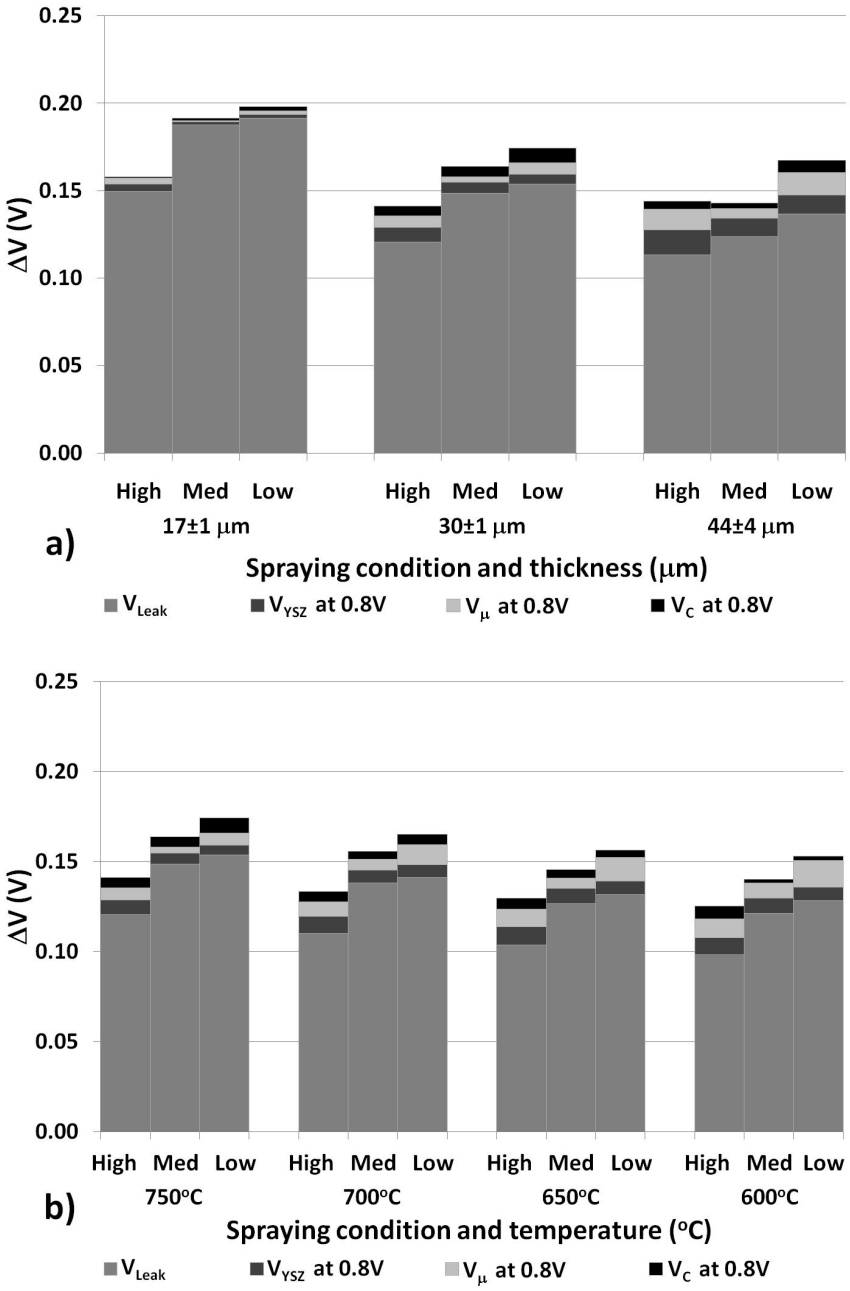

Figure 6.10: Comparison of the ΔV values for the three spraying conditions investigated as a function of a) thickness at 750°C and b) temperature at 30 μm thickness.

6.3.2 Microstructural analysis[32]

SEM images of typical cross-sectional microstructures for the SOFCs produced at the high, medium, and low flow rate electrolyte spraying conditions after fuel cell testing are shown in Figures 6.11, 6.12, and 6.13, respectively. Cathodes and anodes were sprayed under identical conditions, and it can be seen in Figures 6.11 to 6.13 that there is little cell-to-cell variation in electrode layer thickness or microstructure. The cathode layer components (LSM and YSZ) were well mixed, there was some porosity present in the layers, and the cathode layers were able to fill and cover the large, deep pores present in the support material. There was excellent coverage and strong adhesion between the stainless steel support, cathode and electrolyte layers, even after a number of slow thermal cycles introduced during cell testing. Anode layers were quite thick and had unevenly distributed porosity. The larger, unevenly distributed pores present in the anode layer are likely due to the flour pore former used, while the smaller, more evenly distributed pores present are likely due to the porosity introduced as the sprayed NiO is reduced. Small detached areas (see Figure 6.13b) were occasionally present at the electrolyte – anode interface. These areas may have been caused by the decrease in the anode layer volume as it was reduced or by thermal cycling effects during cell testing. Both anode and cathode layers likely have insufficient porosity for high cell performance, as seen by the diffusion limitations present in the electrochemical testing at the higher temperatures and current densities. Further electrode material and microstructural development is being performed in separate studies.

Electrolyte layers were reasonably dense with the same three main defect types: vertical cracking, medium sized defects, and small pores seen previously [11]. Vertical cracking was likely caused by thermally induced residual stresses produced during spraying, the medium sized defects may be caused by unmelted particles present within the deposited layer or by cathode layer surface topography (see Figure 6.12b), and the small pores present are likely

[32] Additional SEM images of the deposited layers can be found in Appendix H.

intersplat porosity, visible in all coatings. Qualitatively, electrolyte layers produced from high flow conditions appeared to be the most dense, followed by those produced by medium and low flow conditions. This density trend was confirmed both by permeation rate measurements done previously [7] and by open circuit voltage measurements done in this work.

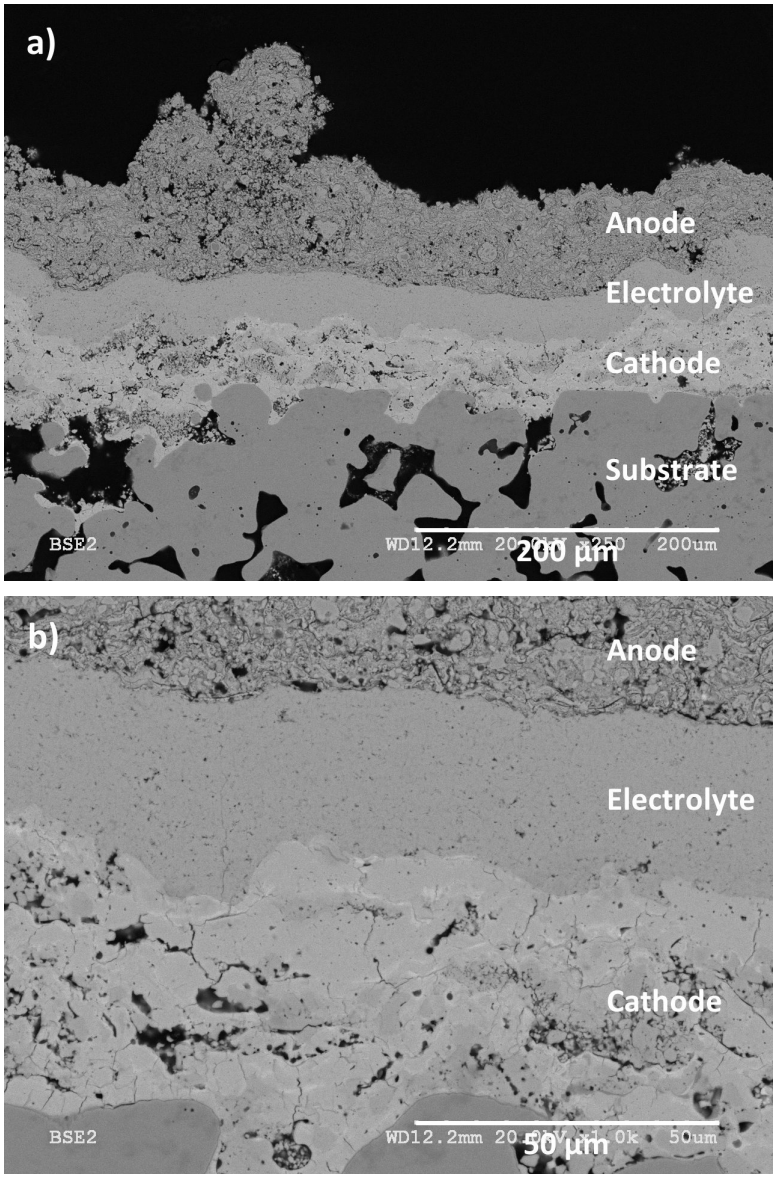

Figure 6.11: BSE SEM images of typical high flow condition microstructures at: a) 250x magnification and b) 1000x magnification.

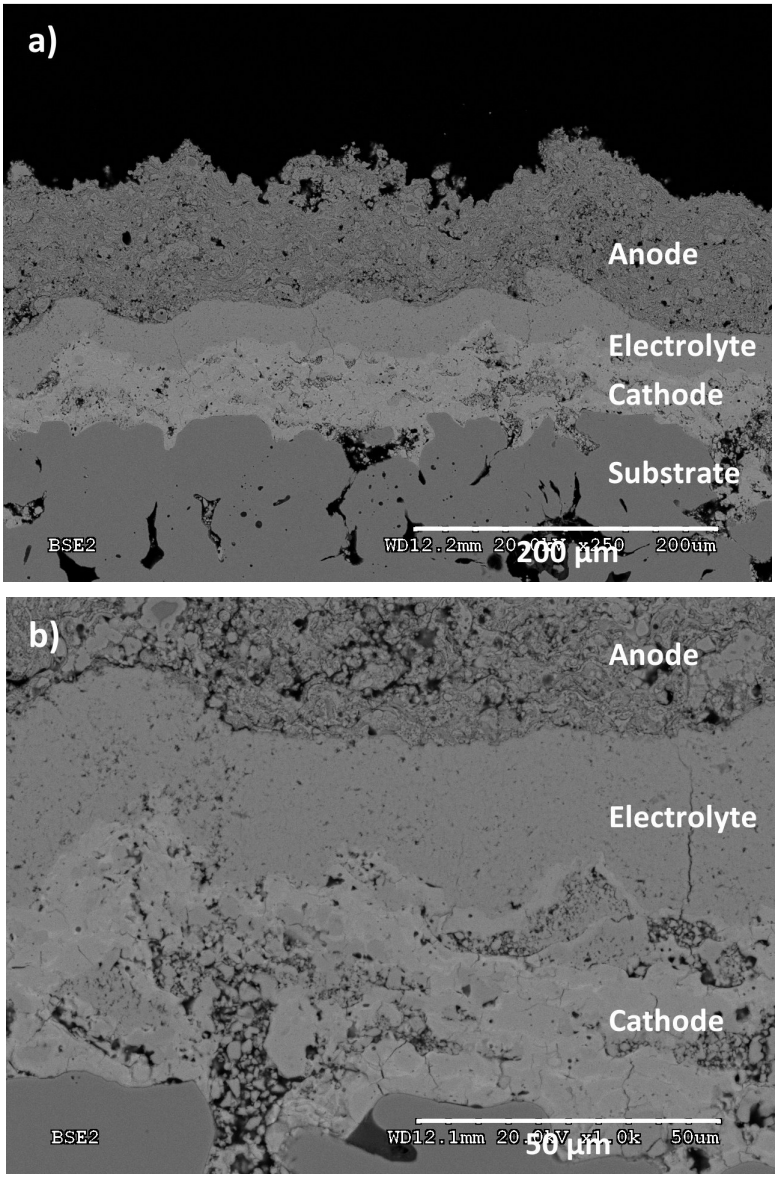

Figure 6.12: BSE SEM images of typical medium flow rate condition microstructures at: a) 250x magnification and b) 1000x magnification.

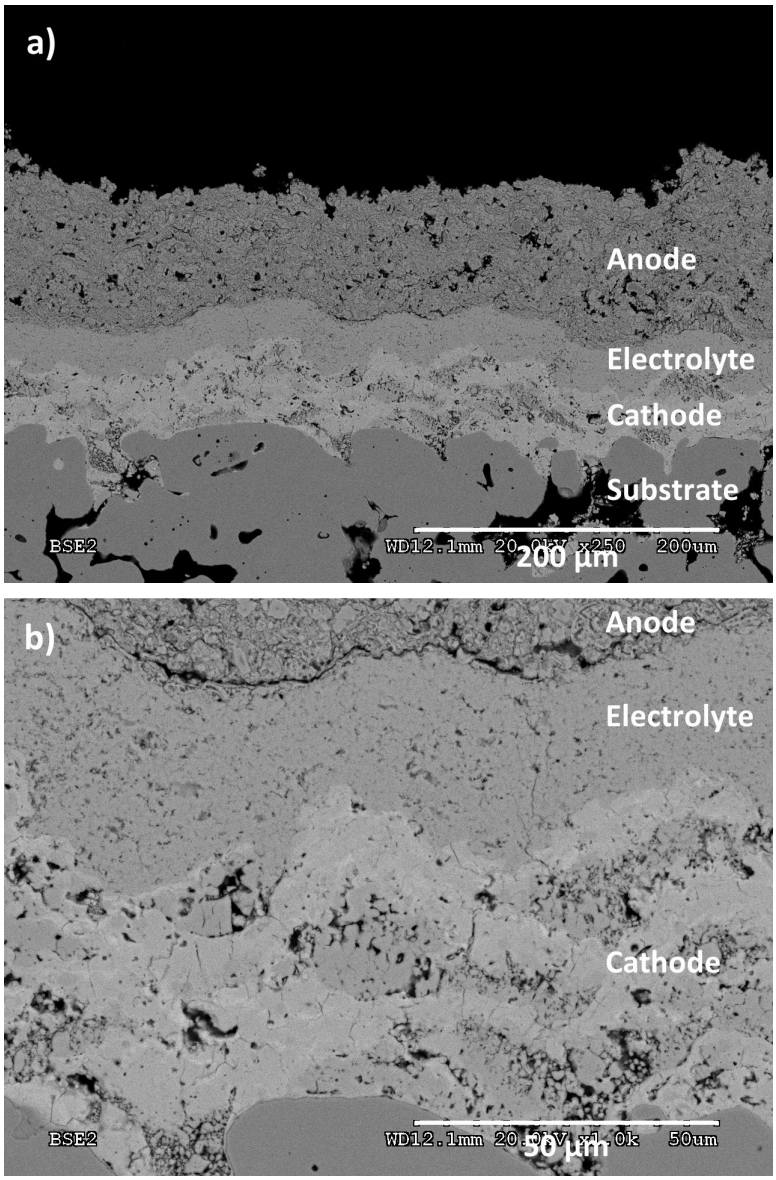

Figure 6.13: BSE SEM images of typical low flow rate condition microstructures at: a) 250x magnification and b) 1000x magnification.

6.4 Conclusions

Metal supported plasma sprayed (PS) SOFC fabrication techniques have the potential to overcome many of the cost and durability issues that have held back widespread adoption of SOFCs. This study characterized the electrochemical performance of PS SOFCs with three different electrolyte microstructures and thicknesses in order to determine the effects of

electrolyte thickness and microstructure on electrochemical properties such as open circuit voltage (OCV) and series resistance (R_s). Metal supported PS SOFCs were produced with OCV values approximately 10% lower than the OCV values predicted by thermodynamics and with electrolyte area specific resistances of < 0.1 Ωcm^2 at 750^oC for electrolyte thicknesses < 20 μm. In order to better understand the root causes of the various electrolyte losses, measured R_s values were separated into YSZ material resistance losses, electrolyte microstructural resistance losses, and contact resistance losses. The highly dense electrolyte layers produced from high plasma gas flow rate conditions had the lowest permeation rates, the highest OCV values, and the lowest total electrolyte-related losses. Medium flow rate conditions produced more permeable electrolyte layers that had lower OCV values and higher total electrolyte-related losses than the high flow rate microstructures; however, these electrolyte layers had the lowest microstructural resistivities. Low flow rate coatings had poor electrolyte microstructures with high permeabilities, low OCV values, high total R_s, and high microstructural resistivities. In order to better understand the combined effect of gas leakage and electrolyte resistance losses on the cell voltage, the OCV and R_s losses were calculated for operating points of 0.8 V and 0.7 V and temperatures between 600 and 750^oC. These calculations may allow an electrolyte thickness that minimizes the voltage losses to be chosen for each operating point and electrolyte microstructure.

6.5 Acknowledgements

The authors gratefully acknowledge financial support from the Natural Sciences and Engineering Research Council of Canada, Northwest Mettech Corporation, and the BC Innovation Council, the Flexitallic Group for providing seal samples, and the helpful assistance of Craig Metcalfe, Joel Kuhn, and Michael Poon.

6.6 References

1. Z.G. Yang, International Materials Reviews, 53(1) (2008), 39–54.
2. M.J. Verkerk, A.J.A. Winnubst, A.J. Burggraaf, Journal of Materials Science, 17(11) (1982), 3113-3122.
3. X. Zhang, C. Deces-Petit, S. Yick, M. Robertson, O. Kesler, R. Maric, D. Ghosh, Journal of Power Sources, 162(1) (2006), 480–485.
4. J.M. Vohs, R.J. Gorte, Advanced Materials, 21(9) (2009), 943-956.
5. D. Gallagher, Master of Engineering Project Report, University of Toronto, Toronto, ON, Canada, 2009.
6. Department of Energy - Fossil Energy: DOE's Fuel Cell R&D Program. Retrieved May 1, 2010, from http://www.fossil.energy.gov/programs/powersystems/fuelcells.
7. D. Waldbillig, O. Kesler, Journal of the American Ceramic Society, to be submitted.
8. B.D. White, O. Kesler, L. Rose, Journal of Power Sources, 178(1) (2008), 334-343.
9. J. Harris, O. Kesler, Journal of Thermal Spray Technology, 19(1-2) (2010), 328-335.
10. N. Benoved, O. Kesler, Journal of Power Sources, 193(2) (2009), 454-461.
11. D. Waldbillig, O. Kesler, Journal of Power Sources, 191(2) (2009), 320-329.
12. I.R. Gibson, G.P. Dransfield, J.T.S. Irvine, Journal of Materials Science 33(17) (1998), 4297-4305.
13. A.C. Fox, T.W. Clyne, Surface & Coatings Technology, 184(2-3) (2004), 311-321.
14. Aremco: High Temperature Adhesives, Ceramics, Potting Compounds, Sealants, Screen Printers, Dicing Saws, Furnaces. Retrieved May 1, 2010, from http://www.aremco.com/a2.html.
15. M. Lang, T. Franco, G. Schiller, N. Wagner, Journal of Applied Electrochemistry, 32 (2002), 871.
16. R. Hui, J. Oberste Berghaus, C. Decès-Petit, W. Qu, S. Yick, J.G. Legoux, C. Moreau, Journal of Power Sources, 191(2) (2009), 371–376.
17. A. Weber and E. Ivers-Tiffee, Journal of Power Sources, 127(1-2) (2004), 273-283.

7 Conclusions

The research in this thesis can be broadly separated into three main areas of study: suspension development, which is covered in chapters 2 and 3, spraying parameter studies, which are detailed in chapters 4 and 5, and electrochemical testing, which is presented in chapters 4 and 6.

7.1 Suspension characterization studies

The purpose of these studies was to characterize the properties of the input suspensions in order to determine the effect of suspending liquid, solid content, and pH on the particle dispersion and to determine whether particle dispersion can be improved by dispersant additions. Well-dispersed particles in the suspension are very important to enable the formation of the uniform suspension droplets that are required to produce high quality coatings and facilitate suspension feeding processes.

The viscosity study detailed in chapter 2 examined the viscosity of YSZ suspension at various solid contents and investigated the effect of three dispersants on the viscosity of a high solid content (20 vol%) aqueous YSZ suspension. The viscosity of the suspensions with various dispersant contents was measured and an optimal dispersant content at which the suspension viscosity was minimized was determined for each dispersant type.

Coatings were produced from 5 vol% YSZ suspensions containing the optimal dispersant concentration, and microstructural studies of the deposited layers detailed the effect of the dispersants on the coating thicknesses and microstructures. It was observed that suspensions with PBTCA produced thicker coatings; therefore, this dispersant was chosen for the subsequent spraying parameter studies.

The spraying section of this study was performed using the second generation pressurized canister suspension delivery system, and YSZ layers were deposited on cathode layers that had been previously deposited on stainless steel substrates. This commonality allows these spraying results to be compared to subsequent spraying studies. Although coating thicknesses were measured in this study, the coating weight increase after spraying was not

measured, which made it impossible to determine the coating density, an important parameter measured in later studies.

The viscosity measurements in chapters 2 used a Thermo Haake VT550 viscometer in the coaxial cylinder configuration. This viscometer gave excellent reproducible results at suspension viscosities greater than ~20 mPas, but the instrument was less precise at lower viscosities. In order to enhance confidence in the viscosity studies, measurements were repeated in chapter 3 using a sine-wave vibro viscometer that had a greater precision at low viscosities. In addition, optimal dispersant content measurements were repeated for a wider level of dispersant additions. The new measurements observed similar optimum PAA and PBTCA contents, but showed a larger stability range and slightly lower viscosities at higher PEI contents compared to previous studies.

The study detailed in chapter 3 also examined some of the more fundamental properties of the YSZ suspensions, investigating the suspension native pH, ion dissolution behaviour, and zeta potential and isoelectric point. Zeta potential measurements were performed using both electrophoretic and electroacoustic methods, and the results were compared. Electrophoretic measurements can only be done at very low solid contents, and thus give a more fundamental understanding of the zeta potential behaviour without particle-particle interactions, while electroacoustic measurements can be used for concentrated suspensions and thus may give a better understanding of the stability of the suspensions at the solid contents used during the spraying studies. Although the zeta potential and isoelectric point values differed for the two zeta potential measurement techniques, similar trends were observed.

Finally, the effect of dispersants on the particle size distribution present in the suspension and on zeta potential behaviour was evaluated and was used to confirm the optimum dispersant concentrations determined from rheometry.

The fundamental understanding of the suspension behaviour developed during the suspension development study allowed a well characterized, aqueous YSZ suspension that

contained well dispersed particles aided by the presence of a polyelectrolyte dispersant to be produced. This suspension was used as the feedstock for the PS studies.

7.2 Spraying studies

The primary aim of the spraying studies was to improve the understanding of the relationships between substrate, feedstock, and plasma spraying parameters and the resulting coating characteristics such as microstructure, density, permeability, and deposition efficiency.

The investigations reported in chapter 4 examined the effect of substrate type and detailed the first spraying parameter studies performed in the thesis work. Previously reported studies used identical spraying conditions in order to investigate the effect of substrate, cathode and suspension parameters on the deposited electrolyte layers while keeping PS parameters constant.

The substrate characterization studies focused on MG 2 and MG 5 substrates and compared the microstructures and surface roughness of these two substrates with other substrate grades that were determined to have either too-coarse microstructures (MG 40) or too-fine porosity (MG 0.5). The study also identified some of the defects commonly seen in the SPS electrolyte layers and suggested root causes of each defect type. Large continuity defects in the electrolyte layer due to the inability of cathode layers to fully bridge the larger surface pores were observed for layers deposited on the larger MG 5 substrates, but these defects did not appear to have a significant effect on cell open circuit voltages, likely due to the frequency of other defects.

The spraying studies described in chapter 4 investigated the effect of the number of deposition passes, substrate preheat temperature, and stand-off distance on the relative deposition efficiency (i.e. electrolyte thickness) and permeation rate. For this study, the deposition efficiency is a relative measurement comparing the measured electrolyte thicknesses for coatings that were sprayed for a similar number of passes but had other parameters varied. This value cannot be compared to subsequent spraying studies in which

deposition efficiency values compared the weight of YSZ delivered to the weight of the YSZ coating deposited on the substrate surface. It was found that as the number of deposition passes increased, the electrolyte thickness increased and the permeation rate decreased. However, the permeability of the coatings increased as the coating thickness increased, which may suggest that the porosity of subsequently deposited coating layers was higher than the porosity of the initial layers in the coatings, or that thicker layers are more likely to have vertical cracks that increase permeation rates. Preheat temperatures appeared to have no effect on coating deposition efficiency, but preheating substrates to temperatures of 325 or 450^{o}C produced coatings that had microstructures with fewer pores and lower permeation rates compared to those that were not preheated. Stand-off distance appeared to have little effect on the deposition efficiency for the conditions examined, but coatings produced at 80 mm stand-off distance were less porous than the other coatings and had lower permeation rates.

The research in chapter 5 continued the initial spray parameter studies begun in chapter 4 and broadly investigated the effects of nozzle size, plasma gas flow rate, and plasma power on coating and process properties such as coating density, deposition efficiency, and permeation rate. The studies observed that high velocity conditions created by small nozzles or high plasma gas flow rates produced coatings with high densities and low permeation rates; however, these conditions may result in lower deposition efficiencies. Five specific spraying conditions were chosen from the range of conditions investigated for further microstructural investigations and the feasibility of the coatings produced from these conditions to serve as SOFC electrolytes was evaluated. Permeation rates measured in this study are comparable to those in previous studies; however this study introduced new measurements of layer density and deposition efficiency, which are not comparable to previous studies.

Chapter 5 also developed a simple thermodynamic analysis that compared the power requirements of SPS to those of conventional atmospheric plasma spraying processes with dry powder feedstock. The study showed that SPS coatings require significantly greater amounts of plasma energy to fully treat the feedstock suspensions.

The spraying studies performed in this work developed an understanding of the effect of substrate and cathode properties and plasma spraying parameters on the microstructure, density, permeation rate, and deposition efficiency of aqueous SPS YSZ layers. The studies also identified some of the defect types commonly found within the coatings. The thorough understanding of the substrate, suspension, and PS processing effects on the resulting coating properties allowed several spraying conditions to be developed that produced SPS YSZ coatings that had a potentially desirable combination of the properties required for SOFC electrolyte layers. These SPS electrolyte layers were electrochemically characterized in the subsequent sections of the thesis.

7.3 Electrochemical studies

Using the understanding of the processing – property relationships developed in the coating development studies, plasma sprayed full cells (cathode, electrolyte and anode) were produced for electrochemical testing in order to determine the property-performance relationships of the electrolyte coatings. Initial proof-of-concept testing confirmed the ability of PS to produce a working SOFC and subsequent electrochemical testing investigated the effect of electrolyte microstructure and thickness on the open circuit voltage (OCV) and series resistance (R_s) values. In order to better understand the root causes of the various electrolyte losses, the measured total series resistance (R_s) was separated into three parts, which allowed the resistance caused by the microstructural features within the electrolyte layer such as porosity or splat boundaries to be determined. Characterizing the microstructural resistance of the electrolyte layer is very important for plasma spray produced electrolytes in order to determine the effect of the unique PS microstructural features on the electrolyte performance.

Proof-of-concept electrochemical testing of PS SOFCs is reported in chapter 4. In the study, the OCV and peak power density of PS SOFCs produced on MG 2 and MG 5 substrates were compared. During polarization tests, an OCV of ~0.87 and peak power densities between 90 and 100 mW/cm^2 were observed at 750^{o}C with 20% H_2 fuel, and no difference in cell performance was observed between the cells produced on each substrate.

Chapter 6 summarized the detailed electrochemical polarization and impedance studies for PS SOFCs with electrolytes fabricated from one of three promising SPS conditions identified during the plasma spray parameter studies performed in chapter 5. In the study, open circuit voltage (OCV) and series resistance (R_s) values were determined for the three unique electrolyte microstructures and the effect of permeation rate and electrolyte thickness on these values was characterized. Cells were tested at temperatures between 600 and 750^{o}C and at three different nominal electrolyte thicknesses (15 μm, 30 μm and 45 μm).

Open circuit voltage values for the three electrolyte microstructures were very similar for coatings with equivalent permeation rates. Electrolyte R_s values increased as the electrolyte thickness increased and as the temperature decreased. In order to better understand the root causes of the various electrolyte losses, the measured series resistance (R_s) was separated into three parts: R_{YSZ}, R_{μ}, and R_C. R_{YSZ} corresponded to the area specific resistance caused by the limited ionic conductivity of YSZ, R_{μ} was the resistance due to the microstructural features within the electrolyte layer such as porosity or splat boundaries, and R_C was the resistance due to the contact interfaces present between the cell and test station. It was found that the microstructural resistivity of the electrolyte layer decreased by approximately an order of magnitude as the temperature was increased from 600 to 750^{o}C and that the three different electrolyte layer microstructures had different resistivity values, likely due to the differences in microstructural features such as porosity and splat boundaries. The lowest resistance electrolytes had microstructural and material resistivity values lower than 10 Ω cm at 750^{o}C, which will produce electrolyte layers with an area specific resistance of less than 0.1 Ω cm^2 at 750^{o}C for electrolyte thicknesses below 20 μm. This study is to the author's knowledge the first electrochemical study of PS SOFCs that successfully isolated the contributions of plasma sprayed electrolyte layer microstructures from the electrolyte resistance resulting from the bulk material properties.

In order to maximize cell performance, the electrolyte thickness resulting in the lowest voltage losses should be chosen for a given electrolyte microstructure and its corresponding permeability. Therefore, in order to better understand the effect of gas leakage and

electrolyte resistance losses on the cell voltage, the open circuit voltage losses and voltage losses resulting from the series resistance contributions of both the bulk electrolyte material and electrolyte microstructure were calculated for operating points of 0.8 V and 0.7 V, which allowed the relative effect of each loss type to be compared. Generally it can be observed that when contact losses are not considered, the V_{Leak} term contributes between 65 and 99% of the electrolyte-related losses in the test compared to the other electrolyte-related loss types. This indicates that the electrolyte, seal and test station leakages are the primary sources of electrolyte-related losses for these cell tests.

The electrochemical studies in this work demonstrated that metal supported SOFCs can be fabricated using PS processes with electrolytes fabricated from aqueous suspensions, and characterized and separated the various electrochemical losses present in the cells. The electrochemical losses due to the unique microstructural features present in the plasma sprayed electrolyte layer were separated from the other electrolyte losses.

7.4 Project summary

This project developed a thorough understanding of the relationships between the base layers (substrate and cathode), suspension and plasma spraying parameters, and the resulting electrolyte layer properties. Using this understanding, plasma sprayed full cells (cathode, electrolyte and anode) with optimized electrolyte microstructures were produced and electrochemically tested. Calculations based on the electrochemical testing allowed the microstructural resistivity of the SPS electrolyte layers to be separated from the other resistances.

7.5 Project contributions

Seven main contributions to the greater body of knowledge can be identified from this thesis work.

1. Characterization of 8 mol% YSZ aqueous suspensions

    - Most characterization studies have investigated the properties of partially stabilized YSZ (3 mol% yttria). The amount of yttria has a significant effect on the isoelectric point and dissolution behaviour of the YSZ material.

2. Use of atmospheric, axial injection SPS with aqueous suspensions

    - Most suspension plasma spraying research is done either at lowered pressures, with radial injection, or with non aqueous suspensions. The combination of atmospheric conditions, axial injection, and aqueous suspensions presents the best combination of lowered process and material costs, higher deposition efficiencies, and porosity control.

3. Focus on porous substrates and multilayer coatings

    - This study investigated the effect of substrate and electrode layers on the electrolyte layer properties and thus developed an understanding of the plasma sprayed electrolyte properties under realistic fuel cell substrate conditions. Many other plasma sprayed fuel cell studies investigate single layer configurations on polished, dense steel substrates or plasma sprayed electrolyte layers on pre-deposited layers that had been polished to remove surface topography.

4. Investigation of the effect of spray parameters on both coating parameters such as density and process parameters such as deposition efficiency

    - Most studies report density or porosity values for plasma sprayed layers, but very few measure the deposition efficiency of the spray conditions. The best plasma spray conditions to produce SOFC electrolytes must produce layers with high density, but these conditions should also have good deposition efficiencies to make the process economical for large-scale production.

5. Electrochemical testing of multiple electrolyte microstructures and thicknesses

    - Most studies produce a single plasma sprayed electrolyte microstructure and thickness and test this single specimen. In this thesis work, a thorough knowledge

of the relationships between the processing parameter and coating properties was used to produce different electrolyte spraying conditions with different deposition efficiencies and coating densities and microstructures at three electrolyte thicknesses. This allowed the effect of electrolyte microstructure and thickness on the electrochemical behaviour of the electrolytes to be investigated.

6. Series resistance separation to determine plasma sprayed microstructural contributions
    - To the author's knowledge no other study to date has used this method to separate the measured series resistance values into their constituent components and thus allow the contributions of the plasma sprayed microstructures to electrolyte resistivity to be quantified.
7. ΔV calculations to determine optimum thickness trade-off between OCV and R_s
    - These calculations are not commonly done and allow the relative contributions of leakage and electrolyte resistance to be compared at different operating points. These calculations can then be used to determine the optimum electrolyte thickness for a given microstructure and operating point in order to minimize the total voltage losses caused by the electrolyte layer.

7.6 Significance of PS SOFCs

PS is a rapid, easy to automate deposition process than produces fully sintered thin ceramic layers with no requirements for post-deposition heat treatments. This elimination of high temperature sintering steps allows less expensive and higher performing metallic support layers to be used and expands the potentially usable SOFC materials set by limiting the time that diffusion based inter-reaction can occur. Thus plasma spray manufacturing methods may have the ability to both reduce cell fabrication and material costs and improve cell performance, making them an important step toward successful SOFC commercialization. The work performed in this thesis developed a low porosity SPS SOFC electrolyte layer that has an open circuit voltage less than 10% lower than the theoretical maximum value and low resistivity. This electrolyte layer, when combined with the other optimized PS SOFC

electrode layers, has the potential to be a cost-effective alternative to current state-of-the-art wet-ceramic based SOFC fabrication processes.

7.7 Selected summary of current research in PS and SPS SOFCs

A number of groups are investigating the relationships between PS and SPS parameters and the resulting coating properties for numerous applications, including hydroxyapatite to enhance biocompatibility, TiO_2 for photocatalysts, wear resistant coatings, thermal barrier coatings, and SOFCs. Unfortunately, it is difficult to directly compare the results of many studies due to the large number substrate, feedstock powder, and suspension materials, suspension feeding and injection configurations, and plasma spray torch types used.

The largest centres for PS SOFC development are currently in Germany, France, and Canada, though there are a number of groups working in other countries throughout the world.

DLR, the German aerospace research centre, has been developing vacuum plasma sprayed SOFCs for over 15 years [1]. They have successfully sprayed Ni/YSZ anodes, YSZ and SSZ electrolytes, and LSM cathodes with pore formers, and have optimized layer microstructures [2]. Full cells have been fabricated and have been electrochemically tested [3,4]. They have also focused much effort on the development of porous metallic supports and have tested cells deposited on Ni, ferritic stainless steel, and Cr based alloy felts, foams, and knitted wires [5]. Current efforts focus on scaling up cell areas from 100 cm^2 (10x10cm) to 400 cm^2 (20x20cm) and stack development. All cell fabrication efforts to date have focused on vacuum plasma spraying. Figures 7.1 and 7.2 show a DLR metal supported VPS SOFC and polarization curves for the cell at temperatures between 750 and 900^oC [6].

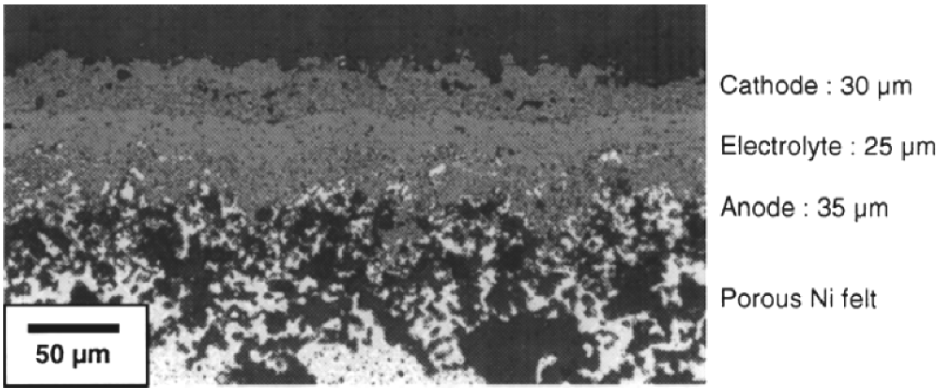

Figure 7.1: VPS metal supported SOFC fabricated by DLR[33] [6].

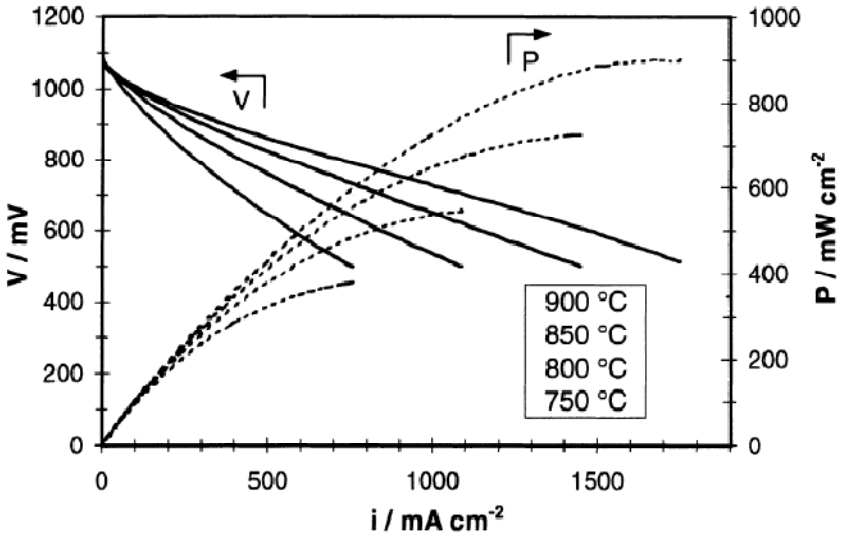

Figure 7.2: Polarization curve for a metal supported VPS SOFC[34] [6].

[33] With kind permission from Springer Science+Business Media: Journal of Applied Electrochemistry, Electrochemical characterization of vacuum plasma sprayed thin-film solid oxide fuel cells (SOFC) for reduced operating temperatures, 32, 2002, 871, M. Lang, T. Franco, G. Schiller, N. Wagner, Figure 2.

[34] With kind permission from Springer Science+Business Media: Journal of Applied Electrochemistry, Electrochemical characterization of vacuum plasma sprayed thin-film solid oxide fuel cells (SOFC) for reduced operating temperatures, 32, 2002, 871, M. Lang, T. Franco, G. Schiller, N. Wagner, Figure 3.

Forschungszentrum Julich has also developed metal supported APS SOFCs and electrochemically characterized the cells. The PS cells had electrolyte thicknesses of approximately 40 μm for cell areas as large as 100 cm^2 and had excellent cell performance at temperatures of 800^oC; however, electrochemical results at lower temperatures were not reported [7].

The University of Limoges has published numerous review papers on topics such as plasma spraying and suspension plasma spraying and has developed an excellent fundamental knowledge of radial injection SPS processes. This group has mainly focused on producing thin, dense YSZ electrolyte layers [8] and porous $LaMnO_3$ cathode layers [9,10] using suspension plasma spraying (SPS) and have done many studies to gain a better understanding of the liquid plasma spraying process [11-14]. However, this group has not produced SOFC layers on porous substrates, has not focused on stacking individual fuel cell layers together to form full cells, and has not performed any electrochemical or permeation testing on the deposited layers to date.

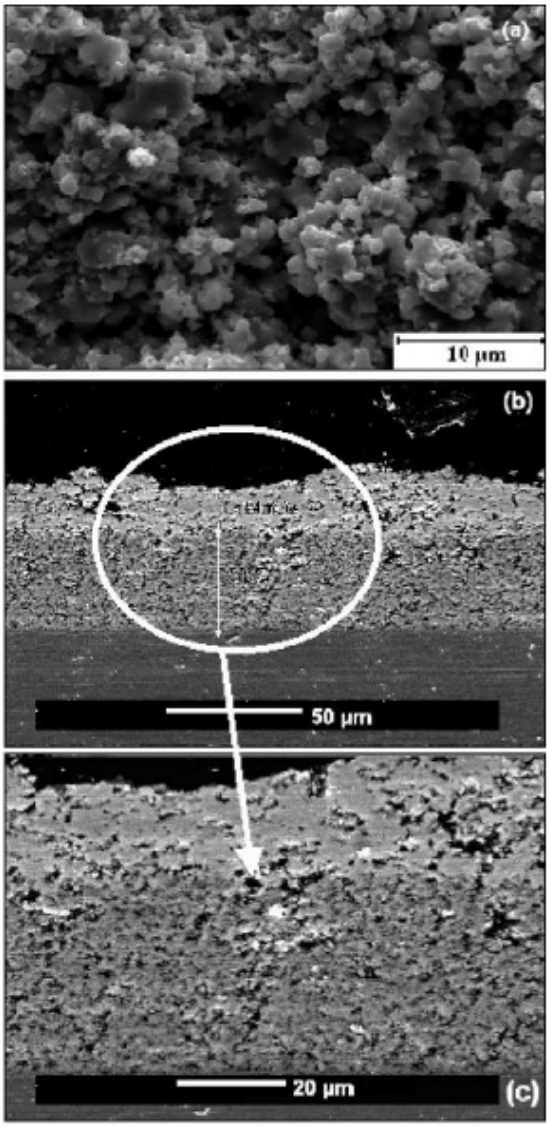

Figure 7.3: a) SEM image of the surface of an SPS deposited $LaMnO_3$ layer, b) low magnification SEM image of an SPS deposited LSM layer on an SPS deposited YSZ layer, c) high magnification SEM image of the layers in b[35] [15].

Other French groups at the University of Technology at Belfort Montbeliard and at the University of Pierre and Marie Curie are also developing SOFC electrolyte layers using radial

[35] Reprinted from Surface and Coatings Technology, 200 / 12-13, C. Monterrubio-Badillo, H. Ageorges, T. Chartier, J.F. Coudert, P. Fauchais, Preparation of LaMnO3 perovskite thin films by suspension plasma spraying for SOFC cathodes, 3743, Copyright (2006), with permission from Elsevier.

injection SPS and SOFC cathode, electrolyte and anode layers using low pressure PS from nitrate solutions, respectively [16,17].

Many other groups throughout the world are investigating PS SOFCs and have produced individual SOFC layers or PS SOFC full cells. A group at the Shanghai Institute of Ceramics has sprayed and electrochemically tested an APS SOFC deposited on a nickel substrate [18]. US Nanocorp and Inframat have fabricated and electrochemically tested an SOFC with a Ni/YSZ anode, an LSGM electrolyte, and an LSM cathode using APS [19]. A group in Taiwan has produced and electrochemically tested PS SOFC with LSGM electrolyte layers [20].

Within Canada, most PS SOFC work occurs at the University of Sherbrooke, at the National Research Council's Industrial Materials Institute (NRC IMI), and at the University of British Columbia and the University of Toronto. The University of Sherbrooke has produced thin, dense ceria coatings both from suspensions [21] and by liquid precursor spraying [22] using a low pressure plasma spray system. The work at NRC-IMI is most similar to the research presented in this thesis and used axial injection SPS to deposit many different types of materials including YSZ and SDC, and have produced thin (~40 micrometres), dense YSZ and SDC layers using APS, SPS, and HVOF systems [23,24]; however, the IMI studies do not use aqueous suspensions. Recently, button cell and 5 cm x 5 cm metal supported SOFCs with PS anodes, HVOF electrolyte layers, and screen printed cathode layers were electrochemically tested and were found to have good performance [25].

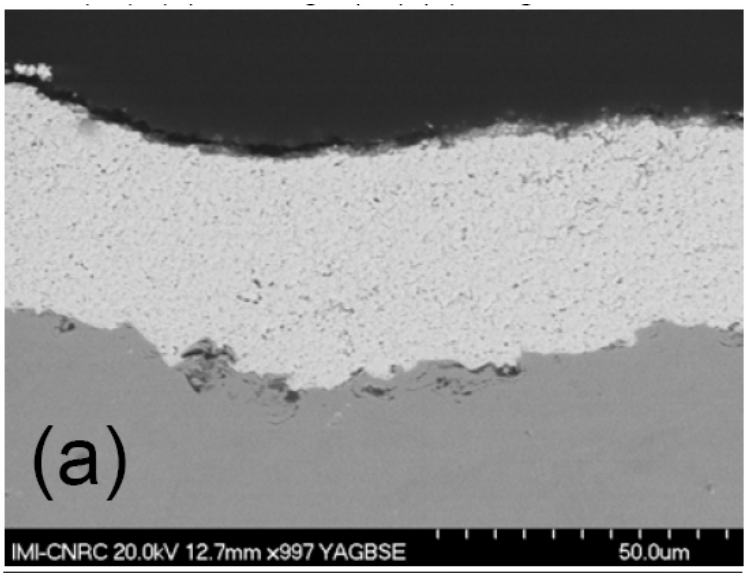

Figure 7.4: Cross-sectional SEM image of an SPS deposited CeO_2 layer[36] [24].

7.8 Future work

There are always areas of a project that could be explored further if time and budget permit. This section lists a few additional studies that might of interest. These spraying studies used a very simple robot arm that only moved in the vertical direction and produced relative horizontal motion by rotating the sample holder. It would be of great interest to use the spraying conditions developed during this study with a modern 6 axis robot setup. During spraying, the substrate was preheated by the plasma torch, but the sample temperature was not controlled afterward, and frequently the substrate temperature would exceed 700^{o}C during electrolyte spraying runs. It would be interesting to investigate the effect of active substrate temperature control on electrolyte coating quality. All spraying studies in this work were done on 2.54 cm diameter button cells, but practical fuel cell systems will require much larger cells; therefore, it would be interesting to scale up the cell size to 5 cm x 5 cm square substrates to examine the challenges that larger spraying

[36] Reprinted with permission of ASM International.

areas impart. Further spray parameter studies will also be interesting. Of most interest would be studies of conditions that might reduce the prevalence of defects seen in the YSZ layers, especially the vertical cracks, and of conditions that may provide higher deposition efficiencies. This work only looked at one feedstock particle size. It might be interesting to examine the effects of other sizes of feedstock particles on the coating properties. The heat transfer ability of the plasma to the feedstock will likely be significantly affected by the droplet size and distribution; therefore, it could be interesting to investigate the effects of injection and atomization parameters and the effect of different atomizing nozzle configurations. Finally, it would be of interest to better characterize the droplet size and the particle temperature and velocity using commercially available characterization equipment such as Tecnar's Accuraspray [26].

7.9 References

1. M. Lang, T. Franco, R. Henne, P. Metzger, G. Schiller, S. Ziehm, pp. 1059 in proceedings of SOFC VIII, Edited by S.C. Singhal and M. Dokiya, The Electrochemical Society Proceedings Series. Paris, France, 2003.
2. G. Schiller, R. Henne, M. Lang, M. Muller, Materials Science Forum, 426-432 (2003), 2359.
3. M. Lang, R. Henne, S. Schaper, G. Schiller, Journal of Thermal Spray Technology, 10 (2000), 618.
4. G. Schiller, R. Henne, M. Lang, R. Ruckdaschel, S. Schaper, Fuel Cells Bulletin, 21 (2000), 7.
5. T. Franco, R. Henne, M. Lang, P. Metzher, G. Schiller, P. Szabo, S. Ziehm, pp. 923 in proceedings of SOFC VIII, Edited by S.C. Singhal and M. Dokiya, The Electrochemical Society Proceedings Series. Paris, France, 2003.
6. M. Lang, T. Franco, G. Schiller, N. Wagner, Journal of Applied Electrochemistry, 32 (2002), 871.
7. D. Stöver, D. Hathiramani, R. Vassen, R.J. Damani, Surface & Coatings Technology, 201 (2006), 2002–2005.
8. C. Delbos, J. Fazilleau, J.F. Coudert, P. Fauchais, L. Bianchi, K. Wittmann-Teneze, pp. 661-669 in Proceedings of Thermal Spray 2003: Advancing the Science and Applying the Technology, Edited by B.R. Marple and C. Moreau, ASM International. Orlando, FL, USA, 2003.
9. C. Monterrubio-Badillo, H. Ageorges, T. Chartier, J.F. Coudert, P. Fauchais, pp. 687 in Proceedings of Thermal Spray 2003: Advancing the Science and Applying the Technology, Edited by B.R. Marple and C. Moreau, ASM International. Orlando, FL, USA, 2003.
10. C. Monterrubio-Badillo, H. Ageorges, T. Chartier, J.F. Coudert, P. Fauchais, pp. 562 in the Proceedings of the 2004 International Thermal Spray Conference (ITSC).
11. C. Delbos, J. Fazilleau, V. Rat, J.F. Coudert, P. Fauchais, L. Bianchi, pp. 534 in the Proceedings of the 2004 International Thermal Spray Conference (ITSC).

12. C. Delbos, V. Rat, C. Bonhomme, J. Fazilleau, J.F. Coudert, P. Fauchais, High Technology Plasma Processes, 8 (2004), 397.
13. P. Fauchais, V. Rat, C. Delbos, J.F. Coudert, T. Chartier, L. Bianchi, IEEE Transactions on Plasma Science, 33(2) (2005).
14. J. Fazilleau, C. Delbos, M. Violier, J.F. Coudert, P. Fauchais, L. Bianchi, K. Wittmann-Teneze in the Proceedings of Thermal Spray 2003: Advancing the Science and Applying the Technology, 889.
15. C. Monterrubio-Badillo, H. Ageorges, T. Chartier, J.F. Coudert, P. Fauchais, Surface & Coatings Technology, 200 (2006), 3743.
16. C. Zhang, A.F. Kanta, C.X. Li, C.J. Li, M.P. Planche, H. Liao, C. Coddet, Surface & Coatings Technology 204 (2009) 463–469.
17. F. Rousseau, S. Awamat, M. Nikravech, D. Morvan, J. Amouroux, Surface & Coatings Technology, 202 (2007) 1226–1230.
18. R. Zheng, X.M. Zhou, S.R. Wang, T.L. Wen, C.X. Ding, Journal of Power Sources, 140 (2005), 217.
19. X.Q. Ma, H. Zhang, J. Dai, J. Roth, R. Hui, T.D. Xiao, D.E. Reisner, Journal of Thermal Spray Technology, 14(1) (2005), 61.
20. C.H. Lo, C.H. Tsai, C. Hwang, International Journal of Applied Ceramic Technology, 6 (4) (2009), 513-524.
21. M. Bonneau, F. Gitzhofer, M. Boulos, pp. 929-934 in Proceedings of the International Thermal Spray Conference (ITSC). Montreal, Canada, 2000.
22. J. Lu, C. Dossou-Yovo, C. Gahlert, F. Gitzhofer, pp. 85 in the Proceedings of the International Thermal Spray Conference (ITSC). Osaka, Japan, 2004.
23. J. Oberste Berghaus, S. Bouaricha, J.G. Legoux, C. Moreau, pp. 1434-1440 in Proceedings of International Thermal Spray Conference (ITSC), Edited by E. F. Lugscheider, German Welding Society. Basel, Switzerland, 2005.
24. S. Bouaricha, J. Oberste-Berghaus, J.G. Legoux, D. Ghosh, C. Moreau in Proceedings of the International Thermal Spray Conference (ITSC). German Welding Society. Basel Switzerland, 2005.

25. R. Hui, J. Oberste Berghaus, C. Decès-Petit, W. Qu, S. Yick, J.G. Legoux, C. Moreau, Journal of Power Sources, 191(2) (2009), 371–376.
26. Tecnar. Retrieved May 1, 2010, from http://www.tecnar.com/

Appendices

A Suspension plasma spraying of solid oxide fuel cell electrolytes[37,38]

A.1 Introduction

Fuel cells are a clean, efficient, energy generation technology that produces electricity by the direct electrochemical combination of a fuel with an oxidant. This direct production of electricity effectively bypasses the conversion of the fuel's chemical energy into thermal and mechanical energy and thus allows higher theoretical efficiencies to be achieved, compared to combustion-based processes for electricity production.

Solid oxide fuel cells (SOFCs) are a type of fuel cell that uses a solid, ionically conducting ceramic oxide as an electrolyte. Electrolyte layers have two main requirements: high ionic conductivity to minimize resistive losses and high density to prevent the mixing of anode and cathode gases. The most commonly used SOFC electrolyte material is yttria (Y_2O_3) stabilized zirconia (ZrO_2), (YSZ).

Typical SOFCs are fabricated using wet ceramic cell fabrication methods such as tape casting and screen printing followed by a number of high temperature (up to 1400°C) firing steps [1]. These high temperature firing steps lower cell production rates, increase production costs, and limit the materials that can be used due to incompatibilities with either the maximum sintering temperature (e.g. CuO melts at temperatures less than 1400°C) or with other cell components at high temperatures (e.g. many perovskite materials react with YSZ at temperatures above 1000 to 1200°C) [2]. Eliminating the requirement for a high temperature firing step by developing a new cell fabrication method

---

[37] A version of this chapter has been published. D. Waldbillig, O. Kesler, Z. Tang, A. Burgess, pp. 677-682 in Proceedings of the International Thermal Spray Conference (ITSC), Edited by B. Marple, M. Hyland , Y.C. Lau, C. J. Li, R. Lima, and G. Montavon. ASM International. Beijing, China, 2007.

[38] Reprinted with permission of ASM International.

such as plasma spraying would remove these limitations and thus could significantly improve both cell production rates and performance.

Plasma spraying is a thermal spraying method in which finely divided materials are deposited in a molten or semi-molten state. The thermal source used is a plasma which may reach temperatures up to 10000 K. In typical plasma spraying configurations, powdered materials are injected radially or axially into the plasma flame using a carrier gas, which accelerates and melts the particles. The particles impact onto a substrate, where they flatten and rapidly cool to form solid “splats”. A coating is built up by the layering of subsequent splats.

One of the biggest drivers to develop plasma sprayed SOFCs is to increase cell production rates and the process manufacturability. SOFCs can be fabricated by plasma spraying in one deposition step by changing the feedstock materials, or in three steps, where the anode, electrolyte, and cathode are deposited by dedicated plasma spray torches. Either of these processes would be extremely easy to automate and very fast, due to the inherently fast deposition rates for plasma spraying.

Plasma spray fabrication of SOFCs also would eliminate the costly and time consuming high temperature firing steps. Typically, cells are fired multiple times at temperatures between 1200 and 1400°C to sinter deposited layers, and may require up to 24 hours for each firing due to organic burnout steps and to prevent thermal shock. These firing steps are frequently the bottleneck in the entire process, resulting in the need for additional sintering furnaces in order to scale up the production of the cells. The elimination of the high temperature firing steps will also significantly expand the range of materials that can be used for SOFCs, which will enable more cost effective and higher performing materials to be used.

Plasma spray processing for SOFC fabrication has many advantages; however, there are still a number of technical challenges that need to be overcome.

Plasma spraying typically produces microstructures composed of in-plane splats with porosity between 5 and 15% [3]. This range is too porous for dense electrolytes and not

porous enough for electrodes. This means that significant modifications to plasma spray conditions already developed for other applications must be made in order to deposit SOFC layers with sufficient porosity or density.

Spraying the composite structures required for high performing SOFC electrodes may also be very challenging. Optimal spray conditions must be developed for components that may have more than a 1000°C difference in melting temperatures, or that may be unstable in some spraying conditions. For example, plasma gases containing H_2 may decompose LSM during deposition [4]. It is therefore challenging to find compromise spray conditions that sufficiently melt stable ceramics such as YSZ, but do not over melt or decompose less stable materials such as LSM or CuO.

Traditional plasma spray system configurations use powders typically between 25 and 150 µm in diameter, which are delivered by a carrier gas. This results in a somewhat coarse microstructure of laminae of flattened splats and interlaminar pores. Unfortunately, the microstructures produced by traditional plasma spraying methods are too coarse to make thin (<10µm), dense SOFC electrolytes. Therefore, finer feedstock materials are required in order to fabricate plasma sprayed SOFCs with sufficiently thin and dense electrolytes to provide both high ionic conductance and low gas permeability. This is a non-trivial challenge, as particles smaller than approximately 10 – 25 µm often require carrier gas flow rates so large that they significantly perturb the plasma jet in traditional radial injection plasma torches [5]. In order to address these issues, the feedstock supply system can be modified to allow liquid delivery. This allows nanoparticles to be suspended in a carrier liquid such as water or ethanol and sprayed directly. Suspension spraying has been used successfully to produce fine microstructured layers for SOFCs; however, significant modifications to the plasma spray system are required, and significant work is involved to optimize the suspension by choosing the best suspending liquid, solid concentration, and dispersant.

A number of groups have been working to overcome these challenges [6, 7, 8], but much work remains to be done to produce optimized SOFC microstructures in order to improve fuel cell performance.

This paper presents the initial results of a study that aims to produce thin, dense YSZ coatings that could be used as SOFC electrolytes by using an atmospheric plasma torch with axially injected aqueous suspension feedstock materials. The goal of the work presented here is to gain an improved understanding of the effects of different suspension liquids and solid loadings on the viscosity of the suspension feedstocks and on the microstructure and deposition efficiency of the resulting coatings.

A.2 Experimental procedure

This study used an Axial III Series 600 Torch (Northwest Mettech Corp., North Vancouver, BC, Canada) atmospheric plasma spray system. This torch injects powder axially between 3 electrodes, which ensures that virtually all of the powder injected passes through the hottest part of the jet.

8 mol% yttria-stabilized zirconia (YSZ) powder (Inframat Advanced Materials, Farmington, CT., USA) was used as the feedstock material. The as-received powder had a d_{50} agglomerate size (on a volume basis) of approximately 1.5 µm, with sizes ranging from 0.5 µm to 15 µm, as determined by laser light scattering (Mastersizer 2000, Malvern Instruments, Worcestershire, UK). An SEM image of the feedstock powder is shown in Figure A.1.

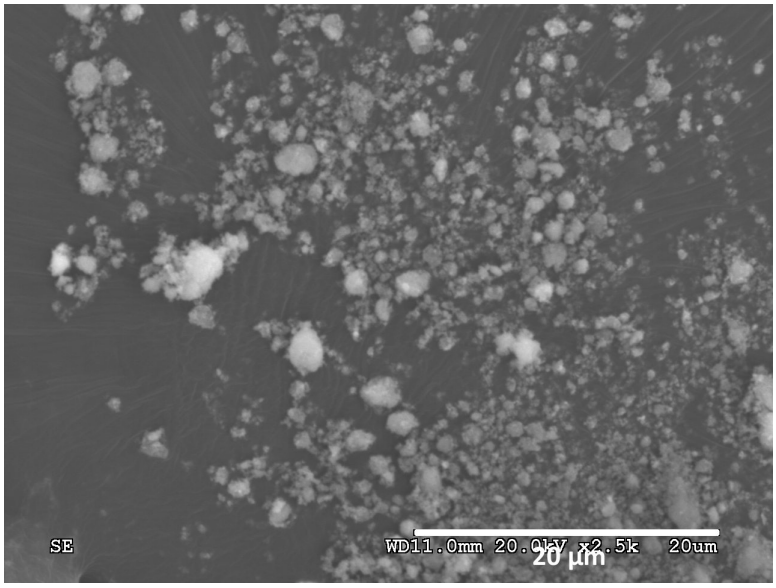

Figure A.1: SEM image of the feedstock YSZ powder.

Aqueous YSZ suspensions with varying solids loadings were prepared and the suspension viscosity was measured using a Thermo Haake VT550 viscometer (Thermo Electron Corporation, Karlsruhe, Germany).

The plasma spraying system was modified to add a pump to deliver the suspension feedstock to the feed tube of the plasma torch [9]. A two-fluid atomizing nozzle was used in order to produce small suspension droplets which were directly injected into the centre of the plasma jet.

Deposition was carried out onto tape cast and fired NiO/YSZ ceramic substrates mounted onto a rotating turntable. The substrates had a composition and microstructure similar to that of SOFC anode layers. Fracture cross sections of the deposited layers were examined in a Hitachi S-3000N scanning electron microscope (SEM) (Hitachi High Technologies America, Pleasanton, CA., USA).

A.3 Results and discussion

A.3.1 Suspension viscosity measurements

The viscosities of aqueous and ethanol based YSZ suspensions with a variety of solids loadings were measured and are shown in Figure A.2. It can be seen that the viscosity increases significantly as the solids content increases.

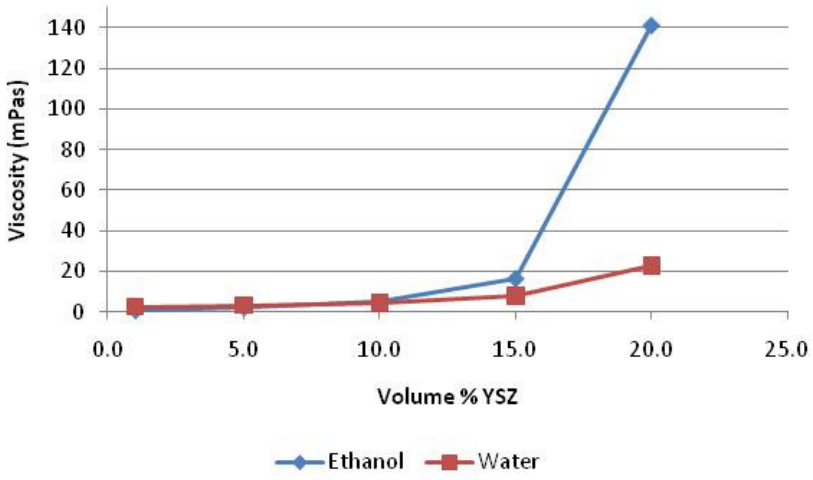

Figure A.2: Viscosity measurements of YSZ suspensions.

Based on the viscosity measurements, aqueous suspensions with three different solid loadings were identified as being potentially easiest to feed to the plasma torch, and were therefore chosen for further studies of coating properties and deposition efficiency. One ethanol based suspension was also chosen in order to examine the effect of solvent liquid on the coating deposition process. The suspension parameters are summarized in Table A.1.

Table A.1: Summary of suspension parameters.

Solvent	Solids loading (volume %)	Solids loading (weight %)	Viscosity (mPa s)
Water	1.0	5.3	2.6
Water	5.0	22.7	3.2
Water	10.0	38.3	4.4
Ethanol	1.0	6.7	1.0

A.3.2 Suspension flow rate measurements

In order to determine the amount of suspension dispensed during a spraying run, suspension flow rates were directly measured by observing the amount of time required to pump a specific volume of suspension at a constant pump setting and atomizing gas flow rate. These measurements are summarized in Table A.2. It can be seen that higher solid loadings significantly lower the suspension flow rate for constant values of pump speed and atomizer gas flow rate.

Table A.2: Summary of suspension flow rate measurements.

Suspension solid loading	Suspension volumetric flow rate (mL/min)	Solids volumetric flow rate (mL/min)	Solids mass flow rate (g/min)
1 vol% YSZ	30.4	0.30	1.70
5 vol% YSZ	27.0	1.35	7.55
10 vol% YSZ	16.9	1.69	9.44

A.3.3 Suspension plasma spraying

Suspensions with 1, 5, and 10 vol% solid loadings were plasma sprayed under identical conditions in order to determine the effect of solid loadings on coating thickness and density. Plasma spraying parameters are summarized in Table A.3 below.

Table A.3: Plasma spraying parameter values.

Parameter	Value
Plasma gas flow rate (slpm)	150
Plasma gas composition	100% N_2
Torch current (A per electrode)	250
Nozzle size (inch)	0.5
Standoff distance (mm)	80

After the spraying runs were complete, coatings produced from aqueous suspensions appeared white and homogeneous, while the ethanol based suspensions clogged the atomizer nozzle, resulting in little YSZ deposition at the spray conditions tested. This result may indicate that atomizer nozzle modifications or less energetic plasma conditions are required in order to spray ethanol based suspensions.

A.3.4 SEM of plasma sprayed coatings

Cross sections of the deposited coatings were examined in the SEM. Samples were fractured and then gold coated in order to provide sufficient sample conductivity. SEM images of fractured cross sections of the deposited coatings are shown in Figures A.3 to A.8.

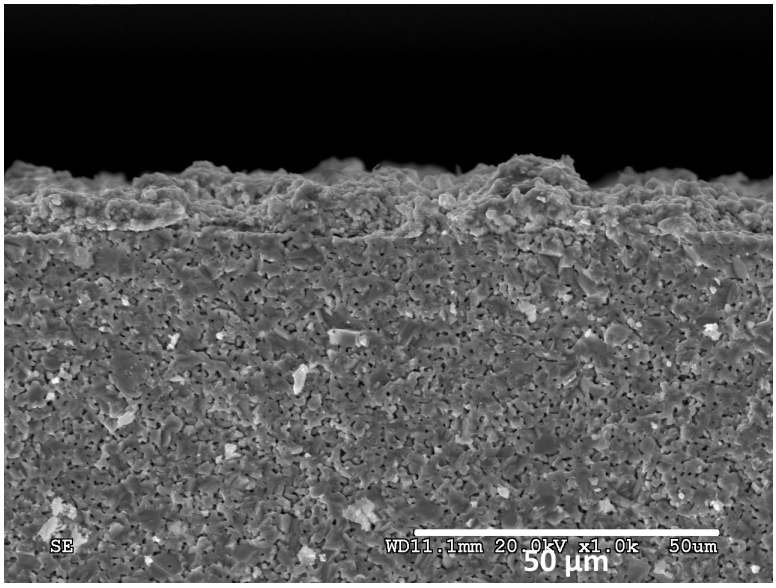

Figure A.3: Low magnification SEM image of the coating produced from the 1 vol% YSZ suspension.

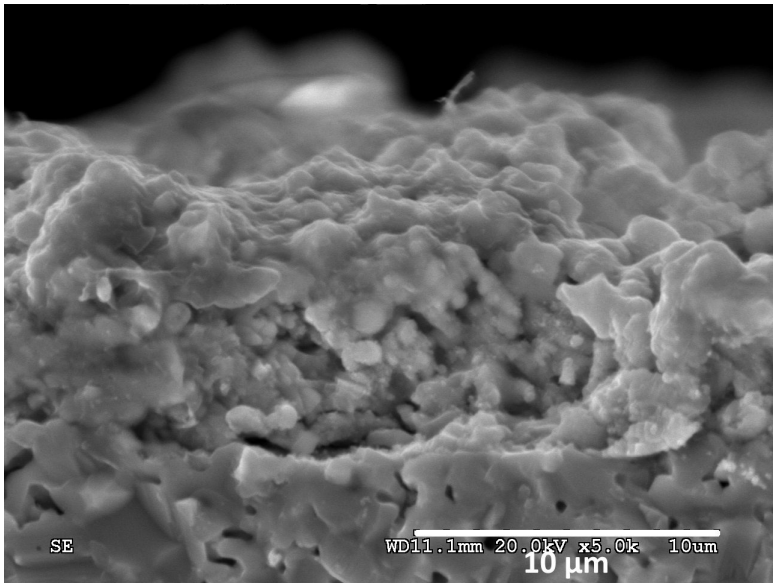

Figure A.4: Higher magnification SEM image of the coating produced from the 1 vol% YSZ suspension.

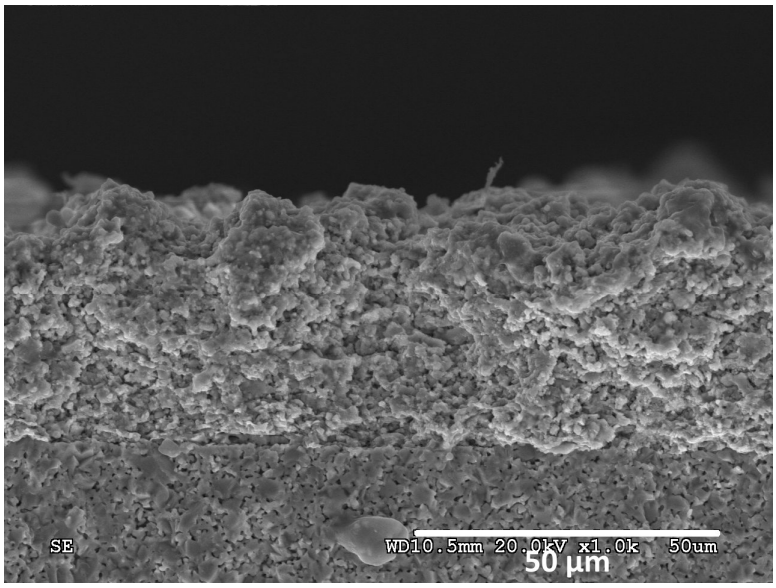

Figure A.5: Low magnification SEM image of the coating produced from the 5 vol% YSZ suspension.

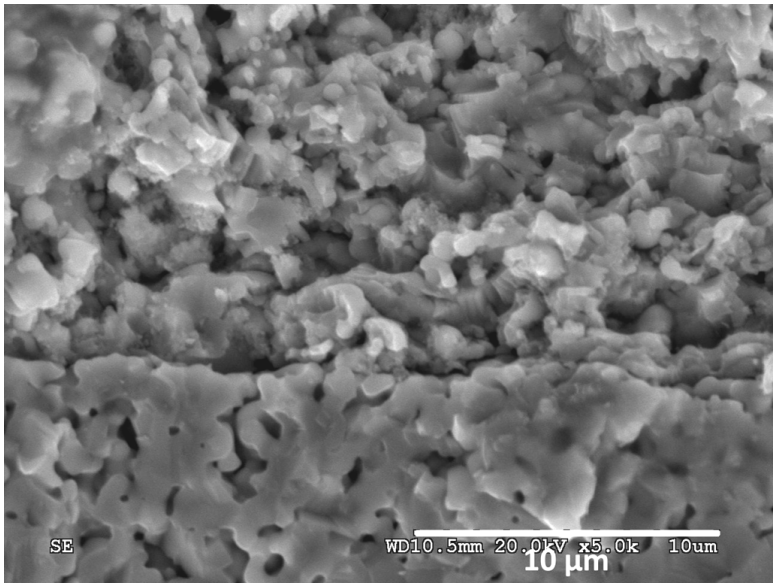

Figure A.6: Higher magnification SEM image of the coating produced from the 5 vol% YSZ suspension.

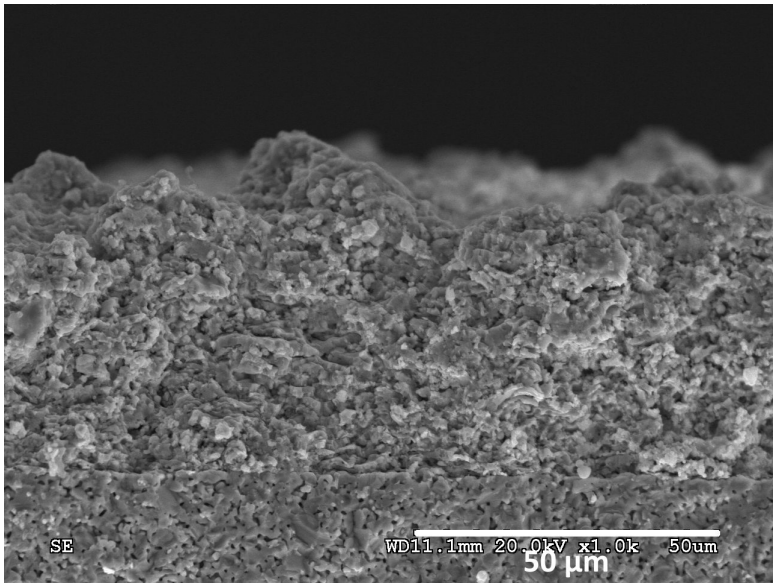

Figure A.7: Low magnification SEM image of the coating produced from the 10 vol% YSZ suspension.

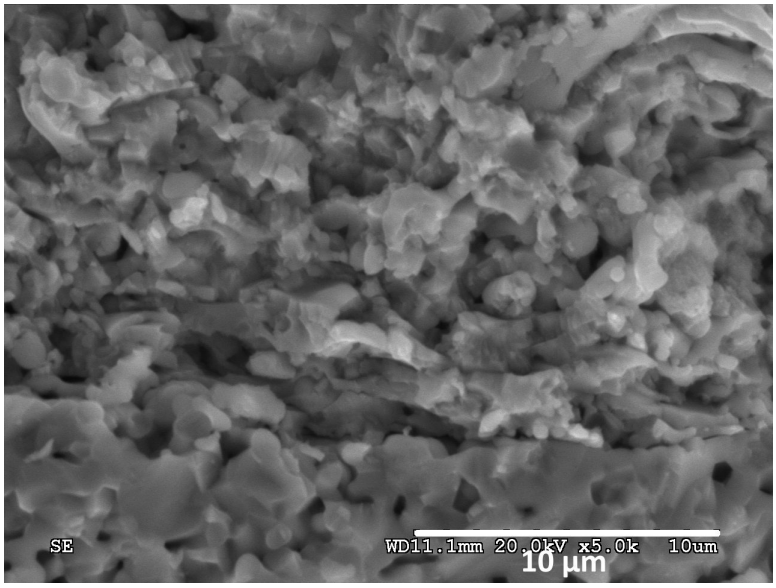

Figure A.8: Higher magnification SEM image of the coating produced from the 10 vol% YSZ suspension.

In the figures above, it can be seen that continuous coatings have been deposited and appear to be built up of splats approximately 0.5 µm thick with some intersplat porosity. The coating produced from the 1 vol% YSZ suspension (Figure A.4) appears to be somewhat

denser than the higher solid loading coatings (Figures A.6 and A.8). All coatings appear to be well bonded to the NiO/YSZ ceramic substrates.

Coating thicknesses increased as the suspension solid loadings were increased, as expected. The coating produced from the 1 vol% YSZ suspension is approximately 10 µm thick (Figure A.3), while the coating fabricated from the 5 vol% YSZ suspension measures approximately 40 µm thick (Figure A.5), and the coating made from the 10 vol% YSZ suspension is approximately 45 µm thick (Figure A.7).

A relative deposition efficiency was calculated in order to compare the effect of solid loading on the amount of YSZ deposited for the fixed spraying conditions used. A deposition efficiency of 90% was calculated for the suspension containing 5 vol% YSZ, while an 81% deposition efficiency was calculated for the suspension with a solids loading of 10 vol%, relative to the deposition efficiency of the suspension with 1 vol% YSZ content. This may indicate that increased suspension solid loadings serve to lower the coating deposition efficiency, with all other factors being equal.

For the conditions studied, the suspension with the smallest solids loading (1 vol% YSZ) exhibits both the highest density and deposition efficiency (DE). However, a trade-off exists between these desirable properties and the slower processing time, since slower processes require more equipment as quantities are scaled up to large-scale production. Therefore, it may be desirable to adjust the plasma spraying conditions to increase the plasma enthalpy in order to partially compensate for the difference in porosities and deposition efficiencies by allowing a higher degree of melting in the suspensions with higher solids loadings.

A.4 Conclusions

Plasma spray processing has the potential to be a rapid and cost effective method to fabricate SOFCs; however, significant modifications to conventional plasma spray processing techniques are required to obtain the desired coating properties. Suspension plasma spraying allows smaller feedstock particles to be used, resulting in electrolyte coatings with fine microstructures and low open porosity.

This study produced YSZ coatings that could be used as SOFC electrolytes from aqueous suspensions using an axial feed atmospheric plasma spray torch. Three different aqueous feedstock suspensions with varying solid contents were sprayed, along with one ethanol-based suspension with low solids loading. The aqueous suspensions resulted in coatings with splat thicknesses of approximately 0.5 μm and some intersplat porosity. The ethanol-based suspension clogged the atomizer nozzle at the spray conditions tested. Total coating thickness increased as the suspension solid content was increased, but suspension flow rates and relative deposition efficiency of the solid decreased.

Future work will investigate the effect of varying a number of plasma spraying parameters such as plasma gas composition and flow rate, arc current, nozzle size, and standoff distance on the deposited coating thicknesses and microstructures. As well, coating porosities will be more quantitatively analyzed through the use of techniques such as image analysis, gas permeability testing, and electrochemical testing.

A.5 Acknowledgements

The authors gratefully acknowledge financial support from the Natural Science and Engineering Research Council of Canada and from Northwest Mettech Corporation, as well as tape-cast substrate preparation by Lars Rose, suspension feed apparatus assembly by Paul Daniel, and assistance from Bradley White with plasma spraying.

A.6 References

1. E. Tang , F. Martell, R. Brulé, K. Marcotte, B. Borglum, pp. 935-943 in Proceedings of SOFC VIII, Edited by S.C. Singhal and M. Dokiya, The Electrochemical Society Proceedings Series. Paris, France, 2003.
2. J.M. Ralph, A.C. Schoeler, M. Krumpelt, Journal of Materials Science, 36(5) (2001), 1161-1172.
3. O. Kesler, Materials Science Forum, 539-543 (2007), 1385-1390.
4. B.D. White, O. Kesler, Advanced Materials Research, 15-17 (2006), 299-304.
5. P. Fauchais, Journal of Physics D: Applied Physics, 37(9) (2007), R86-R108.
6. V. Rat, C. Delbos, C. Bonhomme, J. Fazilleau, J.F. Coudert, P. Fauchais, 8(1) (2004), 95-117.
7. J. Oberste Berghaus, S. Bouaricha, J.G. Legoux, C. Moreau, pp. 1434-1440 in Proceedings of International Thermal Spray Conference (ITSC), Edited by E. F. Lugscheider, German Welding Society. Basel, Switzerland, 2005.
8. C. Delbos, J. Fazilleau, J.F. Coudert, P. Fauchais, L. Bianchi, K. Wittmann-Teneze, pp. 661-669 in Proceedings of Thermal Spray 2003: Advancing the Science and Applying the Technology, Edited by B.R. Marple and C. Moreau, ASM International. Orlando, FL, USA, 2003.
9. P. Daniel, M.Eng. Project Report, University of British Columbia, Vancouver, Canada, 2006.

B Effect of substrate and cathode parameters on the properties of suspension plasma sprayed solid oxide fuel cell electrolytes[39,40]

B.1 Introduction

Solid oxide fuel cells (SOFCs) are clean, efficient energy conversion devices that produce electricity by the direct electrochemical combination of a fuel with an oxidant. SOFCs have a number of advantages over other fuel cell types, including higher efficiencies, greater fuel flexibility, and the ability to use the high quality waste heat for cogeneration.

SOFCs use a solid, ionically conductive ceramic oxide as the electrolyte layer. Electrolyte layers should have high ionic conductivity to minimize resistive losses and low porosity to act as a physical barrier to prevent anode and cathode gases from mixing. The most commonly used SOFC electrolyte material is fully stabilized yttria-stabilized zirconia (YSZ).

Currently, the majority of SOFCs are fabricated using wet ceramic methods such as tape casting and screen printing [1]. Multiple steps are required to deposit each fuel cell layer (anode, electrolyte, cathode, and interconnect) with sintering or co-sintering steps at temperatures up to 1400°C interspersed between deposition operations. Multiple deposition and firing steps are required in order to fully sinter each deposited layer and limit any interreactions that might occur between different cell materials. These firing steps lower production rates, increase manufacturing costs, and limit the types of materials that can be used.

SOFC electrochemically active layers are typically mechanically supported on a thicker substrate layer. Currently, the state-of-the-art support is a Ni/YSZ cermet; however, this cermet is expensive, brittle, and has poor thermal properties. There is a drive to move

---

[39] A version of this chapter has been published. D. Waldbillig, O. Kesler, Z. Tang, A. Burgess, pp. 201-206 in Proceeding of the International Thermal Spray Conference (ITSC), Edited by E. Lugscheider. German Welding Society. Maastricht, the Netherlands, 2008.

[40] Reprinted with permission of ASM International.

towards the use of inexpensive stainless steel mechanical supports which have better thermal, electronic, and mechanical properties than cermet supports. However, use of a metallic support in wet ceramic-processed cells requires sintering to be done in an inert atmosphere and lowers the maximum allowable sintering temperature. These requirements increase sintering costs and make it difficult to fully densify the electrolyte layer. Sintering aids may be used in order to fully densify the electrolyte; however, these materials may have detrimental effects on electrolyte ionic conductivity [2].

Plasma spraying is a well established thermal spray technique that is used commercially to deposit wear resistant or thermal barrier coatings. In plasma spraying, an electric arc is used to ionize a gas in order to produce an energetic plasma. Feedstock particles are injected into the plasma, where they are melted and accelerated to velocities of up to 500 m/s [3]. The molten particles splat onto a substrate and rapidly solidify. A coating is built up by the layering of subsequent splats.

Plasma spray processes can be adapted to rapidly produce the thin ceramic layers required for SOFCs without the need for post-deposition sintering steps. The elimination of the high temperature sintering steps relaxes material restrictions and facilitates the use of metallic substrates [4-6].

Unfortunately, the microstructures produced by traditional plasma spraying methods are too coarse to make thin (<10μm), dense SOFC electrolytes as traditional plasma spray configurations use feedstock powders typically between 25 and 150 μm in diameter. Finer feedstock materials are required in order to fabricate plasma sprayed SOFCs with sufficiently thin and dense electrolytes to provide both high ionic conductance and low gas permeability. In order to address these issues, the feeding system can be modified to allow liquid delivery. This allows smaller particles to be suspended in a carrier liquid such as water or ethanol and the suspensions to be plasma sprayed directly [7-11].

This project investigates the fabrication of thin, dense YSZ coatings that could be used as SOFC electrolytes by using an atmospheric plasma torch with axially injected aqueous suspension feedstock materials. In the present work, the influence of the substrate and

previously-deposited layers on subsequent layer properties was examined by spraying YSZ layers on top of plasma sprayed composite lanthanum strontium manganite (LSM)/YSZ cathode layers that were first deposited on porous ferritic stainless steel substrates. Three-layer half cells consisting of a porous stainless steel substrate, composite cathode, and suspension plasma sprayed electrolyte layer were then characterized.

A systematic study was performed in order to investigate the effect of parameters such as substrate and cathode layer roughness, substrate surface pore size, and cathode microstructure and thickness on electrolyte deposition efficiency, cathode and electrolyte permeability, and layer microstructure.

B.2 Experimental procedure

B.2.1 Material preparation

8 mol% yttria-stabilized zirconia (YSZ) powder (Inframat Advanced Materials, Farmington, CT., USA) was used as the electrolyte feedstock for this study. The as-received powder had a d_{50} agglomerate size of approximately 1.5 µm, with sizes ranging from 0.5 µm to 15 µm, as determined by laser light scattering (Mastersizer 2000, Malvern Instruments, Worcestershire, UK).

Aqueous YSZ suspensions with a solid loading of 5 vol% (23.7 wt%) were prepared using deionized water.

B.2.2 Plasma spray processing

This study used an Axial III Series 600 (Northwest Mettech Corp., North Vancouver, BC, Canada) atmospheric plasma spray system. This torch injects the feedstock axially between 3 electrodes, which ensures that virtually all of the powder injected passes through the hottest part of the plasma jet.

The plasma spraying system was modified to add a pressure vessel in order to deliver the suspension to the feed tube of the plasma torch. A two-fluid atomizing nozzle positioned

directly behind the torch convergence was used in order to produce small suspension droplets which were then directly injected into the centre of the plasma jet.

Deposition was carried out onto 2.54 cm diameter porous ferritic stainless steel 430 substrates (Mott Corporation, Farmington, CT, USA) mounted onto a rotating turntable. Three grades of substrates were studied: media grades (MG) 1, 2 and 5, where the media grade corresponds to the smallest particle size in micrometers that would be trapped upon passage of a suspension of particles through the porous metal. Two cathode thicknesses, ~35 μm and ~67 μm, were examined.

YSZ electrolyte layers were deposited on top of plasma sprayed composite lanthanum strontium manganite (LSM)/YSZ cathode layers that were first deposited on the porous stainless steel substrates in order to provide substrate conditions that are similar to those in actual fuel cells for deposition of the electrolytes.

Cathode layers were deposited using Ar/N_2 plasmas with spraying conditions developed previously [12]. Two cathode thicknesses (thin and thick) were deposited by varying the number of deposition passes.

The conditions used during plasma spraying are summarized in Table B.1 below.

Table B.1: Plasma spraying parameter values.

Parameter	Value
Plasma gas flow rate (slpm)	220
Plasma gas composition	80% N_2, 20% H_2
Torch current (A per electrode)	250
Nozzle size (mm)	12.7
Standoff distance (mm)	80

B.2.3 Coating characterization

The surface roughness of the uncoated and coated samples was measured using surface profilometry (Form Talysurf Series 2, Taylor Hobson Ltd., Leicester, UK). The form analysis software was used to correct for any deviation from horizontal in the substrate-coating pair by using a least squares arc geometric reference. Average roughness values were then calculated.

Polished cross sections of the deposited layers were examined in a Hitachi S-3000N scanning electron microscope (SEM) (Hitachi High Technologies America, Pleasanton, CA., USA). Samples were cut using a low speed diamond saw, mounted in epoxy, and then polished using diamond polishing suspensions. The polished samples were gold coated in order to enable sufficient sample conductivity for SEM imaging.

Helium permeation measurements using an in-house designed jig were performed in order to measure the gas permeability of the uncoated and coated substrates. The supply of helium gas was regulated by a pressure controller (Alicat Scientific, model PCD-5PSIG-D, Tucson, AZ, USA). The flow through the sample was measured at the outlet of the jig by a mass flow meter (Alicat Scientific, model M-0.5SCCM-D_H2, Tucson, AZ, USA).

B.3 Results and discussion

B.3.1 Substrate characterization

The porosity of each media grade was determined by measuring the weight and dimensions of each substrate and then dividing the calculated density value by the density of a fully dense sample of stainless steel 430. Porosity values are shown in Table B.2.

Table B.2: Substrate porosity values.

Substrate	% Porosity
Media grade 1	21.5
Media grade 2	25.9
Media grade 5	28.6

Polished cross sections of the three media grades are shown in Figures B.1 to B.3. As the substrate media grade increases, both the amount of porosity and average size of pores increase. If these porous media are to perform as SOFC mechanical supports, a balance must be struck between high porosity and large pores that facilitate good gas diffusion through the supports to the fuel cell electrode and low porosity and small pores that allow splats to "bridge" over surface pores to produce coatings with better mechanical integrity. Media grades 1, 2, and 5 were chosen as they appear to have the best compromise of porosity (20 to 30%) and pore size (1 to 25 μm) for this application. Media grades with larger pores appeared to have pore sizes too large for the coating to bridge over, and those with smaller pores have been found to have a porosity too low to allow sufficient gas flow through the substrate, particularly after some oxidation has occurred.

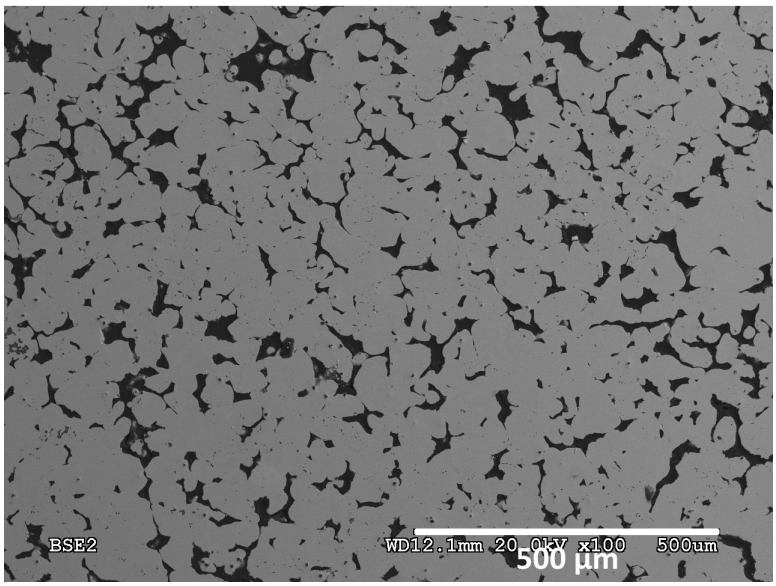

Figure B.1: SEM image of the polished cross section of the MG 1 substrate.

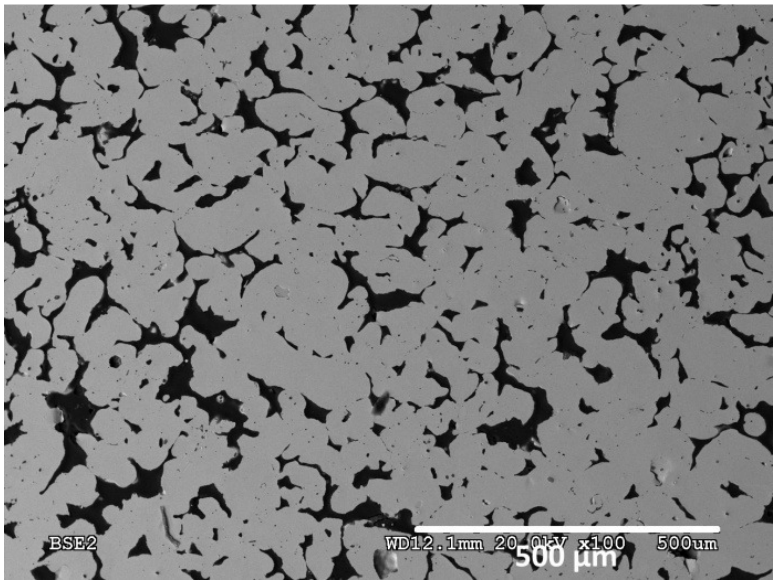

Figure B.2: SEM image of the polished cross section of the MG 2 substrate.

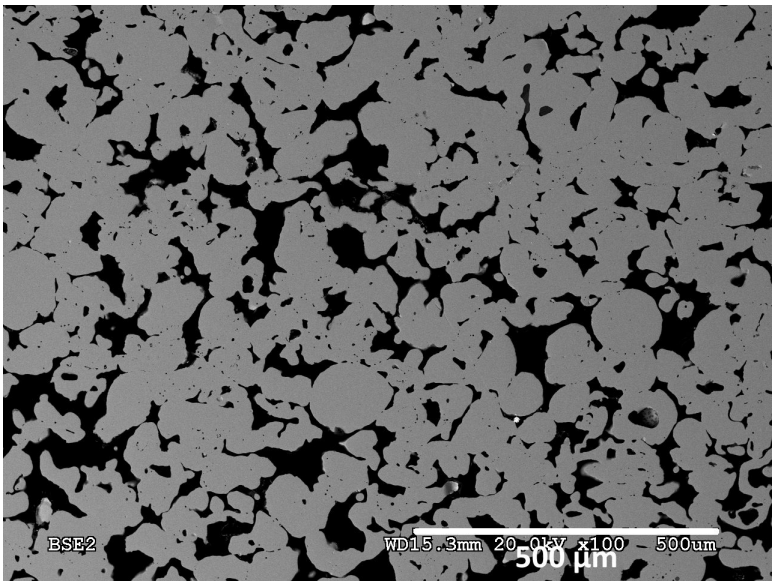

Figure B.3: SEM image of the polished cross section of the MG 5 substrate.

B.3.2 Plasma sprayed coating characterization

The profilometer surface roughness measurements indicated that for uncoated substrates, the surface roughness increases with the media grade. However, once a cathode coating was deposited on the porous metal substrates, there was no measurable difference in average surface roughness between cathode surfaces on the 3 substrates studied here. Surface roughness measurements are summarized in Figure B.4.

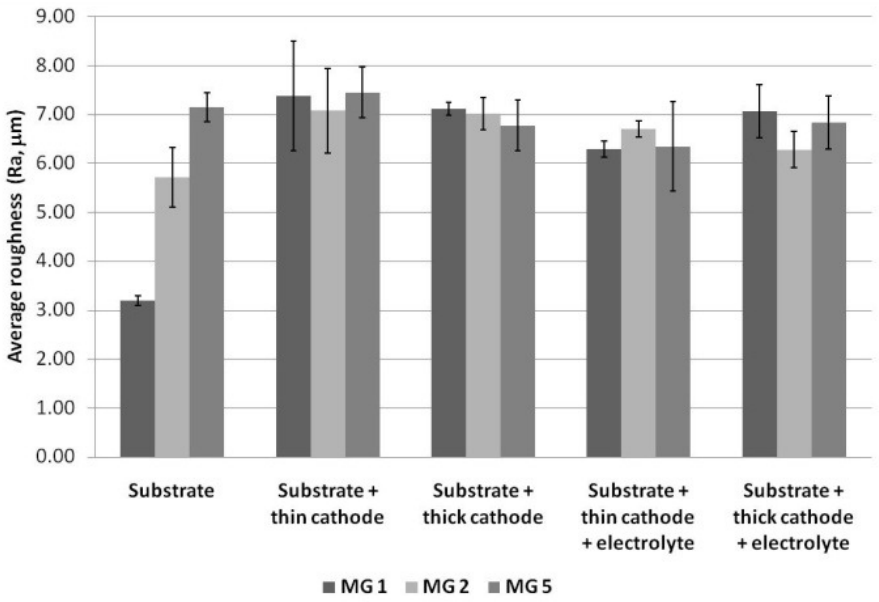

Figure B.4: Summary of surface roughness measurements.

SEM micrographs of polished cross sections of the coatings are shown in Figures B.5 to B.10.

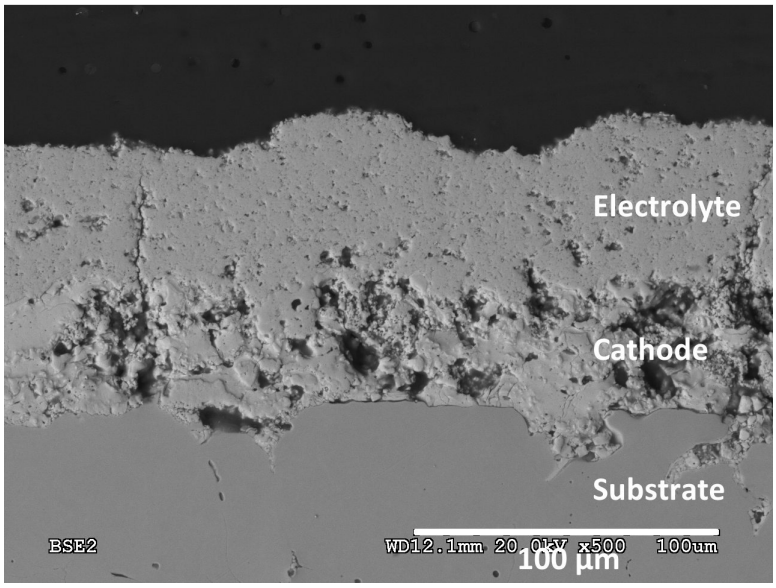

Figure B.5: SEM image of a thinner cathode and an electrolyte layer on the MG 1 substrate.

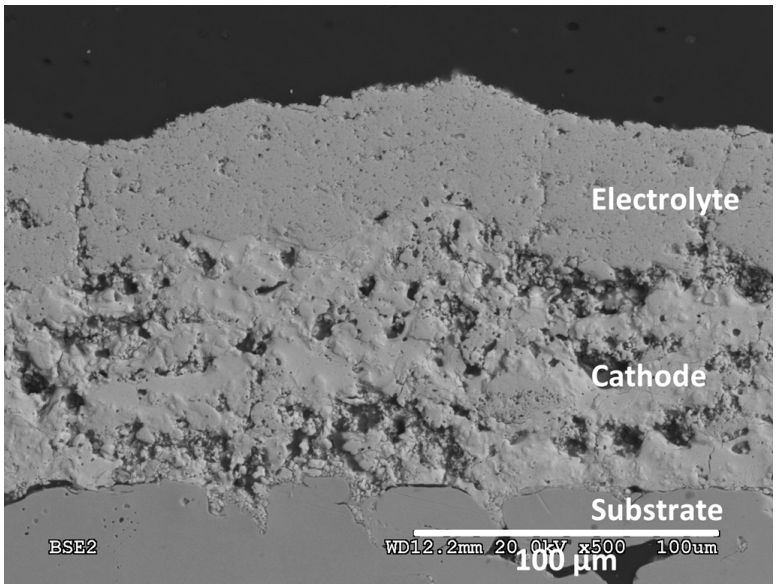

Figure B.6: SEM image of a thicker cathode and an electrolyte layer on the MG 1 substrate.

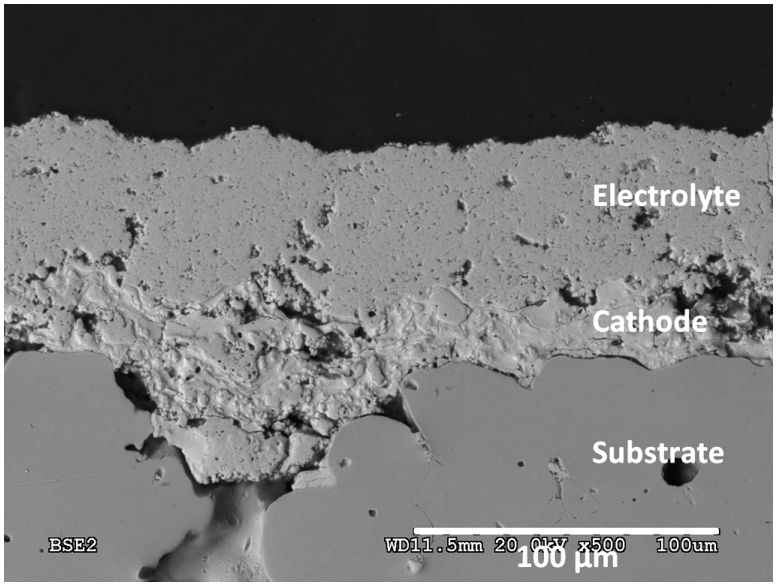

Figure B.7: SEM image of a thinner cathode and an electrolyte layer on the MG 2 substrate.

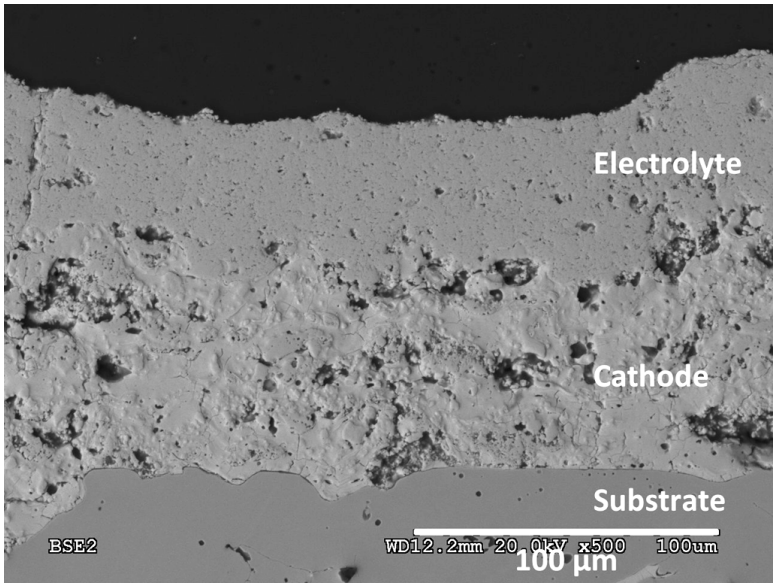

Figure B.8: SEM image of a thicker cathode and an electrolyte layer on the MG 2 substrate.

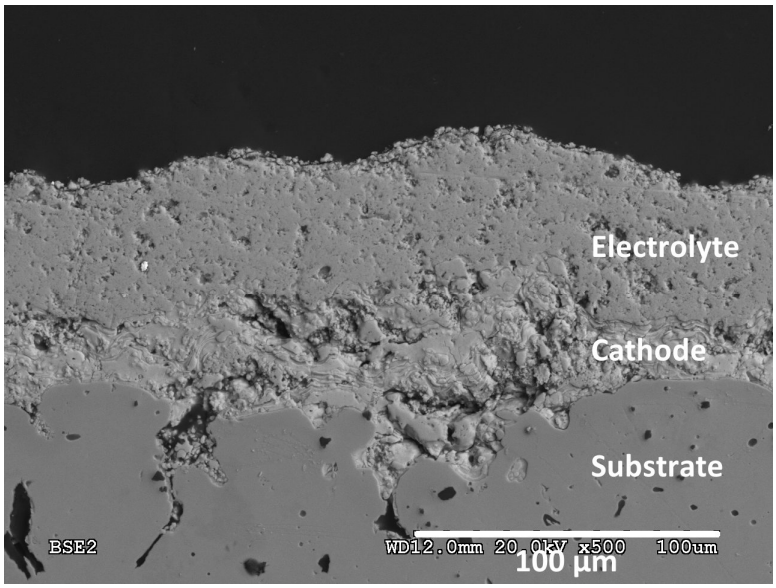

Figure B.9: SEM image of a thinner cathode and an electrolyte layer on the MG 5 substrate.

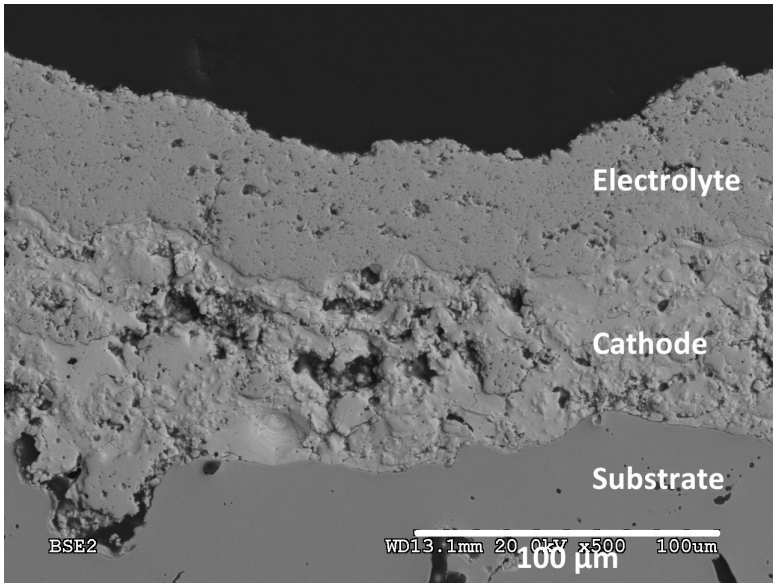

Figure B.10: SEM image of a thicker cathode and an electrolyte layer on the MG 5 substrate.

Layers deposited on media grade 1 and 2 substrates and electrolyte layers deposited on thick cathodes had good continuity and appeared to have desirable low open porosity levels. Some vertical cracking was seen in the deposited layers likely due to thermal stresses in the layers. This cracking would be detrimental to the electrolyte performance, but can potentially be alleviated by more precise control of substrate temperature or by the introduction of a compositionally graded interface between the two coating layers [13].

Occasionally, thin cathode layers deposited on media grade 5 substrates had difficulty filling in and bridging the large surface pores that are more likely to occur in this substrate type. Figure B.11 shows the effect of a large surface pore on the integrity of the cathode and electrolyte layers. Since such surface defects can potentially lead to short circuiting between the electrodes in a fuel cell [14], the combination of a thin cathode layer with a coarse substrate is therefore undesirable.

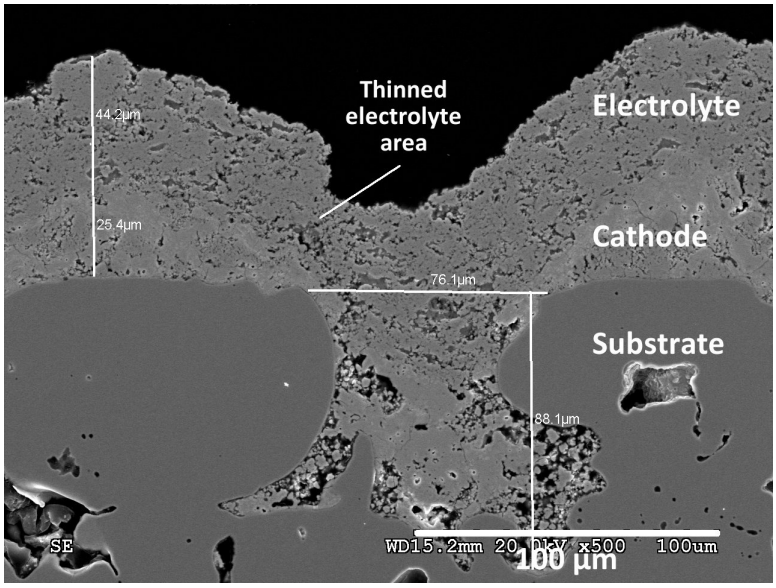

Figure B.11: SEM image of a polished cross section showing a large surface pore (MG 5 substrate) and the resulting deformation in the thin cathode and electrolyte layers.

The thickness of the cathode and electrolyte layers was measured on the polished cross sectional SEM images. "Thin" cathode layers were approximately 35µm thick, while "thick" cathode layers were approximately 67µm thick. Electrolyte layers were approximately 45µm thick. There appeared to be no significant effect of substrate type on the deposited layer thicknesses. This indicates that the cathode and electrolyte deposition efficiencies are not dependent on the substrate type for the three substrates examined in this study. Thickness measurements are summarized in Figure B.12.

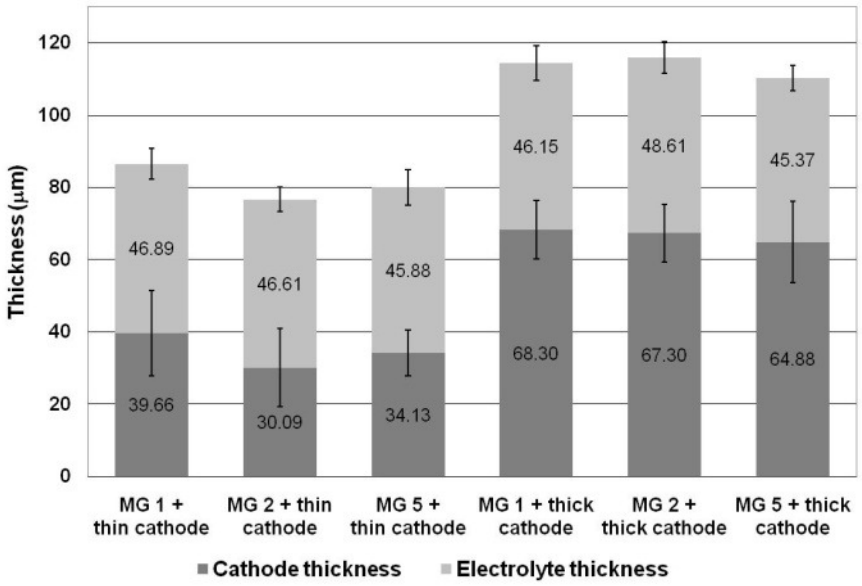

Figure B.12: Summary of thickness measurements.

The permeation rate of the samples was measured by passing helium at a pressure of 0.5 psi through the samples. The resulting flow was then measured at the jig exit with a mass flow meter. The permeation rates of uncoated samples were very high and it was difficult to differentiate between the substrate types. This effect is likely due to helium leakage out of the edges of the sample. Permeation rates were lower for thicker cathodes and for samples with electrolyte layers. Average permeation rates were similar for the three media grades examined, but the measurements for MG 5 samples were much more variable, especially for samples with thin cathodes. This is likely due to the increased probability of large surface pores in the MG 5 substrates. These large pores are difficult for the cathode layer to bridge, resulting in a higher probability of large continuity defects within the layers (see Figure B.11). Permeation results are summarized in Figure B.13.

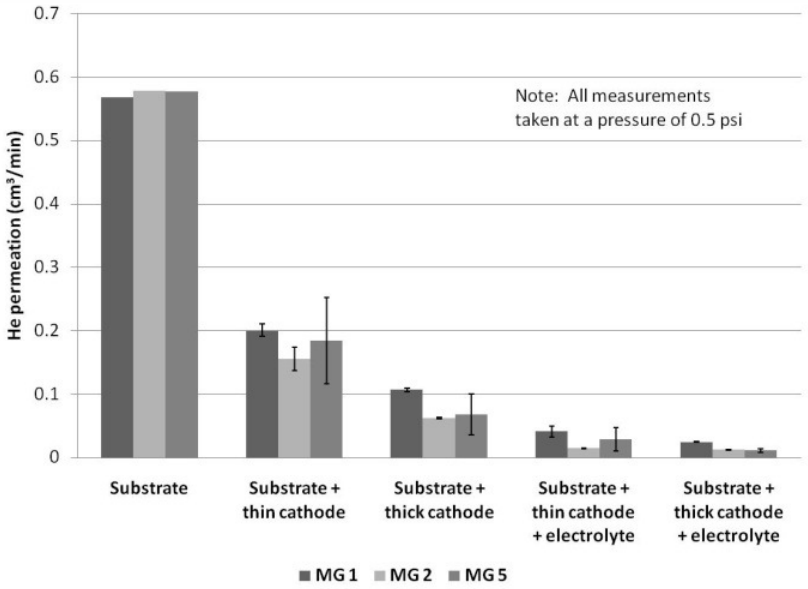

Figure B.13: Summary of permeation testing results.

B.4 Conclusions

Suspension plasma sprayed SOFC electrolytes have been successfully deposited on LSM/YSZ composite cathodes that were first deposited on porous stainless steel substrates. The effect of substrate morphology and cathode thickness on subsequent layer properties was examined by measuring the surface roughness, characterizing the cross sectional microstructures, and measuring the helium permeation rates for three grades of stainless steel substrates (MG 1, 2, 5) with two different cathode thicknesses.

As the media grade increases, the pore size increases and porosity increases from 21.5% to 28.6%.

The average surface roughness of uncoated samples increased from ~3 µm to 7 µm as the media grade increased, but once a cathode coating was deposited, there was no measurable difference in surface roughness between the metal substrates of different porosities.

Cathode and electrolyte microstructures and thicknesses did not appear to vary with substrate type or cathode thickness, with one exception. For media grade 5 samples with

thin cathodes it was noticed that occasionally the cathode was unable to bridge over especially larges pores which resulted in major coating continuity defects. The lack of variability in coating thicknesses indicates that the substrate type has no effect on cathode or electrolyte deposition efficiency for the substrates examined in this study.

Helium permeation rates were measured using an in-house developed jig. Uncoated substrates had high permeation rates and it was difficult to differentiate between the substrate types, probably due to edge leakage. Permeation rates lowered as cathode thicknesses increased and for samples with electrolyte layers. Permeation measurements for the media grade 5 samples with thin cathodes had significant scatter, likely due to the increased probability of the presence of large unbridgeable pores in the media grade 5 substrates.

Based on the observed results, the MG 2 substrates were found to provide the best compromise between reasonably high porosity with acceptable permeation rates and sufficiently low surface roughness to allow deposition of coatings with good integrity.

B.5 Acknowledgements

The authors gratefully acknowledge financial support from the Natural Sciences and Engineering Research Council of Canada, Northwest Mettech Corporation, and the BC Innovation Council, as well as the assistance of Bradley White and Dr. Michael Poon with plasma spraying.

B.6 References

1. E. Tang , F. Martell, R. Brulé, K. Marcotte, B. Borglum, pp. 935-943 in Proceedings of SOFC VIII, Edited by S.C. Singhal and M. Dokiya, The Electrochemical Society Proceedings Series. Paris, France, 2003.
2. X. Zhang, C. Deces-Petit, S. Yick, M. Robertson, O. Kesler, R. Maric, D. Ghosh, Journal of Power Sources, 162(1) (2006), 480-485.
3. P. Fauchais, Journal of Physics D: Applied Physics, 37(9) (2004), R86-R108.
4. O. Kesler, Materials Science Forum, 539-543, (2007), 1385-1390.
5. R. Hui, Z. Wang, O. Kesler, L. Rose, J. Jankovic, S. Yick, R. Maric, D. Ghosh, Journal of Power Sources, 170(2) (2007), 308-323.
6. R. Henne, Journal of Thermal Spray Technology, 16(3) (2007), 381-403.
7. J. Oberste Berghaus, S. Bouaricha, J.G. Legoux, C. Moreau, pp. 1434-1440 in Proceedings of International Thermal Spray Conference (ITSC), Edited by E. F. Lugscheider, German Welding Society. Basel, Switzerland, 2005.
8. J. Oberste Berghaus, S. Bouaricha, J.G. Legoux, C. Moreau, T. Chráska, pp. 512-518 in Proceedings of International Thermal Spray Conference (ITSC), Edited by E. F. Lugscheider, German Welding Society. Basel, Switzerland, 2005.
9. C. Delbos, J. Fazilleau, J.F. Coudert, P. Fauchais, L. Bianchi, K. Wittmann-Teneze, pp. 661-669 in Proceedings of Thermal Spray 2003: Advancing the Science and Applying the Technology, Edited by B.R. Marple and C. Moreau, ASM International. Orlando, FL, USA, 2003.
10. V. Rat, C. Delbos, C. Bonhomme, J. Fazilleau, J.F. Coudert, P. Fauchais, High Temperature Material Processes, 8(1) (2004), 95-117.
11. M. Bonneau, F. Gitzhofer, M. Boulos, pp. 929-934 in Proceedings of the International Thermal Spray Conference (ITSC). Montreal, Canada, 2000.
12. B.D. White, O. Kesler, L. Rose, Journal of Power Sources 178(1) (2008), 334-343.
13. O. Kesler, M. Finot, S. Suresh, S. Sampath, Acta Materialia, 45, (1997), 3123-3134.
14. B.D. White, O. Kesler, Journal of Power Sources, 177(1) (2008), 104-110.

C Permeation measurements

C.1 Permeation measurement equipment

Helium permeation measurements were performed using an in-house designed fixture in order to measure the gas permeability of the substrates and each deposited layer. The supply of helium gas was regulated at a gage pressure of 3.5 kPa by a pressure controller (Alicat Scientific, model PCD-5PSIG-D, Tucson, AZ, USA). The flow through the sample was then measured at the outlet of the fixture by a mass flow meter (Alicat Scientific, model M-0.5SCCM-D_H2, Tucson, AZ, USA). The sample was held in a custom designed jig that sealed around the porous substrate in order to limit leakage out of the sides of the porous substrate material. A schematic diagram of the permeation testing equipment is shown in Figure C.1.

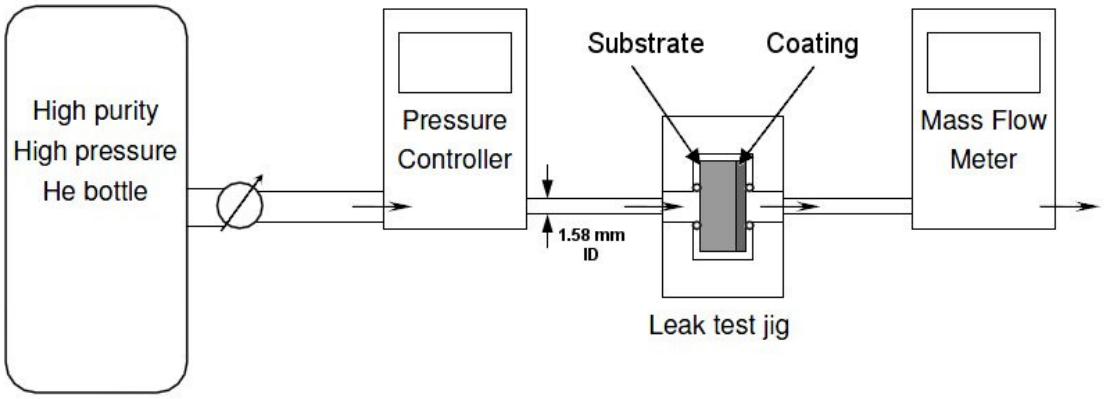

Figure C.1: Schematic diagram of the permeation testing equipment.

C.2 Permeability calculations

Permeability is a measure of the ability of a porous medium to transmit a fluid. The flow rate through the sample can be related to the layer permeability using Darcy's law [1].

$$Q = \frac{-\kappa A}{\mu}\frac{(\Delta P)}{L}$$

where: Q is the flow rate (m^3/s)

κ is the permeability (m^2)

A is the cross-sectional area to flow (m^2)

(ΔP) is the pressure drop across the substrate (Pa)

μ is the dynamic viscosity (Pa s)

L is the length over which the pressure drop takes place (m)

C.3 Discussion of measurements

The effects of the substrate and cathode layers on the full cell permeation rates were neglected because substrate and cathode layers were similar for all tested cells and uncoated substrate and substrate + cathode layer permeation rates were more than an order of magnitude and 50% greater, respectively, compared to specimens with substrate, cathode, and electrolyte layers.

In many cases within this thesis, both permeabilities and permeation rates were reported. Coating permeation rates are specific to the electrolyte layer microstructure and thickness, which makes them more difficult to compare to the results from other groups; however, permeation rate is a more relevant SOFC characterization parameter, as it is a direct measurement of the gas flow through the electrolyte layer, and thus can more easily be correlated to other leakage-based electrolyte parameters such as open circuit voltages. Permeability is a more general material property and is reported to facilitate comparison of the results presented with literature results.

In many cases measured permeability values increased with electrolyte layer thickness. Since permeability is a material property it should not be dependent on the coating thickness. This phenomenon may have been caused by an increase in the volumetric strain energy within the coating as the coating thickness increases. This increase in strain energy

may facilitate the formation of vertical cracks within the electrolyte layer that can act to enhance gas transport and thus change the coating permeability value.

C.4 Sample calculation

A sample calculation illustrating the permeability calculation procedure is shown below.

Darcy's Law: $$Q = \frac{-\kappa A}{\mu}\frac{(\Delta P)}{L}$$

Rearrange to solve for permeability: $$\kappa = \frac{-Q\mu L}{A(\Delta P)}$$

If: $Q = 3.783 \times 10^{-9}\ m^3/s$ (measured)

$\mu = 1.992 \times 10^{-5}$ Pa s (for Helium)

$L = 4.442 \times 10^{-5}$ m (electrolyte thickness as measured from SEM images)

$A = 1.000 \times 10^{-4}\ m^2$ (size of o-ring seal)

$(\Delta P) = -3.447 \times 10^{3}$ Pa (set by pressure controller)

$$\kappa = \frac{-(3.783\times10^{-9})(1.992\times10^{-5})(4.442\times10^{-5})}{(1.000\times10^{-4})(-3.447\times10^{3})} = 9.712 \times 10^{-18}\ m^2$$

C.5 Reference

1. A.C. Fox, T.W. Clyne, Surface & Coatings Technology, 184(2-3) (2004), 311-321.

D Suspension delivery and injection equipment

D.1 Suspension delivery system

D.1.1 Generation 1: Progressive cavity pump

The first generation suspension delivery system was designed by Paul Daniel as part of his M.Eng. project [1]. The system used a progressive cavity pump (Seepex Model - 0005-24MD/A6-A7-A7-R0-3) with a KB SCR variable frequency speed control. The pump specifications are shown in Table D.1. The pump speed control was connected to a 110V AC power source with 14 Gauge, 3 conductor water resistant electrical wire. Similar wire was used to connect the speed control to the pump motor. Solder-less electrical connections were used at all terminals. When the system was assembled and commissioned, suspension flow rates were very low and small black polymeric particles were visible in the pumped suspension. After a number of spraying runs, the pump was dissembled and it was determined that the rubber coating that is used to seal the pump stator had been damaged, preventing the pressurization of the pump cavity. A new stator was installed and after a short period of operation it was observed that the rubber seals on the new stator were also damaged. Therefore it was decided that this pump was not suitable to deliver the abrasive YSZ suspensions required for this project and an alternate suspension delivery system design was developed.

Table D.1: Progressive cavity pump specifications.

Seepex

Pump type 0005-24 /MD/A6-A7-A7-R0-3

		min	max	nom.	
Capacity	Q	0.05	0.05	0.16	l/min
Differential pressure	P	5.44	5.44	5.44	bar
Pump speed	N	193	193	600	1/min
Operating power	Pb	0.04	0.04	0.13	kW
Operating torque	Mb	2	2	2	Nm
Starting power	Pa			0.10	kW
Starting torque	Ma			2	Nm
Axial load	Fax			43	N
Motor speed	nM	193	193	600	1/min
Frequency	F			60	Hz

D.1.2 Generation 2: Pressurized canister delivery

A second generation suspension delivery system was designed by David Waldbillig in order to address the abrasion issues identified in the first generation system. The delivery system consisted of a pressurized canister that uses a pressure head of gas to deliver the liquid suspension. The suspension flow rate can be controlled by varying the gas pressure. As this setup has no moving parts, it will be inherently more abrasion resistant than the pumping systems previously used and should produce even, reproducible flow rates. After they system was designed, the pressure vessels were fabricated by the Department of Materials Engineering machine shop. A schematic diagram showing the pressurized canister delivery system is shown in Figure D.1. A magnetic stirrer was used to mix the suspension during operation.

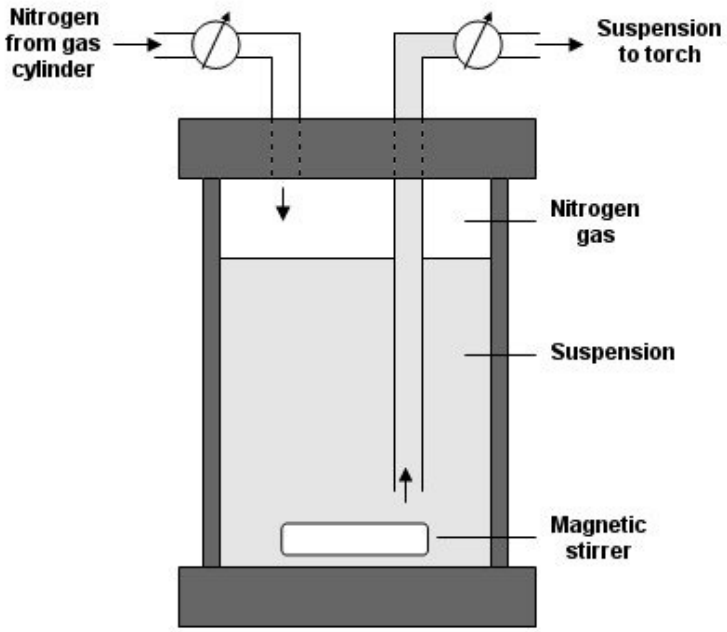

Figure D.1: Schematic diagram of the pressurized canister delivery system.

D.1.3 Generation 3: Pressurized canister delivery design modification

The generation 3 design slightly modified the pressurize vessel in order to improve sealing and ease of use. An image of two pressurized canisters (one for suspensions, one for cleaning water) is shown in Figure D.2.

Figure D.2: Image of the pressurized canister delivery system.

A calibration chart showing the suspension flow rates for various pressurized canister delivery pressures (Figure D.3) was developed by directly measuring the amount of suspension delivered by the system over a time interval 30 seconds.

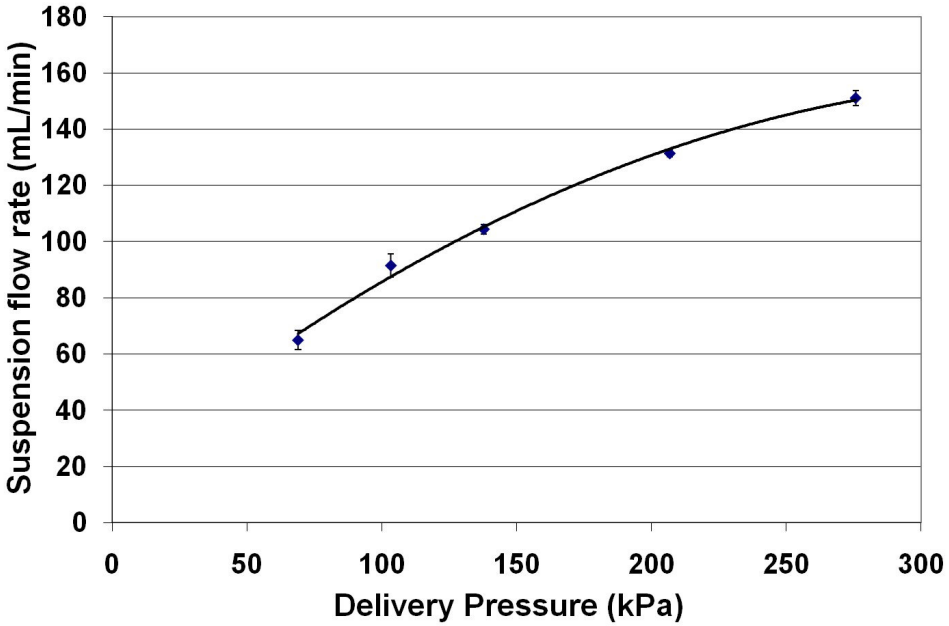

Figure D.3: Calibration chart for the generation 3 suspension delivery system.

D.2 Suspension injection system

A two fluid atomizing nozzle was fabricated to inject and atomize the delivered suspension. The liquid suspension was axially injected into the center of the plasma plume at a position 2 mm behind the torch convergence via a 1.27mm OD stainless steel (SS) syringe injection tube that was fed through the existing 4.76 mm OD polypropylene (PP) feed tube. The outer polypropylene line was used to supply argon as an atomizing gas. A T-shaped compression fitting was used to join the argon atomizing gas line, the suspension feed line from the pressurized canister, and the suspension injection tube, as shown in Figure D.4. An image of the two fluid atomizing nozzle in operation is shown in Figure D.5.

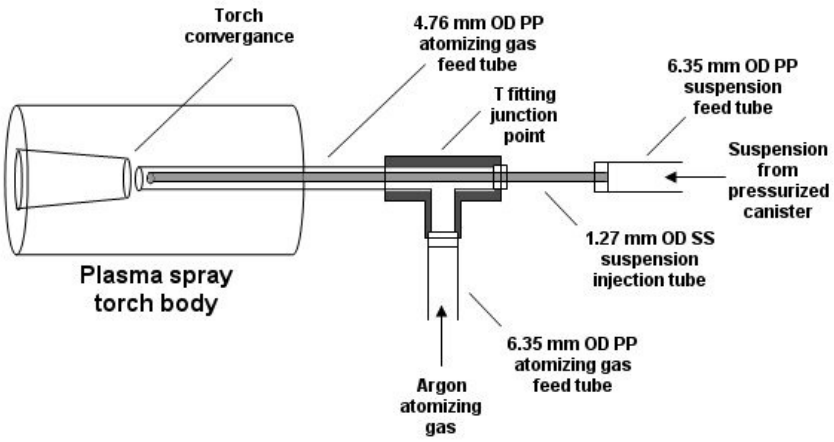

Figure D.4: Schematic diagram showing the two fluid atomizing nozzle and injection configuration.

Figure D.5: Image of the two fluid atomizing nozzle suspension injection system in operation (no plasma).

D.3 Reference

1. P. Daniel, M.Eng. Project Report, University of British Columbia, Vancouver, BC, 2006.

E Electrochemical test equipment and procedure

E.1 Solid oxide fuel cells (SOFCs)

2.54 cm diameter button cells with porous 430 stainless steel metal support layers, plasma sprayed lanthanum strontium manganite (LSM) / yttria stabilized zirconia (YSZ) cathode layers, suspension plasma sprayed YSZ electrolyte layers, and plasma sprayed NiO / YSZ anode layers were tested in a single cell test configuration during all electrochemical tests.

E.2 Test equipment

Single cell test stations (model FCSH-1000, Materials Mates Italia, Milan, Italy) with additional gas flow control hardware and software (Arbin Instruments, College Station, TX, USA) were used for all electrochemical tests. An image of the vertical test station fixture is shown in Figure E.1. A four wire setup with separate voltage and current wires for the working and counter electrodes was used. Anode and cathode side contact layers consisted of platinum meshes that were spring loaded to facilitate contact. An image of the test station fixture contact area is shown in Figure E.2. A list of the test station specifications is given in Table E.1.

Figure E.1: Single cell test station fixture [1].

Figure E.2: Test station fixture contact area [1].

Table E.1: Test station specifications [1].

PHYSICAL FEATURES	
Temperature range	0–1000 ^{o}C
Sample size	12 -26 mm dia, 3 mm thickness max
Contact plates	Platinum gauze, spring loaded
Construction materials	Alumina 99.9 %; platinum 99.5 %; fused silica tube; viton o-rings and membranes
Gas flow	Anode and cathode in/out connections
Sealing pressure	About 20 N
Gas compatibility	Any reducing or oxidizing gas compatible with fused silica and alumina
Gas connections	6 mm Swagelock-type double-ferrule connectors
Gas tightness	Viton O-rings
Orientation	Vertical
ELECTRICAL FEATURES	
Connections	Banana 2 mm
Measuring configuration	2-wire connections + 2 wire compensation
Residual resistance	< 5 mOhm
Effective wire resistance	< 2 Ohm @ 25 ^{o}C
Maximum current capability	5 A
Sample temperature	Type K Inconel shielded thermocouple
DIMENSIONS & OTHERS	
Mechanical	260 x 45 mm (L x Dia) cover tube
	80 x 70 mm (Dia x h) connection body
Water cooling	4 mm copper tubing (0.1 Lt/min recommended)
Weight	1.2 kg

E.3 Sealing

A two part sealing system was utilized to seal the cell to the test station fixture tube. First, a wet ceramic seal (Ceramabond 552-VFG, Aremco Products, Inc., Valley Cottage, NY) was painted on the outside edge of the cells in order to limit any leakage from the porous cell edges. The ceramabond seal was then cured following the manufacturer's recommended

procedure as listed in Table E.2. Between curing temperatures, the cell and seal were heated or cooled at a rate of no more than 1.5°C/min. A commercially available sealing product (Thermiculite 866, The Flexitallic Group, Houston, USA) was used to seal the face of the cell to the test station tube.

Table E.2: Ceramabond curing procedure.

Step	Temperature	Time at temperature
Drying	20°C	1 hour
Curing 1	93°C	2 hours
Curing 2	260°C	2 hours

Using this sealing system, an anode supported cell with a very dense screen printed and sintered electrolyte achieved an open circuit voltage of 1.02 V at 750°C with a hydrogen concentration of 20%. This open circuit voltage value may be compared to the predicted Nernst voltage at these conditions, which is 1.04 V. Schematic diagrams showing a top view and a side view of the cell orientation and sealing configuration are shown in Figures E.3 and E.4, respectively.

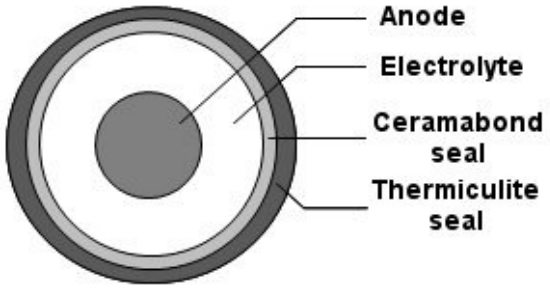

Figure E.3: Top view schematic diagram of the cell and seal configuration.

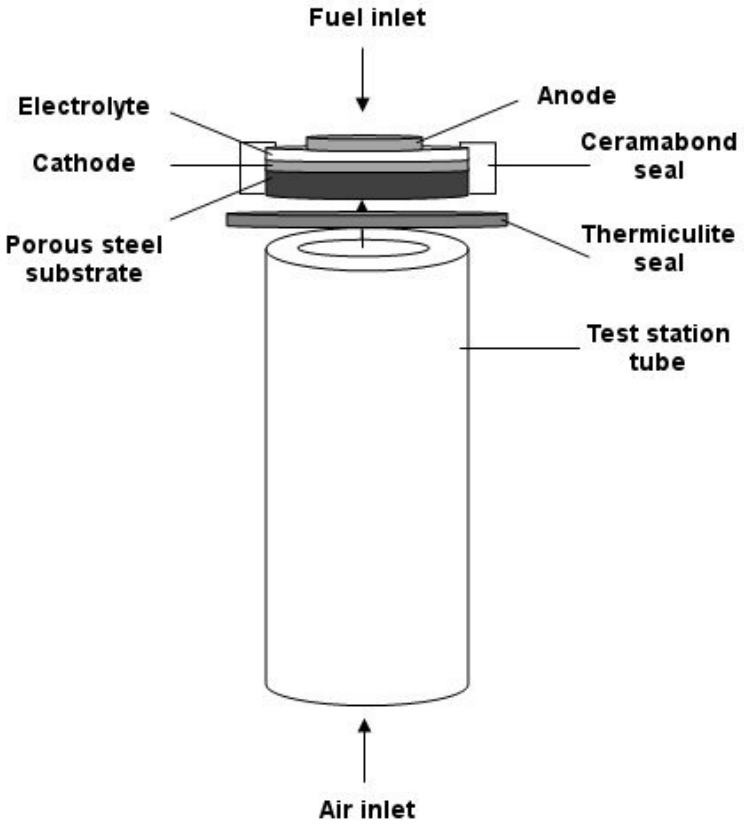

Figure E.4: Side view schematic diagram of the cell and seal configuration.

E.4 Heating, reduction and testing procedure

After the cell was loaded in the test station and sealed, the test procedure detailed in Table E.3 was followed. All heating or cooling steps during the tests occurred at a ramp rate of 1.5^{o}C/min. Anode gases were humidified to 3% by passing the gasses through a humidifier containing deionized water at room temperature. During reduction, the NiO present in the deposited anode layer was reduced to the desired metallic Ni phase by slowly increasing the anode gas H_2 content from 4% to 20%.

Table E.3: Electrochemical testing procedure.

Step	Temp (^{o}C)	Step time (hour)	Cathode flow (cm^3/min)	Cathode gas	Anode flow (cm^3/min)	Anode gas
Heat to 750^{o}C	750	8.1	0	79% N_2, 21% O_2	500	4% H_2 96% N_2
Reduction 1	750	0.5	950	79% N_2, 21% O_2	950	10% H_2 90% N_2
Reduction 2	750	0.25	950	79% N_2, 21% O_2	950	15% H_2 85% N_2
Reduction 3	750	0.25	950	79% N_2, 21% O_2	950	20% H_2 80% N_2
Polarization and impedance tests	750	0.5	950	79% N_2, 21% O_2	950	20% H_2 80% N_2
Cool to 700^{o}C	700	0.6	950	79% N_2, 21% O_2	950	20% H_2 80% N_2
Polarization and impedance tests	700	0.5	950	79% N_2, 21% O_2	950	20% H_2 80% N_2
Cool to 650^{o}C	650	0.6	950	79% N_2, 21% O_2	950	20% H_2 80% N_2
Polarization and impedance tests	650	0.5	950	79% N_2, 21% O_2	950	20% H_2 80% N_2
Cool to 600^{o}C	600	0.6	950	79% N_2, 21% O_2	950	20% H_2 80% N_2
Polarization and impedance tests	600	0.5	950	79% N_2, 21% O_2	950	20% H_2 80% N_2
Cool to 20^{o}C	20	6.4	500	79% N_2, 21% O_2	500	4% H_2 96% N_2

E.5 Electrochemical test details

Electrochemical tests were performed using a Solartron 1470E multi-channel potentiostat and 1260 frequency response analyzer (London Scientific, London, ON, Canada) at temperatures of 750, 700, 650, and 600^{o}C with 20% H_2 anode gas.

Polarization curves were measured using the potentiodynamic test setting in the MultiStat software (Scribner Associates Inc., Southern Pines, NC, USA) and were tested from the open circuit voltage to a voltage of 0.27 V. Tests were ended at this potential in order to limit any cell damage that might occur from testing at low potentials.

Cell impedance values were measured using the impedance test setting in the Multistat and ZPlot software (Scribner Associates Inc., Southern Pines, NC, USA) at open circuit voltage for the four test temperatures. Measurements were taken from frequencies of 100000 Hz to 0.1 Hz using an AC amplitude of 10 mV. It was found during preliminary testing that this range of frequencies provided a complete coverage of the electrochemical processes that occurred and that higher or lower frequencies provided no additional information. A blank impedance measurement in which no cell was loaded was performed in order to determine the amount of inductance present in the system due to the wires and test station. This inductance value was subtracted from the measured impedance in order to isolate the cell impedance.

E.6 Reference

1. Material Mates Italia. FCSH1000 Fuel Cell Sample Holder. Retrieved May 26, 2010 from http://www.mmates.com/media/pro/FCSH1000.pdf

F R_s measurement and separation

F.1 Series resistance

In SOFC electrochemical measurements the cell series resistance (R_s) is the high frequency (left most) intercept on the Nyquist impedance plot. The R_s value is a measure of the cell resistance due to the electrolyte material and microstructural resistivity and any contact resistances that are present in the test system. Cell impedance values were measured at frequencies between 100000 Hz and 0.1 Hz with an AC amplitude of 10 mV. It was found during early testing that this range of frequencies provided a complete coverage of the electrochemical processes that occurred and that higher or lower frequencies provided no additional information. Nyquist plots showing the behaviour of a PS SOFC at temperatures between 600 and 750^{o}C with 20% H_2 fuel on the anode side and air on the cathode side are shown in Figure F.1. A detailed summary of the entire electrochemical testing procedure can be found in Appendix E.

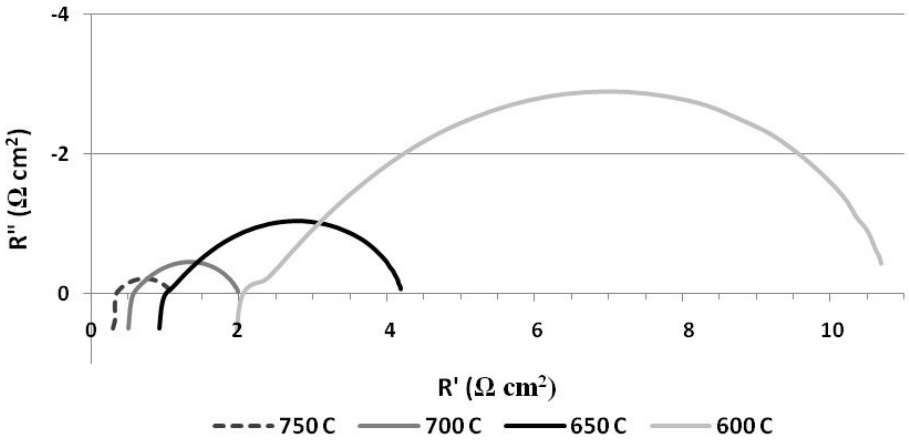

Figure F.1: Nyquist impedance plots of a PS SOFC.

F.2 Inductance subtraction

The high frequency data points on the positive side of the imaginary axis of the Nyquist plot in Figure F.1 can be attributed to the inductance present in the system due to the wires and test station. This inductance affects the Nyquist plot by shifting the measured R_s values. A blank impedance measurement with no cell loaded can be run to measure this inductance, which can then be subtracted from the measured impedance to isolate the cell impedance. A Nyquist plot showing the blank impedance measurement is shown in Figure F.2.

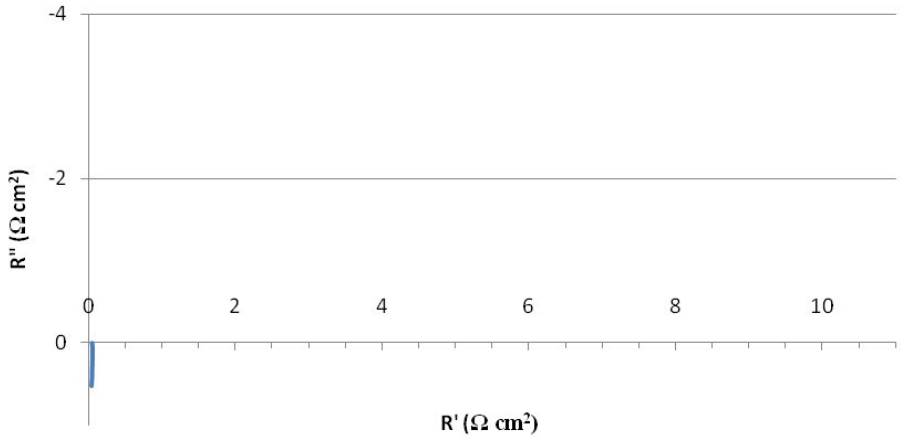

Figure F.2: Nyquist plot showing a blank impedance measurement.

F.3 R_s determination

The blank inductance measurement shown in Figure F.2 was subtracted from the Nyquist plot in Figure F.1 to produce the corrected Nyquist plots shown in Figure F.3. The R_s values were determined from the high frequency intercepts of the inductance corrected Nyquist plots. After inductance correction, all cell tests had high frequency results that crossed or were very close to the x-axis. For the cases in which the data did not cross the x-axis at high frequencies, the real value of the highest frequency data point that was closest to the x-axis was used (see Figure F.4). On average, the inductance measurement corrections decreased the measured R_s values by 17.4 ± 9.3 % for the 17 cell tests performed.

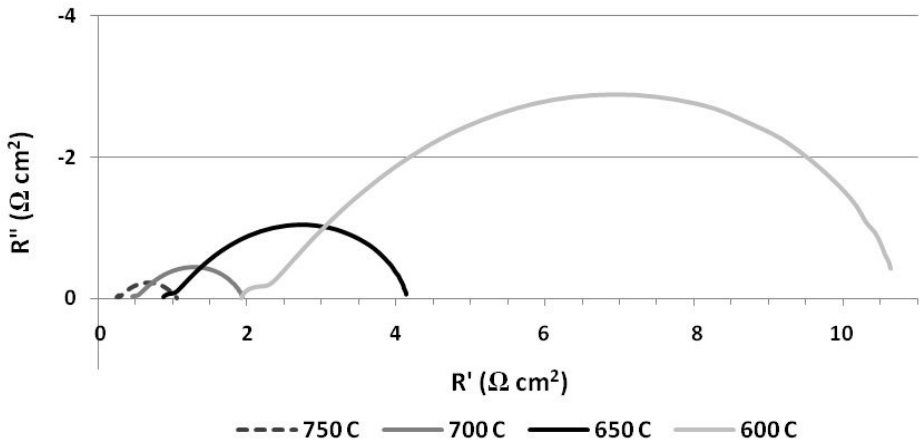

Figure F.3: Corrected Nyquist impedance plots for a PS SOFC.

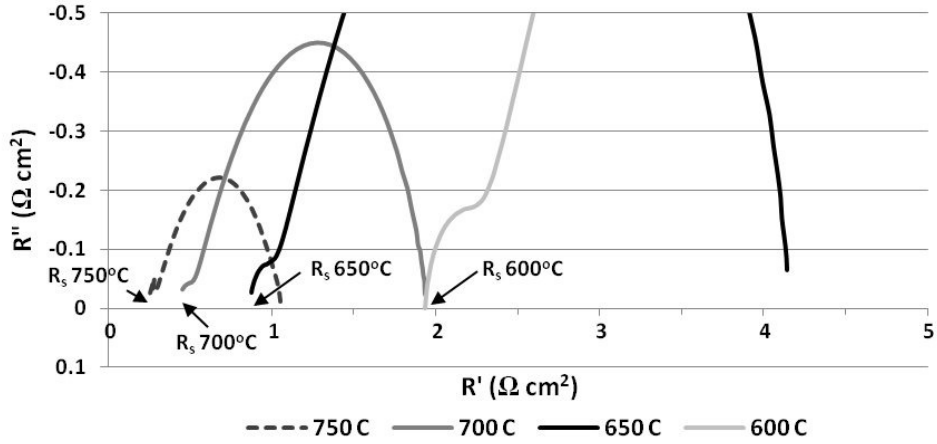

Figure F.4: Larger scale Nyquist plots showing the R_s determination methodology.

F.4 R_s separation procedure

In order to better understand the root causes of the various electrolyte losses, the measured series resistance (R_s) was separated into three parts, as shown in the following equation:

$$R_s = R_{YSZ} + R_{\mu} + R_C$$

R_{YSZ} corresponds to the area specific resistance caused by the limited ionic conductivity of YSZ and was calculated directly by dividing the electrolyte layer thickness by the conductivity of YSZ [1].

After the R_{YSZ} component was subtracted from the measured series resistance, a value that corresponded to the contributions of $R_\mu + R_C$ remained. R_μ is the area specific resistance due to microstructural features within the electrolyte layer such as porosity or splat boundaries, while R_C is the area specific resistance due to the contact interfaces present between the cell and test station. In order to determine the relative contributions of R_μ and R_C, a least-squares fitting method was used. The following procedure was used for each set of data.

1. Set up the equation: $R_s = R_{YSZ} + R_\mu + R_C$ where R_s has been measured and R_{YSZ} calculated.

Cell name	Electrolyte microstructure	Temp	Thickness	R_s	R_{YSZ}	ρ_μ	R_μ	R_C
1	Low flow	750	t_1	R_{s1}	R_{YSZ1}		$\rho_\mu * t_1$	$R_{s1} - R_{YSZ1} - R_{\mu1}$
2	Low flow	750	t_2	R_{s2}	R_{YSZ2}		$\rho_\mu * t_2$	$R_{s2} - R_{YSZ2} - R_{\mu2}$
3	Low flow	750	t_3	R_{s3}	R_{YSZ3}		$\rho_\mu * t_3$	$R_{s3} - R_{YSZ3} - R_{\mu3}$
4	Low flow	750	t_4	R_{s4}	R_{YSZ4}		$\rho_\mu * t_4$	$R_{s4} - R_{YSZ4} - R_{\mu4}$
5	Low flow	750	t_5	R_{s5}	R_{YSZ5}		$\rho_\mu * t_5$	$R_{s5} - R_{YSZ5} - R_{\mu5}$

2. Make an initial guess for the microstructural resistivity value (ρ_μ) that is calculated by dividing the R_μ value by the measured electrolyte thickness. The ρ_μ value represents the intrinsic resistivity of the electrolyte microstructure and thus should

be constant for a given test temperature and spraying condition (i.e. electrolyte microstructure), which allows the data from several cell tests to be compared.

Cell name	Electrolyte microstructure	Temp	Thickness	R_s	R_{YSZ}	ρ_μ	R_μ	R_C
1	Low flow	750	t_1	R_{s1}	R_{YSZ1}	$\rho_{\mu 1}$	$\rho_\mu * t_1$	$R_{s1} - R_{YSZ1} - R_{\mu 1}$
2	Low flow	750	t_2	R_{s2}	R_{YSZ2}		$\rho_\mu * t_2$	$R_{s2} - R_{YSZ2} - R_{\mu 2}$
3	Low flow	750	t_3	R_{s3}	R_{YSZ3}		$\rho_\mu * t_3$	$R_{s3} - R_{YSZ3} - R_{\mu 3}$
4	Low flow	750	t_4	R_{s4}	R_{YSZ4}		$\rho_\mu * t_4$	$R_{s4} - R_{YSZ4} - R_{\mu 4}$
5	Low flow	750	t_5	R_{s5}	R_{YSZ5}		$\rho_\mu * t_5$	$R_{s5} - R_{YSZ5} - R_{\mu 5}$

3. Set the ρ_μ values for each comparable test equal to each other.

Cell name	Electrolyte microstructure	Temp	Thickness	R_s	R_{YSZ}	ρ_μ	R_μ	R_C
1	Low flow	750	t_1	R_{s1}	R_{YSZ1}	$\rho_{\mu 1}$	$\rho_\mu * t_1$	$R_{s1} - R_{YSZ1} - R_{\mu 1}$
2	Low flow	750	t_2	R_{s2}	R_{YSZ2}	$\rho_{\mu 1}$	$\rho_\mu * t_2$	$R_{s2} - R_{YSZ2} - R_{\mu 2}$
3	Low flow	750	t_3	R_{s3}	R_{YSZ3}	$\rho_{\mu 1}$	$\rho_\mu * t_3$	$R_{s3} - R_{YSZ3} - R_{\mu 3}$
4	Low flow	750	t_4	R_{s4}	R_{YSZ4}	$\rho_{\mu 1}$	$\rho_\mu * t_4$	$R_{s4} - R_{YSZ4} - R_{\mu 4}$
5	Low flow	750	t_5	R_{s5}	R_{YSZ5}	$\rho_{\mu 1}$	$\rho_\mu * t_5$	$R_{s5} - R_{YSZ5} - R_{\mu 5}$

4. Calculate the sum of the squared residual values for each cell test combination, where R_{Cx} is the contact resistance determined for each cell test (x = 1 to 5 in this example). The residual represents the difference between calculated values and measured values. Contact resistances were expected to be similar for each cell test and the calculated residual is a measure of the accuracy of this assumption.

Residual = $(R_{C1} - R_{C2})^2 + (R_{C1} - R_{C3})^2 + (R_{C1} - R_{C4})^2 + (R_{C1} - R_{C5})^2 + (R_{C2} - R_{C3})^2 + (R_{C2} - R_{C4})^2 + (R_{C2} - R_{C5})^2 + (R_{C3} - R_{C4})^2 + (R_{C3} - R_{C5})^2 + (R_{C4} - R_{C5})^2$

5. Use the solver feature within Microsoft Excel to set the sum of the squared residuals equation to a minimum value by changing the ρ_μ value. This will give the most likely R_μ and R_C values for each tested cell. When solving the equation the constraints that ρ_μ and R_C are greater than or equal to 0 should be used.

6. Repeat the procedure for each electrolyte microstructure and testing temperature.

F.5 R_s separation sample calculation

The procedure for separating the Rs parameters detailed in the previous section is demonstrated by the following sample calculation.

1. Set up the equations: $R_s = R_{YSZ} + R_\mu + R_C$ where R_s has been measured and R_{YSZ} calculated

Cell name	Microstructure	Temp ^oC	El thickness cm	R_s Ωcm^2	R_{YSZ} Ωcm^2	ρ_μ Ωcm	R_μ Ωcm^2	R_c Ωcm^2
358	Low flow	750	1.558E-03	0.172	0.051		0.000	0.121
360	Low flow	750	1.598E-03	0.174	0.052		0.000	0.122
364	Low flow	750	2.905E-03	0.204	0.094		0.000	0.110
366	Low flow	750	2.943E-03	0.352	0.096		0.000	0.256
363	Low flow	750	4.612E-03	0.418	0.150		0.000	0.268

2. Make an initial guess for the microstructural resistivity values (ρ_μ).

It was found that any number could be used as an initial guess and the system always converged to the same final value.

Cell name	Microstructure	Temp °C	El thickness cm	R_s Ωcm^2	R_{YSZ} Ωcm^2	ρ_μ Ωcm	R_μ Ωcm^2	R_c Ωcm^2
358	Low flow	750	1.558E-03	0.172	0.051	10	0.016	0.106
360	Low flow	750	1.598E-03	0.174	0.052		0.000	0.122
364	Low flow	750	2.905E-03	0.204	0.094		0.000	0.110
366	Low flow	750	2.943E-03	0.352	0.096		0.000	0.256
363	Low flow	750	4.612E-03	0.418	0.150		0.000	0.268

3. Set the ρ_μ values for each comparable test equal to each other

Cell name	Microstructure	Temp °C	El thickness cm	R_s Ωcm^2	R_{YSZ} Ωcm^2	ρ_μ Ωcm	R_μ Ωcm^2	R_c Ωcm^2
358	Low flow	750	1.558E-03	0.172	0.051	10	0.016	0.106
360	Low flow	750	1.598E-03	0.174	0.052	10	0.016	0.106
364	Low flow	750	2.905E-03	0.204	0.094	10	0.029	0.081
366	Low flow	750	2.943E-03	0.352	0.096	10	0.029	0.227
363	Low flow	750	4.612E-03	0.418	0.150	10	0.046	0.222

4. Set up an equation that is a summation of the squared residual values (R_{C1} - R_{C2}) for each cell test combination.

Residual = $(R_{C1} - R_{C2})^2 + (R_{C1} - R_{C3})^2 + (R_{C1} - R_{C4})^2 + (R_{C1} - R_{C5})^2 + (R_{C2} - R_{C3})^2 + (R_{C2} - R_{C4})^2 + (R_{C2} - R_{C5})^2 + (R_{C3} - R_{C4})^2 + (R_{C3} - R_{C5})^2 + (R_{C4} - R_{C5})^2$

Residual = $(0.106 - 0.106)^2 + (0.106 - 0.081)^2 + (0.106 - 0.227)^2 + (0.106 - 0.222)^2 + (0.106 - 0.081)^2 + (0.106 - 0.227)^2 + (0.106 - 0.222)^2 + (0.081 - 0.227)^2 + (0.081 - 0.222)^2 + (0.227 - 0.222)^2$

Residual = 0.099

5. Use the solver feature within Microsoft Excel to set the summation of the squared residuals to a minimum value by changing the ρ_μ value to give the most likely R_μ and R_C values for each tested cell. Use the constraints that ρ_μ and R_C are greater than or equal to 0.

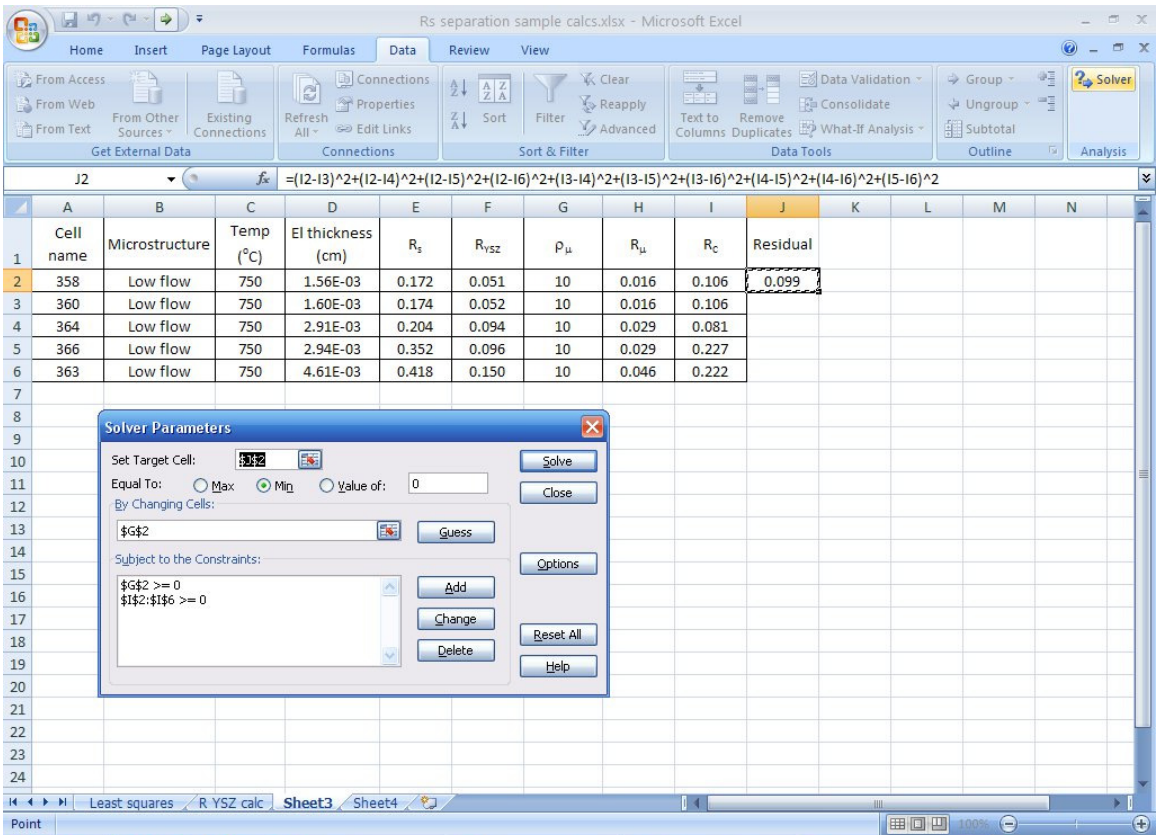

The values of R_μ, R_C, and ρ_μ after solving to produce the minimized sum of the squared residual value are shown in the table below.

Cell name	Microstructure	Temp (°C)	El thickness (cm)	R_s Ωcm^2	R_{YSZ} Ωcm^2	ρ_μ Ωcm	R_μ Ωcm^2	R_c Ωcm^2
358	Low flow	750	1.558E-03	0.172	0.051	37.76775	0.059	0.062
360	Low flow	750	1.598E-03	0.174	0.052	37.76775	0.060	0.061
364	Low flow	750	2.905E-03	0.204	0.094	37.76775	0.110	0.000
366	Low flow	750	2.943E-03	0.352	0.096	37.76775	0.111	0.145
363	Low flow	750	4.612E-03	0.418	0.150	37.76775	0.174	0.094

Residual = 0.056

F.6 Summary of R_s separation values

A summary of the calculated R_μ, R_C, and ρ_μ and squared residual values is shown in Table F.1.

Table F.1: Summary of R_μ, R_C, and ρ_μ and squared residual values.

Cell #	Electrolyte microstructure	Temp °C	Thickness μm	R_s Ωcm^2	R_{YSZ} Ωcm^2	ρ_μ Ωcm	R_μ Ωcm^2	R_c Ωcm^2	Residual
358	Low flow	750	15.58	0.172	0.051	37.769	0.059	0.062	0.0561
360	Low flow	750	15.98	0.174	0.052	37.769	0.060	0.061	
364	Low flow	750	29.05	0.204	0.094	37.769	0.110	0.000	
366	Low flow	750	29.43	0.352	0.096	37.769	0.111	0.145	
363	Low flow	750	46.12	0.418	0.150	37.769	0.174	0.094	
362	Low flow	750	46.32	0.616	0.151	37.769	0.175	0.290	
350	Medium flow	750	15.98	0.120	0.052	17.115	0.027	0.041	0.0076
348	Medium flow	750	16.53	0.239	0.054	17.115	0.028	0.157	
355	Medium flow	750	28.99	0.265	0.094	17.115	0.050	0.121	
356	Medium flow	750	29.00	0.235	0.094	17.115	0.050	0.091	
351	Medium flow	750	39.06	0.229	0.127	17.115	0.067	0.036	
353	Medium flow	750	40.90	0.260	0.133	17.115	0.070	0.056	
374	High flow	750	18.51	0.115	0.060	26.180	0.048	0.006	0.0094
377	High flow	750	29.91	0.240	0.097	26.180	0.078	0.064	
375	High flow	750	30.50	0.246	0.099	26.180	0.080	0.067	
380	High flow	750	44.42	0.261	0.145	26.180	0.116	0.000	
379	High flow	750	45.90	0.318	0.149	26.180	0.120	0.049	
358	Low flow	700	15.58	0.296	0.083	81.945	0.128	0.084	0.0449
360	Low flow	700	15.98	0.272	0.086	81.945	0.131	0.055	
364	Low flow	700	29.05	0.394	0.156	81.945	0.238	0.000	
366	Low flow	700	29.43	0.528	0.158	81.945	0.241	0.129	
363	Low flow	700	46.12	0.707	0.247	81.945	0.378	0.082	
362	Low flow	700	46.32	0.725	0.248	81.945	0.380	0.098	
350	Medium flow	700	15.98	0.205	0.086	43.121	0.069	0.050	0.0132
348	Medium flow	700	16.53	0.304	0.088	43.121	0.071	0.145	
355	Medium flow	700	28.99	0.415	0.155	43.121	0.125	0.135	
356	Medium flow	700	29.00	0.377	0.155	43.121	0.125	0.097	
351	Medium flow	700	39.06	0.469	0.209	43.121	0.168	0.091	
353	Medium flow	700	40.90	0.423	0.219	43.121	0.176	0.028	
374	High flow	700	18.51	0.208	0.099	44.131	0.082	0.027	0.0132
377	High flow	700	29.91	0.366	0.160	44.131	0.132	0.074	

Cell #	Electrolyte microstructure	Temp ^{o}C	Thickness μm	R_s Ωcm^2	R_{YSZ} Ωcm^2	ρ_μ Ωcm	R_μ Ωcm^2	R_c Ωcm^2	Residual
375	High flow	700	30.50	0.400	0.163	44.131	0.135	0.102	
380	High flow	700	44.42	0.434	0.238	44.131	0.196	0.000	
379	High flow	700	45.90	0.540	0.246	44.131	0.203	0.091	
358	Low flow	650	15.58	0.509	0.147	167.32	0.261	0.100	
360	Low flow	650	15.98	0.449	0.151	167.32	0.267	0.031	
364	Low flow	650	29.05	0.761	0.275	167.32	0.486	0.000	0.0751
366	Low flow	650	29.43	0.922	0.279	167.32	0.492	0.151	
363	Low flow	650	46.12	1.320	0.436	167.32	0.772	0.112	
362	Low flow	650	46.32	1.510	0.438	167.32	0.775	0.297	
350	Medium flow	650	15.98	0.378	0.151	62.432	0.100	0.127	
348	Medium flow	650	16.53	0.474	0.156	62.432	0.103	0.215	
355	Medium flow	650	28.99	0.692	0.274	62.432	0.181	0.236	0.0051
356	Medium flow	650	29.00	0.612	0.274	62.432	0.181	0.156	
351	Medium flow	650	39.06	0.724	0.370	62.432	0.244	0.110	
353	Medium flow	650	40.90	0.789	0.387	62.432	0.255	0.147	
374	High flow	650	18.51	0.374	0.175	92.995	0.172	0.026	
377	High flow	650	29.91	0.603	0.283	92.995	0.278	0.042	
375	High flow	650	30.50	0.752	0.289	92.995	0.284	0.179	0.0818
380	High flow	650	44.42	0.834	0.420	92.995	0.413	0.000	
379	High flow	650	45.90	1.035	0.434	92.995	0.427	0.174	
358	Low flow	600	15.58	0.998	0.279	361.39	0.563	0.155	
360	Low flow	600	15.98	0.864	0.286	361.39	0.577	0.000	
364	Low flow	600	29.05	1.574	0.520	361.39	1.050	0.004	
366	Low flow	600	29.43	1.760	0.527	361.39	1.064	0.169	0.1649
363	Low flow	600	46.12	2.671	0.826	361.39	1.667	0.178	
362	Low flow	600	46.32	2.825	0.830	361.39	1.674	0.321	
350	Medium flow	600	15.98	0.724	0.286	175.46	0.280	0.157	
348	Medium flow	600	16.53	0.862	0.296	175.46	0.290	0.276	
355	Medium flow	600	28.99	1.365	0.519	175.46	0.509	0.337	
356	Medium flow	600	29.00	1.159	0.520	175.46	0.509	0.131	0.0039
351	Medium flow	600	39.06	1.520	0.700	175.46	0.685	0.135	
353	Medium flow	600	40.90	1.619	0.733	175.46	0.718	0.169	
374	High flow	600	18.51	0.812	0.332	195.57	0.362	0.119	
377	High flow	600	29.91	1.121	0.536	195.57	0.585	0.000	
375	High flow	600	30.50	1.542	0.546	195.57	0.596	0.399	0.3741
380	High flow	600	44.42	1.836	0.796	195.57	0.869	0.172	
379	High flow	600	45.90	2.006	0.822	195.57	0.898	0.285	

F.7 Reference

1. A. Weber and E. Ivers-Tiffee, Journal of Power Sources, 127(1-2) (2004), 273-283.

G Yttria stabilized zirconia phase diagram

The phase diagram for yttria and zirconia is shown in Figure G.1 [1]. Yttria stabilized zirconia powders containing 8 mol% Y_2O_3 (or 16 mol% $YO_{1.5}$) were used for all studies within this thesis. According to the phase diagram, the powders should be cubic in phase at room temperature.

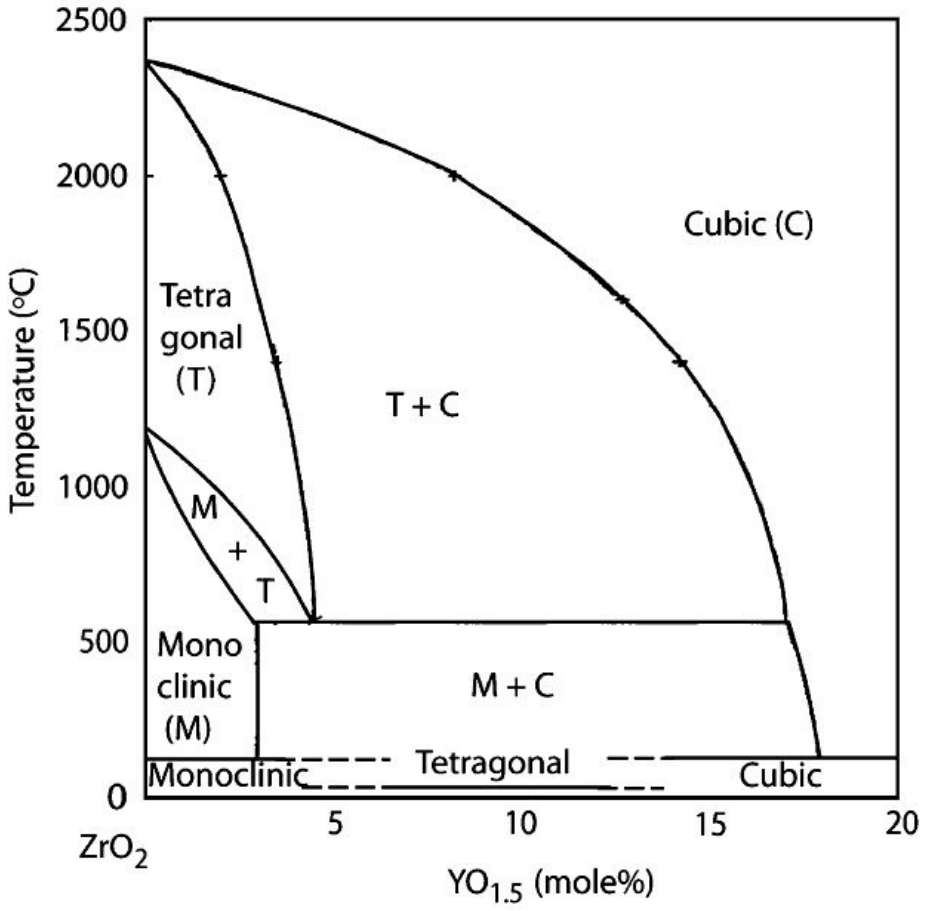

Figure G.1: Yttria and zirconia phase diagram[41].

[41] Reprinted from Journal of the American Ceramic Society, 90 / 9, G. Witz, V. Shklover, W. Steurer, S. Bachegowda, and H.P. Bossmann, Phase Evolution in Yttria-Stabilized Zirconia Thermal Barrier Coatings Studied by Rietveld Refinement of X-Ray Powder Diffraction Patterns, 2935-2940, Copyright (2007), with permission from John Wiley and Sons.

G.1 Reference

1. G. Witz, V. Shklover, W. Steurer, S. Bachegowda, and H.P. Bossmann, Journal of the American Ceramic Society, 90(9) (2007), 2935–2940.

H Extended PS SOFC microstructural study

H.1 PS SOFC layer microstructures

Figures H.1 to H.6 show microstructures observed for electrochemically tested plasma sprayed (PS) solid oxide fuel cells (SOFCs) and metal support layers in greater detail compared to the thesis chapters. Figure H.1 shows the general microstructure for a PS SOFC, while Figure H.2 shows an energy dispersive x-ray analysis (EDX) map showing the mixing and distribution of key elements within each of the anode, electrolyte, cathode, and substrate layers. 8 mole % yttria-stabilized zirconia (YSZ) was used to produce the suspension plasma sprayed (SPS) electrolyte layers shown in Figure H.3. Porous NiO / YSZ anode layers (Figure H.4) were deposited by plasma spraying (PS) and the NiO component was reduced to Ni metal during cell electrochemical testing. 9.3 wt% of a commercially available flour (Robin Hood All-purpose Flour, Smuckers Foods of Canada, Markham, ON, Canada) was added to the anode powder before plasma spraying to serve as a pore former. PS porous lanthanum strontium manganite (LSM) / YSZ cathode layers are shown in Figure H.5. Figure H.6 shows the microstructure of the porous media grade 2 ferritic stainless steel 430 metal substrates.

There was excellent coverage and strong adhesion between the stainless steel support, cathode and electrolyte layers, even after a number of slow thermal cycles introduced during cell testing. Electrolyte layers were thin and continuous and had low porosities. Anode layers were quite thick and had unevenly distributed porosity. The larger, unevenly distributed pores present in the anode layer are likely due to the flour pore former used, while the smaller, more evenly distributed pores present are likely due to the porosity introduced as the sprayed NiO is reduced. The cathode layer components (LSM and YSZ) were well mixed, there was some porosity present in the layers, and the cathode layers were able to fill and cover the large, deep pores present in the support material.

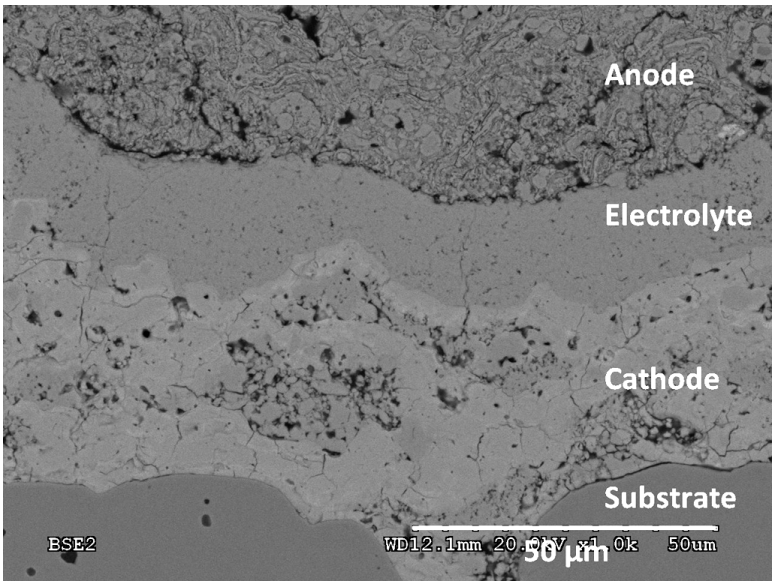

Figure H.1: General microstructure of a PS SOFC.

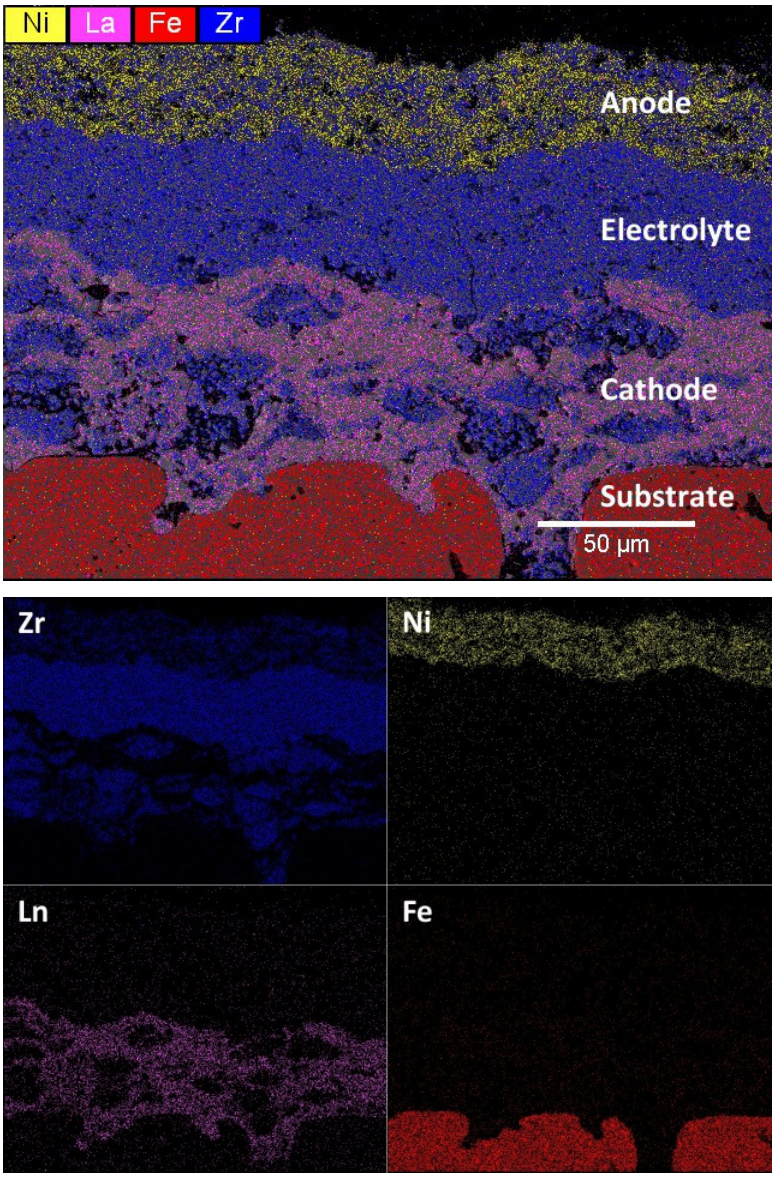

Figure H.2: SEM EDX map showing the various cell components in a PS SOFC.

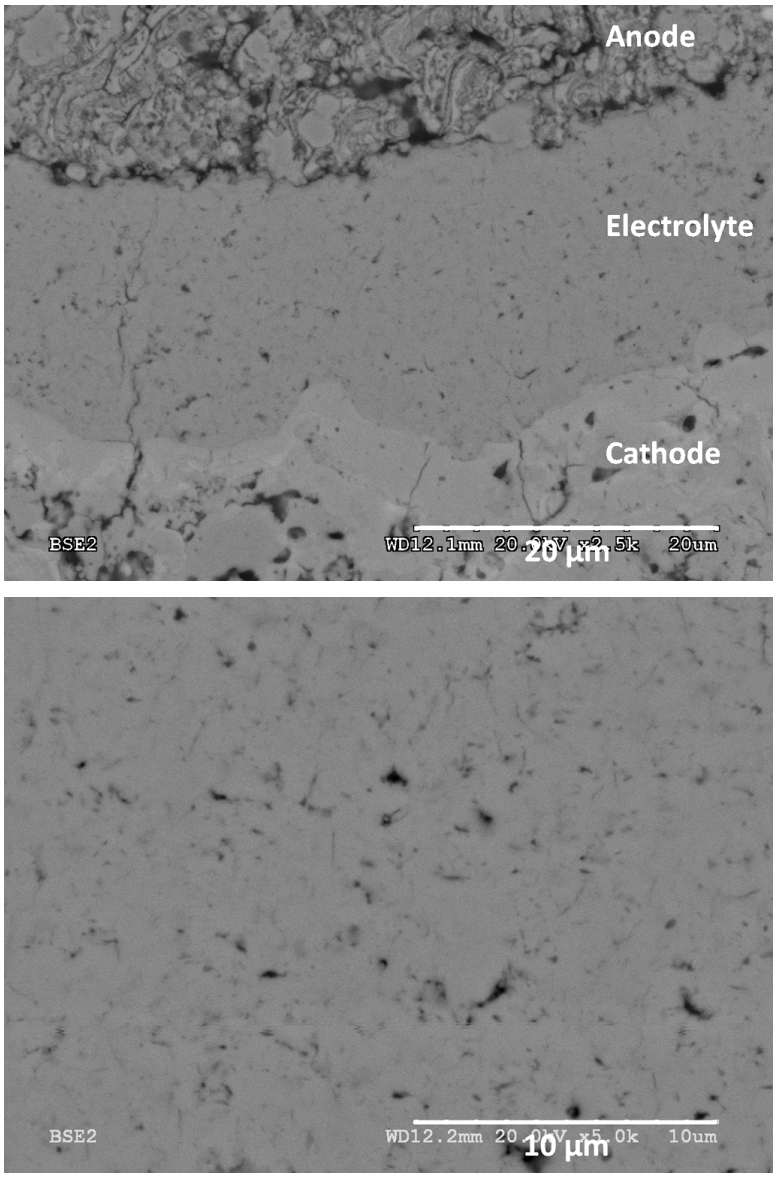

Figure H.3: SPS YSZ SOFC electrolyte microstructure.

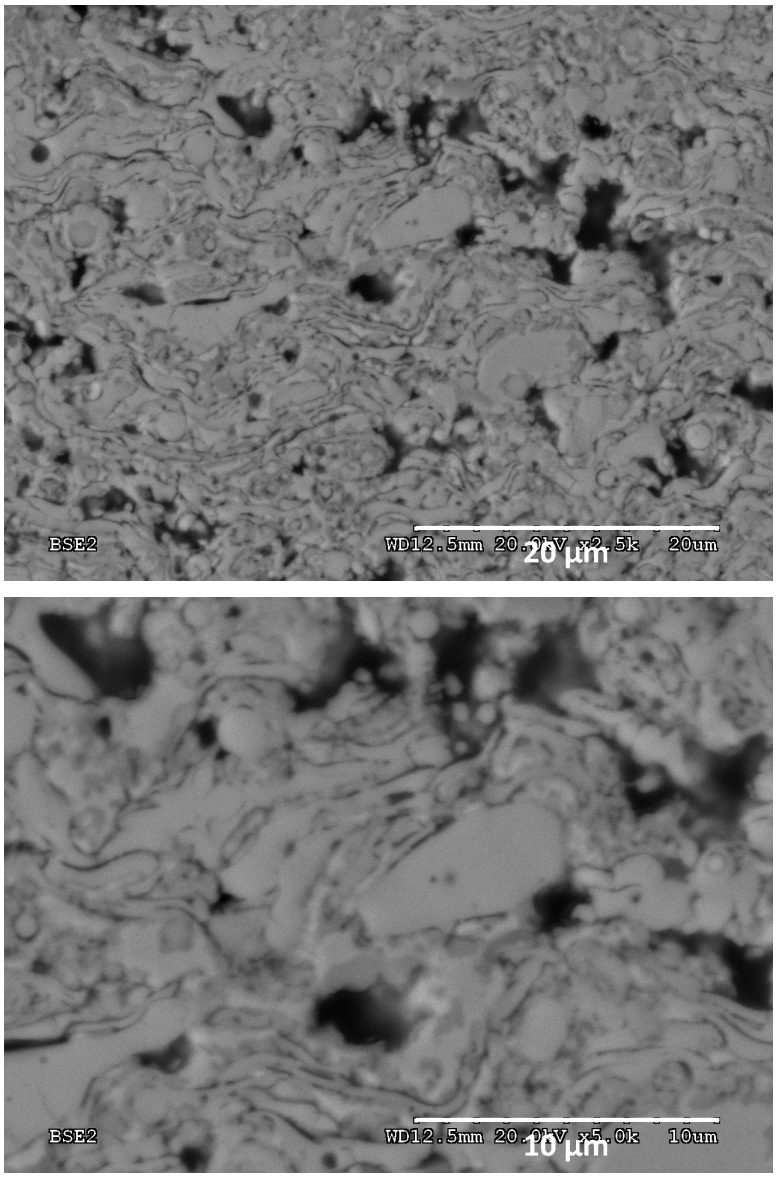

Figure H.4: PS Ni / YSZ SOFC anode microstructure.

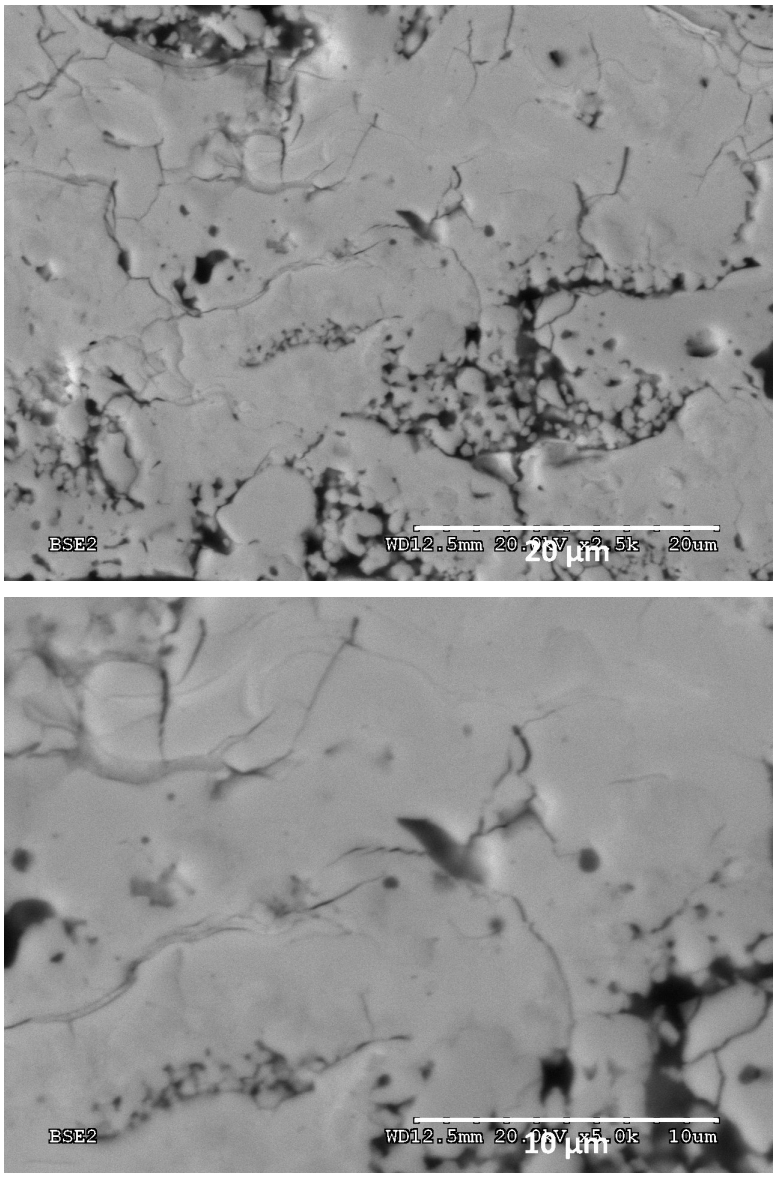

Figure H.5: PS LSM / YSZ SOFC cathode microstructure.

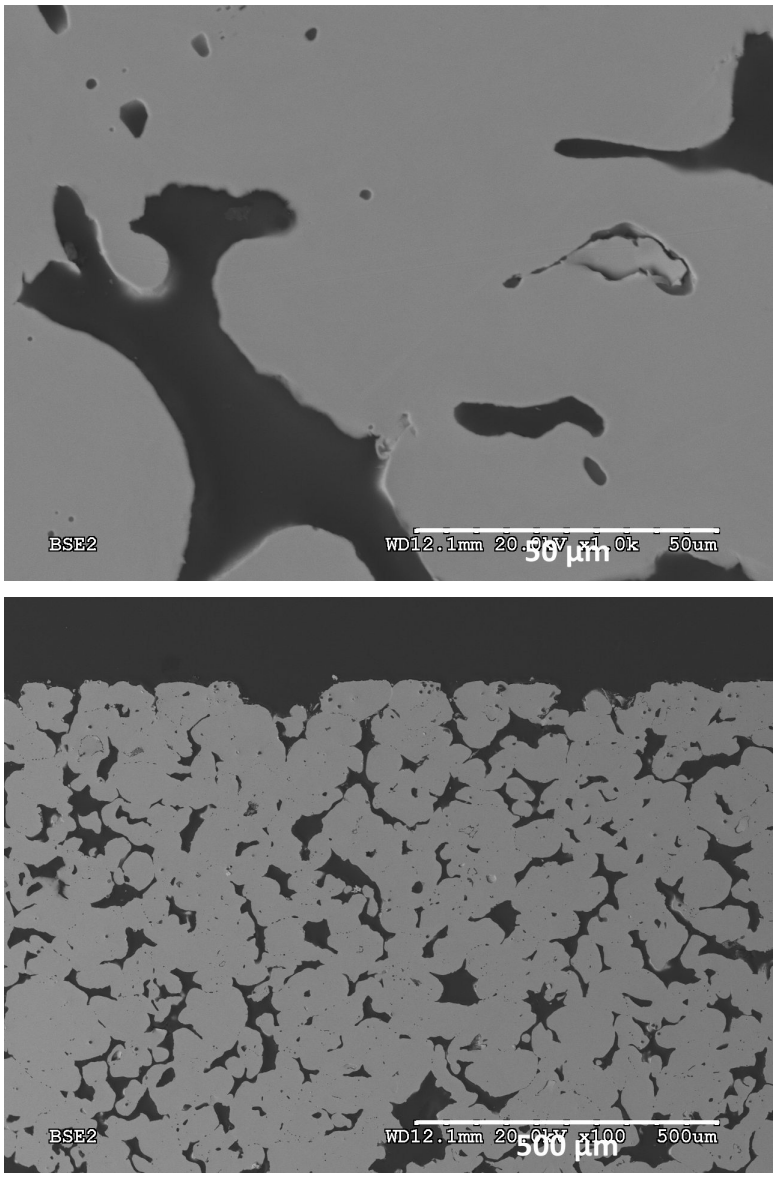

Figure H.6: Porous stainless steel 430 substrate microstructure.

H.2 Comparison between PS and wet ceramic SOFC microstructures

The microstructure and open circuit voltage values of PS SOFC were compared to conventional wet ceramic produced SOFCs that were produced by the National Research Council Institute for Fuel Cell Innovation (NRC-IFCI). This comparison allowed a qualitative assessment of PS fuel cell layer and metal support microstructures to be made and compared to traditional wet ceramic microstructures. In addition, open circuit voltage

measurements of the two cell configurations allowed a comparison of the electrochemical performance between the low porosity PS electrolyte layers and the approximately fully dense, sintered electrolyte layers and allowed an estimate of the leakage rate of the gasket seals to be made (see Appendix E for sealing details).

Electrolyte microstructures are compared in Figure H.7. Wet ceramic electrolyte layers appear to be very dense and to have few connected pores or defects. SPS electrolyte layers are less dense and contain areas with connected porosity and vertical cracking, which reduce electrolyte performance. The electrochemically tested wet ceramic layers achieved an open circuit voltage (OCV) of 1.02 V, while SPS electrolytes had an OCV of 0.93 V, both at 750^{o}C with 20% H_2 fuel. These values can be compared to the theoretically predicted Nernst voltage of 1.04 V for these conditions. This result indicates that approximately 20 mV of the OCV losses can be attributed to seal leakage.

Figure H.8 compares the microstructures of PS and wet ceramic produced SOFCs, while Figure H.9 compares the microstructure of a tape cast Ni / YSZ cermet anode substrate and a porous stainless steel metal substrate. It can be seen in Figure H.8 that the wet ceramic produced electrode layers have finer, more evenly distributed microstructures and porosity compared to the PS layers. Tape cast supports layers appear to be flatter than the metal supports and plasma sprayed layers, which may make it easier for the wet ceramic methods to produce dense electrolyte layers, and that the tape cast substrates have much finer microstructures and porosities compared to the metal support layers.

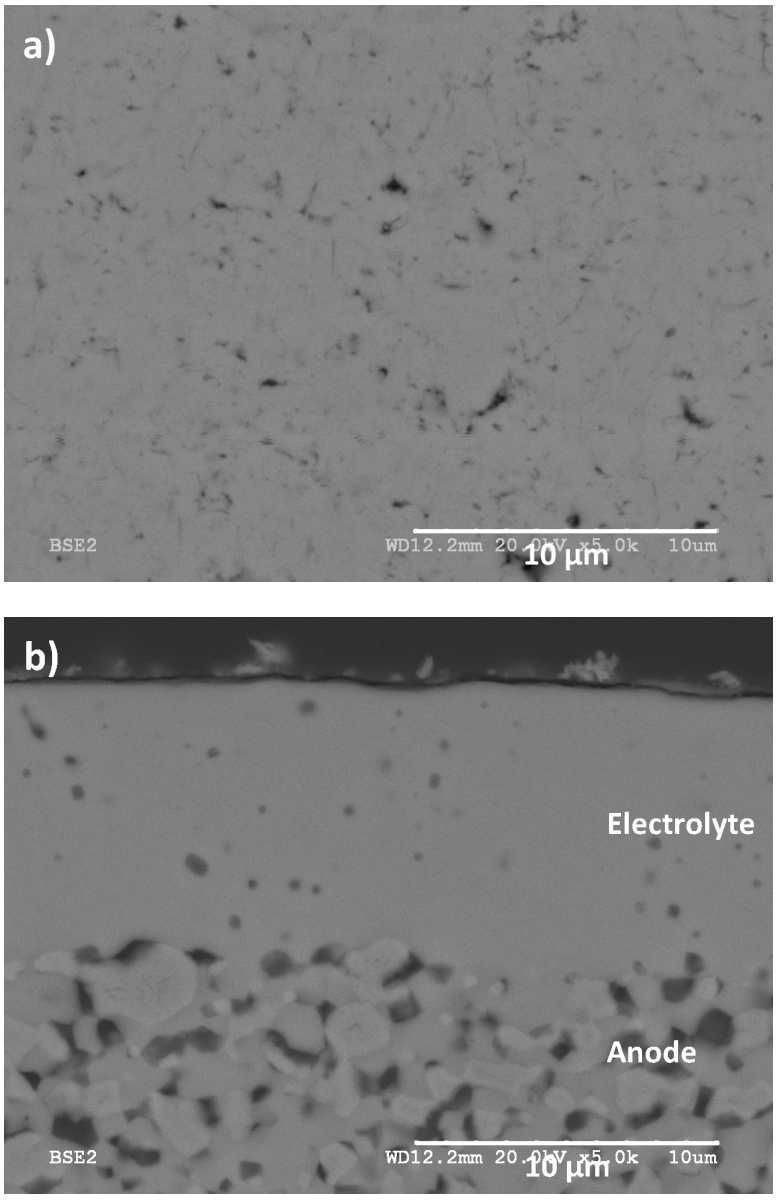

Figure H.7: Comparison between the microstructure of a) an SPS SOFC electrolyte and b) a screen printed and sintered SOFC electrolyte.

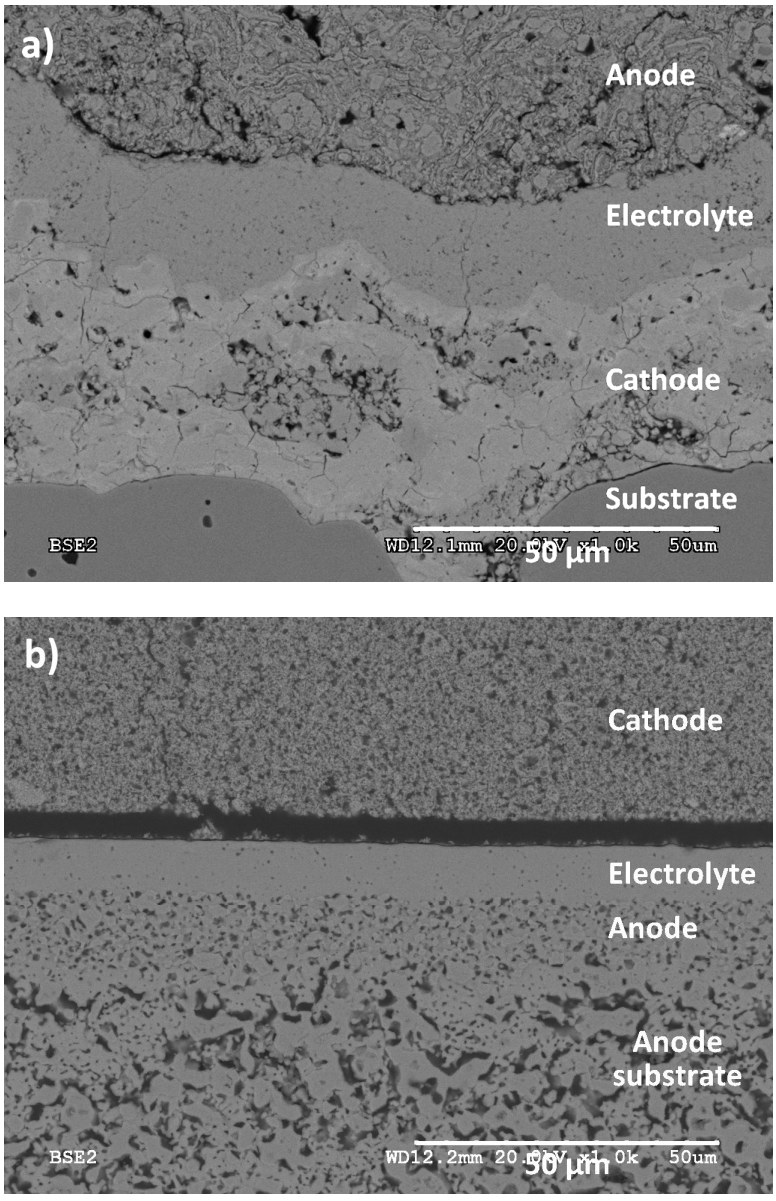

Figure H.8: Comparison between the microstructure of a) a PS SOFC and b) a wet ceramic produced (tape cast and screen printed) SOFC.

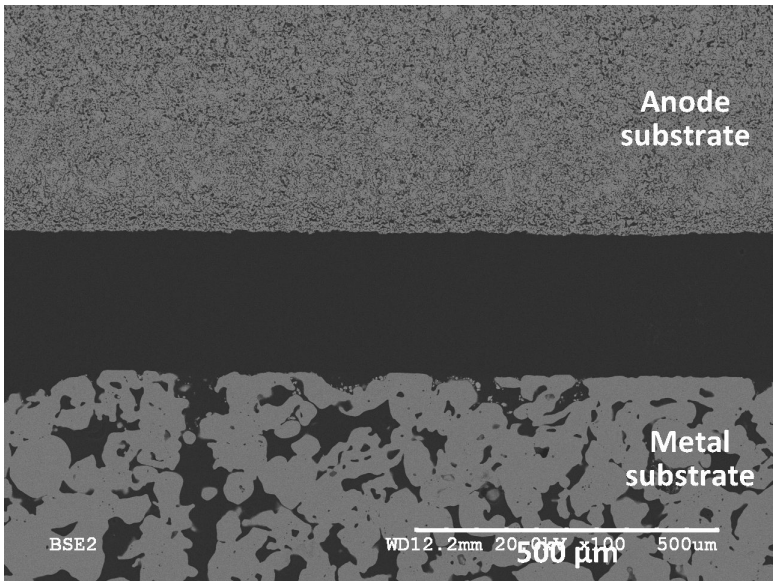

Figure H.9: Comparison between the microstructure of a tape cast anode substrate (top) and a media grade 2 stainless steel 430 metal substrate (bottom).

H.3 PS SOFCs from Chapter 6

In chapter 6 of the thesis, PS SOFCs with suspension plasma sprayed electrolyte layers were produced from one of three conditions listed in Table H.1. The spraying conditions were labelled as having high, medium, or low flow rates, which indicates the relative plasma gas flow rates used. Electrolytes having nominal thicknesses of 15, 30, or 45 µm were produced in order to examine the effect of electrolyte thickness on the physical and electrochemical properties of the cell. The cell microstructures and electrolyte microstructures of the cells produced with each spraying condition and electrolyte thickness are shown in Figures H.10 to H.18. It can be seen in the figures that electrolyte layers produced from high flow conditions appeared to be the most dense, followed by those produced by medium and low flow conditions, respectively.

Table H.1: Electrolyte suspension plasma processing parameters.

Parameter	High flow rate	Medium flow rate	Low flow rate
Plasma gas flow rate (slpm)	275	250	230
Plasma gas composition (%)	70% N_2, 25% Ar, 5% H_2	80% N_2, 15% Ar 5% H_2	87% N_2, 13% Ar
Current (A per cathode)	250	250	250
Nozzle size (mm)	9.5	9.5	9.5
Preheat temperature (°C)	300 - 350	300 - 350	300 - 350
Standoff distance (mm)	90	80	80

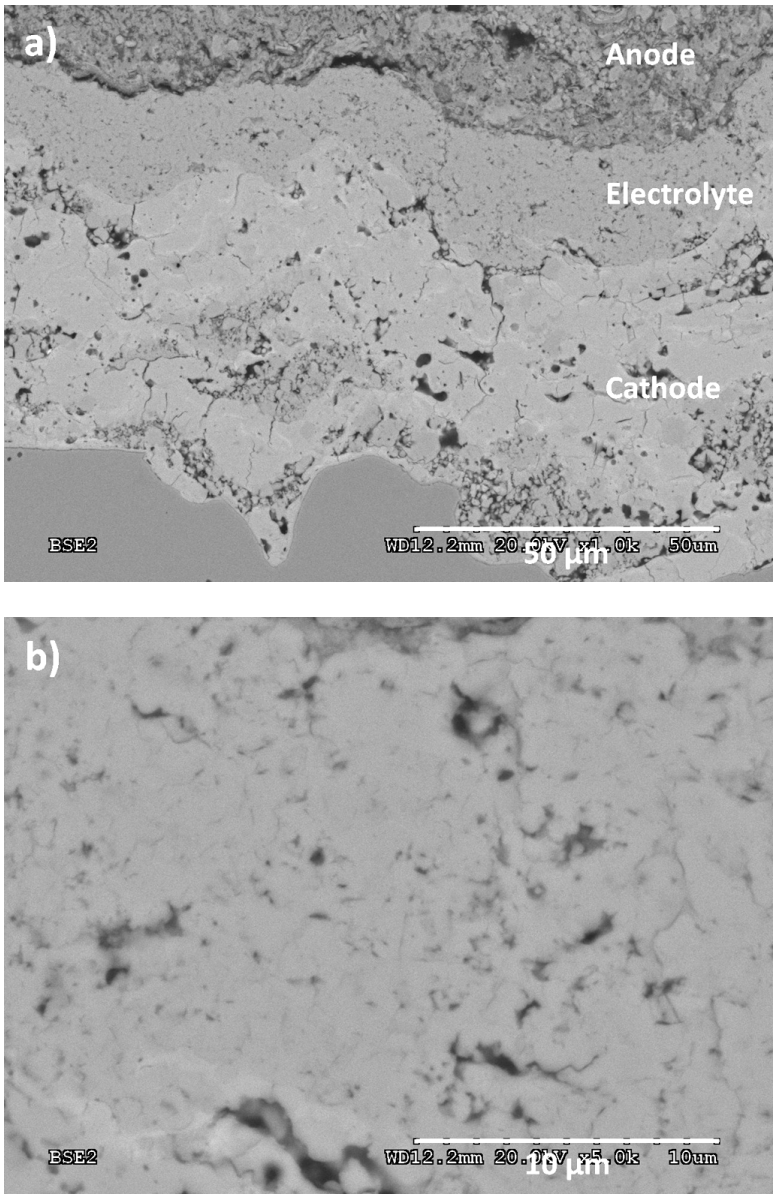

Figure H.10: a) Microstructure of a PS SOFC with a nominally 15 µm thick electrolyte layer that was produced from the low flow rate SPS conditions and b) and high magnification image of the SPS electrolyte layer.

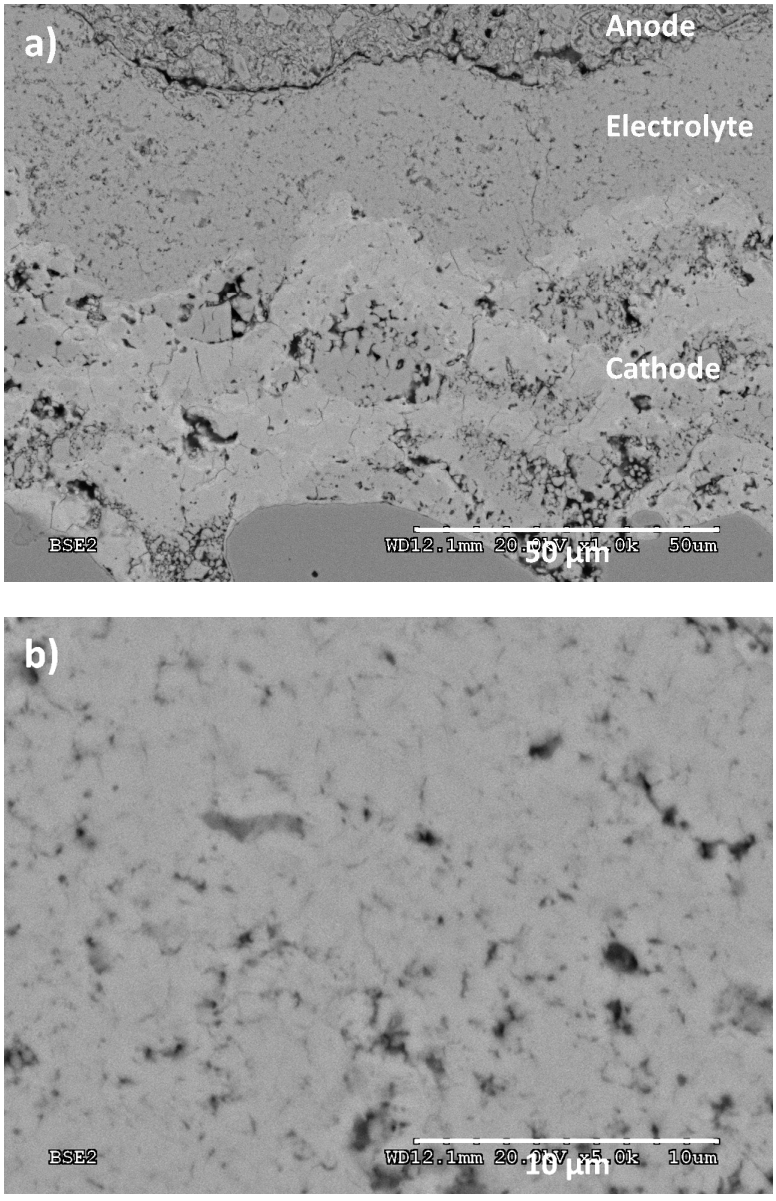

Figure H.11: a) Microstructure of a PS SOFC with a nominally 30 µm thick electrolyte layer that was produced from the low flow rate SPS conditions and b) and high magnification image of the SPS electrolyte layer.

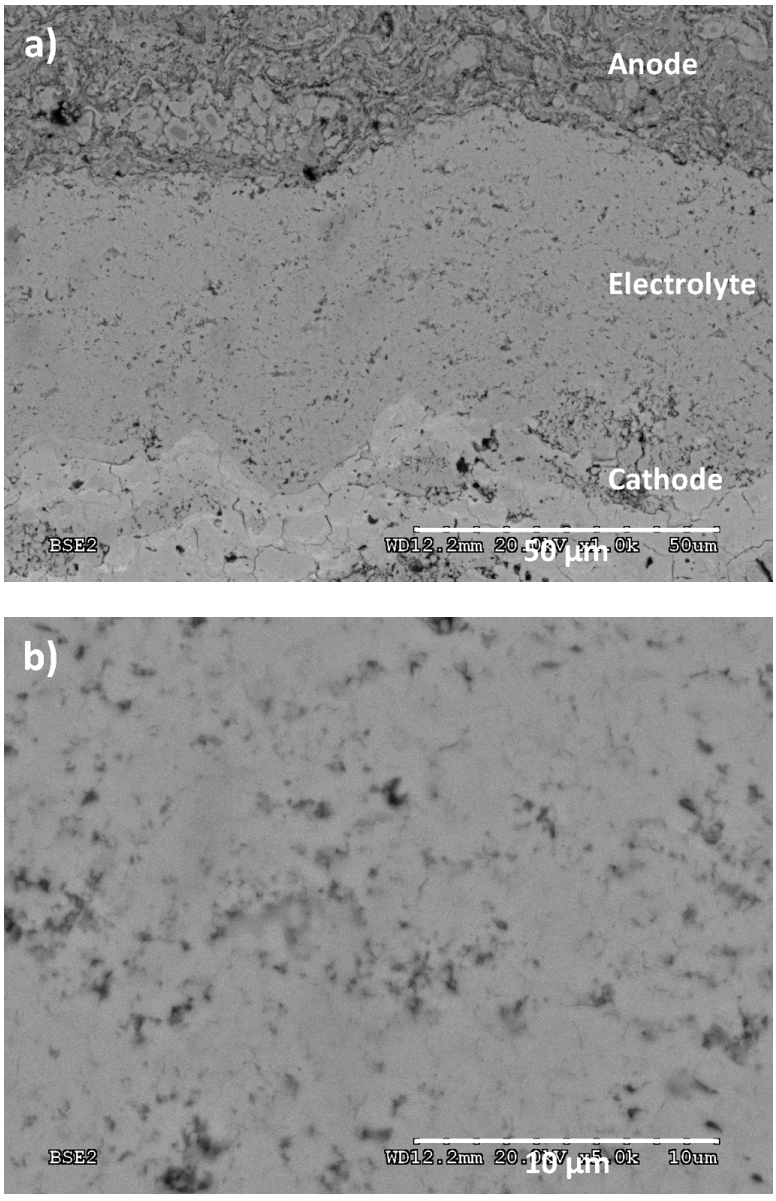

Figure H.12: a) Microstructure of a PS SOFC with a nominally 45 µm thick electrolyte layer that was produced from the low flow rate SPS conditions and b) and high magnification image of the SPS electrolyte layer.

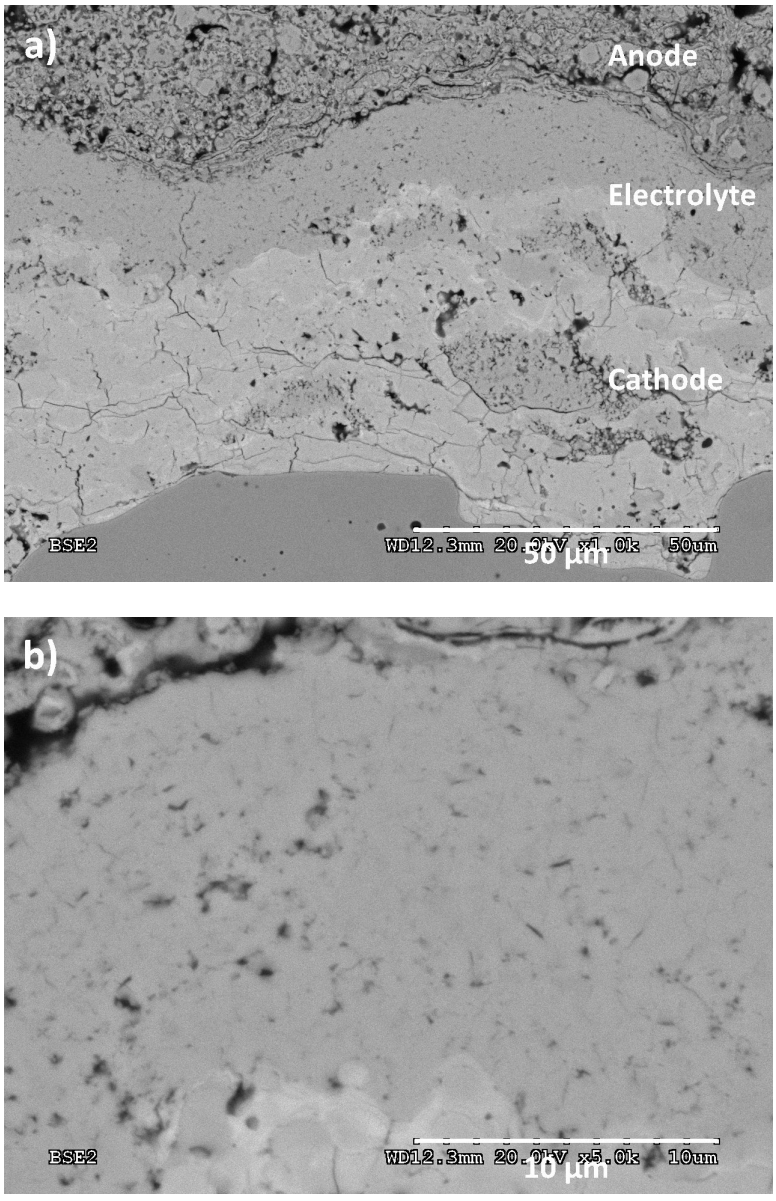

Figure H.13: a) Microstructure of a PS SOFC with a nominally 15 µm thick electrolyte layer that was produced from the medium flow rate SPS conditions and b) and high magnification image of the SPS electrolyte layer.

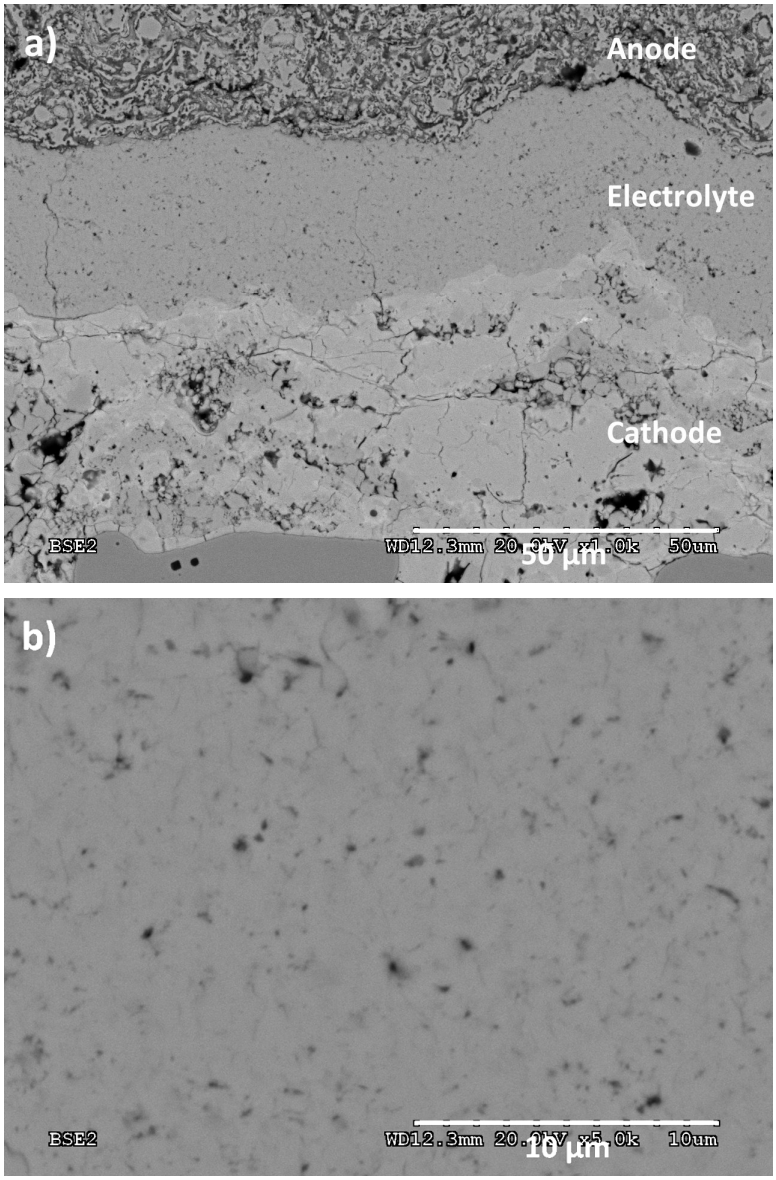

Figure H.14: a) Microstructure of a PS SOFC with a nominally 30 µm thick electrolyte layer that was produced from the medium flow rate SPS conditions and b) and high magnification image of the SPS electrolyte layer.

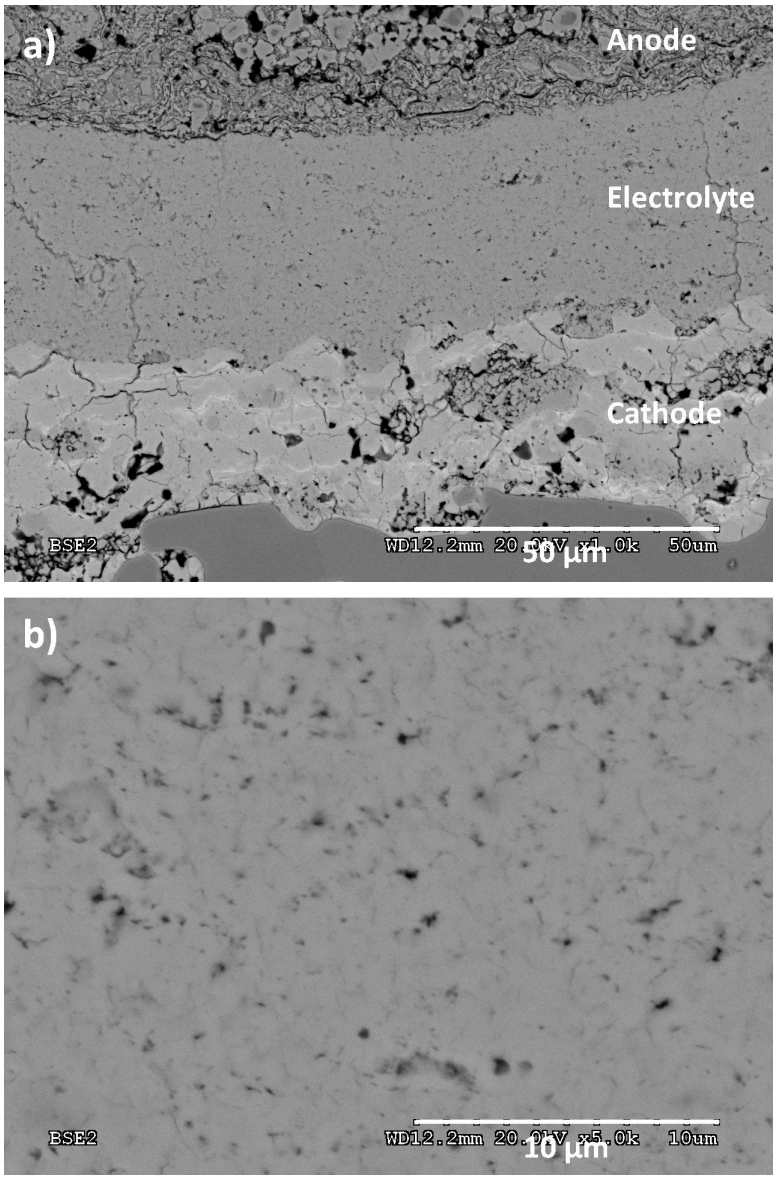

Figure H.15: a) Microstructure of a PS SOFC with a nominally 45 µm thick electrolyte layer that was produced from the medium flow rate SPS conditions and b) and high magnification image of the SPS electrolyte layer.

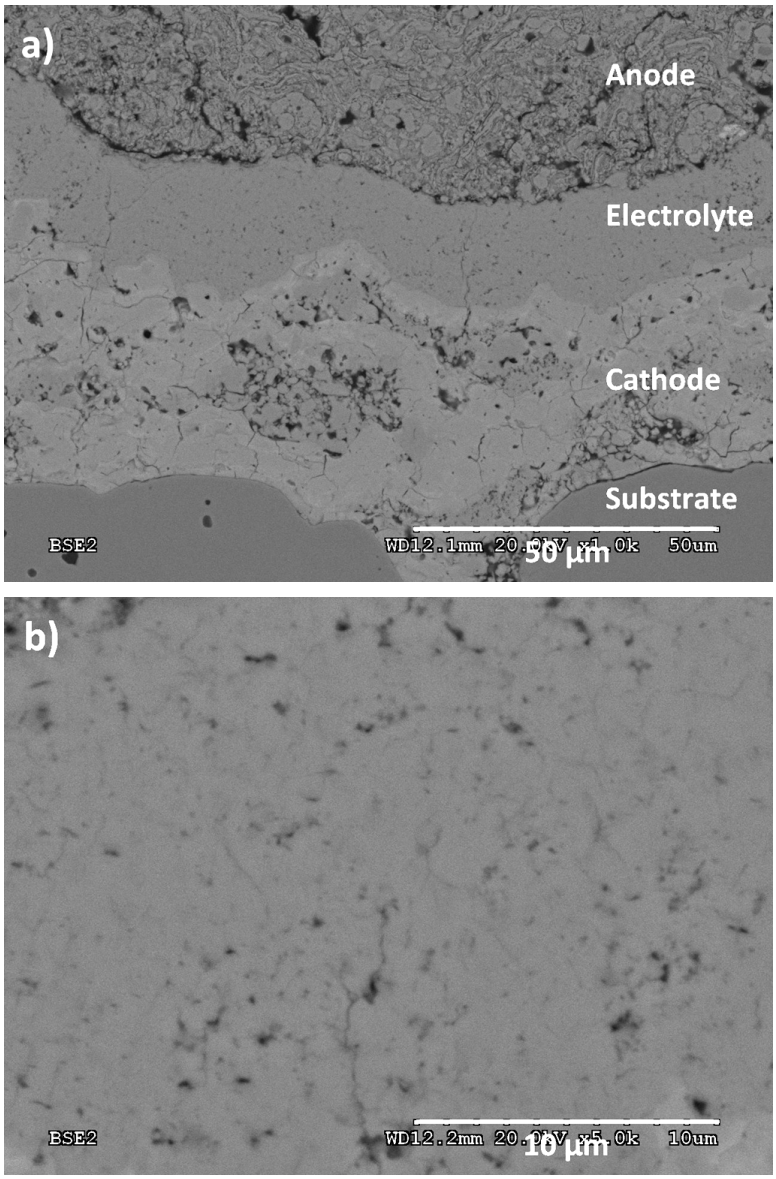

Figure H.16: a) Microstructure of a PS SOFC with a nominally 15 µm thick electrolyte layer that was produced from the high flow rate SPS conditions and b) and high magnification image of the SPS electrolyte layer.

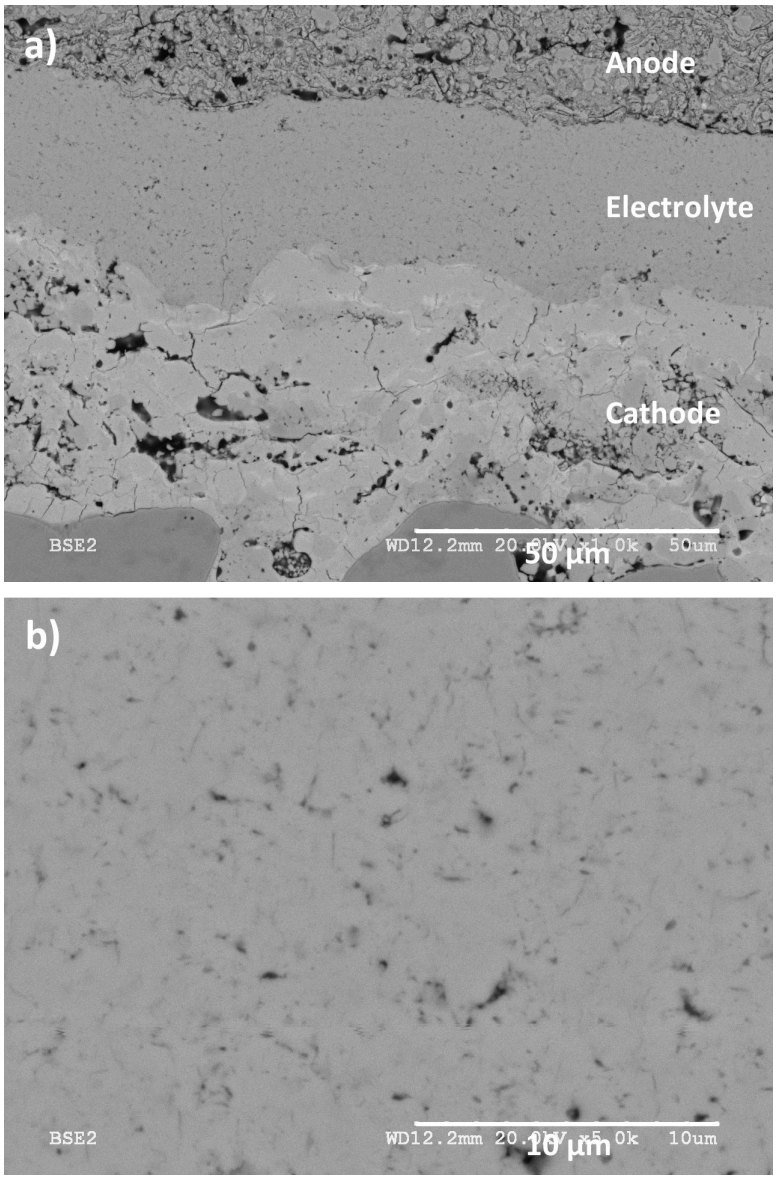

Figure H.17: a) Microstructure of a PS SOFC with a nominally 30 µm thick electrolyte layer that was produced from the high flow rate SPS conditions and b) and high magnification image of the SPS electrolyte layer.

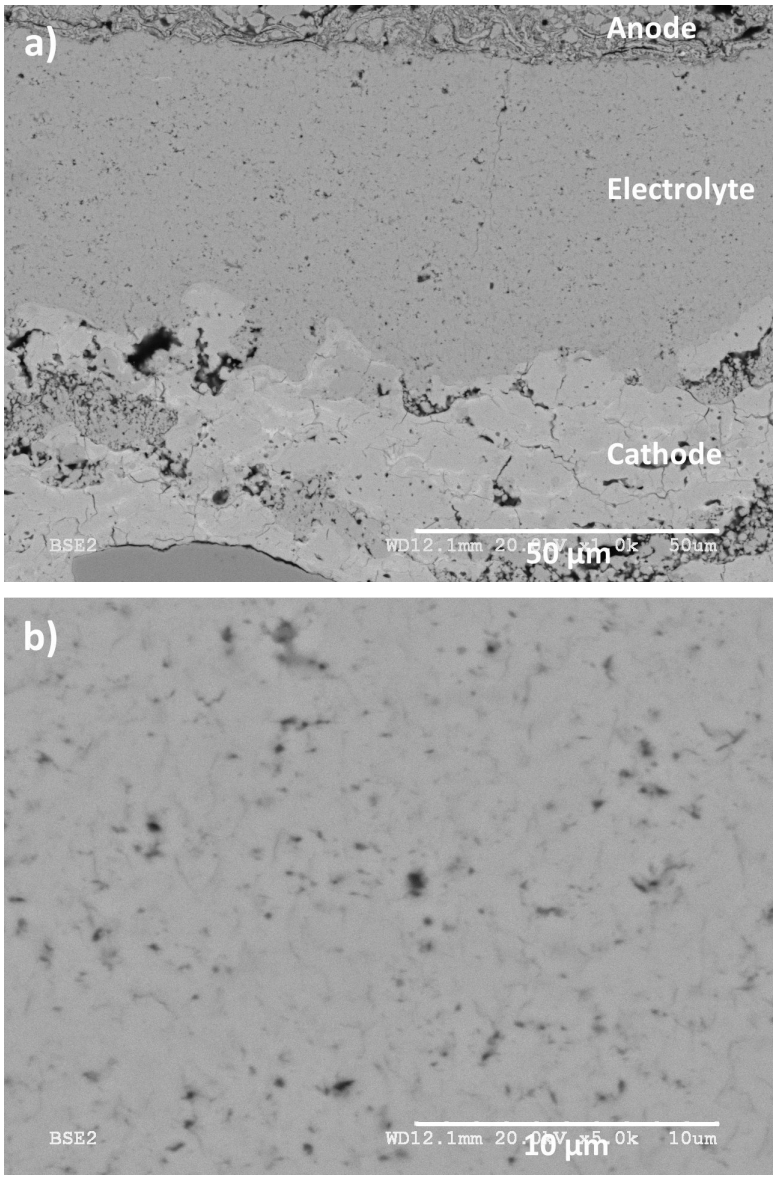

Figure H.18: a) Microstructure of a PS SOFC with a nominally 45 µm thick electrolyte layer that was produced from the high flow rate SPS conditions and b) and high magnification image of the SPS electrolyte layer.

I Dispersant background

I.1 Polyelectrolyte dispersants

Polyelectrolyte dispersants can provide both electrostatic and steric stabilization. These polyelectrolytes typically consist of an ionizable group such as carboxylic acid and a polymeric, chain-like structure. These dispersants may be positively (cationic) or negatively (anionic) charged, depending on the functional group they contain. Cationic dispersants contain positive functional groups such as amines, while anionic dispersants contain negative functional groups such as carboxylic or sulfonic acid. The adsorption properties of these polyelectrolytes are very dependent on the chemical and physical properties of the particle surfaces and solvent medium [1].

I.2 Dispersant choice

In order to improve the dispersion of the YSZ particles in the suspension, the effect of three dispersant materials on suspension viscosity and zeta potential was investigated. After a study of the relevant literature, polyacrylic acid (PAA), polyethyleneimine (PEI), and 2-phosphonobutane-1,2,4-tricarboxylic acid (PBTCA) were chosen. PAA under the trade name Dispex A40 was sourced from Ciba Specialty Chemicals. PEI was purchased from Sigma Aldrich. PBTCA under the trade name Dequest 7000 was received from Solutia Inc. The properties of the three dispersant materials are given in Table I.1.

Table I.1: Dispersant materials.

Chemical name	Trade name	Average molecular weight (M_w)	Anionic or cationic	pH	Method of stabilization
Ammonium – PAA	Dispex A40	4000	Anionic	8.0	Electrostatic
PBTCA	Dequest 7000	270	Anionic	2.0	Electrostatic and steric
PEI	N/A	25000	Cationic	11.0	Electrostatic and steric

I.2.1 Polyacrylic acid

Polyacrylic acid (PAA) is one of the most commonly used anionic dispersants for YSZ and is usually utilized at pH values close to 9. It consists of a number of carboxylic acid groups that act as binding agents. The structure of PAA is shown in Figure I.1.

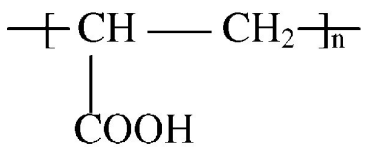

Figure I.1: PAA structure[42] [2].

I.2.2 2-phosphonobutane-1,2,4-tricarboxylic acid

2-phosphonobutane-1,2,4-tricarboxylic acid (PBTCA) is most commonly used as a scale and corrosion inhibitor, but has also been identified as having anionic dispersant properties [2]. The molecule contains three carboxylic acid groups and one phosphonyl group that act as

[42] Reprinted from Materials Chemistry and Physics, 78 / 2, Y. Liu, L. Gao, Deflocculation study of aqueous nanosized Y–TZP suspensions, 480-485, Copyright (2002), with permission from Elsevier.

binding agents. It has been proposed that phosphonyl groups may have higher affinity for metal oxides such as zirconia and alumina compared to carboxylate groups [2]. This may mean that PBTCA, which contains both carboxylate and phosphonyl groups, may bond more strongly to the particle surfaces than dispersants such as PAA that only have carboxylate groups. The structure of PBTCA is shown in Figure I.2.

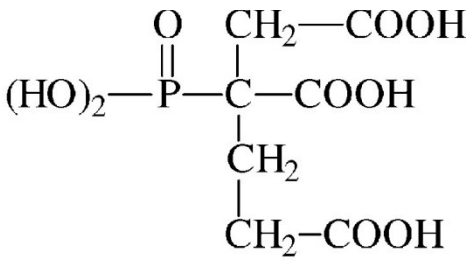

Figure I.2: PBTCA structure[43] [2].

In this study, very low levels of PBTCA additions (0.005 – 0.01%) increased the positive zeta potential value and shifted the isoelectric point to higher pH values (Figure I.3). This behaviour is not expected from the anionic nature of the molecule, but may be caused by PBTCA's ability to act as a steric dispersant [3]. At low PBTCA concentrations, this steric effect may be more significant compared to the electrostatic effect, which may allow the anionic PBTCA to enhance the stability of the suspensions at pH values below the isoelectric point. However, as the amount of PBTCA increases, the electrostatic effects become dominant, which makes the suspension less stable at pH values below the isoelectric point.

Suspensions with larger PBTCA additions (≥0.5%) followed the expected behaviour for an anionic dispersant, increasing the negative zeta potential magnitude and shifting the isoelectric point to a lower pH value (Figure I.3). This result indicates that PBTCA is an

[43] Reprinted from Materials Chemistry and Physics, 78 / 2, Y. Liu, L. Gao, Deflocculation study of aqueous nanosized Y–TZP suspensions, 480-485, Copyright (2002), with permission from Elsevier.

effective electrostatic dispersant at pH values higher than the isoelectric point, while below the isoelectric point, stabilization at low concentrations is due to steric effects.

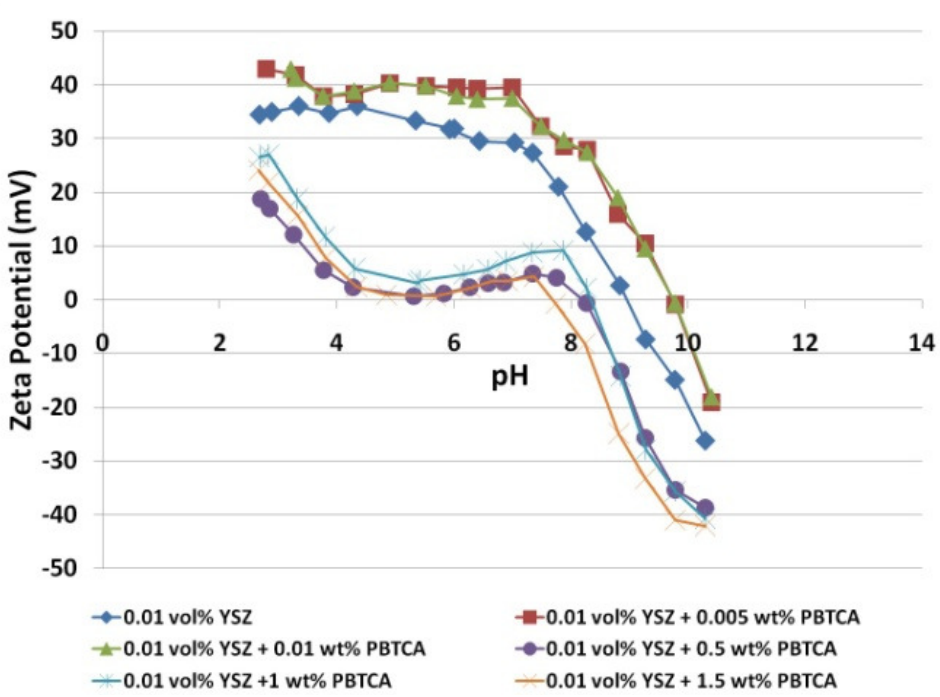

Figure I.3: Zeta potential behaviour of YSZ suspensions containing PBTCA dispersant.

I.2.3 Polyethyleneimine

A branched form of the cationic dispersant polyethyleneimine (PEI) was used for these studies. PEI has a positive charge due to the amine groups present in the molecule [4]. The structure of PEI is shown in Figure I.4. The high molecular weight and branched nature of the polymer may allow PEI to serve both as an electrostatic and a steric dispersant material.

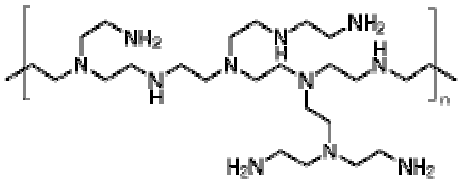

Figure I.4: PEI structure[44] [5].

PEI additions increased the positive zeta potential value and shifted the isoelectric point to higher pH values (Figure I.5). This behaviour is expected for a cationic dispersant and indicates that PEI effectively improves the suspension stability at pH values lower than the isoelectric point.

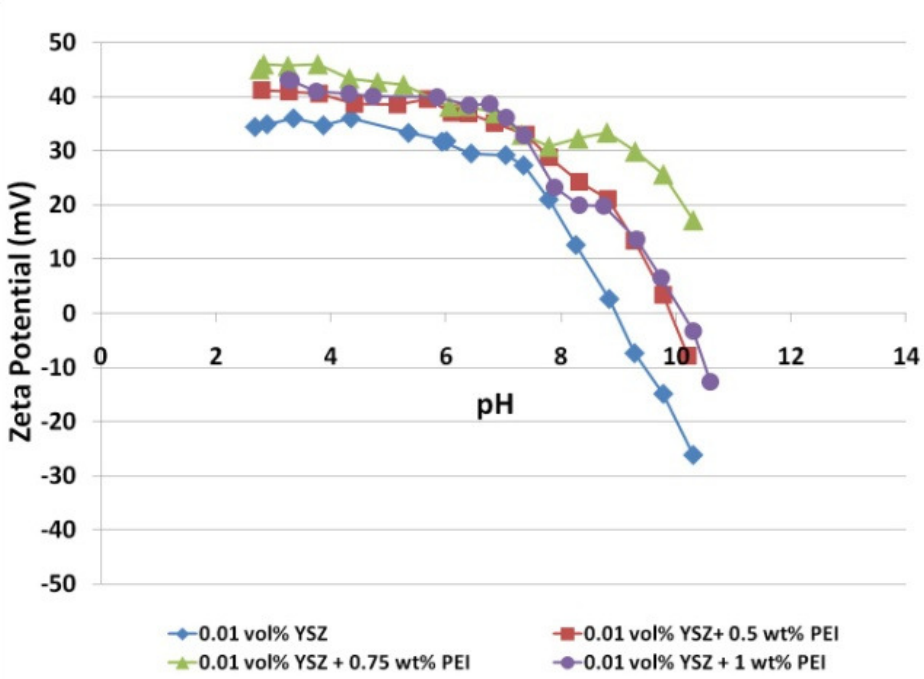

Figure I.5: Zeta potential behaviour of YSZ suspensions containing PEI dispersant.

[44] Copyrights © 2010 Sigma-Aldrich Co.

I.3 YSZ and SDC zeta potential measurements

YSZ and SDC dispersions exhibited different zeta potential behaviours likely due to the differences in surface chemistry. Little has been reported in the literature comparing the zeta potential behaviour of these materials.

I.4 Viscosity measurements

The viscosity measurements performed in the Chapter 2 work used a Thermo Haake VT550 coaxial cylinder viscometer at shear rates between 0 and 400 s^{-1}. At shear rates below 100 s^{-1}, the spindle acceleration rate had not yet reached a constant value, and as a result, the viscosity measurements were erratic. At shear rates greater than 100 s^{-1}, viscosity measurements were consistent and repeatable and the suspension followed Newtonian behaviour. Chapter 3 viscosity measurements used a sine-wave vibro viscometer in order to allow lower viscosity suspensions to be characterized with greater precision.

Initial viscosity measurements were performed at 20 vol% solid content in order to characterize the viscosity behaviour of high solid loading suspensions. High solid loading suspensions were initially targeted to provide high solid feed rate conditions to enhance the efficiency of plasma spray processes. However, subsequent spraying studies indicated that high solid loading suspensions provided too much of a thermal load on the plasma, which resulted in lower deposition efficiencies and poor coating properties. In order to improve the coating properties, later thermal spray studies used suspensions with 5 or 3 vol% solid content.

I.5 References

1. J. A. Lewis, Journal of the American Ceramic Society, 83(10) (2000), 2341-2359.
2. Y. Liu, L. Gao, Materials Chemistry and Physics 78, (2002), 480–485.
3. Y. Liu, L. Gao, Journal of the American Ceramic Society, 86(7) (2003), 1106–1113.
4. F. Tang, X. Huang, Y. Zhang, J. Guo, Ceramics International, 26 (2000), 93-97.
5. Sigma Aldich online product catalog. Retrieved May 26, 2010 from http://www.sigmaaldrich.com/catalog/ProductDetail.do?lang=fr&N4=408727|ALDRICH&N5=SEARCH_CONCAT_PNO|BRAND_KEY&F=SPEC#

J Plasma spray parameter studies

J.1 Introduction

The plasma spray parameter studies used a series of systematic experimental investigations to improve the understanding of the relationships between substrate, feedstock, and plasma spraying parameters and the resulting coating and process characteristics such as thickness, permeability, porosity, and deposition efficiency for aqueous axial injection suspension plasma sprayed YSZ layers. In total more than 300 suspension plasma sprayed coatings were produced over the course of the studies.

J.2 List of parameters studied

Table J.1 lists the parameters that were studied during the course of the thesis experiments and the range of values investigated.

Table J.1: List of parameters varied

Parameter type	Parameter	Range of values	Units
Substrate	Substrate type	Tape cast anode support, 430 stainless steel: media grade 0.2. 0.5, 1, 2, 5	
	Substrate pretreatment	Roughen with diamond file, roughen with SiC paper, sand blast, fill pores with epoxy	
Cathode	Cathode thickness	30 – 70	μm
	Cathode preheat temperature	100, 300	^{o}C
	Cathode pretreatment	No treatment, polished with 15 μm diamond paste, polished with 6 μm diamond paste	
	Cathode pore formers	No pore formers, carbon black pore formers	
Suspension	Solid content	1, 3, 5, 10, 20	vol%
	Liquid type	Water, ethanol	
	Dispersant type	None, PAA, PEI, PBTCA at concentrations determined from rheometry	
	Suspension flow rate	15 – 200	mL/min
	Suspension delivery system	Progressive cavity pump, pressurized canister	
	Suspension atomization	Atomizing gas, no atomizing gas	
Plasma spray	Preheat temperature	20, 275 - 550	^{o}C
	Stand-off distance	60 -100	mm
	Electrolyte thickness	10 - 100	μm
	Nozzle size	9.53, 11.11, 12.70, 14.30	mm
	Plasma gas flow rate	150 - 300	slpm
	Plasma gas composition	N_2: 60 – 100%, Ar: 0 – 25 %, H_2: 0 – 20%	%

J.3 Detailed list of SPS studies

J.3.1 Initial SPS studies and generation 1 suspension delivery system

The main goal of the first plasma spray study was to commission and develop the suspension delivery and injection system. These studies used the Generation 1 progressive cavity pump suspension delivery system and tape cast NiO / YSZ anode substrates. Most studies used standard plasma spray conditions that had low plasma gas flow rates (150 slpm), energetic plasma gases (100% N_2), and high currents (250 A) in order to allow the other parameters of interest to be compared (see Table J.2). The plasma spray parameters were chosen to produce conditions with long residence times and hot plasmas in order to enable good melting of the YSZ particles. A few preliminary studies that modified these standard conditions to look at the effect of solid content and liquid (water or ethanol) were made and were presented as a poster and conference paper at the 2007 International Thermal Spray Conference (ITSC) (see Appendix A). A final study was made that investigated spraying conditions with 80% N_2 / 20% H_2 plasma gas. Adding H_2 to the plasma gas increases the plasma thermal conductivity. A summary of these studies and their key findings is given in Table J.3.

Table J.2: Standard plasma spray condition parameters for early-stage spraying studies.

Parameter	Value
Plasma gas flow rate (slpm)	150
Plasma gas composition	100% N_2
Torch current (A per cathode)	250
Nozzle size (mm)	12.7
Standoff distance (mm)	80
Electrolyte preheat passes	None
Atomizing gas flow rate (slpm)	15
Suspension delivery system	Progressive cavity pump
Suspension flow rate (mL/min)	15 - 30
Suspension concentration (vol%)	5
Suspending liquid	Water
Substrate type	Tape cast NiO/ YSZ anode substrate

Table J.3: Summary of early-stage spraying studies.

Date	Parameters studied	Parameter ranges	Cell #	Key findings
Oct 2006	Gen 1 suspension delivery system commissioning	Suspension flow rate, pump speed, atomizing gas	1 - 11	• Range of delivery parameters that limited clogging was determined
Nov – Dec 2006	Liquid type and solid content	Water or Ethanol and 1, 5, 10 vol% YSZ	12 -26	• Ethanol causes clogging • Lower solid contents have higher relative DE
Jan 2007	Plasma gas composition	100% N_2 80% N_2, 20% H_2	27-30	• H_2 containing plasmas have higher DE

These initial studies also produced two additional key findings:

1. The generation 1 suspension delivery system did not provide adequate, reproducible suspension flow conditions due to the abraded stator seals.
2. Tape cast NiO / YSZ anode substrates are often broken during plasma spraying and therefore are likely too brittle to serve as support layers.

As a result of these findings, the suspension delivery system was redesigned to make it more abrasion resistant and the NiO / YSZ ceramic anode supports were replaced by porous stainless steel 430 metal supports, which are both tougher and less expensive than the NiO / YSZ ceramic supports, but require an anode or cathode layer to be deposited on the substrate before the electrolyte layer is deposited in order to provide realistic fuel cell substrate conditions.

J.3.2 Generation 2 suspension delivery system

The next series of plasma spraying studies mainly aimed to commission and develop the second generation pressurized canister suspension delivery system. These studies used standard plasma spray conditions with intermediate plasma gas flow rates (220 slpm), energetic, high thermal conductivity plasma gases (80% N_2, 20% H_2), and high currents (250

A) in order to allow the other parameters of interest to be compared (see Table J.4). The plasma spray parameters were chosen to produce conditions with faster particle velocities and hotter, more thermally conductive plasmas in order to produce denser, higher deposition efficiency coatings. Substrates were preheated before YSZ layers were deposited by passing the plasma spray torch over the substrate 10 times in an attempt to improve coating adhesion. Unfortunately it was not possible to measure the preheat temperature that was used during these early experiments. Since metal substrates were now being used, a cathode layer was deposited on the substrate first and the electrolyte layer was then deposited on the cathode layer. Cathode layer materials and spraying conditions were developed by Brad White as part of his M.A.Sc thesis work [1]. Additional studies that modified these standard conditions were made that investigated the effect of stand-off distance, suspension flow rate, cathode thickness, substrate modification, and atomizing gas on the YSZ layer thickness and permeation rate. A summary of the spraying studies and their key findings is given in Table J.5.

Table J.4: Standard plasma spray parameters for the Generation 2 suspension delivery system studies.

Parameter	Value
Plasma gas flow rate (slpm)	220
Plasma gas composition	80% N_2, 20% H_2
Torch current (A per cathode)	250
Nozzle size (mm)	12.7
Standoff distance (mm)	80
Electrolyte preheat passes	10
Atomizing gas flow rate (slpm)	15
Suspension delivery system	Generation 2 – Pressurized canister
Suspension delivery pressure (kPa)	276
Suspension flow rate (mL/min)	150
Suspension concentration (vol%)	5
Suspending liquid	Water
Substrate type	Stainless steel 430, media grade 5
Cathode type	#25, ~67 μm thick [1]

Table J.5: Summary of Generation 2 suspension delivery system studies.

Date	Parameters studied	Parameter ranges	Cell #	Key findings
July 2007	Gen 2 suspension delivery system commissioning	Canister pressure setting, suspension flow rate, atomizing gas flow	100 - 101	• Delivery parameters that produced reproducible flow rates and limited clogging were determined
July 2007	Stand-off distance	60, 80, 100 mm	102 - 105	• 100 mm SOD has higher permeation rate
Aug 2007	Suspension flow rate	105, 165 mL/min	106 – 107	• Lower suspension flow rates have lower permeation rates
Aug 2007	Cathode thickness	~ 35 and ~67 µm	108 – 110	• No clear trend – more study needed
Sept 2007	Substrate modification	Diamond file, SiC paper, sand blasting, epoxy pore filling	111 – 116	• No modification method reduced surface roughness without filling in surface pores • Epoxy was very difficult to burn out of pores without oxidizing the substrate
Sept 2007	Atomizing gas	15 slpm Ar or no atomizing gas	117 – 122	• Layers produced with no atomizing gas had similar permeation rates and greater thicknesses than layers produced with atomizing gases

These studies successfully demonstrated the ability of the second generation suspension delivery system to reliably deliver YSZ suspension without excessive wear and showed the feasibility of using porous metal substrate layers.

J.3.3 Substrate and cathode studies

The effects of metal substrate type and cathode layer thickness on the suspension plasma sprayed YSZ layer properties were investigated for four media grades of substrate and two cathode thicknesses. The same energetic plasma conditions used in previous studies were used with lower suspension flow rates and lack of atomizing gas that were shown to lower coating permeation rates and increase coating thicknesses in previous studies. The spraying

conditions used for this set of experiments are shown in Table J.6 and the spraying study results are summarized in Table J.7. These results were presented at the 2008 International Thermal Spray Conference (ITSC) and presented in a conference paper (see Appendix B).

Table J.6: Standard spray parameters for the substrate and cathode studies.

Parameter	Value
Plasma gas flow rate (slpm)	220
Plasma gas composition	80% N_2, 20% H_2
Torch current (A per cathode)	250
Nozzle size (mm)	12.7
Standoff distance (mm)	80
Electrolyte preheat passes	10
Atomizing gas flow rate (slpm)	0
Suspension delivery system	Generation 2 – Pressurized canister
Suspension delivery pressure (kPa)	138
Suspension flow rate (mL/min)	105
Suspension concentration (vol%)	5
Suspending liquid	Water
Substrate type	Stainless steel 430
Cathode type	#25 [1]

Table J.7: Summary of substrate and cathode spraying studies.

Date	Parameters studied	Parameter ranges	Cell #	Key findings
Nov 2007	Substrate type and cathode thickness	MG 0.5, 1, 2, 5 with thin (35 μm) or thick (67 μm) cathodes	123 – 137	• YSZ layers on MG 5 substrates had higher permeation rates • Thin cathode layers had difficulty filling in substrate pores

J.3.4 Dispersant studies

The effect of 3 types of dispersants (PAA, PEI, and PBTCA) on the resulting coating properties was investigated. Optimal dispersant contents were determined by rheometry.

The spraying conditions used for the experiments are shown in Table J.8 and the spraying study results are summarized in Table J.9.

Table J.8: Standard plasma spray parameters for the dispersant studies.

Parameter	Value
Plasma gas flow rate (slpm)	220
Plasma gas composition	80% N_2, 20% H_2
Torch current (A per cathode)	250
Nozzle size (mm)	12.7
Standoff distance (mm)	80
Electrolyte preheat passes	10
Atomizing gas flow rate (slpm)	15
Suspension delivery system	Generation 2 – Pressurized canister
Suspension delivery pressure (kPa)	138
Suspension flow rate (mL/min)	105
Suspension concentration (vol%)	5
Suspending liquid	Water
Substrate type	Stainless steel 430, media grade 5
Cathode type	#25, ~67 µm thick [1]

Table J.9: Summary of the dispersant spraying studies.

Date	Parameters studied	Parameter ranges	Cell #	Key findings
Dec 2007 – Jan 2008	Effect of dispersant type	0.005 wt% PAA, 0.01 wt% PBTCA, 0.01 wt% PEI	138 – 146	• Coatings made from suspensions with PBTCA additions were thicker compared to the other dispersants • Less suspension build up on the torch convergence was observed for suspensions with PBTCA dispersants

J.3.5 Preliminary SOFC testing

At this point, a good understanding of the suspension delivery system, effect of substrates, cathode layers, and suspension dispersants had been developed for the standard high energy plasma spray conditions. Therefore, a number of PS SOFCs with two different electrolyte thicknesses were produced for electrochemical testing. In addition, a thermocouple system was installed on the substrate mount that enabled the temperature of the cells to be monitored during preheating and layer deposition. A preheat temperature of 325^{o}C was used in this study based on literature values. All cells were sprayed on media grade 2 substrates with ~ 67 μm cathodes that had previously been determined to have a desirable combination of permeability and substrate pore sizes that are small enough for the cathode layer to successfully bridge over. The spraying conditions used for the experiments are shown in Table J.10 and the spraying study results are summarized in Table J.11.

Table J.10: Standard plasma spray parameters for the preliminary SOFC testing studies.

Parameter	Value
Plasma gas flow rate (slpm)	220
Plasma gas composition	80% N_2, 20% H_2
Torch current (A per cathode)	250
Nozzle size (mm)	12.7
Standoff distance (mm)	80
Electrolyte preheat temperature (^{o}C)	325
Atomizing gas flow rate (slpm)	0
Suspension delivery system	Generation 2 – Pressurized canister
Suspension delivery pressure (kPa)	138
Suspension flow rate (mL/min)	105
Suspension concentration (vol%)	5
Dispersant concentration (wt%)	0.01% PBTCA
Suspending liquid	Water
Substrate type	Stainless steel 430, media grade 5
Cathode type	#25, ~67 μm thick

Table J.11: Summary of the preliminary SOFC testing studies.

Date	Parameters studied	Parameter ranges	Cell #	Key findings
Feb – Apr 2008	El thickness, PS SOFC full cells for electrochemical testing	~30 or ~60 µm	147 – 163	• First electrochemical characterization of PS SOFC with SPS electrolytes at UBC • Low open circuit voltage values (~0.85 V) indicate further electrolyte development is required • Diffusional losses seen in electrochemical testing indicate that cathodes have insufficient porosity and cathode delamination after testing indicates that the cathode layers were not well adhered to the substrate

J.3.6 Cathode pore formers and preheat

The diffusional losses that were seen in the PS SOFCs at high current densities and cathode layer delamination from the substrate layer indicated that further cathode layer development was required. In order to address these issues, carbon black pore formers were added to the feedstock powder and the cathode layer spraying parameters were modified to add a substrate preheat to 300^{o}C in order to enhance substrate – cathode adhesion. The spraying conditions used for this set of experiments are shown in Table J.12 and the spraying study results are summarized in Table J.13.

Table J.12: Standard plasma spray parameters for cathode pore former and preheat studies.

Parameter	Value
Plasma gas flow rate (slpm)	220
Plasma gas composition	80% N_2, 20% H_2
Torch current (A per cathode)	250
Nozzle size (mm)	12.7
Standoff distance (mm)	80
Electrolyte preheat temperature (^oC)	325
Atomizing gas flow rate (slpm)	0
Suspension delivery system	Generation 2 – Pressurized canister
Suspension delivery pressure (kPa)	138
Suspension flow rate (mL/min)	105
Suspension concentration (vol%)	5
Dispersant concentration (wt%)	0.01% PBTCA
Suspending liquid	Water
Substrate type	Stainless steel 430, media grade 5
Cathode type	#25 + carbon black, ~67 μm thick
Cathode preheat temperature (^oC)	300

Table J.13: Summary of cathode pore former and preheat studies.

Date	Parameters studied	Parameter ranges	Cell #	Key findings
Apr 2008	Cathode pore formers and cathode preheating	No pore former or 16 wt% carbon black, no preheat or 300^{o}C cathode preheat	164 – 170	• Cathodes with pore formers had higher permeation rates • PS SOFC full cells with cathodes containing carbon black had lower diffusional losses during electrochemical testing • Cathode layer delamination did not occur for cathode layers that had been preheated

J.3.7 Electrolyte passes, preheat temp and stand-off distance

Once a stable substrate, cathode, and suspension platform had been developed, the effects of spraying parameters including number of electrolyte spraying passes, electrolyte

deposition preheat temperature, and stand-off distance on the coating thickness and permeation rate were investigated. The spraying conditions used for the experiments are shown in Table J.14 and the spraying study results are summarized in Table J.15. This study marked the beginning of the use of the Generation 3 suspension delivery system. This system was identical in concept to the Generation 2 system, but had been redesigned slightly in order to improve the canister sealing.

Table J.14: Standard plasma spray parameters for electrolyte pass, preheat temperature, and stand-off distance studies.

Parameter	Value
Plasma gas flow rate (slpm)	220
Plasma gas composition	80% N_2, 20% H_2
Torch current (A per cathode)	250
Nozzle size (mm)	12.7
Standoff distance (mm)	80
Electrolyte preheat temperature (^oC)	325
Atomizing gas flow rate (slpm)	0
Suspension delivery system	Generation 3 – Pressurized canister
Suspension delivery pressure (kPa)	138
Suspension flow rate (mL/min)	105
Suspension concentration (vol%)	5
Dispersant concentration (wt%)	0.01% PBTCA
Suspending liquid	Water
Substrate type	Stainless steel 430, media grade 2
Cathode type	#25 + carbon black, ~67 µm thick
Cathode preheat temperature (^oC)	300

Table J.15: Summary of electrolyte pass, preheat temperature and stand-off distance studies.

Date	Parameters studied	Parameter ranges	Cell #	Key findings
Sept 2008	Electrolyte passes	25, 50, 100 passes (25, 55, 80 μm)	171-185	• As number of passes increases electrolyte thickness increases and permeation rate decreases
	Preheat temperature	20, 325°C, 450°C		• Electrolyte layers with 20°C preheat temperature had higher permeation rates than those at 325°C or 450°C
	Stand-off distance	70, 80, 90 mm		• Stand-off distances of 80 mm produced coatings with lower permeation rates compared to those at 70 or 90 mm

J.3.8 Solid content, suspension flow rate, amount of YSZ delivered

The next studies looked at the effects of suspension solid contents, suspension flow rates, and amount of YSZ delivered on the thicknesses and permeation rates of the SPS YSZ layers. Lower solid contents and suspension flow rates were chosen for this study compared to previously examined conditions to investigate the trade off between high flow rates and solid contents that lower process time and low flow rates and solid contents that may produce denser coatings and higher deposition efficiencies by decreasing the thermal loading of the plasma.

In previous studies, spraying runs occurred for a predetermined number of passes; however, for conditions with different suspension flow rates or solid contents, this methodology results in different amounts of YSZ being delivered to the substrate and thus different YSZ layer thicknesses. It is desirable to produce coatings with similar thicknesses in order to make it easier to compare permeation rate measurements. In this series of experiments, a desired weight of YSZ was therefore set and then measurements of the suspension flow rate and the solid content within the suspension were used to calculate the number of passes required to deliver this amount of YSZ to the substrate for the desired

combinations of suspension flow rate and suspension solid content. The spraying conditions used for the experiments are shown in Table J.16 and the spraying study results are summarized in Table J.17.

Table J.16: Standard plasma spray parameters for solid content, suspension flow rate and YSZ delivery amount studies.

Parameter	Value
Plasma gas flow rate (slpm)	220
Plasma gas composition	80% N_2, 20% H_2
Torch current (A per cathode)	250
Nozzle size (mm)	12.7
Standoff distance (mm)	80
Electrolyte preheat temperature (^oC)	325
Atomizing gas flow rate (slpm)	0
Suspension delivery system	Generation 3 – Pressurized canister
Amount of YSZ delivered (g)	50
Suspension delivery pressure (kPa)	138
Suspension flow rate (mL/min)	105
Suspension concentration (vol%)	5
Dispersant concentration (wt%)	0.01% PBTCA
Suspending liquid	Water
Substrate type	Stainless steel 430, media grade 2
Cathode type	#25, ~67 μm thick
Cathode preheat temperature (^oC)	300

Table J.17: Summary of results for solid content, suspension flow rate and YSZ delivery amount studies.

Date	Parameters studied	Parameter ranges	Cell #	Key findings
Oct 2008 – Jan 2009, Apr 2009	Solid content	1, 3, 5 vol% YSZ	186 – 228, 238 – 241	• Coatings produced from from 1 and 3 vol% YSZ suspensions had lower permeation rates compared to 5 vol% but DE was unaffected
	Suspension flow rate	65, 90, 105, 135 mL/min		• As suspension flow rate decreased permeation rate was unaffected but deposition efficiency increased
	Amount of YSZ delivered	40, 50, 66.2 g YSZ		• Increasing the amount of YSZ delivered resulted in thicker coatings with lower permeation rates

J.3.9 Plasma gas flow rate

The effect of plasma gas flow rate on coating thickness and permeation rate was examined. Lower plasma gas flow rates were examined in order to increase the residence time of YSZ particles in the hot zone of the plasma in order to facilitate full melting of the particles. The spraying conditions used for those experiments are shown in Table J.18 and the spraying study results are summarized in Table J.19.

Table J.18: Standard plasma spray parameters for plasma gas flow rate studies.

Parameter	Value
Plasma gas flow rate (slpm)	220
Plasma gas composition	80% N_2, 20% H_2
Torch current (A per cathode)	250
Nozzle size (mm)	12.7
Standoff distance (mm)	80
Electrolyte preheat temperature (^oC)	325
Atomizing gas flow rate (slpm)	0
Suspension delivery system	Generation 3 – Pressurized canister
Amount of YSZ delivered (g)	50
Suspension delivery pressure (kPa)	138
Suspension flow rate (mL/min)	105
Suspension concentration (vol%)	5
Dispersant concentration (wt%)	0.01% PBTCA
Suspending liquid	Water
Substrate type	Stainless steel 430, media grade 2
Cathode type	#25, ~67 μm thick
Cathode preheat temperature (^oC)	300

Table J.19: Summary of plasma gas flow rate studies.

Date	Parameters studied	Parameter ranges	Cell #	Key findings
Feb 2009	Plasma gas flow rate	150, 185, 220 slpm	229 - 237	• Coatings produced from 150 slpm conditions were much thinner than the other coatings for the same amount of YSZ delivered • As plasma gas flow rate increased the coating permeation rate decreased

J.3.10 Plasma gas composition and flow rate and nozzle size

Previous results had indicated that higher plasma gas flow rates had a beneficial effect on permeation rate. Therefore, the effect of higher plasma gas flow rates on coating properties was investigated in this study. Another potential method to increase particle

velocity is to decrease the nozzle size. Therefore, the effect of using a smaller 11.1 mm nozzle on the coating properties was examined.

In this study, the standard spraying condition was modified to use 3 vol% YSZ suspensions and to incorporate lower suspension feed rates. Previous studies had indicated that coatings produced from lower suspension flow rates and solid contents had lowered permeation rates and increased deposition efficiencies. The choice of 3 vol% suspensions and 90 mL/min flow rates enabled the beneficial lower solid flow conditions to be used, but still maintained reasonable process times compared to using 1 vol% suspensions.

During these studies the amount of YSZ that was deposited on the substrate during SPS runs was measured. This parameter allowed the YSZ layer density to be calculated by dividing the weight gained by the substrate during electrolyte spraying runs by the spraying area and the coating thickness as measured by scanning electron microscopy (SEM). The process deposition efficiency could also be calculated as the ratio of the weight gained by the substrate during the electrolyte spraying run per unit area multiplied by the full spray area to the weight of YSZ delivered during the spraying run, as determined from suspension flow rate measurements performed during initial calibration tests without plasma gas flow.

Since these new standard conditions had lowered solid delivery rates, less energetic plasma spray conditions were also investigated to determine whether less energetic plasmas could fully melt the feedstock suspensions. The spraying conditions used for these experiments are shown in Table J.20 and the spraying study results are summarized in Table J.21.

Table J.20: Standard plasma spray parameters for plasma gas composition, plasma gas flow rate, and nozzle size studies.

Parameter	Value
Plasma gas flow rate (slpm)	220
Plasma gas composition	80% N_2, 20% H_2
Torch current (A per cathode)	250
Nozzle size (mm)	12.7
Standoff distance (mm)	80
Electrolyte preheat temperature (^oC)	325
Atomizing gas flow rate (slpm)	0
Suspension delivery system	Generation 3 – Pressurized canister
Suspension delivery pressure (kPa)	103
Suspension flow rate (mL/min)	90
Suspension concentration (vol%)	3
Dispersant concentration (wt%)	0.01% PBTCA
Suspending liquid	Water
Substrate type	Stainless steel 430, media grade 2
Cathode type	#25, ~67 μm thick
Cathode preheat temperature (^oC)	300

Table J.21: Summary of plasma gas composition, plasma gas flow rate, and nozzle size spraying studies.

Date	Parameters studied	Parameter ranges	Cell #	Key findings
May 2009	Plasma gas composition	80% N_2, 20% H_2 90% N_2, 10% H_2 80% N_2, 20% Ar	276-281	• Coatings produced from 80% N_2 / 20% H_2 and 90% N_2 / 10% H_2 plasma gases had very similar properties • Coatings produced from 80% N_2 / 20% Ar plasmas had lower DE and densities but also had lower permeation rates due to lower vertical crack densities
	Plasma gas flow rate	220, 250, 300 slpm	291 - 296	• Coatings produced using plasma gas flow rates of 250 or 300 slpm had significantly higher DE and densities than those produced at 220 slpm • 300 slpm coatings had many vertical cracks
	Nozzle size	12.7, 11.1 mm	297 - 299	• Coatings produced from 11.1 mm nozzle had higher densities, lower permeation rates, and higher deposition efficiency than those from 12.7 mm nozzles

The deposition efficiency trend seen in which conditions using the 11.1 mm nozzle had higher deposition efficiencies than the 12.7 mm nozzle spray conditions is different compared to most other nozzle studies in which larger nozzle conditions resulted in larger deposition efficiencies compared to smaller nozzles. This differing trend is likely due to the low plasma gas flow rates and high thermal conductivity used in these spray conditions, which still provided sufficient energy transfer to fully treat the particles, even at the higher particle velocities caused by the 11.1 mm nozzle. The lower plasma energies in that case were likely insufficient to keep the particles melted for a long traverse time in the plasma, so that the coatings made with the smaller nozzle and resulting higher velocity were likely

more able to prevent re-solidification prior to impact than coatings sprayed with the larger nozzle and correspondingly lower velocities at low plasma flow rates.

J.3.11 Nozzle size for low energy conditions

Previous studies had indicated that coatings produced from non-H_2 containing plasmas had lower densities but also had lower permeation rates due to the lower frequency of vertical cracking and that smaller nozzles may have a beneficial effect on coating density, permeation rate, and deposition efficiency. Two non-H_2 plasma conditions with lower plasma gas flow rates and smaller nozzles were examined to determine whether denser coatings could be produced without the vertical cracking seen for layers sprayed at high plasma gas flow rates and H_2 containing conditions. The spraying conditions used for these experiments are shown in Table J.22 and the spraying study results are summarized in Table J.23.

Table J.22: Standard plasma spray parameters for nozzle size studies at low plasma energy conditions.

Parameter	Value
Plasma gas flow rate (slpm)	200
Plasma gas composition	100% N_2
Torch current (A per cathode)	250
Nozzle size (mm)	11.1
Standoff distance (mm)	80
Electrolyte preheat temperature (^oC)	325
Atomizing gas flow rate (slpm)	0
Suspension delivery system	Generation 3 – Pressurized canister
Suspension delivery pressure (kPa)	103
Suspension flow rate (mL/min)	90
Suspension concentration (vol%)	3
Dispersant concentration (wt%)	0.01% PBTCA
Suspending liquid	Water
Substrate type	Stainless steel 430, media grade 2
Cathode type	#25, ~67 μm thick
Cathode preheat temperature (^oC)	300

Table J.23: Summary of nozzle size studies at low plasma energy conditions.

Date	Parameters studied	Parameter ranges	Cell #	Key findings
July 2009	Plasma gas flow rate, composition, and nozzle size	• 200 slpm, 100% N_2, 11.1 or 9.5 mm nozzle • 230 slpm, 87% N_2 / 13% Ar, 11.1 or 9.5 mm nozzle	303 - 321	• Coatings produced from 230 slpm conditions had higher densities, deposition efficiencies and lower permeation rates compared to 200 slpm coatings produced with the same nozzle for both nozzles studied • Coatings produced from 230 slpm conditions with 9.5 mm nozzles had increased densities and decreased permeation rates compared to 11.1 mm nozzle coatings, but also had lower deposition efficiencies

J.3.12 Small nozzle, high plasma gas flow rate

The benefit of small nozzles on coating density and permeation rate was further investigated using the smallest nozzle size investigated (9.5 mm) for high flow rate conditions. Plasma spray conditions with the maximum N_2 plasma gas flow (200 slpm) were used in order to ensure high plasma energies, 5% H_2 was added to improve plasma thermal conductivity, and Ar was added to increase the total plasma gas flow rate. It was hoped that the low H_2 content would reduce the high number of vertical cracks seen during high plasma gas flow rate conditions investigated previously with 10 or 20% H_2. The spraying conditions used for these experiments are shown in Table J.24 and the spraying study results are summarized in Table J.25.

Table J.24: Standard plasma spray parameters for studies with high plasma gas flow rates and small nozzles.

Parameter	Value
Plasma gas flow rate (slpm)	250, 275
Plasma gas composition	80% N_2, 5% H_2, 15% Ar 70% N_2, 5% H_2, 25% Ar
Torch current (A per cathode)	250
Nozzle size (mm)	9.5
Standoff distance (mm)	80
Electrolyte preheat temperature (^oC)	325
Atomizing gas flow rate (slpm)	0
Suspension delivery system	Generation 3 – Pressurized canister
Suspension delivery pressure (kPa)	103
Suspension flow rate (mL/min)	90
Suspension concentration (vol%)	3
Dispersant concentration (%)	0.01% PBTCA
Suspending liquid	Water
Substrate type	Stainless steel 430, media grade 2
Cathode type	#25, ~67 μm thick
Cathode preheat temperature (^oC)	300

Table J.25: Summary of high plasma gas flow rate, small nozzle spraying studies.

Date	Parameters studied	Parameter ranges	Cell #	Key findings
Aug 2009	Plasma gas flow rate, composition, and nozzle size	• 250 slpm, 80% N_2, 5% H_2, 15% Ar 9.5 mm nozzle • 275 slpm, 70% N_2, 5% H_2, 25% Ar 9.5 mm nozzle	322 - 337	• Coatings produced from 275 slpm conditions had higher densities, lower permeation rates, but also decreased deposition efficiencies compared to 250 slpm coatings

J.3.13 Larger stand-off distances

Coatings produced from 275 slpm plasma spray flow rates had the highest density values and lowest permeation rates of all sprayed YSZ layers but had low deposition efficiency. These trends are likely due to the high particle velocities achieved for these conditions. In order to increase the amount of time that the particles spend in the plasma and thus

potentially improve the condition deposition efficiency, larger stand-off distances were investigated. The spraying conditions used for these experiments are shown in Table J.26 and the spraying study results are summarized in Table J.27.

Table J.26: Standard plasma spray parameters for high flow rate, large stand-off distance studies.

Parameter	Value
Plasma gas flow rate (slpm)	275
Plasma gas composition	70% N_2, 5% H_2, 25% Ar
Torch current (A per cathode)	250
Nozzle size (mm)	9.5
Standoff distance (mm)	80
Electrolyte preheat temperature (^oC)	325
Atomizing gas flow rate (slpm)	0
Suspension delivery system	Generation 3 – Pressurized canister
Suspension delivery pressure (kPa)	103
Suspension flow rate (mL/min)	90
Suspension concentration (vol%)	3
Dispersant concentration (%)	0.01% PBTCA
Suspending liquid	Water
Substrate type	Stainless steel 430, media grade 2
Cathode type	#25, ~67 μm thick
Cathode preheat temperature (^oC)	300

Table J.27: Summary of high flow rate, large stand-off distance spraying studies.

Date	Parameters studied	Parameter ranges	Cell #	Key findings
Sept 2009	Stand-off distance (SOD)	80, 90, 100 mm	338 - 343	• Coatings produced at 90 mm SOD had slightly higher deposition efficiencies compared to 80 mm or 100 mm SOD • Coatings produced at 100 mm SOD had higher permeation rates compared to those produced at 80 or 90 mm which had similar permeation rates

J.3.14 PS SOFC electrochemical study

The understanding of the relationships between the substrate, suspension and plasma spray processing parameters and the resulting YSZ layer properties was used to choose three SPS conditions that produce YSZ coatings with high densities and low permeation rates for full cell electrochemical testing. Three distinct electrolyte microstructures were produced in order to determine the effect of electrolyte microstructure on the electrolyte electrochemical properties. The understanding of the process feed rates and of each condition's deposition efficiency was used to tailor the spray duration to produce coatings that were nominally 15 μm, 30 μm, and 45 μm thick in order to investigate the effect of electrolyte layer thickness on electrolyte performance. The spraying conditions used for these experiments are shown in Table J.28.

Table J.28: Summary of SPS electrolyte plasma spray parameters.

Parameter	High flow rate	Medium flow rate	Low flow rate
Plasma gas flow rate (slpm)	275	250	230
Plasma gas composition (%)	70% N_2, 25% Ar, 5% H_2	80% N_2, 15% Ar 5% H_2	87% N_2, 13% Ar
Current (A per cathode)	250	250	250
Nozzle size (mm)	9.5	9.5	9.5
Preheat temperature (°C)	300 - 350	300 - 350	300 - 350
Standoff distance (mm)	90	80	80

Key findings

- The electrochemical results are summarized in Chapter 6.
- The knowledge of the SPS process gained over the course of these experiments enabled good reproducibility of results. Very similar densities and deposition efficiencies were achieved for coatings produced in this study compared to previously deposited coatings at identical spraying conditions, as shown in Table J.29.

Table J.29: Summary of density and deposition efficiency values for coatings produced with identical spraying conditions.

Spraying condition	1st or 2nd time spraying	Cell numbers	Density (g/cm^3)	Deposition efficiency (%)
High flow rate	1st time spraying	341 - 343	5.87	15.9
	2nd time spraying	375 - 378	5.67	16.4
Medium flow rate	1st time spraying	326 - 333	5.40	30.8
	2nd time spraying	354 - 357	5.48	28.0
Low flow rate	1st time spraying	320 - 321	5.14	37.0
	2nd time spraying	364 - 367	5.12	34.8

- On average there was a 5.9 % difference between the desired thickness target and the actual layer thicknesses produced. This is ~1 μm thickness difference for the 15 μm thick coatings. This is extremely good thickness control for plasma sprayed coatings and is an example of the excellent knowledge of the SPS processes developed and the beneficial effect of SPS on PS process thickness control.

J.4 Reference

1. B.D. White, O. Kesler, L. Rose, Journal of Power Sources 178(1) (2008), 334-343.

K Open circuit voltage

K.1 Reversible open circuit voltage at standard pressure

For any chemical reaction, the change in the Gibb's free energy of formation (Δg_f) is a measure of the amount of energy released (or consumed) when the reactants react to form products that can potentially be converted to useful work. A fuel cell using hydrogen fuel combines hydrogen and oxygen reactants to form water as a product, as shown in Reaction I. This reaction requires the transfer of two electrons.

$$H_2 + ½\ O_2 \rightarrow H_2O \qquad \text{(I)}$$

The Δg_f for this reaction is the difference in the Gibb's free energy of the products and reactants, as shown in Equation 1.

$$\Delta g_f = g_{f\ H2O} - g_{f\ H2} - ½\ g_{f\ O2} \qquad (1)$$

If there are no losses in the fuel cell, then all of the Gibb's free energy is converted to electrical energy, and the process is called reversible. The standard reversible open circuit voltage (E^o) with all of the reactants at an activity of 1 can be calculated using Equation 2

$$E^o = \frac{-\Delta g_f^o}{nF} \qquad (2)$$

where: E^o is the standard reversible open circuit voltage (V)
n is the number of electrons transferred to the external circuit during the reaction
F is the charge of one mole of electrons (C/mol)

The value of n in Equation 2 is 2 for the H_2 reaction shown in Reaction I. The standard reversible voltage calculated in Equation 2 assumes that H_2, O_2, and steam are all present at the standard pressure of 1 atm.

K.2 Nernst voltage

If the fuel cell is not operating with all reactants and products at standard pressure conditions, the change in the activity of each component may be accounted for as shown in Equation 3.

$$\Delta g_f = \Delta g_f^o + RT \ln\left(\frac{a_{H_2O}}{a_{H_2}\, a_{O_2}^{1/2}}\right) \qquad (3)$$

where: Δg_f^O is the change in Gibbs free energy of formation when all reactants and products are at 1 atm partial pressure (J/mol)

R is the universal gas constant (J/mol K)

T is the temperature (K)

a_x are the activities of each component, where x = H_2, H_2O, or O_2

If all of the components are gases and the operating temperature is high (for example, 750^{o}C) each component can be treated as an ideal gas [1]. This allows each component's activity to be assumed to be equal to the component partial pressure.

When Equations 2 and 3 are combined and the activities are replaced with partial pressures an expression for the Nernst voltage (E_N) is developed (Equation 4). The Nernst voltage is the reversible cell voltage for a given temperature and partial pressures of the reactants and products.

$$E_N = E^o - \frac{RT}{nF} \ln\left(\frac{P_{H_2O}}{P_{H_2} P_{O_2}^{1/2}}\right) \qquad (4)$$

where: E_N is the Nernst voltage (V)

E^o is the standard reversible voltage when all reactants and products are at 1 atm partial pressure (V)

P_x are the partial pressures of each component, where x = H_2, H_2O, or O_2

The Nernst voltage is the maximum open circuit voltage possible for the test conditions; however, in practice, the measured cell open circuit voltage is always lower than this predicted Nernst voltage due to fuel or oxidant leakage across the electrolyte and seals. The presence of any electronic conductivity within the electrolyte layer also serves to lower the measured open circuit voltage.

K.3 Effect of temperature on Nernst voltage

As the temperature increases, the calculated reversible voltage decreases for an exothermic reaction in which entropy decreases. This occurs as a result of the negative entropy change term within the Gibb's free energy relationship the causes the Δg_f value to become less negative as temperature increases. The change in molar Gibbs free energy of formation (Δg_f), reversible standard voltage (E^o), and Nernst voltage (E_N) values for Reaction I at various temperatures are given in Table K.1. In the table, the Nernst voltages are calculated for hydrogen fuel with 3% humidity at the anode side and air at the cathode side (P_{H2} = 0.97 atm, P_{H2O} = 0.03 atm, P_{O2} = 0.21 atm).

Table K.1: Δg_f, E^o, and E_N values for Reaction 1 at various temperatures.

Temperature (^{o}C)	Δg_f^o (J/mol) [1]	E^o (V)	E_N (V)
100	-225.2	1.167	1.210
250	-217.7	1.128	1.189
500	-204.9	1.062	1.151
750	-191.6	0.993	1.112
1000	-177.4	0.921	1.069

K.4 Effect of reactant partial pressure on Nernst voltage

Reducing the partial pressure of the reactant H_2 or O_2 will cause the second term in Equation 4 to decrease, thus lowering the Nernst voltage. Table K.2 illustrates the range of

Nernst voltages for Reaction I for hydrogen concentrations between 100% and 10%. In the table, H_2 percentage values refer to a dry gas stream, while the H_2 partial pressure values refer to the same gas stream after humidification with 3% steam. The Nernst voltages have been calculated at 600, 650, 700, and 750°C with hydrogen fuel with 3% humidity and a nitrogen dilutant on the anode side and air on the cathode side.

Table K.2: Percent H_2, hydrogen partial pressure, and Nernst voltage values for Reaction I at temperatures between 600 and 750°C at fuel concentrations between 10 and 100% H_2.

Temperature (°C)	Percent H_2	H_2 partial pressure	Nernst voltage (V)
750	100%	0.97	1.112
	50%	0.485	1.081
	20%	0.194	1.041
	10%	0.097	1.010
700	100%	0.97	1.120
	50%	0.485	1.091
	20%	0.194	1.052
	10%	0.097	1.023
650	100%	0.97	1.128
	50%	0.485	1.100
	20%	0.194	1.064
	10%	0.097	1.036
600	100%	0.97	1.136
	50%	0.485	1.110
	20%	0.194	1.075
	10%	0.097	1.049

K.5 Reference

1. J. Larminie and A. Dicks, Fuel Cell Systems Explained, John Wiley & Sons Ltd., West Sussex, England, 2000.

L YSZ ionic conductivity

L.1 YSZ grain ionic conductivity

The most commonly used SOFC electrolyte material is yttria stabilized zirconia (YSZ). Yttria is added to zirconia in order to stabilize the ionically conductive cubic phase and to increase the number of oxygen ion vacancies. When Zr^{4+} ions are replaced by Y^{3+} ions, oxygen ion vacancies are produced in order to maintain charge neutrality within the crystal, and it is these oxygen ion vacancies that allow oxide ion transport through the material to occur [1]. The ionic conductivity of YSZ increases with yttria content until a maximum conductivity is achieved at approximately 8 mol%, as shown in Figure L.1. Above this concentration, the increased number of vacancies interfere with each other, which reduces vacancy mobility and thus decreases the ionic conductivity.

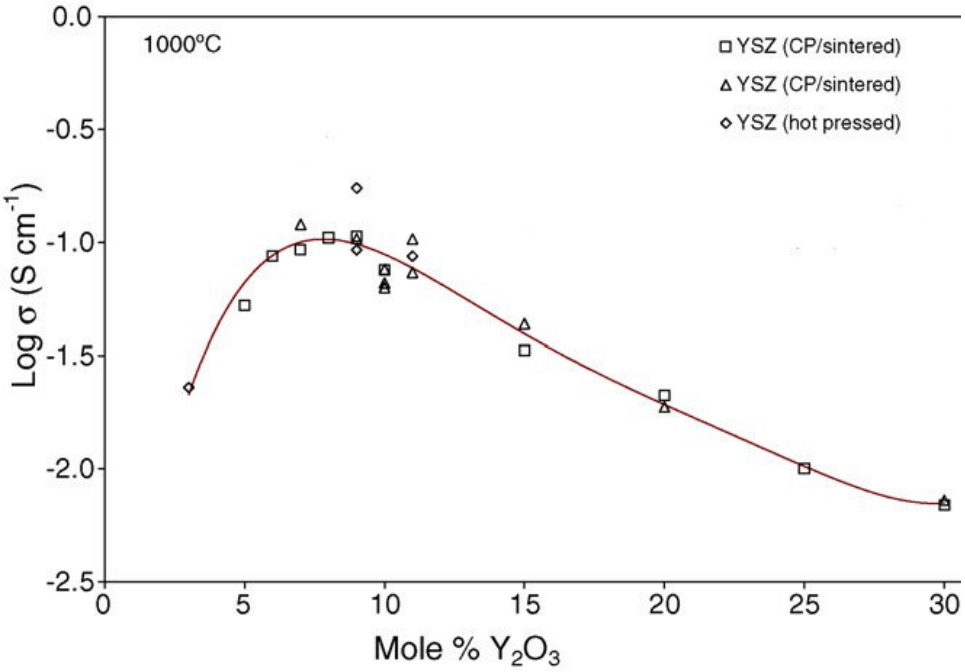

Figure L.1: Ionic conductivity of YSZ as a function of yttria content[45] [2].

[45] Reprinted from Journal of Power Sources, 162 / 1, J.W. Fergus, Electrolytes for solid oxide fuel cells, 30-40, Copyright (2006), with permission from Elsevier.

L.2 Grain boundary ionic conductivity

The grain boundaries present in YSZ may also contribute to ionic conductivity. There is extensive discussion within the literature about the contributions and limitations of grain boundary conductivity to the total ionic conductivity. According to most sources, grain boundary conductivity is at least two orders of magnitude lower than the bulk conductivity, depending on the temperature and impurity level [1,3]. For very pure materials, lower grain boundary conductivities have been attributed to lowered oxygen vacancy concentrations at the grain boundaries compared to within the grains [1]. For less pure materials, lowered grain boundary conductivity may be caused by silicon-containing phases that segregate to the grain boundaries and act as blocking layers to oxygen ion conduction [1,4 ,5].

L.3 Factors affecting conductivity

L.3.1 Porosity

Studies investigating the effect of porosity on ionic conductivity have seen a large decrease in ionic conductivity for porosity values >10% [6]. These pores impede the conduction path between grains, thus lowering the conductivity. Another study observed small decreases in the bulk conductivity and large decreases in the grain boundary conductivity for densities lower than 95%. Above 95% density, the bulk and grain boundary conductivity was unaffected by porosity [7].

L.3.2 Grain size

The effect of grain size on the grain boundary conductivity has been widely investigated and many conflicting results have been presented. It was initially thought that nanostructured YSZ layers may have significantly enhanced grain boundary conductivity, which was attributed either to an increase in the concentration of oxygen vacancies in the grain boundary as the grain size decreases due to decreases in the grain boundary core potential [1,4] or to a dilution in the concentration of impurities as the grain boundary volume

fraction increased [4,8]. Early studies showed increases in grain boundary conductivity of greater than 50 times for grain sizes less than 20 nm compared to conventional microcrystalline layers [9]. A number of later studies determined that although grain boundary conductivities might increase at very small grain sizes, the total conductivity decreases as the grain size decreases. Figure L.2 shows the conductivity of YSZ layers with grain sizes between 5 and 782 nm. The work in [10] found that coatings with smaller grain sizes have conductivities up to 98% lower than coatings with larger grain sizes due to the blocking effect of grain boundaries that impedes charge transport.

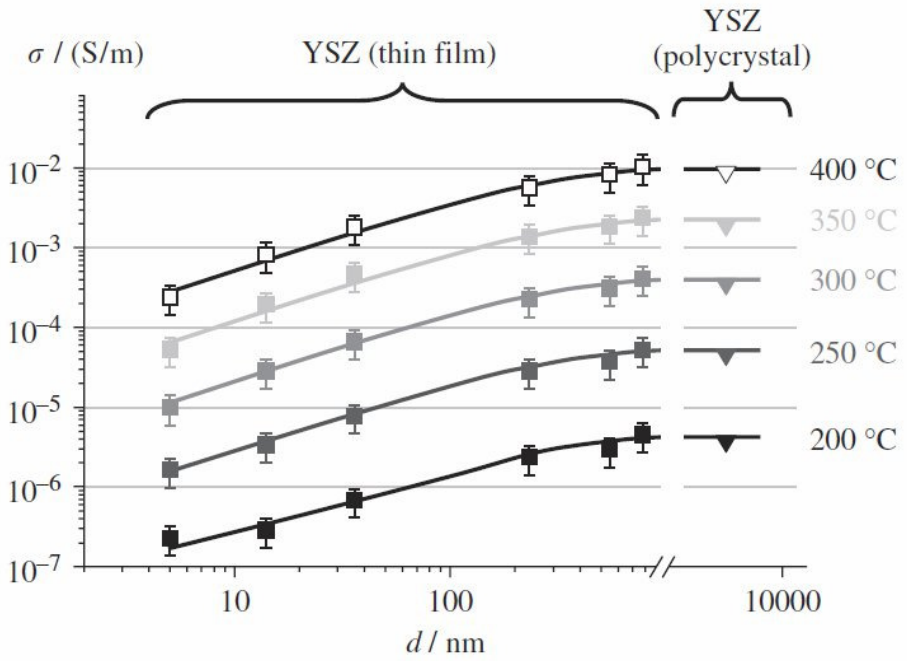

Figure L.2: Ionic conductivity of YSZ layers with various grain sizes[46] [10].

[46] Reprinted from Journal of the American Ceramic Society, 92 / 9, C. Peters, A. Weber, B. Butz, D. Gerthsen, and E. Ivers-Tiffee, Grain-Size Effects in YSZ Thin-Film Electrolytes, 2017-2024, Copyright (2009), with permission from John Wiley and Sons.

L.3.3 Impurities

Silicon is an extremely common impurity in ceramic materials and even very small Si additions have been shown to segregate at grain boundaries to form insulating phases that block grain boundary ionic conduction [1,3,4,5].

Metallic elements may be introduced to YSZ electrolyte layers during cell processing or operation or may be deliberately added to electrolyte materials to act as scavengers or sinter aids. Transition metals elements such as Mn, Fe, Co, and Ni are common components of SOFC anode and cathode layers, which are in direct contact with the YSZ electrolyte layer. During fabrication and operation, many studies have observed the diffusion of these components into the electrolyte layer [11]. In addition, acidic suspensions used for SPS may dissolve metal components in the delivery system or the plasma spray torch, introducing metal ions such as Fe, Cr, or Cu into the plasma sprayed electrolyte coatings. Metal oxides such as Fe_2O_3, Bi_2O_3, TiO_2 and Al_2O_3 have been added to scavenge the Si present in the system, with varying beneficial or detrimental results, depending on the doping and impurity level [5]. Many metallic elements such as Fe, Ti, Cr, Ni, and Mn have been added to YSZ layers in order to act as sinter aids to lower the sintering temperature required to fully densify the electrolyte layers [11].

These metallic element additions affect both the grain conductivity and the grain boundary conductivity. In most cases, these materials decrease the grain ionic conductivity or introduce mixed ionic and electronic conductivity in the YSZ layers by dissolving in the YSZ lattice [11]. The effect on grain boundary conductivity may be more complicated, depending on the impurity level of the powder, processing conditions, and dopant level. These additions may decrease grain boundary conductivity by introducing insulating phases [12] or they may increase grain boundary conductivities by promoting the formation of denser YSZ layers or by interacting with Si impurities to reduce their blocking effects [1,5,11].

L.4 Conductivity of PS YSZ layers

Two studies of the conductivity of plasma sprayed YSZ layers are highlighted here in order to compare the conductivity of plasma sprayed YSZ layers produced either from 8 mol% YSZ powders between 5 and 25 μm in size [13] or from nanocrystalline 10 mol% YSZ powders consisting of primary particles 80 to 250 nm in size that had been spray dried into spherical agglomerates 10 to 50 μm in diameter [14] to that of SPS layers and of sintered layers.

The larger YSZ powder feedstock produced layers with 8.2% porosity (determined by image analysis) and coarse microstructures with poor interlamellar contact and cracking. YSZ conductivities of 0.00059 S/cm at 600^{o}C and 0.034 S/cm at 1000^{o}C in the direction perpendicular to the coating surface were measured, which are approximately one fifth of the typical ionic conductivity values found in the literature [15]. It was also noticed that the value of ionic conductivity in the direction parallel to the coating surface was approximately double the value of conductivity perpendicular to the coating surface. These reductions in ionic conductivity and anisotropic properties were attributed to poor interlamellar contact within the layer.

Spray dried nanocrystalline feedstock powders produced coatings that were 82.7 % dense (determined by Archimedes method) with bimodal microstructures consisting of micron sized columnar grains in fully melted regions and nanocrystalline grains in partially melted/sintered regions. An ionic conductivity of 0.00198 S/cm at 600^{o}C was measured. This value is 3.3 times higher than the other PS YSZ layer made from 5-25 μm powders by APS. This result was attributed to the nanocrystalline structure of the coatings, which contradicts other results within the literature that show that nanocrystalline coatings have lower ionic conductivity values.

Figure L.3 shows a comparison of the ionic conductivity of the two plasma sprayed YSZ layers discussed above, the suspension plasma sprayed layers produced in this thesis, and a sintered YSZ electrolyte layer [2] and Table L.1 lists the conductivity values for the four compared YSZ layers at 600^{o}C.

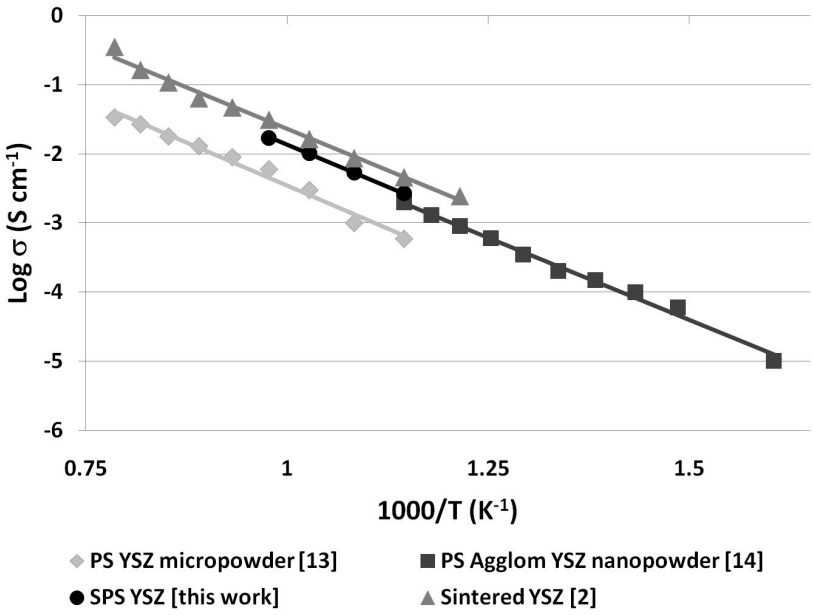

Figure L.3: Comparison of the total ionic conductivity of PS and sintered YSZ layers.

Table L.1: Ionic conductivity of PS, SPS and sintered YSZ layers at 600°C.

Layer deposition method	Feedstock primary particle size	Conductivity (S/cm)	Source
Plasma spray	5 – 25 um	0.0006	13
Plasma spray	80 – 250 nm	0.0020	14
Suspension plasma spray	1 um	0.0027	this work
Wet ceramic and sintered	Not reported	0.004	2

L.5 Comparison of grain, grain boundary, microstructural conductivities

Figure L.4 shows a comparison between literature grain and grain boundary conductivity values for a sintered YSZ layer [16] and the microstructural conductivity values measured for the three suspension plasma sprayed (SPS) microstructures (high flow rate, medium flow rate, low flow rate) studied in this thesis work. The SPS microstructural conductivities

that were measured were between 2.5 and 5 times higher than the literature grain boundary conductivity values.

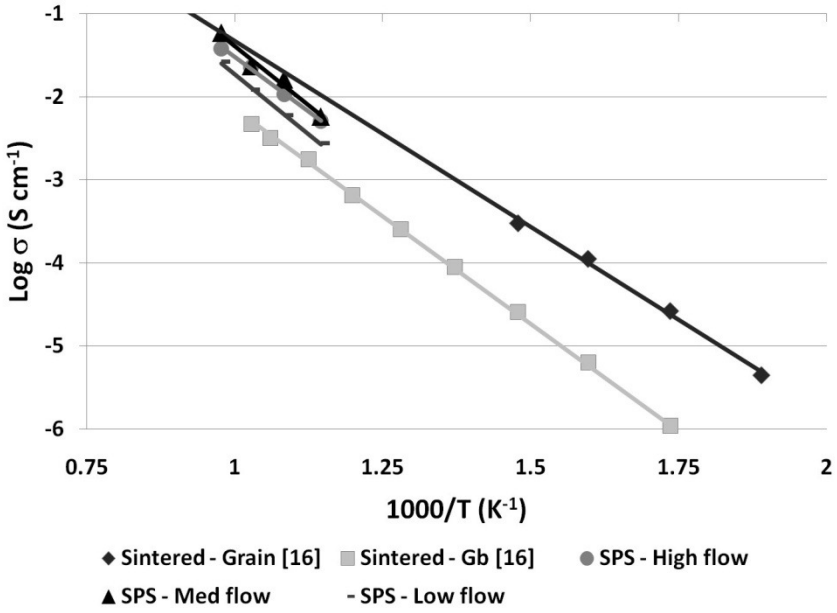

Figure L.4: Comparison of the grain, grain boundary (Gb), and microstructural conductivities for sintered and SPS YSZ layers.

The graphs shown in Figure L.4 illustrate the total value of grain, grain boundary, and microstructural conductivities; however, the spatial frequencies of the grain boundaries and microstructural features such as splat boundaries in the two coating microstructures differ and thus need to be compensated in order to compare the intrinsic grain boundary and microstructural contributions to the coating resistivities. For a certain layer thickness (for example, 10 μm), the total area specific resistance (ASR, Ω cm^2) for the grain boundaries and microstructural features can be estimated by approximating the microstructures as a series of "bricks" or grains with parallel sides, connected by "mortar", i.e., grain boundaries or splat boundaries.

If we assume that the influence of porosity is minimal, as the SPS electrolyte layers produced in high plasma flow rate conditions contain less than 5 % porosity [7], and that

there are few Si-containing blocking phases at the SPS grain boundaries due to the purity of the powder and small amount of time the SPS coating is at elevated temperatures, which limits the ability of Si to diffuse to the grain boundaries, the most influential remaining component of the microstructural resistivity is likely to be the splat boundaries.

For a certain coating thickness, the frequency of defects (grain boundaries in the sintered layer and splat boundaries in the SPS layer in the direction perpendicular to the coating) can be calculated by dividing the coating thickness by the grain size and adding 1. The grain size of the sintered layer was estimated to be ~45 nm [16] and the grain size of the high flow rate SPS layer was estimated to be ~1 μm (from Figure H.3). If the total area specific resistance contribution from each defect type (grain boundary or splat boundary) is then divided by this defect frequency, the intrinsic grain boundary and splat boundary ASR per defect can be estimated.

Calculation results of the intrinsic grain boundary and splat boundary ASR per defect are shown in Table L.2. It can be seen in the table that although the total grain boundary conductivity is 5 times smaller than the total microstructural conductivity value (or total ASR value is 5 times larger), when this value is normalized to account for the number of defects present within each coating, the calculated intrinsic grain boundary ASR is actually approximately 4 times smaller than the intrinsic splat boundary ASR.

Table L.2: Intrinsic grain boundary and splat boundary ASR per defect calculation for 10 μm thick sintered and SPS YSZ layers at 700°C.

	Sintered YSZ	**High flow rate SPS YSZ**
Total grain boundary or microstructural conductivity (S /cm)	0.0046	0.0227
Total grain boundary or microstructural ASR for a 10 μm thick coating (Ω cm^2)	0.2174	0.0441
Grain size (μm)	0.045 [16]	1 (from Fig. H.3)
Defect frequency in a 10 μm thick layer	223	11
Grain boundary or splat boundary intrinsic ASR (Ω cm^2 / defect)	0.00098	0.00401

L.6 References

1. X. Guo, R. Waser, Progress in Materials Science, 51(2) (2006), 151–210.
2. J.W. Fergus, Journal of Power Sources, 162(1) (2006), 30–40.
3. S. Hui, J. Roller, S. Yick, X. Zhang, C. Deces-Petit, Y. Xie, R. Maric, D. Ghosh, Journal of Power Sources, 172(2) (2007), 493–502.
4. N.H. Perry, T.O. Mason, Solid State Ionics, 181(5-7) (2010), 276–284.
5. J.H. Lee, T. Mori, J.G. Li, T. Ikegami, M. Komatsu, and H. Haneda, Journal of the Electrochemical Society, 147 (7) (2000), 2822-2829.
6. T. Okubo and H. Nagamoto, Journal of Materials Science, 30(3) (1995), 749-757.
7. I.R. Gibson, G. P. Dransfield, J.T.S. Irvine, Journal of Materials Science, 33(17) (1998), 4297-4305.
8. I. Kosacki, T. Suzuki, V. Petrovsky, H.U. Anderson, Solid State Ionics, 136 (2000) 1225–1233.
9. I. Kosacki, C.M. Rouleau, P.F. Becher, J. Bentley, D.H. Lowndes, Solid State Ionics, 176(13-14) (2005) 1319–1326.
10. C. Peters, A. Weber, B. Butz, D. Gerthsen, and E. Ivers-Tiffee, Journal of the American Ceramic Society, 92(9) (2009), 2017–2024.
11. T.S. Zhang, Z.H. Du, S. Li, L.B. Kong, X.C. Song, J. Lu, J. Ma, Solid State Ionics, 180(23-25) (2009), 1311–1317.
12. A.J. Feighery, J.T.S. Irvine, Solid State Ionics, 121(1-4) (1999), 209–216.
13. C. Zhang, C.J. Li, G. Zhang, X.J. Ning, C.X. Li, H. Liao, C. Coddet, Materials Science and Engineering B, 137(1-3) (2007), 24–30.
14. Y. Chen, S. Omar, A.K. Keshri, K. Balani, K. Babu, J.C. Nino, S. Seal and A. Agarwal, Scripta Materialia, 60(11) (2009), 1023–1026.
15. E. Ivers-Tiffee, A. Weber, D. Herbstritt, Journal of the European Ceramic Society, 21(10-11) (2001), 1805–1811.
16. H.J. Parka and Y.H. Choa, Electrochemical and Solid-State Letters, 13(5) (2010), K49-K52.

M Error in measurements

M.1 Thickness

Layer thickness values were measured directly from polished SEM cross sectional images. Between 15 and 40 vertical electrolyte thickness measurements evenly spaced over three to five regions of the sample cross sectional length (25.4 mm) were averaged in order to calculate the coating thickness. These vertical measurements represent an average electrolyte thickness value and are thus not entirely representative of the path of gas leakage within the electrolyte layer. Within the electrolyte layers there may be areas of localized thinning that may provide shorter transport paths than predicted, or there may be areas containing connected tortuous porosity that might increase the transport path. The standard deviation of the set of thickness measurements was used to generate error bars for all figures containing thickness. In the figures, the error bars spanned one standard deviation in the positive direction and one standard deviation in the negative direction. Typical standard deviation values were ~10% of the average thickness value. Variations in electrolyte thickness measurements were likely caused in part by the rough LSM/YSZ composite cathode layers on which the electrolyte was deposited. Electrolyte layers deposited on previously-polished cathodes, in contrast, resulted in ~50% lower thickness variability, with ~5% standard deviations from the average thickness values observed. The vertical nature of thickness measurements taken will

M.2 Density

Layer density was calculated by dividing the weight gained by the substrate during electrolyte spraying runs by the spraying area and the coating thickness as measured by scanning electron microscopy (SEM). The large scatter in density values is due to variations in electrolyte coating thickness measurements, which typically had standard deviation values that were ~10% of the average value. Error bars in figures containing density spanned one standard deviation in the positive direction and one standard deviation in the negative direction.

M.3 Deposition efficiency

Deposition efficiency was calculated as the ratio of the weight gained by the substrate during the electrolyte spraying run per unit area multiplied by the full spray area to the weight of YSZ delivered during the spraying run, as determined from suspension flow rate measurements performed during initial calibration tests without plasma gas flow. The primary source of error in the deposition efficiency calculations is variation in the suspension flow rate measurements. Repeated flow rate measurements were observed to vary by approximately 5% for a given feed pressure, and the error bars in the figures plotting deposition efficiency reflect this value.

It should be noted that all such deposition efficiency calculations underestimate the deposition efficiency of powder reaching the substrate area, because acceleration and deceleration times of the torch robot are not taken into account when using the full spray area to calculate the process deposition efficiency. On the other hand, overspray (spraying of powders outside of the substrate area) is also not accounted for in the deposition efficiency calculations. The underestimation of deposition efficiency values, while not quantified in this study, is assumed to be constant for all of the spraying conditions examined, since it is caused by the acceleration and deceleration times of the torch robot, which were the same for all coatings studied.

M.4 Permeation rate

Helium permeation measurements were performed using an in-house designed fixture in order to measure the gas permeability of the substrates and each deposited layer. The supply of helium gas was regulated by a pressure controller and the flow through the sample was then measured at the outlet of the fixture by a mass flow meter. Permeation rate measurements were usually reproducible within approximately a 5% variation in repeated measurements on the same cell. The error bars in the figures containing permeation rates reflect this 5% variability in measurements. Other sources of error in permeation rate could include leakage within the test fixture or fittings or error in the mass flow measurements by the flow meter.

M.5 Permeability

Darcy's law was used to calculate the permeability of the deposited layers from the measured permeation rates and layer thicknesses. Thus error bars for the permeability values include the error values from thickness measurements and from permeation rates. In order to combine error values, the individual thickness and permeation rate errors were converted to percent error values. The individual percent error values were squared and then added together. Finally, the square root of the sum was taken. Permeability error values were typically approximately 10% of the average permeability values.

M.6 Surface roughness

The surface roughness of the uncoated and coated samples was measured using surface profilometry. Average surface roughness values for each sample were calculated from a minimum of 6 individual roughness measurements. The standard deviation of the set of surface roughness measurements was used to generate error bars for all figures containing roughness. In the figures, the error bars spanned one standard deviation in the positive direction and one standard deviation in the negative direction. Surface roughness values typically had standard deviation values that were ~9% of the average roughness value.

Additional error may have been introduced in these measurements due to the form analysis software that was used to correct for any deviation from horizontal, which used a least squares arc geometric reference.

N X-Ray diffraction measurements

N.1 X-Ray diffraction

X-Ray diffraction (XRD) was used to determine the phases present in the deposited YSZ electrolyte layer. The resulting spectrum is shown in Figure N.1. A single cubic YSZ phase was observed in the deposited coatings. This phase was a good match for the 2θ values of a cubic YSZ standard pattern from the powder diffraction file database used to analyze the spectrum (x values on the graph) [1].

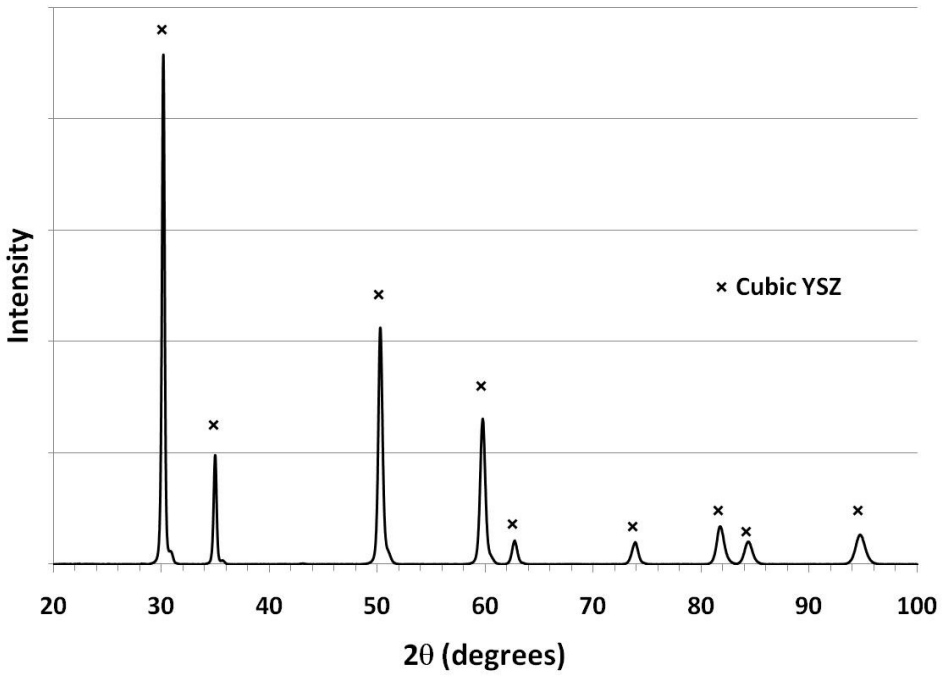

Figure N.1: XRD pattern of the deposited YSZ layer.

N.2 Reference

1. PDF #00-030-1468 in EVA database, Bruker AXS, Madison, WI, USA.